Roberto Serpieri

A Novel Constitutive Model of Composite Materials with Unidirectional Long Fibers

A Novel Constitutive Model of Composite Materials with Unidirectional Long Fibers: Theoretical Aspects and Computational Issues

Roberto Serpieri

Comunità Europea
Fondo Sociale Europeo

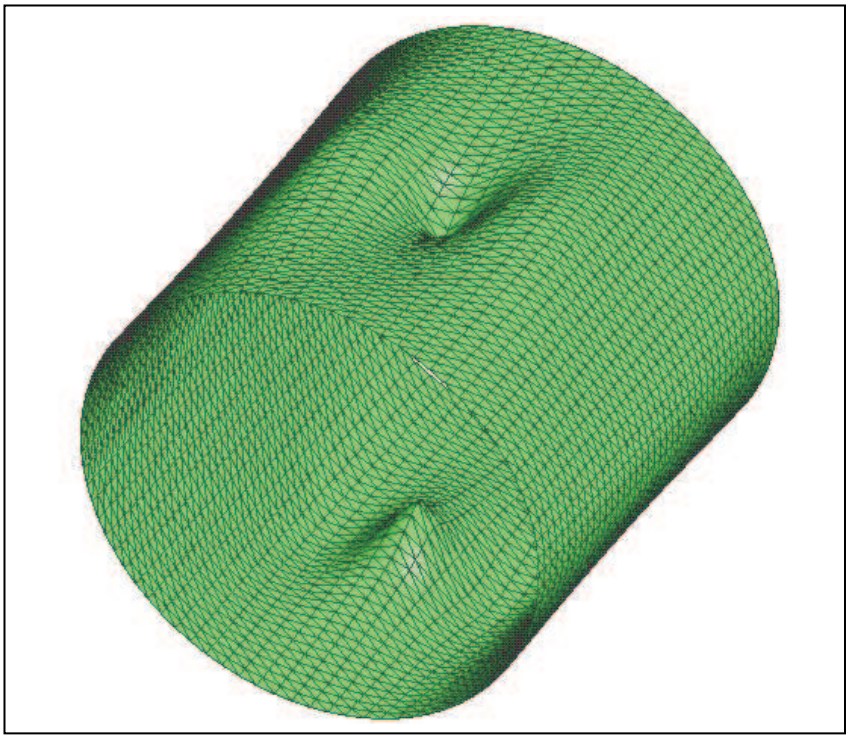

Dottorato di Ricerca in Ingegneria delle Costruzioni

Università degli Studi di Napoli "Federico II"

Facoltà di Ingegneria

Roberto Serpieri

A Novel Constitutive Model of Composite Materials with Unidirectional Long Fibers: Theoretical Aspects and Computational Issues

Tesi di Dottorato

XVIII Ciclo

Comunità Europea
Fondo Sociale Europeo

2005

Dottorato di Ricerca in Ingegneria delle Costruzioni

Università degli Studi di Napoli
Federico II

Facoltà di Ingegneria

A Novel Constitutive Model of Composite Materials with Unidirectional Long Fibers: Theoretical Aspects and Computational Issues

Roberto Serpieri

Dissertation submitted in fulfillment
of the requirements for the degree of
Doctor of Philosophy
in
Structural Engineering

November 2005

Supervisors: prof. Luciano Rosati, prof. Sergio Oller

Co-supervisors: dr. Giulio Alfano, dr. Nunziante Valoroso

Acknowledgements

The present research work has been carried out partly at the Department of Structural Mechanics of the University of Naples Federico II and partly at the Department of Strength of Materials and Structural Engineering of the Polytechnic University of Catalonia. I am indebted to many people for their support and encouragement while preparing this dissertation.

The persons I want to thank, without whom I am sure that this thesis would not exist at all, are: prof. Luciano Rosati, head of the Computational Mechanics Group, for being a guide from a professional and a human point of view and for giving me the uncommon opportunity to study abroad; prof. Sergio Oller, for having kindly received me at Barcelona, opened up the structures of the department and directed me towards the computational mechanics applied to composite materials; prof. Eugenio Oñate for his hospitality at CIMNE; my companion of long days of work, Fernando Rastellini for having shared with me the results of years of his work with COMET, point of departure for a common growth which has finally led to the results presented in this dissertation; last but not least my family who has always supported me in any possible way.

I want to thank warmly dr. Giulio Alfano without whose precious proof-reading and advises this dissertation would exist in a sensibly more imperfect form. I want to thank dr. Nunzio Valoroso for his help in supervising and editing the present document. I also want to thank all the other friends and people who directly or indirectly have supported me or have constituted a positive stimulus for me in any form while writing this dissertation: Loli, Joaquìn, Carlos Labra, Noel, Roberto, Xavi, Riccardo, Giuseppe Viglialoro, Giuseppe Simonelli, Alejandra, Dorian, Sergio, Carlos Ferrari, Guillermo, Pablo, Gerardo, Rosa, dr. Omar Salomon, dr. Alfredo Huespe and dr. Juan Carlos Cante.

Finally, I want to thank my girlfriend Ilaria for her love, support and patience...

Napoli, November 2005

ROBERTO SERPIERI

Contents

List of Figures

List of Tables

Chapter 1

Introduction

The employment of Long Fiber Composites (LFC) has extensively developed in the automotive [67] and aeronautical [55] industry during the last 40 years. This has been due, mainly, to their excellent mechanical properties among which we mention the high strength-to-weight and stiffness-to-weight ratios [59], [57], [12]. During the same period a great theoretical effort has been spent in the analysis of LFC and in the construction of a mathematical basis for the description of their complex micro and macro mechanics [51], [100], [49], [115], [19], [97]; consequently, a large amount of literature addressing constitutive models for LFC has appeared [32], [3], [114], [13].

Despite these considerations, it is remarkable that reliance upon the effectiveness of the failure prediction theories and of the constitutive models devised for Fiber Reinforced Polymer composite materials (FRP) in order to aid the design of composite structures has not coupled to the reliance upon the structural properties of this class of materials. In this respect, it is worth being mentioned the recent ascertainment by Hinton and Soden, [52] who affirmed that *current commercial design practices place little or no reliance on the ability to predict the ultimate strength of the structure with any great accuracy.* To date, the design practice is based mainly on a 'make and test' approach which employs experimental tests on coupons or structural elements.

In the last decade, this perspective has begun to change since the pressing need of industry to continuously reduce the time and cost of bringing new components to the market place is presently calling for improved design methods. Besides, the will of industry to optimize the design of new products and to exploit the performance of FRPs in ever more complex applications requires refined

constitutive models which allow one to perform realistic structural analyses and failure predictions, and at the same time, the possibility of an efficient implementation in a finite element code. In this way it becomes possible to exploit the large amount of Finite Element technology which has been already developed and is currently employed for metallic materials.

The design of a constitutive model with the above mentioned features is not a simple task since, as emerged early in the sixties, a realistic analysis of structural members made of FRP composites requires, both at the micro and macro-scales, a proper account of the non-linear stress-strain relationships. Even the modeling of a single lamina appears to be quite complex since phenomena like fracture, delamination, microbuckling and large deformations have to be considered together with their mutual interactions. Besides, it is well known, when analyzing laminated structures in the non-linear range, that it is essential to consider the behavior of each lamina separately; this circumstance further increases the complexity of the problem.

Furthermore, in the analysis of FRP laminates it is essential to distinguish between fiber failure and matrix failure as well as between fiber degradation and matrix degradation [80]. This observation constitutes a severe limitation for those models which consider the composite as an equivalent continuum and employ exclusively state variables and governing equations which refer to the whole homogenized material. Indeed, the techniques employed in the analysis of homogeneous isotropic materials are not adequate in the analysis of FRP composite materials as well as the modelling of the composite as a single orthotropic material possessing the homogeneized properties proves to be not satisfactory.

The main source of difficulty for the design of an adequate constitutive model is the double-scale nature of the problem. The microstructure of a LFC, even if small when compared to the macroscopic dimensions, has to be thought of as a 'real' structure and consequently it deserves the same degree of accuracy and detail in the approximation as a 'real' structure. In this respect, the direct use of the Finite Element Method would require to tailor of the geometrical dimension of the mesh on the basis of the characteristic microscopic dimensions of the material what unavoidably leads to solving problems with a large number of unknowns. For this reason several different methods based upon a multi-scale approach has recently appeared (see [129] for a survey). However, as shown in [129], the computational cost of a complete double-scale approach for a large scale non-linear structural analysis is still not affordable by ordinary computers, even with parallel computations.

With the aim of designing reliable methods of analysis possessing, at the same time, accuracy and a reasonable computational effort, several models have recently appeared which adopt a compromise solution based on the abstraction of the microscale by means of a *multi-material* approach. The essential feature of these methods is to avoid a complete double-scale analysis by modelling the microscale through an analytical approach which employs one, or even more, set of state parameters associated with each one of the constituent phases of the composite. In this way the composite behaviour is assumed to depend on the constitutive laws of each component material, their volume fractions and their morphological distribution inside the composite.

In particular, to the former category belongs the model proposed by Dvorak et al. [32] denominated Vanishing Diameter Fiber. Such a model accounts for the constraint exerted by aligned continuous elastic fibers embedded in an elasto-plastic matrix. The result is a homogeneous anisotropic elastoplastic material elastically constrained in fiber direction. The model accounts for load sharing between fiber and matrix in the axial direction but fails to consider the interaction fibers-matrix in any other direction. This leads to a response which underestimates the transverse and shear stiffness, as observed by the authors themselves, providing predictions below the lower bounds determined by Hill [50].

The more refined method of cells (MOC) formulated by Aboudi [3], [5] belongs to the same class of models. This method is based on the construction of macroscopic stress-strain equations for the periodic cylindrical Representative Volume Element (RVE) through an approximate elasticity analysis of the repeating unit cell based on discretizing the RVE as a regular arrays of subcells. These equations are used to calculate approximate stress and strain concentration matrices and overall stiffness matrices of the composite which are employed in stiffness predictions, the definition of failure criteria and for carrying out visco-plastic analyses. However, a general non-linear constitutive model for the composite is not formulated except for the application of the Ramberg-Osgood equation to very-special load histories.

A further example of multi-material model is the Classical Mixing Theory (CMT) whose simpler expression is the Rule Of Mixtures (ROM). First studied in 1960 by Truesdell and Toupin [122], who established the basis for subsequent developments [42], [73], [70], CMT takes into account the volumetric fraction of components but not their morphological distribution since it assumes that all component materials exhibit the same strain state in all directions (pure parallel behaviour). This hypothesis represents a strong limitation to the use of the

CMT for predicting the behaviour of most composites so that modifications to this theory have been developed [21], [66], [22], [92], [91].

Within the same framework of multi-material methods, a novel constitutive model and the related computational methodology are presented in the present thesis for modelling the non-linear material behaviour of structures made of composite laminates constituted by a matrix reinforced with unidirectional long fibers. The proposed model is based on the combined use of the constitutive models of component materials, considered to behave as isolated continua, together with additional 'closure equations' that characterize the micromechanics of the composite from a morphological point of view. Though arbitrary constitutive models can be exploited for each phase attention is restricted to linearized kinematics and to a purely mechanical theory.

The rationale of the proposed model is represented by a Serial-Parallel continuum approach which has been developed assuming that components behave in parallel along the fibers alignment direction and in series along all directions orthogonal to the fibers. Its basic version, denominated BSP model, allows for equal component strains in the fiber direction and equal stresses in the transverse directions. A preliminary version of the BSP model has been first sketched by Rastellini and Oller [93] to account for component materials with additive plasticity and/or damage in elastic stiffness. The generalized version illustrated here allows for the composition of materials with any non-linear constitutive behaviours though leaving unaltered the closure equation originally exploited in [32] and in [93].

The Enhanced version of the model, ESP model, encompasses generalized closure equations specifically devised to improve the estimate of the transversal stiffness predicted by the BSP. Nevertheless, it is worth being emphasized that both the BSP and the ESP models are able to capture, though at different levels of accuracy, basic non-linear behaviours of LFC while classical micro-mechanical formulas are restricted to linear elasticity.

Both BSP and ESP models have been implemented in a finite element code used to perform an extensive set of numerical simulations.

To this end both models, which refer to a single composite lamina, are further combined with classical lamination theory to describe the behaviour of laminates consisting of unidirectional continuously reinforced layers.

The accuracy attained in the simulation of the non-linear response of FRP composite laminates has been ascertained by means of a comparative analysis of the numerical results with analogous analytic and experimental results published

in the literature. Specifically, the validation of the constitutive model by means of experimental results has been achieved by adopting the general protocol set forth in the blind prediction named *WorldWide Failure Exercise (WWFE)*, proposed in 1998 in a special edition of the journal *Composites Science and Technology* [52].

The main outcome of this set of validations is a good overall performance of the ESP model which can be summarized as follows:

1. accurate estimates of the initial elastic stiffness, in good agreement with the values provided by Halpin-Tsai formulas;

2. accurate modelling of the nonlinear stress-strain curves of the composite;

3. estimates of the failure envelopes which are comparable with those obtained by Puck [84] and Tsai [63], i.e. the authors who ranked at the first places in the WWFE;

4. quadratic convergence of the nonlinear constitutive algorithm under the assumption that the constitutive algorithms employed for each component material do possess the same feature.

The thesis is organized in six chapters which are briefly summarized hereafter for the reader's convenience.

The second chapter presents a survey of the foremost existing theories for the failure prediction in long fiber composite laminates with the objective of selecting reliable terms of comparison for the models proposed in the present thesis. A second objective is to provide a summary on the existing theories of long fiber composites based upon multi-material approaches.

The purpose of the third chapter is to describe the constitutive model of composite materials with long fibers and to address its implementation in a FE code. The first part outlines the mathematical structure and motivates the equations governing the proposed model, denominated Serial Parallel, both in its Basic (BSP) and Serial Enhanced (ESP) forms, while the second part is concerned with a computational strategy specifically devised for the numerical solution of the local system of nonlinear algebraic equations arising from the above-mentioned constitutive equations.

The fourth chapter shows and discusses the results of several numerical analyses devised to test the response of BSP and ESP models both in terms of reliability of the predicted constitutive response and of the associated computational

burden. The numerical tests are divided in two groups which refer, respectively, to general validations of the two models performed on the unidirectional lamina and tests carried out to assess their predictive capability against experimental data included in the WWFE. All the validations are performed on a isoparametric hexahedral element with a laminated structure, whenever required. The first group refers to stiffness validations against theoretical and experimental data, strength validations against well-established theoretical formulas and computational issues pertaining to the convergence rate of the non-linear algorithm both at the local (Gauss point) level and at the element level. Several constitutive models have been taken into account, namely isotropic linear elasticity, J2 plasticity models exhibiting both a perfectly plastic or a hardening/softening behaviour, a damage model accounting for different limits in tension and compression [24]. The second group of validations is concerned with a direct comparison of the predictive capabilities of the proposed models against some of the experimental tests included in the Worlwide Failure Exercise [109], [108] which is considered to be a reliable and complete set of benchmark test cases.

The fifth chapter is devoted to the theoretical and computational issues concerning an effective FEM analysis of laminated composite large scale structures employing the constitutive model discussed in the previous chapters combined with isoparametric 3D elements and laminated shell elements.

The reason for the use of the latter type of elements is motivated and discussed together with the shortcomings connected with the reliability of Equivalent Single Layer (ESL) theories in the analysis of composite laminated structures. The theoretical issues of the structural theory which has been employed and the tasks aiming to a FEM formulation of a laminated shell element, obtained by assembling at the global level a Discrete Kirchhoff Triangle (DKT) ESL laminated element and an analogous Constant Stress Triangle ESL element, are thoroughly detailed. A subsection is devoted to the assessment of the correct implementation of the proposed laminated shell element in COMET's [28] elements library by means of benchmark tests.

Finally, the sixth chapter presents the comparison of the results predicted by the theoretical models and computational techniques proposed in the thesis with the experimental results obtained on glass-epoxy and carbon-epoxy LFC specimens subject to traction and bending tests. Specifically, the numerical analyses have been performed by employing the ESP constitutive model in conjunction with either exahedral isoparametric first order elements or the laminated ESL-DKT-CST shell elements presented in chapter five. The experimental data have

been kindly provided by CIMNE (Centro Internacional de Métodos Numéricos en Ingeniería) where a large part of the study has been conducted.

Chapter 2

Predicting non-linear response in FRP: theoretical and experimental issues

2.1 Introduction

The objective of this chapter is twofold. On the one hand, it intends to perform a survey on the foremost existing theories for the prediction of failure in long fiber composite laminates with the objective of selecting reliable terms of comparison for the model proposed in the present thesis.

On the other hand, the second objective is to provide a summary on the existing theories of long fiber composites which follow an approach similar to that adopted for the formulation of the novel model presented in this work.

The selection of a 'foremost' theory for the prediction of failure in composite laminates requires a preliminary focus on the current general opinion of the scientific and engineering communities. Since the 1950s, indeed, there has been a continuous stream of work on the investigation of the failure of composite materials within the academic community ([100], [45], [47], [49], [5], [19], just to give some examples). The amount of papers containing a major theoretical content has far exceeded in number the quantity of papers dealing with experimental data on the response of FRP materials when subjected to biaxial and triaxial stresses.

Among the great number of theories, methods and computer programs that have been produced it is not easy to discern the most reliable approaches. The literature contains numerous attempts to conduct comparisons between competing theories and between theory and experiment ([43], [116], [74], [118]).

This previous work has provided valuable insights into the various theoretical approaches at the base of the current failure theories, the variety of modes of failure which laminates exhibit and the many experimental difficulties which tend to preclude the observation of true materials failure. Despite this valuable work it is symptomatic that, at an 'experts meeting' held at St Alban's (UK) in 1991, on the subject of 'Failure of Polymeric Composites and Structures: Mechanisms and Criteria for the Prediction of Performance' [101], the attendees concluded that, even at the lamina or laminate level, there was a "lack of evidence to show whether any of the criteria could provide accurate and meaningful predictions of failure over anything other than a very limited range of circumstances".

This meeting constituted the stimulus for the organization by Hinton and Soden of the 'World Wide Failure Exercise'[52], [109]. This coordinated study, whose first related publication dates to1998 had the objectives of "establishing the current level of maturity of theories for predicting the failure response of fibre reinforced plastic (FRP) laminates; closing the knowledge gap between theoreticians and design practitioners in this field; stimulating the composites community into providing design engineers with more robust and accurate failure prediction methods, and the confidence to use them".

By means of a 'blind-prediction approach' articulated in two stages (Part A and Part B) the organizers assembled a comprehensive description of the current, foremost, failure theories for fibre reinforced plastic laminates; compared their predictive capabilities both with each other and with experimental data.

The final response was that, in predicting the response of a single unidirectional lamina, which is our first concern within our model, the two approaches of Tsai [124], [63] and Puck [81], [84] were the highest ranked and were recommended by the organizers for design practice and reputed capable of ensuring reasonably conservative predictions of all the lamina failure envelopes. These two theoretical approaches showed also a good behaviour in the analysis of laminates,

In particular for the analysis of laminates Puck's theory proved to be reliable in the predictions for the single lamina and, in general, gave conservative predictions of initial failure stress for all the test cases considered in the benchmark. It was therefore recommended for designing against initial failure.

In view of the above mentioned considerations the present chapter provides a

report of the theoretical approach of Tsai and Puck and reports the failure predictions given by the two authors that, within the work carried out for the present thesis, have been simulated also with the novel model presently formulated.

The final sections of the chapter are dedicated to the 'Vanishing Diameter Fibre Model' of Dvorak, to the Method of Cell (MOC) of Aboudi and the mixing theory of Oller. These models which belong respectively to the early 80s and to the 90s have several common points with the model presented in chapter 3. Therefore it is instructive for the reader to get some preliminary details upon these two topics.

2.2 The phenomenological theory by Puck and Schürmann

The method of analysis of FRP and the underlying theory contributed by Puck and Schürmann deserve special attention since the predictions provided by these authors proved to be in good agreement with the experimental results proposed in [53], ranking first within the parameters of evaluation selected by the organizers of the Worldwide Failure Exercise, as shown in figure 2.1. Puck's theoretical failure envelopes for the unidirectional laminae were in very good agreement with the experimental results, while the predicted final failure envelopes and stress/strain curves for the multi-directional laminates were also generally in good agreement with the measured ones.

The theory proposed by these authors is based on extensive experimental studies of the mechanisms by which failure occurs in a lamina when subjected to a biaxial stress state [79], [80]. The 'experimental' origin of Puck's theory is denoted by the great number of different phenomenological models placed on a solid physical basis which contributes to its definition.

The method is rather articulated and its core consists in the analysis of the single lamina through the combination of several fracture criteria and degradation models. The analysis of a whole laminate is performed by a computer program which matches together the ply by ply analysis of stress and strain in the single laminas.

The analysis of the single lamina, even if it employs several micromechanical considerations on the stress and strain of matrix and fiber, is essentially based on fracture criteria and degradation models directly formulated on the stress and

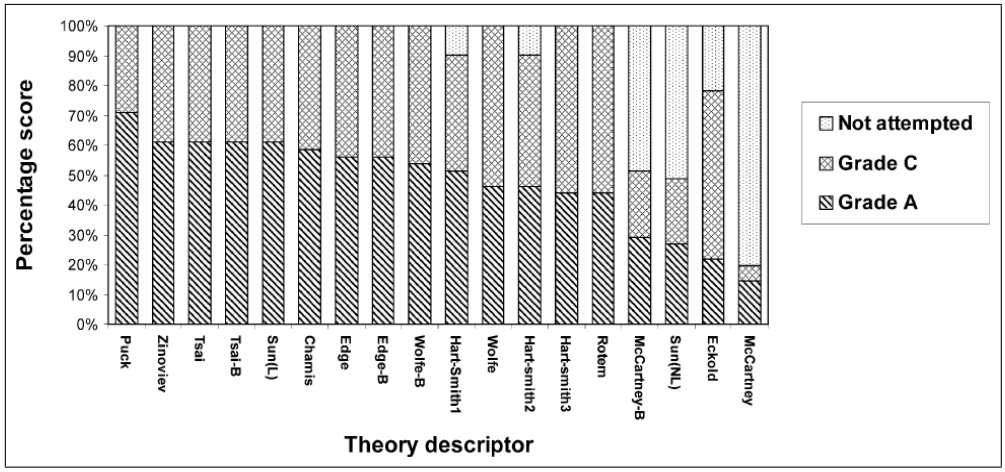

Figure 2.1: WWFE ranking of the failure theories according to their ability to predict the general features exhibited in the test results.

strain of the whole composite. Using the same symbology employed by the authors, the components of stress of the composite are denoted by $\sigma_1, \sigma_2, \sigma_3, \tau_{12}, \tau_{13}, \tau_{23}$, and the corresponding strain components by $\varepsilon_1, \varepsilon_2, \varepsilon_3, \gamma_{12}, \gamma_{13}, \gamma_{23}$ being x_1 the coordinate in the fibre direction and x_3 the coordinate in the thickness direction of the lamina. The stress strain laws are calculated by Puck and Schürmann with the Classical Laminate Theory (CLT) to which are added two fundamental modifications to address the non-linear behaviour: 1) the method employs, instead of the tangent elastic moduli, the secant moduli G_{12} and $E_2(E_2 < 0)$ deduced from the experimental non-linear stress-strain relationships $\tau_{12}(\gamma_{12})$ and $\sigma_2(\varepsilon_2)$ in compression of the unidirectional lamina.; 2) the secant stiffness moduli quantities are subjected to a complex selective degradation after exceeding the crack initiation limit.

Modification one is carried out by approximating the non-linear stress strain curves $\tau_{12}(\gamma_{12})$ and $\sigma_2(\varepsilon_2)$ through splines and by considering also, in presence of related experimental data, an optional interaction effect between these two nonlinearities. The second part of the model that accounts for the degradation due to fibre and inter-fibre cracking is based on a very sophisticated 'continuum damage'-like scheme which requires a detailed description.

The model is based on two scalar 'continuum damage'-like variables that con-

stitute a 'measure' of the damage. More precisely, Puck and Schürmann call the measure of damage in the fibre the *fiber failure effort* , and denote it by $f_{E(FF)}$, while they call the measure of damage in the matrix *inter-fiber failure effort* and denote it by $f_{E(IFF)}$. A value of the effort $f_{E(FF)} < 1$ or $f_{E(IFF)} < 1$ implies that in the load step no further damage has been produced while 'fictitious trial' values greater than one trigger the degradation of the secant stiffness parameters of the whole composite (η reduction factor) and the degradation of the fracture resistances (f_w reduction factor). The reduced strength and stiffness parameters are then used to compute again the stresses until an iterative calculation yields again efforts contained in the admissible $[0, 1]$ range.

The definition of the model requires the specification of the failure conditions for matrix and fibre which provide, as output, respectively $f_{E(FF)}$ and $f_{E(IFF)}$ and the definition of the degradation models whose output are the two parameters: f_w and η.

The theory accounts also for the presence of residual stresses due to the combined effect of cooling the laminate after curing at elevated temperatures and of moisture absorption. When the particular laminate and load condition presuppose (this is the case of not-optimally designed laminates) large shear deformations, due to fibres rotation, the analysis is carried out employing large deformations. In the present survey we will not consider how Puck deals with such effects.

2.2.1 Failure condition for the fiber

The failure in the fibers is considered to be achieved when the following stress condition is met by the stress component σ_{f1} in the fiber:

$$\sigma_{f1} = X_{fT} \quad \text{for} \quad \sigma_{f1} \geq 0$$

$$\sigma_{f1} = -X_{fC} \quad \text{for} \quad \sigma_{f1} \leq 0.$$

X_{fT} and $X_{fC}$are the tensile stress or the compressive stress in the fiber which

are reached under ultimate uniaxial tensile or compressive load and not the resistancces of single fibres or fibre bundles. While X_{fT} can be regarded as the 'true' tensile strength of the fibre (embedded in the composite), X_{fC} is usually not the 'true' compressive strength of the fibre, because, at $\sigma_{f1} < 0$, failure mostly occurs through elastic instability (microbuckling or kinking) [100] of the

fibres embedded elastically in the matrix. σ_{f1} is related by Puck and coworkers in an elastic isotropic fashion to the longitudinal and transverse normal strains of the composite:

$$\sigma_{f1} = E_{f1}\varepsilon_1 + \nu_{f12} m_{\sigma f} \sigma_2,$$

where $m_{\sigma f}$ accounts for a 'stress magnification effect' caused by the different moduli of fibres and matrix in the σ_2 direction, which leads to an uneven distribution of the stress σ_2 from a micromechanical point of view. The failure condition under combined normal loading achieves, accordingly, the following expression:

$$\begin{aligned} \frac{1}{\varepsilon_{1T}} \left(\varepsilon_1 + \frac{\nu_{f12}}{E_{f1}} m_{\sigma f} \sigma_2 \right) &= 1 \quad \text{for extension,} \\ \frac{1}{\varepsilon_{1C}} \left(\varepsilon_1 + \frac{\nu_{f12}}{E_{f1}} m_{\sigma f} \sigma_2 \right) &= -1 \quad \text{for compression,} \end{aligned}$$

where $\varepsilon_{1T} = \dfrac{X_{fT}}{E_{f1}}$ and $\varepsilon_{1C} = \dfrac{X_{fC}}{E_{f1}}$.

The previous failure criteria is further enhanced to account for the well known experimental results (microbuckling) showing that the compressive strength X_C is strongly reduced when a significant shear stress τ_{12} is superimposed. Puck does not agree with the interaction formula provided by Edge [35] (the experimental literature on this subject is rather controverse, see also [78], [46]) and, instead, includes the shear effect in the previous failure criteria by the introduction of a merely empirical correction factor depending from the shear strain γ_{12}:

$$\frac{1}{\varepsilon_{1C}} \left| \left(\varepsilon_1 + \frac{\nu_{f12}}{E_{f1}} m_{\sigma f} \sigma_2 \right) \right| + (10\gamma_{12})^2 = 1 \quad \text{for compression.}$$

The left side of this failure condition, when regarded as a function of the variables in the first side, provides the fiber effort $f_{E(FF)}$:

$$f_{E(FF)} = \frac{1}{\varepsilon_{1C}} \left| \left(\varepsilon_1 + \frac{\nu_{f12}}{E_{f1}} m_{\sigma f} \sigma_2 \right) \right| + (10\gamma_{12})^2.$$

2.2.2 Failure conditions for the inter-fibre failure

The model used to analyze matrix cracking is founded by Puck on a complex fracture criteria based on a phenomenological approach which gathers together several experimental evidences. The experimental evidence that carbon-fibre/epoxy

and glass-fibre/epoxy laminates behave in a very brittle manner at failure [48] induces Puck to formulate a Mohr-like failure criteria. In analogy with Mohr's criterion Puck proceeds on the hypothesis that fracture is exclusively originated by the stresses which act on the fracture plane. Different experimental considerations are then introduced. At the basis of the whole model Puck puts the consideration that, due to the morphology of the fibrous structure the main responsibility for the potential onset of fracture and subsequent degradation has to be addressed to the family of inclined planes parallel to the fibres direction which can be individuated by the angle formed with the thickness direction θ. Accordingly, the stress acting on these planes is decomposed in σ_n, τ_{n1} and τ_{nt}, where τ_{n1} is the component parallel to fibre direction and τ_{nt} the transverse component; as shown in figure 2.2.

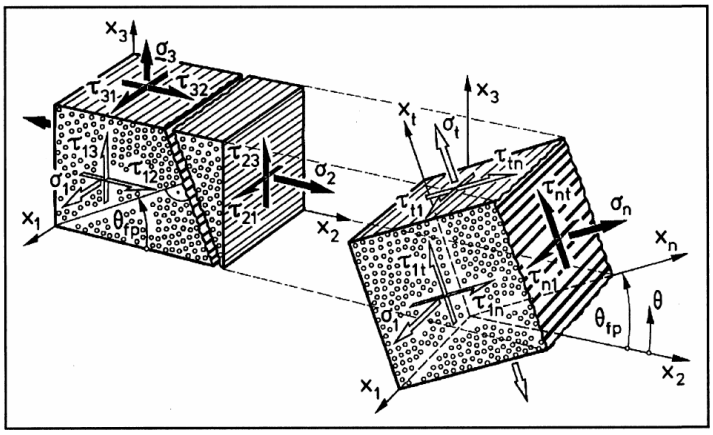

Figure 2.2: Decomposition of stresses acting on a potential fracture plane.

In perfect analogy with Mohr's criterion, the model proceeds on the hypothesis that fracture is exclusively created by the stresses which act on the fracture plane. The fracture criteria is defined accordingly involving the stress components acting on the plane σ_n, τ_{n1} and τ_{nt} and quantities that measure the resistance of the potential fracture plane: $R_{\perp}^{(+)A}$, $R_{\perp\perp}^{A}$, $R_{\perp//}^{A}$. $R_{\perp}^{(+)A}$ is the resistance attained on such planes when only tensile normal stress is applied, $R_{\perp\perp}^{A}$ is the resistance attained when only shear stress in the transverse direction is applied and $R_{\perp//}^{A}$ is the resistance attained when only shear stress in fibre direction is applied.

Symmetry considerations confirmed by experimental evidence lead to the occurrence that the sign of the shear stress components τ_{n1} and τ_{nt} does not have influence in the fracture criteria. Conversely, it is extremely important, as usual when dealing with brittle materials, to consider the different effect of a compressive and a tensile normal stress σ_n. In particular, in presence of a compressive stress Puck considers a friction-like law for shear resistances:

$$R^A_{\perp\perp\sigma} = R^A_{\perp\perp} - p^-_{\perp\perp}\sigma_n,$$

$$R^A_{\perp//\sigma} = R^A_{\perp//} - p^-_{\perp//}\sigma_n,$$

being $p^-_{\perp\perp}$ and $p^-_{\perp//}$ the counterpats of the friction angles in a Mohr-Coulomb criterion.

In view of the previous considerations, the most general failure criteria employed by Puck and Schürmann for a 3D epoxy LFC material are the following:

$$\left(\frac{\sigma_n}{R^{(+)A}_{\perp}}\right)^2 + \left(\frac{\tau_{nt}}{R^A_{\perp\perp}}\right)^2 + \left(\frac{\tau_{n1}}{R^A_{\perp//}}\right)^2 = 1 \quad \text{for} \quad \sigma_n \geq 0 \qquad (2.1)$$

$$\left(\frac{\tau_{nt}}{R^A_{\perp\perp} - p^-_{\perp\perp}\sigma_n}\right)^2 + \left(\frac{\tau_{n1}}{R^A_{\perp//} - p^-_{\perp//}\sigma_n}\right)^2 = 1 \quad \text{for} \quad \sigma_n \leq 0. \qquad (2.2)$$

Both fracture conditions of equations (2.1) or (2.2) have been further modified, as follows, to agree with experimental results and to reduce the computational burden:

$$c_2\left(\frac{\sigma_n}{R^{(+)A}_{\perp}}\right)^2 + c_1\frac{\sigma_n}{R^{(+)A}_{\perp}} + \left(\frac{\tau_{nt}}{R^A_{\perp\perp}}\right)^2 + \left(\frac{\tau_{n1}}{R^A_{\perp//}}\right)^2 = 1 \quad \text{for} \quad \sigma_n \geq 0, \qquad (2.3)$$

$$\left(\frac{\tau_{nt}}{R^A_{\perp\perp}}\right)^2 + \left(\frac{\tau_{n1}}{R^A_{\perp//}}\right)^2 + 2\left(\frac{p}{R}\right)\sigma_n = 1 \quad \text{for} \quad \sigma_n \leq 0, \qquad (2.4)$$

where it is assumed that:

$$\frac{p^-_{\perp\perp}}{R^A_{\perp\perp}} = \frac{p^-_{\perp//}}{R^A_{\perp//}} = \left(\frac{p}{R}\right),$$

and c_1 and c_2 are modification factors introduced in [83], in order to achieve a better agreement with experimental results. The fracture surface in the (σ_n,

τ_{n1}, τ_{nt}) space is an ellipsoid on the tensile side and a paraboloid with parabolic contours and elliptical cross-sections in the compressive one; see figure 2.3.

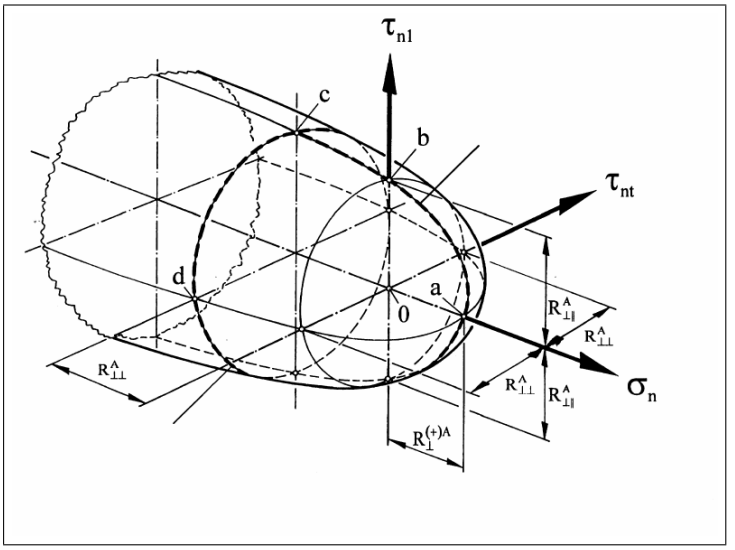

Figure 2.3: Puck's fracture domain in the (σ_n, τ_{n1}, τ_{nt}) space.

As it will be detailed in the next sections, the attainment of the failure through (2.3) or (2.4) strongly determines the post-cracking degradation in relation to crack opening or closure and is an information of the greatest relevance in Puck's degradation model.

Equations (2.3) and (2.4) are associated to a single plane π_θ. The left-hand sides determine the inter-fiber failure effort $f_{E(IFF)\theta}$ for such θ inclined layer. The overall inter-fiber failure effort $f_{E(IFF)}$ for the material point is defined as the maximum upon the whole family of layers parallel to the direction of fibres. This calculation is performed by Puck, in the general three-dimensional case, by imposing the stationary condition:

$$\frac{d}{d\theta} f_{E(IFF)}(\theta) = 0. \tag{2.5}$$

To define a fracture criteria, equation (2.5) has to be expressed as a function of the stresses referred to the global reference frame.

For the particular case of a unidirectional lamina with an in-plane plane-stress state the previous equation undergoes a sensible simplification. In this case $\sigma_3 = 0$, $\tau_{13} = 0$, $\tau_{23} = 0$ and the following trasformation holds for stresses:

$$\begin{aligned} \sigma_n &= \sigma_2 \cos^2\theta, \\ \tau_{nt} &= -\sigma_2 \sin\theta\cos\theta, \\ \tau_{n1} &= \tau_{12}\cos\theta. \end{aligned}$$

In this case it is both intuitive, and confirmed by equation (2.3), that $R_{\perp}^{(+)A}$ and $R_{\perp//}^{A}$ can be identified, respectively, with the transverse tensile normal strength Y_T and with the in-plane shear strength S_{12} of the unidirectional lamina:

$$R_{\perp}^{(+)A} = Y_T$$

$$R_{\perp//}^{A} = S_{12}.$$

The previous result is due to the fact that if $\sigma_2 \geq 0$ then equation (2.3) implies that the fracture angle θ is always equal to zero, i.e. the fracture plane is produced in the thickness direction. In this case equation (2.3) achieves the expression:

$$c_2\left(\frac{\sigma_2}{R_{\perp}^{(+)A}}\right)^2 + c_1\frac{\sigma_2}{R_{\perp}^{(+)A}} + \left(\frac{\tau_{21}}{R_{\perp//}^{A}}\right)^2 = 1 \quad \text{for} \quad \sigma_2 \geq 0. \tag{2.6}$$

Puck in [83] obtains for (2.6) the alternative expression:

$$\sqrt{\left(\frac{\tau_{21}}{R_{\perp//}^{A}}\right)^2 + \left(1 - \frac{p_{\perp//}^{+}}{R_{\perp//}^{A}}R_{\perp//}^{(+)A}\right)^2\left(\frac{\sigma_2}{R_{\perp}^{(+)A}}\right)^2} + \frac{p_{\perp//}^{+}}{R_{\perp//}^{A}}\sigma_2 = 1 \quad \text{for} \quad \sigma_2 \geq 0. \tag{2.7}$$

The fracture mechanism described by equation (2.7) is denomitated Mode A. For the domain of compression, where fracture is governed by equation (2.4), two kinds of fracture can occur. There is a part of the envelope where the fracture angle is $\theta = 0$; this fracture mechanism is called Mode B. Equation (2.4) admits also a fracture mechanism, denominated Mode C, which is originated at a fracture angle around 45°. The existence of such mechanism is confirmed by the experimental analysis of such laminates and, since the angle can not be determined a priori, the exact determination of the inter-fiber failure effort $f_{E(IFF)}$ is less straightforward.

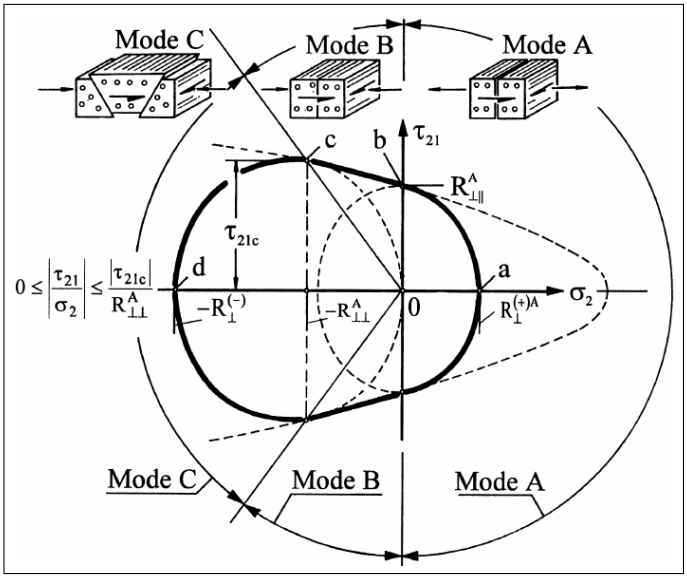

Figure 2.4: Fracture domain in the plane (σ_2, τ_{21}).

2.2.3 Degradation due to the single fibre failure

Since fibre strength follows a statistical distribution, single fibres already break under uniaxial σ_1 tensile stress long before the fracture of the majority of fibres leads to ultimate failure when Y_T is reached. These preliminary breaks of isolated fibers cause local damage in the vicinity of the breaks in the form of debonding of fibre and matrix and microcracks in the matrix. The fracture resistances that the composite opposes to inter-fibre fracture are decreased by the damage due to the above mentioned debonding and microcracks. This phenomenon is taken into account by Puck by equally decreasing all fracture resistances $R_{\perp}^{(+)A}$, $R_{\perp\perp}^{A}$, $R_{\perp//}^{A}$ with a weakening factor f_w. Within the iterative method described, the following expression is assigned to this factor:

$$f_w = 1 - \left(0,9 f_{E(FF)}\right)^n,$$

where n is determined experimentally and usually achieves a high value $6 \le n \le 8$. On an experimental basis it is assumed that degradation of the fracture resistances can only be detected when $\sigma_{1d} \ge 70\% X$. The same degradation is considered for compressive and longitudinal fiber failure efforts $f_{E(IFF)}$.

Puck and Schürmann warn that, apart from single fibre breaks, loading the composite with a longitudinal stress σ_1 always induces also a stress in the matrix in the x_1 direction because fibre and matrix act as parallel springs. In some works ([79], [80], [81], [82]) an additional term in the fracture conditions $(\sigma_1/\sigma_{1mf})^2$ is introduced, where σ_{1mf} represents matrix failure. In other works the authors are inclined to cancel this term out, since it is suspected that a matrix stress acting in the fibre direction does not have a noticeable effect on fracture, as long as the strain to failure of the matrix is considerably higher than that of the fibre. In this case the effect of matrix stresses in the longitudinal direction x_1 is completely neglected.

2.2.4 Degradation due to the inter-fibre crack initiation

Following an approach very similar to continuum damage mechanics, the degradation of matrix due to inter-fibre crack formation is simulated by Puck and Schürmann by means of the reduction of those stiffness parameters that are mainly affected by such degradation i.e. the secant moduli E_{2s} and G_{12s} and the poisson's ratio ν_{12}. The reduction is performed selectively according to the fracture mode activated. For inter-fibre fracture in mode A, since the phenomenon is related to crack opening, the reduction is applied to all the three parameters E_{2s}, G_{12s} and ν_{12} by multiplication for a factor $\eta < 1$ which is decreased gradually until the iterative calculation yields again an 'admissible' effort $f_{E(IFF)} = 1$. For inter-fibre failure of Modes B and C, contact between the cracked surfacesmust be taken into account; accordingly the modulus E_{2s} experiments minor or no reduction and only the secant modulus G_{12s} is reduced by a factor η. In presence of experimental information the curves $\eta(f_{E(IFF)})$ can be determined experimentally as figure 2.5 shows. The reduced stiffness parameters are used to compute again the stresses of the current load step until this iterative calculation yields again $f_{E(IFF)} = 1$.

Figures 2.6, 2.7 and 2.8 report the failure envelopes determined by Puck for the E-Glass/epoxy LY556 laminates compared against the relevant experimental data [36], [62], [58].

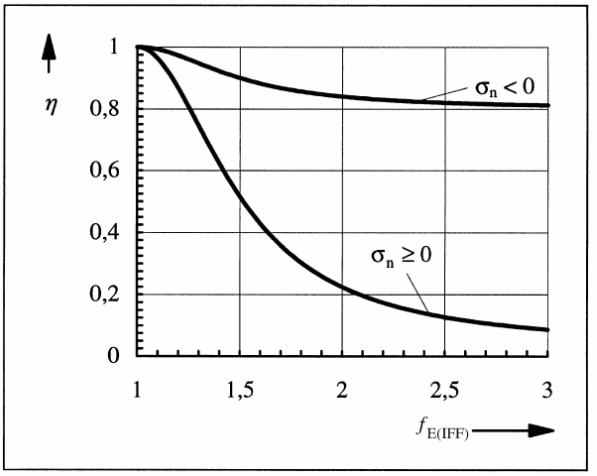

Figure 2.5: Degradation curves for compressive and tensile normal stress.

2.3 The progressive failure methodology by Tsai

The methodology employed by Tsai in [63] is considered in this chapter for two reasons. First of all it proved to be in the leading group of the theories tested in the 'exercise' of Hinton. The second reason is that, despite the good results obtained, Tsai uses a methodological approach which is just the opposite of Puck's one. Tsai's theory is not intended to capture the detailed physics associated with the various failure mechanisms and for this reason it presents the advantage, very important in the design practice, of resulting much simpler. This simplicity is mainly due to the fact that Tsai's theory is based on the quadratic Tsai–Wu failure criterion. The price of this simplicity is, as Hinton has remarked, that the initial fracture envelopes predicted for the multidirectional laminates are in poor agreement with the experiments. Besides, for the unidirectional lamina and for the quasi-isotropic multidirectional laminates, the theory predicts an enhancement of the strength under compression-compression biaxial loading which is not realistic. The theory is linear-elastic and it cannot predict the large non-linear strains observed in test cases where high lamina shear is involved.

The methodology is based on the 'progressive failure scenario' outlined by the flow chart of figure 2.9. For a given load step, a ply by ply linear analysis is used to determine the ply in which the minimum strength ratio R emerging from

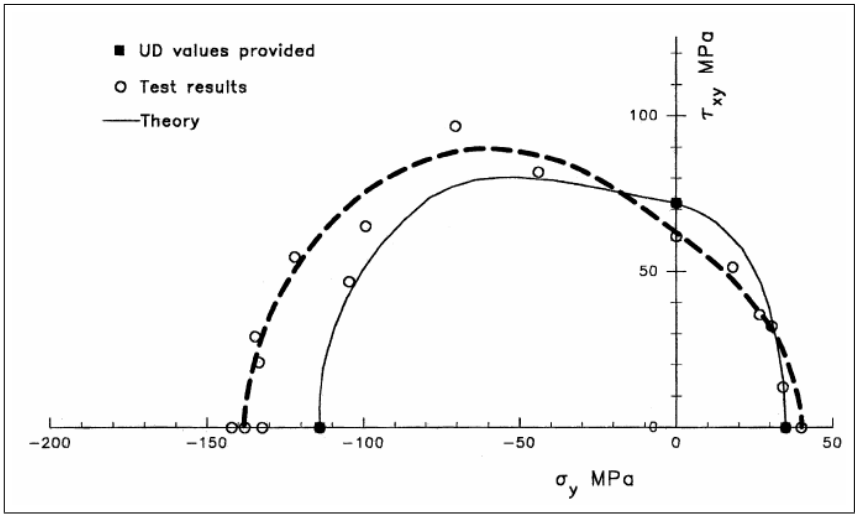

Figure 2.6: - Biaxial failure stress envelope for 0° unidirectional lamina made of E-Glass LY556 under combined transverse and shear loading -. Prediction by Puck and Schürmann compared against experimental data.

the quadratic failure criterion of Tsai-Wu is achieved. For this ply a selective degradation of the elastic properties is carried out. The process of progressive failures on a ply-by-ply basis is iterated until the ultimate load of the laminate is determined as the maximum load reached, beyond which the load reduces as additional plies fail.

2.3.1 Quadratic failure criterion

The failure of the single ply in plane-stress is described by the following two-dimensional specialization of a general quadratic criterion in the stress space:

$$\frac{\sigma_x^2}{XX'} + \frac{2F_{xy}^*\sigma_x\sigma_y}{\sqrt{XX'YY'}} + \frac{\sigma_y^2}{YY'} + \frac{\sigma_{xy}^2}{S^2} + \left[\frac{1}{X} - \frac{1}{X'}\right]\sigma_x + \left[\frac{1}{Y} - \frac{1}{Y'}\right]\sigma_y = 1. \quad (2.8)$$

In equation (2.8) X and X' are the longitudinal tensile and compressive strengths; Y and Y' are the transverse tensile and compressive strengths; σ_{xy} is the in-plane component of shear stress; S is the in-plane shear strength and F_{xy}^* is an interaction term between σ_x and σ_y that, in order to ensure that the failure envelope

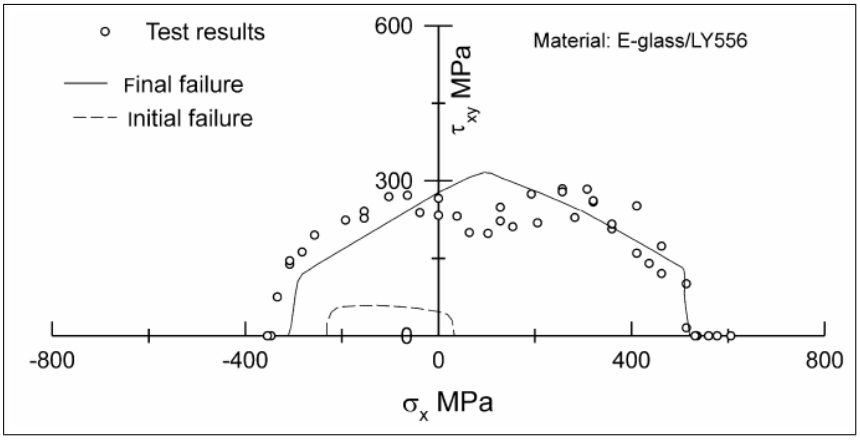

Figure 2.7: - Biaxial failure stress envelope for $90°/\pm 30°/90°$ laminate made of E-Glass LY556 under combined longitudinal and shear loading -. Prediction by Puck and Schürmann compared against experimental data.

is bounded, has to fulfill:

$$-1 < F^*_{xy} < 1.$$

This interaction term has to be determined by combined stress tests. Further bounds for this term are obtained by considering a more restrictive shape of the envelope (e.g. enforcing convexity). The values adopted by Tsai for the materials proposed in the failure exercise and for two additional common CFRP and GRP materials are reported in the table of figure 2.10.Tsai adopts for all the four materials of the 'worldwide failure exercise' the average value $F^*_{xy} = -1/2$ which characterizes the so-called generalized Von Mises model. Associated to a quadratic criterion and to a generic plane-stress state $\sigma_i (i = x, y, xy)$ one can introduce the strength ratio R. This is classically defined as the amplification factor which makes the stress state attain the failure condition. Assuming $\sigma_1 = \sigma_y$ Re-writing the quadratic failure condition as:

$$F_{ij}\sigma_i^{\max}\sigma_j^{\max} + F_i\sigma_i^{\max} = 1,$$

since $\sigma_i^{\max} = R\sigma_i$, the strength ratio is provided by the resolution of the following quadratic equation:

$$\left(F_{ij}\sigma_i\sigma_j\right)R^2 + \left(F_i\sigma_i\right)R - 1 = 0.$$

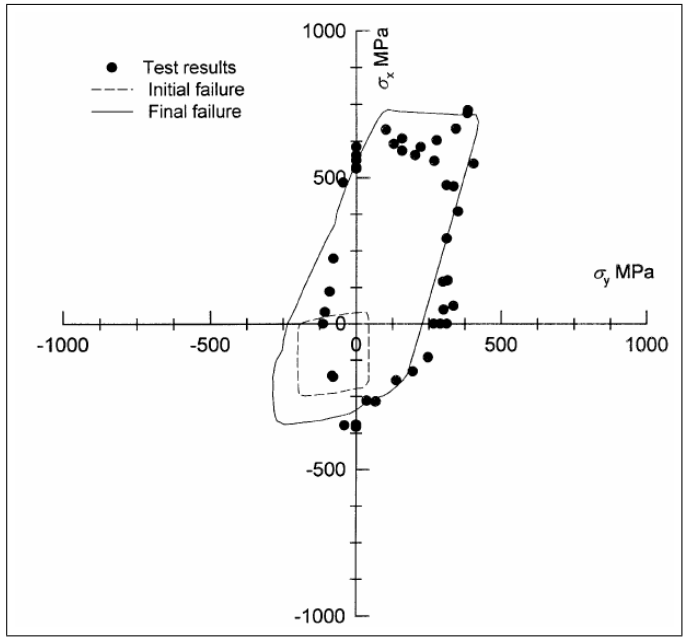

Figure 2.8: - Biaxial failure stress envelope for $90°/\pm 30°/90°$ laminate made of E-Glass LY556 under combined σ_x and σ_y stresses -. Prediction by Puck and Schürmann compared against experimental data.

The same strength ratio can be determined from the equivalent quadratic criterion in strain space. Since in a laminate subject to membrane stresses the strain is the same in each ply, a strain criterion may be preferred.

2.3.2 Degradation factors

The model of Tsai accounts for the achievement of the failure condition in a ply by introducing factors that decrease its stiffness.

The phenomenon of microcracking in the matrix is considered by Tsai as follows. When in a ply the condition for a significative presence of micro-cracks is met, the model reduces only the transverse and shear moduli of the unidirectional lamina considering that the ply can still transfer longitudinal load. This degradation is introduced by a reduction of matrix stiffness down to a 15% of the undamaged value. On the basis of micromechanical considerations, this reduc-

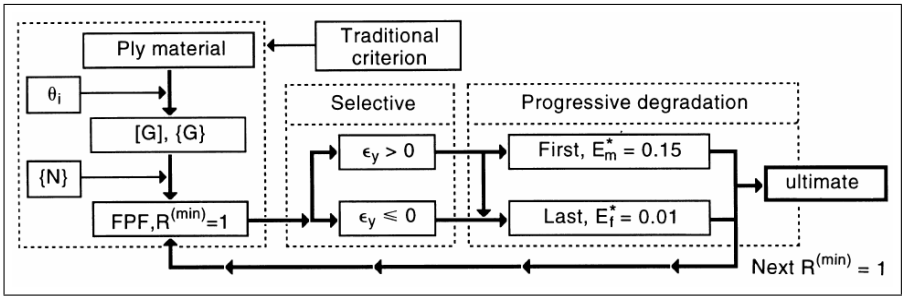

Figure 2.9: Flow chart of the 'progressive failure methodology' employed by Tsai.

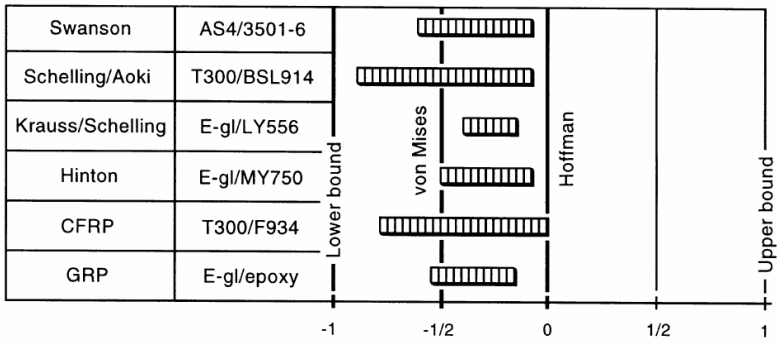

Figure 2.10: Values of the interaction term F^*_{xy}.

tion leads to reduced values of transverse and shear stiffness that for the materials proposed in the exercise range from 11% to 19% of the respective original values.

The well known experimental evidence of the loss of lamina longitudinal compressive strength in presence of micro-cracks in the matrix is accounted for by the simple law:

$$\frac{X'}{X'^0} = \left(\frac{E_s}{E_s^0}\right)^n,$$

where X' and X'^0 are the decreased and undamaged lamina longitudinal compressive strengths; E_s and E_s^0 are the decreased and undamaged shear stiffnes moduli; Tsai recommends an exponent $n = 0.1$.

As for the fibres, degradation is accounted for with a reduction factor of 0.01. This value is intended to simulate a catastrophic collapse.

When a ply fails the model uses the transverse strain of the failed ply ε_y as the discriminant between fiber degradation and matrix degradation. When this component is positive micro-cracking is considered to have occured and, accordingly, the ply is degraded by reducing the matrix modulus. Conversely, if, when the failure condition is achieved, the transverse strain is zero or compressive, the failure is attributed to fibres and the arbitrary degradation factor of 0.01 is applied to longitudinal stiffness. The selective degradation method devised by Tsai provides also that if a ply has already experimented a 'matrix-type' degradation, it can undergo, in the following iterations, only a 'fiber-type' degradation. Conversely, a 'fiber-type' degradation impedes any further degradation.

In the following pages we report the failure envelopes determined by Tsai for the E-Glass/epoxy LY556 laminates.

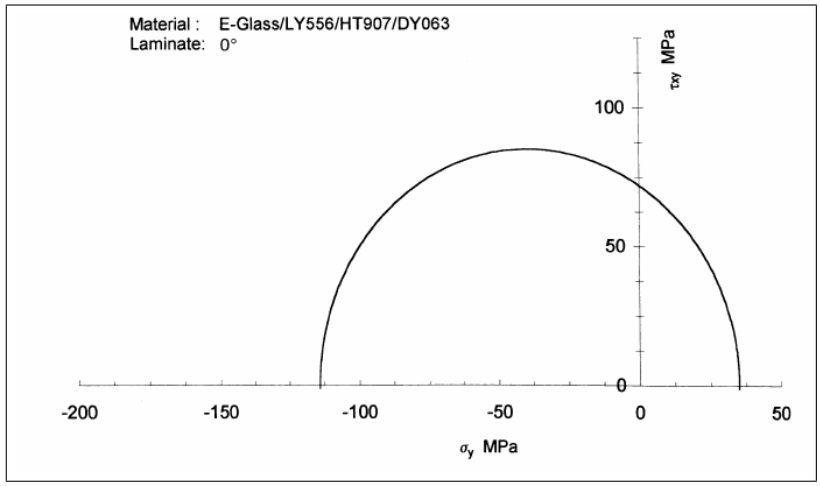

Figure 2.11: - Biaxial failure stress envelope for 0° unidirectional lamina made of E-Glass LY556 under combined transverse and shear loading -. Prediction provided by Tsai.

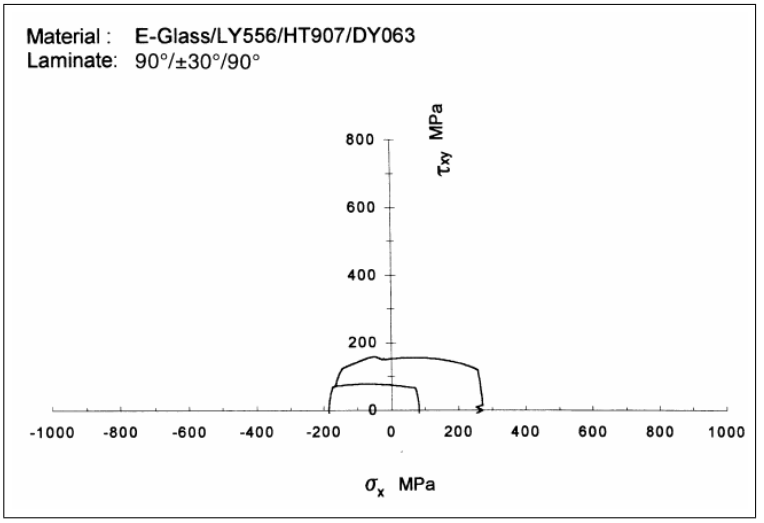

- Biaxial failure stress envelope for $90°/\pm 30°/90°$ laminate made of E-Glass LY556 under combined longitudinal and shear loading -. Prediction provided by Tsai.

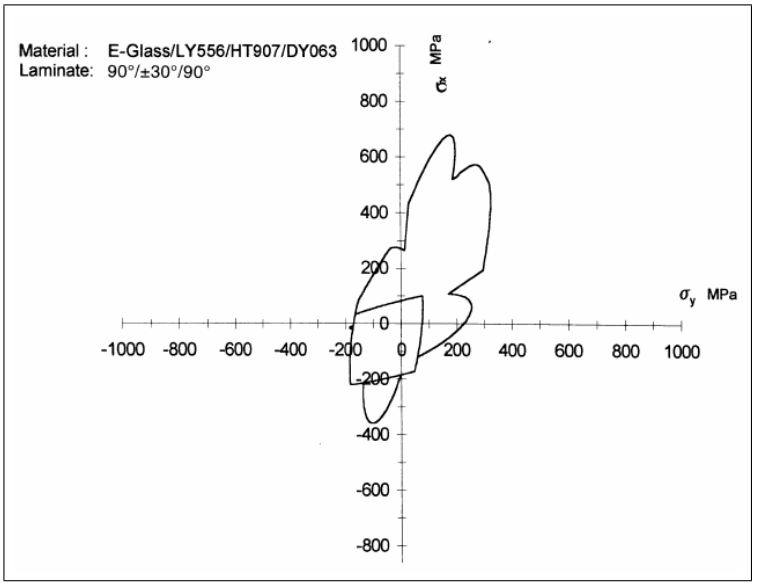

- Biaxial failure stress envelope for $90°/\pm 30°/90°$ laminate made of E-Glass LY556 under combined σ_x and σ_y stresses -. Prediction provided by Tsai.

2.4 The 'Vanishing Diameter Fibre' model by Dvorak

Dvorak and co-workers ([32], [33], [9], [10]) formulated and developed an elastic-plastic model , based on specific micromechanical assumptions, called Vanishing Fiber Diameter (VFD) model. This model is based on the morphological assumption that the composite can be regarded as a continuum reinforced by cylindrical fibres of infinitesimal small diameter but finite volume fraction. This assumption implies (1) a constraint in the longitudinal direction x_1 that enforces equal axial deformation in the two component materials and (2) a constraint in the transverse direction which enforces equal stress in fiber and matrix. These hypotheses are exploited to derive the incremental elastic-plastic constituve equations for the composite. We provide a brief resume of the developements of this theory for the specific case of isotropic component phases.

Let $d\boldsymbol{\sigma}$ and $d\boldsymbol{\varepsilon}$ denote the stress and strain increments in the composite, and $d_f\boldsymbol{\sigma}$, $d_m\boldsymbol{\sigma}$, $d_f\boldsymbol{\varepsilon}$, $d_m\boldsymbol{\varepsilon}$ denote the stress and strain increments in matrix and fiber. The VFD model is based on the constraint expressed by the following equations:

$$d\sigma_{ij} = d_f\sigma_{ij} = d_m\sigma_{ij}, \quad ij \neq 11 \tag{2.9}$$

$$d\sigma_{11} = {}_fc\, d_f\sigma_{11} + {}_mc\, d_m\sigma_{11}, \tag{2.10}$$

$$d\varepsilon_{ij} = {}_fc\, d_f\varepsilon_{ij} + {}_mc\, d_m\varepsilon_{ij}, \quad ij \neq 11 \tag{2.11}$$

$$d\varepsilon_{11} = d_f\varepsilon_{11} = d_m\varepsilon_{11}, \tag{2.12}$$

where ${}_fc$ and ${}_mc$ denote the volumetric fractions of fiber and matrix, respectively.

Dvorak designs an elastoplastic model for the composite in which the fibres are assumed to behave elastically until failure while the matrix is assumed to obey a yield condition of the Von Mises type with kinematic hardening. In the matrix stress space such yielding condition reads:

$$f({}_m\boldsymbol{\sigma}) = {}_m\boldsymbol{\sigma}^T \begin{bmatrix} \mathbf{c} & \mathbf{0} \\ \mathbf{0} & 3\mathbf{i} \end{bmatrix} {}_m\boldsymbol{\sigma} - Y^2 = 0,$$

where ${}_m\boldsymbol{\sigma} = \{{}_m\sigma_{11}, {}_m\sigma_{22}, {}_m\sigma_{33}, {}_m\sigma_{12}, {}_m\sigma_{23}, {}_m\sigma_{13}\}$ and $\mathbf{c}$ is the symmetric 3×3 matrix:

$$\mathbf{c} = \begin{bmatrix} 1 & \frac{1}{2} & \frac{1}{2} \\ \frac{1}{2} & 1 & \frac{1}{2} \\ \frac{1}{2} & \frac{1}{2} & 1 \end{bmatrix}.$$

The matrix and fibre concentration factors are respectively denoted by $\mathbf{B}_{me}$ and $\mathbf{B}_{fe}$ and defined by:

$$\begin{aligned} {}_m\boldsymbol{\sigma} &= \mathbf{B}_{me}\,{}_{me}\boldsymbol{\sigma}, \\ {}_f\boldsymbol{\sigma} &= \mathbf{B}_{fe}\,{}_{fe}\boldsymbol{\sigma}. \end{aligned}$$

For isotropic elastic matrix and fiber equations (2.9-2.12) determine the following elastic concentration factors:

$$\mathbf{B}_{me} = \begin{bmatrix} \mathbf{b}'_m & \mathbf{0} \\ \mathbf{0} & \mathbf{i} \end{bmatrix}; \mathbf{B}_{fe} = \begin{bmatrix} \mathbf{b}'_f & \mathbf{0} \\ \mathbf{0} & \mathbf{i} \end{bmatrix}, \tag{2.13}$$

with:

$$\begin{aligned} \mathbf{b}'_m &= \left(\frac{1}{E_c}\right) \begin{bmatrix} E_m & (1-{}_mc)a_m & (1-{}_mc)a_m \\ 0 & E_c & 0 \\ 0 & 0 & E_c \end{bmatrix}, \\ \mathbf{b}'_f &= \left(\frac{1}{E_c}\right) \begin{bmatrix} E_f & (1-{}_fc)a_f & (1-{}_fc)a_f \\ 0 & E_c & 0 \\ 0 & 0 & E_c \end{bmatrix}, \end{aligned}$$

and where:

$$\begin{aligned} E_c &= {}_fcE_f + {}_mcE_m \\ a_f &= (\nu_f E_m - \nu_m E_f) = -a_m, \end{aligned}$$

and $\mathbf{i}$ is the 3×3 identity matrix.

The matrix stress concentration factor of (2.13) is employed to change the formulation of the plasticity model from a formulation in the matrix stress space to a composite stress space based one:

$$f(\boldsymbol{\sigma}) = f(\mathbf{B}_{me}\,{}_m\boldsymbol{\sigma}) = \boldsymbol{\sigma}^T \begin{bmatrix} (\mathbf{b}'_m)^T\,\mathbf{c}\mathbf{b}'_m & \mathbf{0} \\ \mathbf{0} & 3\mathbf{i} \end{bmatrix} \boldsymbol{\sigma} - Y^2 = 0$$

The constraint enforced by equations (2.10) and (2.12) determines, when a irreversible deformation is produced in the elasto-plastic matrix, the development of a residual auto-equilibrated axial normal stress between fibre and matrix. This is very similar to an additional hardening effect and is referred to by Dvorak as constraint hardening. Combining the effect of constraint hardening and of the

local work hardening due to plastic deformation in the matrix, the general form of the yield condition in the composite stress space may be written as:

$$f(\boldsymbol{\sigma} - \boldsymbol{\alpha}) = 0,$$

where $\boldsymbol{\alpha}$ is a translation vector which contains both the translation due to constraint hardening and the translation due to matrix hardening.

The employment of an associated flow rule provides for the matrix strain:

$$d\,{}_m\boldsymbol{\varepsilon} = d\,{}_m\boldsymbol{\varepsilon}^e + d\,{}_m\boldsymbol{\varepsilon}^p = \mathbf{C}_{me}^{-1}\mathbf{B}_{me}d\boldsymbol{\sigma} + d\lambda_m \left(\frac{\partial f}{\partial_m \boldsymbol{\sigma}}\right),$$

where $d\lambda_m$ is a scalar multiplier.

The overall strain increment expression results:

$$d\boldsymbol{\varepsilon} = {}_fc\, d\,{}_f\boldsymbol{\varepsilon} + {}_mc\, d\,{}_m\boldsymbol{\varepsilon} = {}_fc\, \mathbf{C}_{fe}^{-1}\mathbf{B}_{fe}\, d\boldsymbol{\sigma} + {}_mc\, \mathbf{C}_{me}^{-1}\mathbf{B}_{me}\, d\boldsymbol{\sigma} + {}_mc\, d\lambda_m \left(\frac{\partial f}{\partial\,{}_m\boldsymbol{\sigma}}\right). \tag{2.14}$$

Dvorak chose to adopt Prager's hardening rule with kinematic hardening [131] that provides for $d\lambda_m$ the following expression:

$$d\lambda_m = \frac{\left(\dfrac{\partial f}{\partial\,{}_m\boldsymbol{\sigma}}\right)^T d\,{}_m\boldsymbol{\sigma}}{H_m \left(\dfrac{\partial f}{\partial\,{}_m\boldsymbol{\sigma}}\right)^T \left(\dfrac{\partial f}{\partial\,{}_m\boldsymbol{\sigma}}\right)}.$$

H_m is the hardening parameter of the matrix and is defined by:

$$d\,{}_m\hat{\sigma} = H_m d_m\hat{\varepsilon}^p,$$

where:

$$d\,{}_m\hat{\sigma} = \sqrt{\frac{3}{2} d\,{}_m\boldsymbol{\sigma} \cdot d\,{}_m\boldsymbol{\sigma}},$$

$$d\,{}_m\hat{\varepsilon}^p = \sqrt{\frac{2}{3} d\,{}_m\boldsymbol{\varepsilon}^p \cdot d\,{}_m\boldsymbol{\varepsilon}^p}.$$

In the case of a Von Mises type matrix:

$$d\lambda_m = \frac{({}_m\boldsymbol{\sigma} - \boldsymbol{\alpha}_m)^T \mathbf{L} d\,{}_m\boldsymbol{\sigma}}{3H_m \left\{Y^2 + 3\left[({}_m\sigma_{12} - {}_m\alpha_{12})^2 + ({}_m\sigma_{13} - {}_m\alpha_{13})^2 + ({}_m\sigma_{23} - {}_m\alpha_{23})^2\right]\right\}}, \tag{2.15}$$

where:

$$\mathbf{L} = \begin{bmatrix} \mathbf{c} & \mathbf{0} \\ \mathbf{0} & 3\mathbf{i} \end{bmatrix}.$$

Defining:

$$q = \frac{1}{6} \frac{\left[-\left({}_m\sigma_{22} - {}_m\alpha_{22} \right)^2 - \left({}_m\sigma_{33} - {}_m\alpha_{33} \right)^2 Y^2 + 2\left({}_m\sigma_{11} - {}_m\alpha_{11} \right)^2 \right]}{\left\{ Y^2 + 3\left[\left({}_m\sigma_{12} - {}_m\alpha_{12} \right)^2 + \left({}_m\sigma_{13} - {}_m\alpha_{13} \right)^2 + \left({}_m\sigma_{23} - {}_m\alpha_{23} \right)^2 \right] \right\}},$$

and:

$$\boldsymbol{\eta} = [\eta_1, \eta_2, \eta_3, \eta_4, \eta_5, \eta_6] = 2q\mathbf{L}({}_m\boldsymbol{\sigma} - \boldsymbol{\alpha}_m),$$

then equation (2.15) can be written:

$$d\lambda_m = \frac{q\boldsymbol{\eta}^T \mathbf{B}_m}{H_m \eta_1} d\boldsymbol{\sigma}; \tag{2.16}$$

analogously:

$$\left(\frac{\partial f}{\partial \, {}_m\boldsymbol{\sigma}} \right) = \frac{\boldsymbol{\eta}}{q}. \tag{2.17}$$

Substituting (2.16) and (2.17) in (2.14) one obtains:

$$d\boldsymbol{\varepsilon} = \left({}_f c \mathbf{C}_{fe}^{-1} \mathbf{B}_{fe} + {}_m c \mathbf{C}_{me}^{-1} \mathbf{B}_{me} + {}_m c \frac{\boldsymbol{\eta}^T \boldsymbol{\eta}}{H_m \eta_1} \mathbf{B}_m \right) d\boldsymbol{\sigma}.$$

Dvorak obtains the following expressions for the istantaneous stress concentration factors:

$$\mathbf{B}_m = \begin{bmatrix} \mathbf{u} & \mathbf{v} \\ \mathbf{0} & \mathbf{i} \end{bmatrix},$$

where:

$$\mathbf{u} = \begin{bmatrix} (B_m)_{11} & (B_m)_{12} & (B_m)_{13} \\ 0 & 1 & 0 \\ 0 & 0 & 1 \end{bmatrix},$$

$$\mathbf{v} = \begin{bmatrix} (B_m)_{14} & (B_m)_{15} & (B_m)_{16} \\ 0 & 1 & 0 \\ 0 & 0 & 1 \end{bmatrix},$$

and:

$$
\begin{aligned}
(B_m)_{12} &= \left(\frac{{}_fc}{H_mE_c + {}_fcE_fE_m\eta_1}\right)(H_ma_m - E_mE_f\eta_2)\,,\\
(B_m)_{13} &= \left(\frac{{}_fc}{H_mE_c + {}_fcE_fE_m\eta_1}\right)(H_ma_m - E_mE_f\eta_3)\,,\\
(B_m)_{11} &= \frac{H_mE_m}{H_mE_c + {}_fcE_fE_m\eta_1},\\
(B_m)_{14} &= -\left(\frac{{}_fc}{H_mE_c + {}_fcE_fE_m\eta_1}\right)E_mE_f\eta_4,\\
(B_m)_{15} &= -\left(\frac{{}_fc}{H_mE_c + {}_fcE_fE_m\eta_1}\right)E_mE_f\eta_5,\\
(B_m)_{16} &= -\left(\frac{{}_fc}{H_mE_c + {}_fcE_fE_m\eta_1}\right)E_mE_f\eta_6.
\end{aligned}
$$

The Vanishing Diameter Fiber model allows the derivation of analytical expressions for the overall stiffness and compliance of the composite in terms of the properties of the single component materials. As noted by the authors, it underestimates the transverse elastic moduli.

For the general case of transversely isotropic component phases (clearly with the axes of transverse isotropy coinciding with the axis of cylindrical symmetry for the RVE), indicating with k_f and k_m, respectively, the transverse bulk moduli of fiber and matrix, the transverse modulus of the composite k determined by the model of Dvorak is:

$$k = \left(\frac{{}_fc}{k_f} + \frac{{}_mc}{k_m}\right)^{-1}.$$

Hill [50], determined for the transverse bulk modulus of biphasic composite materials with cylindrical symmetry and transversely isotropic components the following lower bound:

$$k' = \left({}_fc\frac{1}{k_f + G_{Tm}} + {}_mc\frac{1}{k_m + G_{Tm}}\right)^{-1} - m_m,$$

where k_m denotes the transverse bulk moduli, G_T the transverse shear moduli and it is assumed that the transverse shear moduli of the fiber and of the matrix satisfy the condition: $G_{Tf} \geq G_{Tm}$.

It can be demonstrated that the transverse bulk modulus provided by Dvorak k is lower than k'. The same is true for the remaining overall moduli of the composite.

Dvorak proposes a correction of the elastic properties of component materials in order to adjust such low estimates.

Another concern on the VDF model regards the behaviour in the plastic range. The model, in fact, predicts low constraint hardening rates in the transverse direction at high fibre concentrations and does not provide a correct shape of the yielding surface in the axisymmetric plane. Dvorak observes that these aspects of the predictions provided by the model indicate that this theory should be applied preferably to materials with low or moderate fiber volumetric fractions.

Hsu and co-workers [56] have tested the VDF model introducing certain empirical corrections based on a systematic modification of the physical properties of the matrix material. Their clonclusion is that altough their method can provide accurate predictions for the unidirectional composites, it does not provide satisfactory results for more complex laminates.

2.5 The Method of Cells by Aboudi.

The Method of Cells (MOC) in its standard [2], [3], and generalized formulations [4], [77] is another micromechanical model developed by Aboudi for predicting the response of unidirectional long fiber composites with periodic microstructure. This method is based on the construction of algebraic macroscopic stress-strain equations for the periodic cylindrical RVE through an approximate elasticity analysis of the repeating unit cell. These equations can be used to calculate: approximate stress and strain concentration matrices, and approximate overall stiffness matrices of the composite. Such equations can also be conveniently used in the construction of non-linear models for the composite based on the non-linear models of the component materials.

The approach relies on two effective approximations: (1) the original geometry of the unit cell is modeled as a regular arrangement of $N_\alpha \times N_\beta \times N_\gamma$ hexhaedral subregions (quadrilateral if the problem is in 2D); (2) each one of the subcells is considered to be occupied by one single material and for each one a linear displacement field is assumed. In its most general form, for a 3D unit cell in which each side is divided in an equal number of N_c segments, this approximation provides that the kinematic of the whole RVE is determined by $9 \times N_c^3$

unknown components of the subcells deformation gradients plus the $3 \times N_c^3$ displacements of the center of mass of each subcell . These unknowns are balanced by $3 \times 3 \times N^2(N-1)$ displacement continuity conditions imposed in an average sense at the interfaces of the subcells, by $3 \times 3 \times N^2$ equations that originate from the kinematic conditions of indistiguishibility of the unit cell from its neighbours and by the $3 \times N_c^3$ independent conditions of equilibrium for the subcells. of this method

Teply and Reddy [119] have demonstrated that the MOC can be reformulated and cast in the form of a finite element analysis employing the Hellinger-Reissner variational principle.

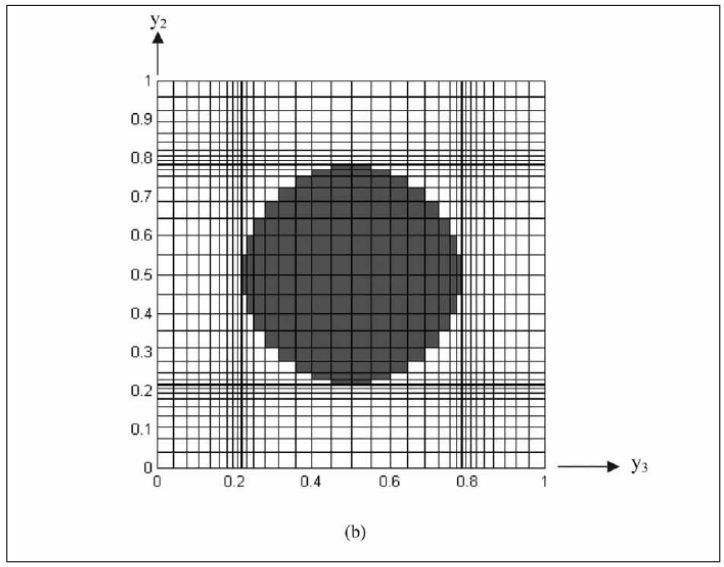

Figure 2.12: Example of the volume discretization of the repeating unit cells employed in the analysis of unidirectional fiber reinforced, metal-matrix composites with the GMOC.

We will provide a brief sumary of this method within its original, less general, formulation for a unidirectional long fibre composite in the small deformation regime. The original version of the method of cells consists in modeling the geometry of the exahedral RVE of a LFC, as a 2×2 array of exahedral subregions. In view of the cylindrical symmetry it is sufficient to analyze a representative

cell as shown in figure 2.13.

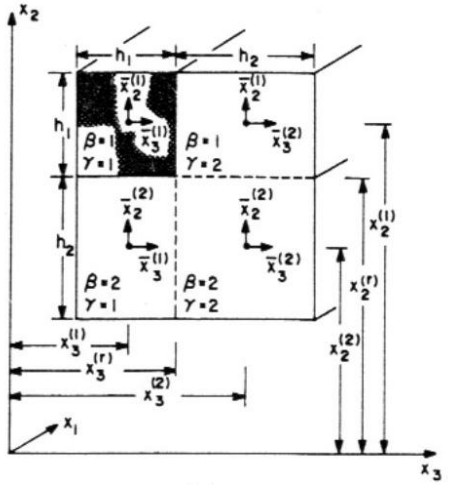

Figure 2.13: Scheme of the representative cell, composed of an array of four subcells, considered by Aboudi for LFC.

One of these subregions is considered to be occupied by the fiber and the remaining three ones by the matrix. The model is based on a linear representation of the displacements of each subcell and thus the kinematic of the RVE results to be defined by the 6 components of strain in each subcell (6x4 unknowns). A homogeneization condition which ensures that the response of a given unit cell is indistinguishable from that of its neighbors is also applied. The area of the cross section of the square fiber is h_1^2 and h_2 represents the spacing between the adjacent fibres. The subcells are located by the indexes $\beta = 1, 2$ and $\gamma = 1, 2$. Let's consider a global orthogonal reference frame with the coordinate x_1 in the direction of fibre axis and the remaining axes x_2 and x_3 oriented as the sides of the square cells. In the center of each subcell $(\beta\gamma)$ a local reference frame whose coordinates are $\boldsymbol{x}^{(\beta\gamma)} = (x_1, x_2^{(\beta)}, x_3^{(\gamma)})$ is positioned. Subcell strains, and therefore subcell stresses are piece-wise uniform throughout the the repeating unit cell. The small displacements kinematics is approximated with the affine representation defined by the displacements of the centers of the subcells: $\boldsymbol{u}_0^{(\beta\gamma)}$ and by the related gradients: grad $\boldsymbol{u}^{(\beta\gamma)}$:

$$\boldsymbol{u}^{(\beta\gamma)} = \boldsymbol{u}_0^{(\beta\gamma)} + \text{grad}\, \boldsymbol{u}^{(\beta\gamma)} \boldsymbol{x}^{(\beta\gamma)}.$$

Accordingly the small strain tensor, uniform in each subcell, is:

$$\boldsymbol{\varepsilon}^{(\beta\gamma)} = \text{sym grad}\, \boldsymbol{u}^{(\beta\gamma)}.$$

The components of the stress and strain tensors are arranged in a vector array and denoted by:

$$\begin{aligned} \boldsymbol{\varepsilon}^{(\beta\gamma)} &= [\varepsilon_{11}^{(\beta\gamma)}, \varepsilon_{22}^{(\beta\gamma)}, \varepsilon_{33}^{(\beta\gamma)}, 2\varepsilon_{12}^{(\beta\gamma)}, 2\varepsilon_{13}^{(\beta\gamma)}, 2\varepsilon_{23}^{(\beta\gamma)}] \\ \boldsymbol{\sigma}^{(\beta\gamma)} &= [\sigma_{11}^{(\beta\gamma)}, \sigma_{22}^{(\beta\gamma)}, \sigma_{33}^{(\beta\gamma)}, \sigma_{12}^{(\beta\gamma)}, \sigma_{13}^{(\beta\gamma)}, \sigma_{23}^{(\beta\gamma)}] \end{aligned}$$

The area of the square cross section of each subcell and the area of the cross section of thel RVE are denoted, respectively, by $V^{(\beta\gamma)} = h_\beta h_\gamma$ and $V = (h_\beta + h_\gamma)^2$. Aboudi assumes that the stress of the composite $\boldsymbol{\sigma}$ is provided by the volume average of the stress in the RVE:

$$\boldsymbol{\sigma} = \sum_{\beta,\gamma=1}^{2} V^{(\beta\gamma)} \boldsymbol{\sigma}^{(\beta\gamma)}.$$

A first group of equations is determined by imposing in an average sense the continuity of tractions along the interfaces of the subcells:

$$\begin{aligned} \sigma_{2i}^{(1\gamma)} &= \sigma_{2i}^{(2\gamma)}, \quad i = 1,2,3 \quad \gamma = 1,2, \\ \sigma_{3i}^{(\beta 1)} &= \sigma_{3i}^{(\beta 2)}, \quad i = 1,2,3 \quad \beta = 1,2. \end{aligned} \tag{2.18}$$

By imposing conditions of displacements continuity in an average sense at the interfaces of the subcells and conditions of periodicity at the outer boundary of

the RVE the following set of equations is obtained:

$$
\begin{aligned}
h_1\varepsilon_{22}^{(1\gamma)} + h_2\varepsilon_{22}^{(2\gamma)} &= (h_1+h_2)\varepsilon_{22} \quad \gamma = 1,2 \\
h_1\varepsilon_{33}^{(\beta 1)} + h_2\varepsilon_{33}^{(\beta 2)} &= (h_1+h_2)\varepsilon_{33} \quad \beta = 1,2 \\
h_1\varepsilon_{12}^{(1\gamma)} + h_2\varepsilon_{12}^{(2\gamma)} &= (h_1+h_2)\varepsilon_{12} \quad \gamma = 1,2 \\
h_1\varepsilon_{13}^{(\beta 1)} + h_2\varepsilon_{13}^{(\beta 2)} &= (h_1+h_2)\varepsilon_{13} \quad \beta = 1,2 \\
h_1\frac{\partial u_3^{(1\gamma)}}{\partial x_2} + h_2\frac{\partial u_3^{(2\gamma)}}{\partial x_2} &= (h_1+h_2)\frac{\partial u_3}{\partial x_2} \quad \gamma = 1,2 \\
h_1\frac{\partial u_2^{(\beta 1)}}{\partial x_3} + h_2\frac{\partial u_2^{(\beta 2)}}{\partial x_3} &= (h_1+h_2)\frac{\partial u_2}{\partial x_3} \quad \beta = 1,2 \\
\varepsilon_{11}^{(\beta\gamma)} &= \varepsilon_{11} \quad \beta = 1,2 \quad \gamma = 1,2.
\end{aligned}
\tag{2.19}
$$

The straightforward use of equations (2.18) and (2.19) is used by Aboudi to determine the elastic stiffness properties of the composite. In the developments a great simplification is obtained considering that due to the cylindrical symmetry the normal and shear response of the RVE are decoupled. Aboudi for transversely isotropic components derives the formulas that provide the effective elastic stiffness and compliance moduli together with the stress concentration matrices in the four subcells. Such formulas are not reported here, for sake of brevity, and the interested reader may consult [3].

This model provides an orthotropic material with square symmetry. A transversely isotropic stiffness matrix is subsequently obtained by rotating the stiffness matrix around fiber axis by an angle θ and calculating its average in the interval $[0, \pi]$. The effective moduli obtained are compared against the results given by elasticity solutions, by the generalized self-consistent scheme [51] and against experimental test results. In particular, in all cases considered the agreement is very good as shown by figures: 2.14, 2.15, 2.16, 2.17 and 2.18.

The MOC is extended in order to define a failure criteria for a unidirectional lamina. The key idea is to use the stress concentration matrixes emerging from

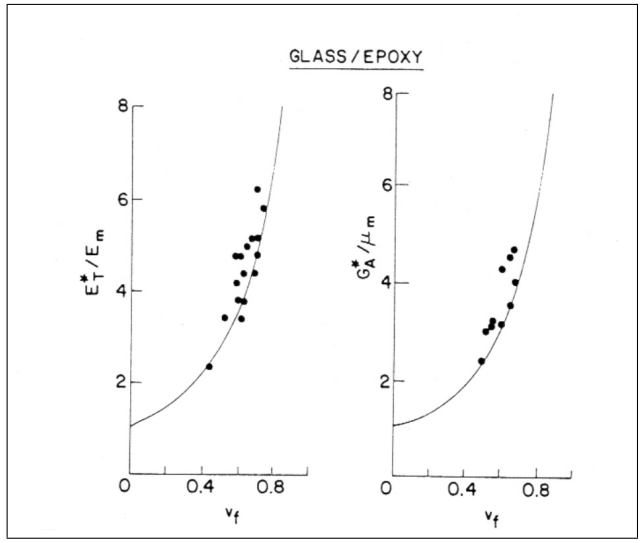

Figure 2.14: Comparison between the measured values (Tsai and Hahn, 1980) of the transverse Young modulus and the axial shear modulus and the correspondig predictions of the MOC.

the previously described formulations and use them to relate the overall stress to the average stress in each of the four hexahedral cells. In a straightforward way, failure in the composite is assumed to occurr whenever a limit stress is reached in any one of the cells. The author warns that the strength parameters for fiber and matrix may differ from the strength parameters characterizing the bulk materials and proposes to use the stress concentration matrixes with an inverse approach, i.e. in order to calibrate the component materials strength parameters from the knowledge of the allowable stresses of the unidirectional composite in the principal material directions. When this calibration procedure is adopted, the author reports an excellent agreement between the micromechanical prediction and measured strengths in most cases [1]. The predicted off-axis strength curve for AS/3501 is compared with measured experimental data and the agreement results to be very good; see figures 2.19 and 2.20.

Aboudi exploits equations (2.18) and (2.19) also to formulate a complete non-linear constitutive model for resin matrix composites. The determination of the overall response of the composite, differently from macromechanical theories, is

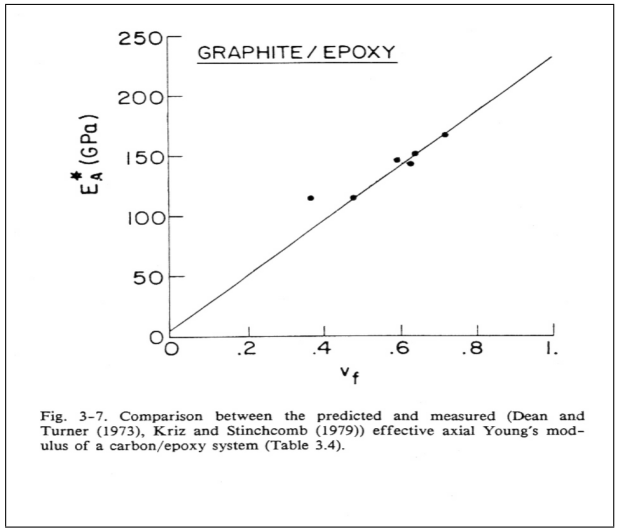

Fig. 3-7. Comparison between the predicted and measured (Dean and Turner (1973), Kriz and Stinchcomb (1979)) effective axial Young's modulus of a carbon/epoxy system (Table 3.4).

Figure 2.15: Comparison between the measured values (Tsai and Hahn, 1980) of the axial Young modulus and the corresponding prediction provided by the MOC.

based on micromechanical considerations from the knowledge of the properties of fiber and matrix and using the method of cells. The non-linear behavior of the polymeric matrix is characterized by a generalization to multiaxial loading of the Ramberg-Osgood equations [90]. In short, the matrix response is modeled through a linear isotropic stress-strain law with an additional deviatoric non-linear term which depends on the two parameters σ_0 and the exponent n taken from Ramberg-Osgood formulas. These parameters are determined by fitting the measured in-plane shear response of a unidirectional lamina with the curve predicted by this micromechanics theory. The fiber, instead, is modeled as a linear elastic transversely isotropic material as usual. The problem thus results to be defined by a system of 28 non-linear equations in 28 unknowns. This system is reported to be easily solved with general purpose solvers by applying the load progressively in a stepwise manner. This law is then combined with a basic laminate theory, (assuming essentially the same strain state in the different laminas composing the laminate). The results given by the overall resulting model for a $[\pm 30]_S$ boron/epoxy laminate are compared with experimental data and good agreement is noticed by the author (see figures 2.21 and 2.22. The

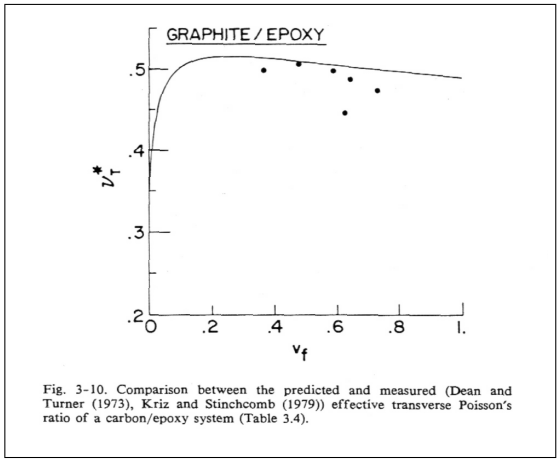

Fig. 3-10. Comparison between the predicted and measured (Dean and Turner (1973), Kriz and Stinchcomb (1979)) effective transverse Poisson's ratio of a carbon/epoxy system (Table 3.4).

Figure 2.16: Comparison between measured values of the transverse Poisson ratio and correspondig predictions provided by the MOC.

same approach of fitting the measured shear response for the determination of σ_0 and n is also used for the prediction of the non-linear behavior of a glass/epoxy composite.

2.6 The Mixing theory by Oller and Car.

Another important stream of research in the framework of a multi-material approach is the computational methodology of Oller and co-workers. [70], [71], [20], [21], [130].

Differently from the theories of Dvorak and Aboudi, where anisotropy originates from the equations characterizing the morphology of the microstructure, in Oller's approach the anisotropy is implemented through the concept of mapped stress tensor [17], [18], while the behaviour of the different materials is combined by means of the mixing theory [42], [70], [122], [73].

At the base of this theory lays the hypothesis that all materials are characterized by the same total strain. For a biphasic composite and small strain kinematics such hypothesis reads:

$$ {}_f\varepsilon_{ij} = {}_m\varepsilon_{ij}, \quad i = 1,2,3, \quad j = 1,2,3 $$

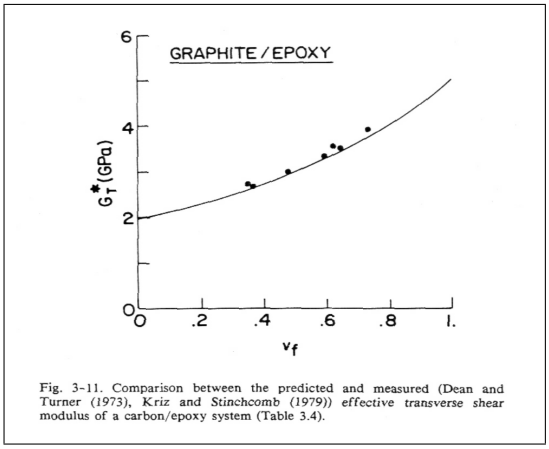

Fig. 3-11. Comparison between the predicted and measured (Dean and Turner (1973), Kriz and Stinchcomb (1979)) effective transverse shear modulus of a carbon/epoxy system (Table 3.4).

Figure 2.17: Comparison between the measured values (Tsai and Hahn, 1980) of the transverse shear modulus and the correspondig predictions of the MOC.

The mixing theory also assumes that in each material point the component substances contribute with their own constitutive law in the assigned volume proportion. Within a basic condition of additivity of the free energy of the components this assumption is written as follows:

$$\rho\psi\left(\boldsymbol{\varepsilon},\theta,\boldsymbol{\beta}\right) = {}_f c\rho_f\psi_f\left[\boldsymbol{\varepsilon},(\boldsymbol{\varepsilon}^p)_f,\theta,\boldsymbol{\beta}_f\right] + {}_m c\rho_m\psi_m\left[\boldsymbol{\varepsilon},(\boldsymbol{\varepsilon}^p)_m,\theta,\boldsymbol{\beta}_m\right]$$

where ρ, ρ_m and ρ_f are the densities, ψ, ψ_f and ψ_m the free energy corresponding respectively to the composite and to the two compounding substances of the mixture, ${}_f c$ and ${}_m c$ the volumetric fractions, $(\boldsymbol{\varepsilon}^p)_f$ and $(\boldsymbol{\varepsilon}^p)_m$ the plastic strain deformation of each phase and $\boldsymbol{\beta}_f$, $\boldsymbol{\beta}_m$ are the internal variables of each phase which define the physical behavior of the phase and θ is the temperature.

As a consequence of the previously introduced assumptions the stress state of the composite results:

$$\boldsymbol{\sigma} = \rho\frac{\partial\psi}{\partial\boldsymbol{\varepsilon}} = {}_f c\rho_f\frac{\partial\psi_f}{\partial\boldsymbol{\varepsilon}} + {}_m c\rho_m\frac{\partial\psi_m}{\partial\boldsymbol{\varepsilon}},$$

and the tangent constitutive tensor of the composite is thus given by:

$$\mathbb{C} = {}_f c\,{}_f\mathbb{C} + {}_m c\,{}_m\mathbb{C}.$$

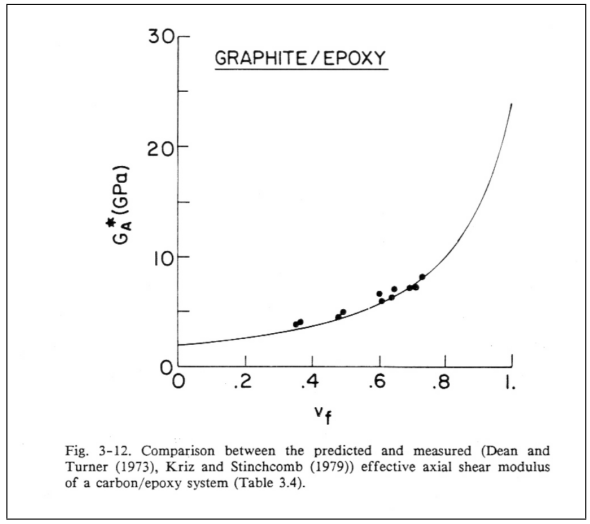

Fig. 3-12. Comparison between the predicted and measured (Dean and Turner (1973), Kriz and Stinchcomb (1979)) effective axial shear modulus of a carbon/epoxy system (Table 3.4).

Figure 2.18: Comparison between the measured values (Tsai and Hahn, 1980) of the axial shear modulus and the correspondig predictions of the MOC.

The treatment of anisotropy consists in the generalization of classical isotropic plasticity theories using the approach of mapped stress tensor, originally proposed by Betten [17], [18]. This approach is based on the definition of a anisotropic yield and a potential functions for the solid exploiting the isotropic potential and yielding functions of an auxiliary isotropic elastoplastic model. To this end the following auxiliary 'fictitious' variables of the auxiliary isotropic model are introduced: $\bar{\boldsymbol{\varepsilon}} \in$ Sym which denotes the 'fictitious' strain, and $\bar{\boldsymbol{\sigma}} \in$ Sym which denotes the 'fictitious' stress. The hypotheses of isotropy of the auxiliary plastic potential $\bar{g}(\bar{\boldsymbol{\sigma}}, \bar{\boldsymbol{\beta}})$ and yield functions $\bar{f}(\bar{\boldsymbol{\sigma}}, \bar{\boldsymbol{\beta}})$ imply that for any orthogonal transformation $\boldsymbol{Q}$ the following relations hold:

$$\bar{f}(\boldsymbol{Q}\bar{\boldsymbol{\sigma}}\boldsymbol{Q}^T, \bar{\boldsymbol{\beta}}) = \bar{f}(\bar{\boldsymbol{\sigma}}, \bar{\boldsymbol{\beta}}),$$

$$\bar{g}(\boldsymbol{Q}\bar{\boldsymbol{\sigma}}\boldsymbol{Q}^T, \bar{\boldsymbol{\beta}}) = \bar{g}(\bar{\boldsymbol{\sigma}}, \bar{\boldsymbol{\beta}}).$$

Real and auxiliary quantities are related by:

$$\bar{\boldsymbol{\sigma}} = \mathbb{A}^{\sigma}\boldsymbol{\sigma},$$

$$\bar{\boldsymbol{\varepsilon}} = \mathbb{A}^{\varepsilon}\boldsymbol{\varepsilon}.$$

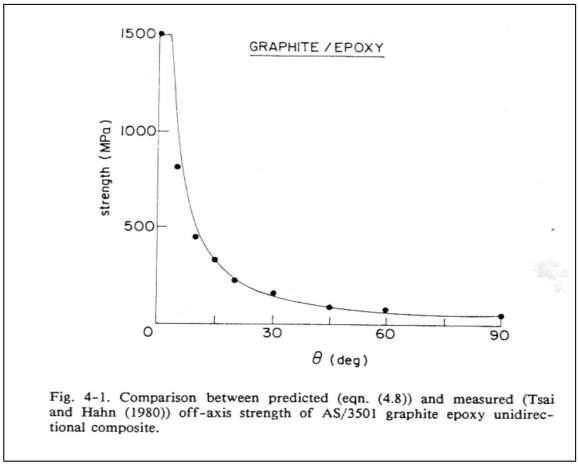

Figure 2.19: Comparison between the measured (Tsai and Hahn, 1980) off-axis strength of AS/3501 graphite epoxy unidirectional lamina and the correspondig prediction of the MOC.

where $\mathbb{A}^{\sigma}$ and $\mathbb{A}^{\varepsilon}$ are fourth order tensors. For tensor $\mathbb{A}^{\sigma}$ Car and co-workers provide the expression [20]:

$$\mathbb{A}^{\sigma}_{ijkl} = \bar{\boldsymbol{S}}_{\boldsymbol{ij}} \boldsymbol{S}^{-1}_{kl},$$

where $\bar{\boldsymbol{S}}_{\boldsymbol{ij}}$ and $\boldsymbol{S}_{kl}$ are the yield strengths of the material in the isotropic and anisotropic spaces, respectively. For the tensor $\mathbb{A}^{\varepsilon}$ the following expression is provided:

$$\mathbb{A}^{\varepsilon}_{rsmn} = \left(\bar{\mathbb{C}}^{-1}\right)_{ikrs} \mathbb{A}^{\sigma}_{ijkl} \mathbb{C}_{jlmn},$$

where $\bar{\mathbb{C}}$ and $\mathbb{C}$ are the constitutive tensors in the fictitious and real spaces. As for the relationship between the constitutive tensors in the real and the fictitious spaces the following expression is deduced:

$$\mathbb{C}_{jlmn} = \left(\mathbb{A}^{\sigma}\right)^{-1}_{ijkl} \bar{\mathbb{C}}_{ikrs} \mathbb{A}^{\varepsilon}_{rsmn}.$$

With this formulation the anisotropic biaxial yielding envelopes reported in figure 2.23 are obtained.

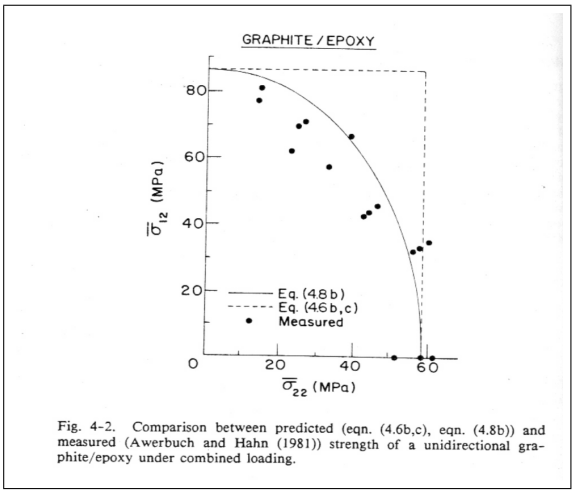

Fig. 4-2. Comparison between predicted (eqn. (4.6b,c), eqn. (4.8b)) and measured (Awerbuch and Hahn (1981)) strength of a unidirectional graphite/epoxy under combined loading.

Figure 2.20: Comparison between the measured values (Tsai and Hahn, 1980) of the $\sigma_2 - \tau_{12}$ failure envelope and the correspondig prediction of the MOC.

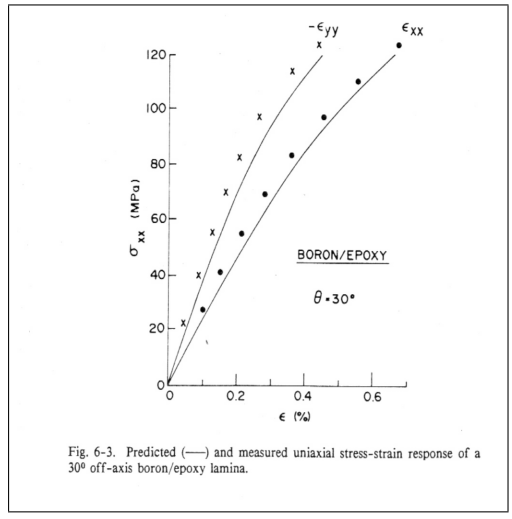

Fig. 6-3. Predicted (—) and measured uniaxial stress-strain response of a 30° off-axis boron/epoxy lamina.

Figure 2.21: Comparison between the measured 30° off-axis $\sigma - \varepsilon$ stress-strain response of a boron/epoxy lamina and the correspondig prediction of the MOC.

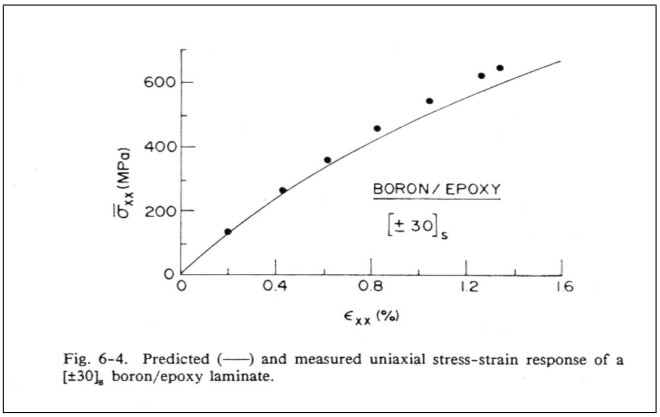

Fig. 6-4. Predicted (——) and measured uniaxial stress-strain response of a $[\pm 30]_s$ boron/epoxy laminate.

Figure 2.22: Comparison between the measured 30° off-axis $\sigma_x - \varepsilon_x$ uniaxial stress-strain response of a $[\pm 30°]_S$ boron/epoxy laminate and the correspondig prediction of the MOC.

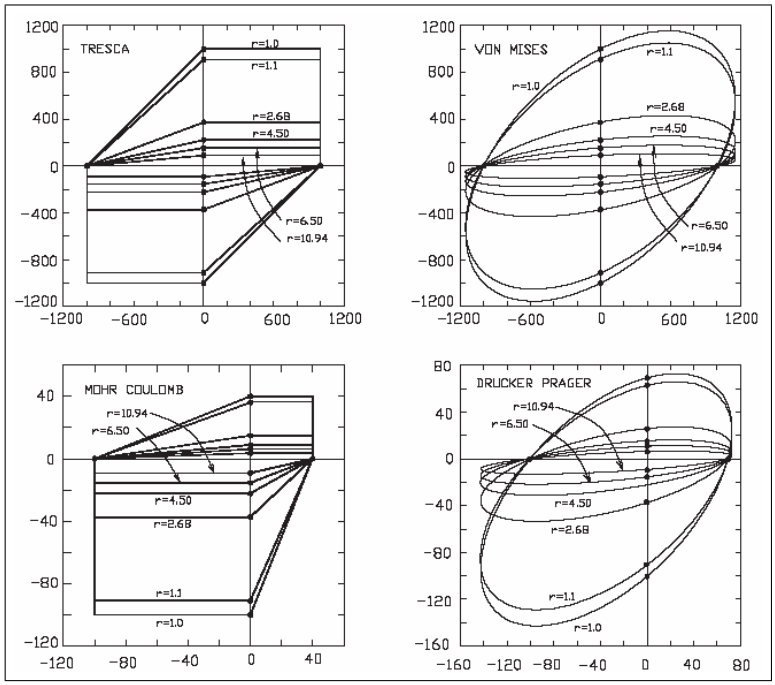

Figure 2.23: Biaxial yielding envelopes corresponding to the anisotropic formulations defined by exploiting thel isotropic yielding criteria of Tresca, Mohr-Coulomb, Von Mises, Drucker-Prager.

Chapter 3

The Serial-Parallel model for the constitutive characterization of composite materials at the microscale

The purpose of this chapter is to describe the formulation of a novel constitutive model for Long Fiber Composite material and illustrate its implementation in a FE code. The first part will outline the mathematical structure and motivate the field equations governing the proposed model, denominated Serial Parallel, both in its Basic (BSP) and in its Serial Enhanced (ESP) forms. The second part will be concerned with a computational strategy specifically devised for the numerical solution of the local system of non-linear algebraic equations obtained.

In this chapter, as well as in the whole thesis, attention is restricted to linearized kinematics and to the purely mechanical theory.

3.1 Basic notation.

The description of the constitutive model presented in the following requires the preliminary introduction of kinematic and stress fields which are related both to the composite, considered as a whole homogeneous material, and to each component phase.

Let $\Omega \subset \mathbb{R}^3$ be the domain occupied by the composite material which is

assumed to be open and bounded while its closure will be denoted by the symbol $\overline{\Omega}$. Indicating by $I_t = [0, T]$ the time interval of interest and by ${}^t\boldsymbol{u} : \overline{\Omega} \times I_t \longrightarrow \mathbb{R}^3$ the displacement field at time $t \in I_t$ of the material point $\boldsymbol{x} \in \Omega$, we can introduce the displacement gradient $\nabla \boldsymbol{u}(\boldsymbol{x}, t)$ and the infinitesimal strain field of the composite as the symmetric part of the displacement gradient:

$$\boldsymbol{\varepsilon} = \mathrm{sym}[\nabla \boldsymbol{u}] = \frac{1}{2}[\nabla \boldsymbol{u} + \nabla \boldsymbol{u}^T],$$

where the explicit dependence on the material point $\boldsymbol{x}$ and on time t will be omitted if not strictly required. The stress tensor field of the composite will be denoted, as usual, by $\boldsymbol{\sigma} : \overline{\Omega} \times I \longrightarrow$ Sym, where Sym indicates the set of symmetric rank-two tensors.

Let us introduce the assumption that the composite material is biphasic and postulate the existence, even if only in a statistical sense, of a periodic Representative Volume Element (RVE)[49]. The two constituent phases will be addressed as 'matrix' and 'fiber' and denoted by the left subscripts f and m. This notation has to be regarded only as a convenient denomination convention since no special role is played by any of the phases which are completely interchangeable.

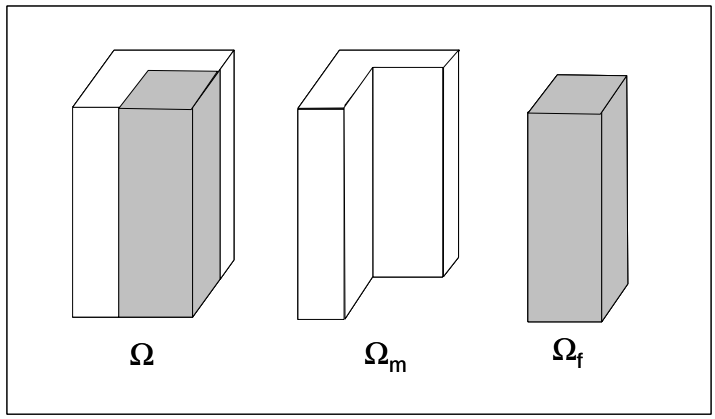

Figure 3.1: Example of the partition of the RVE in subdomains.

We will denote the volumetric fraction of fiber and matrix respectively by

${}_f c$, ${}_m c$:

$$ {}_f c = \frac{\int_{{}_f\Omega} dV}{\int_{\Omega} dV}; \quad {}_m c = \frac{\int_{{}_m\Omega} dV}{\int_{\Omega} dV}; $$

so that, trivially, ${}_f c + {}_m c = 1$.

It is customary to associate with each phase the volumetric strain averages, defined by:

$$ \overline{\boldsymbol{\varepsilon}} := \frac{\int_{\Omega} \boldsymbol{\varepsilon}\, dV}{\int_{\Omega} dV} \qquad \overline{{}_f\boldsymbol{\varepsilon}} := \frac{\int_{{}_f\Omega} \boldsymbol{\varepsilon}\, dV}{\int_{{}_f\Omega} dV} \qquad \overline{{}_m\boldsymbol{\varepsilon}} := \frac{\int_{{}_m\Omega} \boldsymbol{\varepsilon}\, dV}{\int_{{}_m\Omega} dV} \ . \tag{3.1} $$

A superimposed hat $\widehat{\cdot}$ denotes the corresponding quadratic average tensors $\hat{\boldsymbol{\varepsilon}}$, ${}_f\hat{\boldsymbol{\varepsilon}}$, ${}_m\hat{\boldsymbol{\varepsilon}}$ whose components have the following definitions:

$$ \widehat{\varepsilon_{ij}} := (\operatorname{sgn} \bar{\varepsilon}_{ij}) \sqrt{\frac{\int_{\Omega} \varepsilon_{ij}^2\, dV}{\int_{\Omega} dV}}, \qquad \widehat{{}_f\varepsilon_{ij}} := (\operatorname{sgn} \bar{\varepsilon}_{ij}) \sqrt{\frac{\int_{{}_f\Omega} \varepsilon_{ij}^2\, dV}{\int_{{}_f\Omega} dV}}, \tag{3.2} $$

$$ \tag{3.3} $$

$$ \widehat{{}_m\varepsilon_{ij}} := (\operatorname{sgn} \bar{\varepsilon}_{ij}) \sqrt{\frac{\int_{{}_m\Omega} \varepsilon_{ij}^2\, dV}{\int_{{}_m\Omega} dV}}, \tag{3.4} $$

where sgn denotes the *signum* function. In a completely analogous manner are defined the averages ($\overline{\boldsymbol{\sigma}}$, $\overline{{}_f\boldsymbol{\sigma}}$, $\overline{{}_m\boldsymbol{\sigma}}$) and quadratic averages ($\widehat{\boldsymbol{\sigma}}$, $\widehat{{}_f\boldsymbol{\sigma}}$, $\widehat{{}_m\boldsymbol{\sigma}}$) of the stress tensor.

Average quantities are related by:

$$ \bar{\boldsymbol{\varepsilon}} = {}_f c\ {}_f\bar{\boldsymbol{\varepsilon}} + {}_m c\ {}_m\bar{\boldsymbol{\varepsilon}}, \tag{3.5} $$

$$ \bar{\boldsymbol{\sigma}} = {}_f c\ {}_f\bar{\boldsymbol{\sigma}} + {}_m c\ {}_m\bar{\boldsymbol{\sigma}}. \tag{3.6} $$

It is assumed that the current state of the matrix phase at a point $\boldsymbol{x}$ of ${}_m\Omega$ is completely defined by the strain at such point ${}_m\boldsymbol{\varepsilon}(\boldsymbol{x})$ and by a finite set of internal variables denoted by the vector ${}_m\boldsymbol{\beta}$. Indicating by ${}_mI$ the set of admissible internal variables, the set of admissible states for the matrix**,** within a strain driven approach**,** is given by:

$$ {}_mS = \mathrm{Sym} \times {}_mI, $$

while the stress ${}_m\boldsymbol{\sigma}(\boldsymbol{x})$ is instead regarded as a dependent variable. With the fiber, in perfect analogy, are associated ${}_fI$, ${}_fS = \mathrm{Sym} \times {}_fI$ and ${}_f\boldsymbol{\sigma}(\boldsymbol{x})$.

With the term *constitutive law* we will refer to the system of differential equations that defines the evolution of the stress and of the internal variables:

$$ \begin{aligned} {}_m\dot{\boldsymbol{\sigma}} &= {}_m\boldsymbol{g}\left({}_m\boldsymbol{\varepsilon},\ {}_m\boldsymbol{\beta},\ {}_m\dot{\boldsymbol{\varepsilon}} \right). \\ {}_m\dot{\boldsymbol{\beta}} &= {}_m\boldsymbol{h}\left({}_m\boldsymbol{\varepsilon},\ {}_m\boldsymbol{\beta},\ {}_m\dot{\boldsymbol{\varepsilon}} \right). \end{aligned} \tag{3.7} $$

$$ \begin{aligned} {}_f\dot{\boldsymbol{\sigma}} &= {}_f\boldsymbol{g}\left({}_f\boldsymbol{\varepsilon},\ {}_f\boldsymbol{\beta},\ {}_f\dot{\boldsymbol{\varepsilon}} \right). \\ {}_f\dot{\boldsymbol{\beta}} &= {}_f\boldsymbol{h}\left({}_f\boldsymbol{\varepsilon},\ {}_f\boldsymbol{\beta},\ {}_f\dot{\boldsymbol{\varepsilon}} \right). \end{aligned} \tag{3.8} $$

Let us now introduce the free energy per unit volume of the composite U and the related quantities ${}_fU$ and ${}_mU$ defined as free energies per unit volume of the fiber and of the matrix, respectively. Owing to their definitions it turns out to be:

$$ U = {}_fc\,{}_fU \ + {}_mc\,{}_mU. $$

The incremental expression of the free energies can be used for defining the stress $\boldsymbol{\sigma}$ in the composite:

$$ dU = \boldsymbol{\sigma} \cdot d\bar{\boldsymbol{\varepsilon}}, $$

and those in the matrix and fiber phase:

$$ d_fU = {}_f\,\boldsymbol{\sigma} \cdot\ d_f\bar{\boldsymbol{\varepsilon}}, \quad d_mU = {}_m\,\boldsymbol{\sigma} \cdot\ d_m\bar{\boldsymbol{\varepsilon}}. $$

In the particular case of linear elasticity we can write:

$$ U = \frac{1}{2}\boldsymbol{\sigma} \cdot \bar{\boldsymbol{\varepsilon}} = \frac{1}{2}\,\boldsymbol{\sigma} \cdot \left({}_fc\ {}_f\bar{\boldsymbol{\varepsilon}} \ + \ {}_mc\ {}_m\bar{\boldsymbol{\varepsilon}} \right). $$

3.2 Serial/Parallel decomposition

To account for the cylindrical symmetry of the RVE we introduce a Cartesian reference frame and assume that its first axis $\boldsymbol{e}_1$ is parallel to the axis of cylindrical symmetry as shown in figure 3.2.

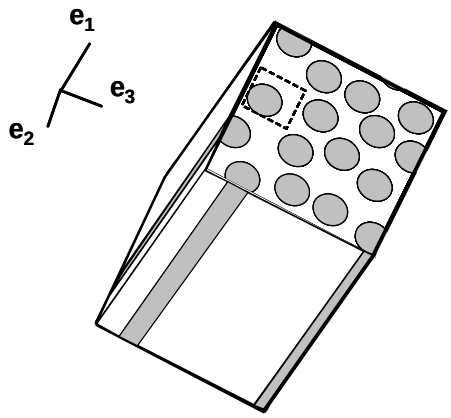

Figure 3.2: Schematic representation of the unit cell and of the fixed reference frame.

The stress and strain tensor fields considered above are decomposed in what, from now onwards, will be called their respective *Serial* and *Parallel* components. Denoting, indeed, with $\boldsymbol{N}_{11}$ the projector corresponding to $\boldsymbol{e}_1$:

$$\boldsymbol{N}_{11} = \boldsymbol{e}_1 \otimes \boldsymbol{e}_1,$$

we can introduce the fourth-order tensor $\mathbb{P}_P$ that extracts the parallel components from the relevant stress and strain tensors:

$$\mathbb{P}_P = \boldsymbol{N}_{11} \otimes \boldsymbol{N}_{11}, \tag{3.9}$$

and the tensor $\mathbb{P}_S$, defined as:

$$\mathbb{P}_S = \mathbb{I} - \mathbb{P}_P, \tag{3.10}$$

which provides the complementary serial component.

Consequently, we can formally define the following decomposed stress and strain fields:

$$ {}_{l}\widetilde{\boldsymbol{\sigma}}_{Q} = \mathbb{P}_{Q}\, {}_{l}\widetilde{\boldsymbol{\sigma}}, \tag{3.11} $$

$$ {}_{l}\widetilde{\boldsymbol{\varepsilon}}_{Q} = \mathbb{P}_{Q}\, {}_{l}\widetilde{\boldsymbol{\varepsilon}}, \tag{3.12} $$

where the superimposed **tilde** $\widetilde{(\cdot)}$ stands either for average $\overline{(\cdot)}$ or quadratic average $\widehat{(\cdot)}$ fields while $Q \in \{P, S\}$ and $l \in \{f, m\}$. For instance:

$$ {}_{f}\overline{\boldsymbol{\sigma}}_{P} = \mathbb{P}_{P}\, {}_{f}\overline{\boldsymbol{\sigma}}, \tag{3.13} $$

$$ {}_{m}\widehat{\boldsymbol{\varepsilon}}_{S} = \mathbb{P}_{S}\, {}_{m}\widehat{\boldsymbol{\varepsilon}}. \tag{3.14} $$

The same decomposition can also be performed on the variables related to the composite considered as a whole:

$$ \boldsymbol{\sigma}_{Q} = \mathbb{P}_{Q}\, \boldsymbol{\sigma}, $$

$$ \widetilde{\boldsymbol{\sigma}}_{Q} = \mathbb{P}_{Q}\, \widetilde{\boldsymbol{\sigma}}, \tag{3.15} $$

$$ \widetilde{\boldsymbol{\varepsilon}}_{Q} = \mathbb{P}_{Q}\, \widetilde{\boldsymbol{\varepsilon}}, \tag{3.16} $$

where the symbols $\widetilde{(\cdot)}$ and Q have the meaning defined above.

Since $\mathbb{P}_P + \mathbb{P}_S = \mathbb{I}$, an additive decomposition of the serial and parallel components of the tensors holds both for the components:

$$ {}_{l}\widetilde{\boldsymbol{\sigma}}_{S} + {}_{l}\widetilde{\boldsymbol{\sigma}}_{P} = {}_{l}\widetilde{\boldsymbol{\sigma}}, \tag{3.17} $$

$$ {}_{l}\widetilde{\boldsymbol{\varepsilon}}_{S} + {}_{l}\widetilde{\boldsymbol{\varepsilon}}_{P} = {}_{l}\widetilde{\boldsymbol{\varepsilon}}, \tag{3.18} $$

and for the whole composite:

$$ \boldsymbol{\sigma}_{S} + \boldsymbol{\sigma}_{P} = \boldsymbol{\sigma}, $$

$$ \widetilde{\boldsymbol{\sigma}}_{S} + \widetilde{\boldsymbol{\sigma}}_{P} = \widetilde{\boldsymbol{\sigma}}, \tag{3.19} $$

$$ \widetilde{\boldsymbol{\varepsilon}}_{S} + \widetilde{\boldsymbol{\varepsilon}}_{P} = \widetilde{\boldsymbol{\varepsilon}}. \tag{3.20} $$

According to such a serial/parallel decomposition, the derivative of the free energy of the composite may also be split up in two separate contributions associated with the serial and the parallel components:

$$ dU = dU_{P} + dU_{S}, $$

where:

$$dU_P = \boldsymbol{\sigma}_P \cdot d\bar{\boldsymbol{\varepsilon}}_P, \quad dU_S = \boldsymbol{\sigma}_S \cdot d\bar{\boldsymbol{\varepsilon}}_S. \tag{3.21}$$

In particular, for a linear stress-strain law, (3.21) provides:

$$U_P = \frac{1}{2}\boldsymbol{\sigma}_P \cdot \bar{\boldsymbol{\varepsilon}}_P, \quad U_S = \frac{1}{2}\boldsymbol{\sigma}_S \cdot \bar{\boldsymbol{\varepsilon}}_S. \tag{3.22}$$

3.3 Composition of constitutive models

In this section we analyze the possibility of defining a class of constitutive models for a binary composite by using the constitutive laws of both component materials. Such class of constitutive models is defined on the basis of the following assumptions.

The volumetric average strain $\bar{\boldsymbol{\varepsilon}}$ is regarded as the independent driving variable of the composite model.

The set of admissible internal variables of the composite I is the Cartesian product of the state variables of component phases ${}_fS$, ${}_mS$:

$$I = {}_fS \times {}_mS = \mathrm{Sym}^2 \times {}_fI \times {}_mI.$$

The strains of fiber and matrix are regarded as volumetric averages in the RVE and, accordingly, are denoted by ${}_f\bar{\boldsymbol{\varepsilon}}$ and ${}_m\bar{\boldsymbol{\varepsilon}}$ and assumed to obey to the average strains equation (3.5).

The internal variables of the new model $({}_f\bar{\boldsymbol{\varepsilon}}, {}_m\bar{\boldsymbol{\varepsilon}}, {}_f\boldsymbol{\beta}, {}_m\boldsymbol{\beta}) \in I$, and the average strain of the composite $\bar{\boldsymbol{\varepsilon}}$ constitute the complete set of state variables of the new constitutive model.

The constitutive laws of each phase still apply to the corresponding state variables averaged over the relevant volume.

The model thus defined is governed by equations (3.7) written for the average variables:

$${}_m\dot{\boldsymbol{\beta}} = {}_m\boldsymbol{h}\left({}_m\bar{\boldsymbol{\varepsilon}}, {}_m\boldsymbol{\beta}, {}_m\dot{\bar{\boldsymbol{\varepsilon}}}\right),$$

and its 'fiber' counterpart (3.8):

$${}_f\dot{\boldsymbol{\beta}} = {}_f\boldsymbol{h}\left({}_f\bar{\boldsymbol{\varepsilon}}, {}_f\boldsymbol{\beta}, {}_f\dot{\bar{\boldsymbol{\varepsilon}}}\right),$$

plus the average strains equation (3.5).

As one can easily recognize the former hypotheses are not sufficient for the definition of a material model. Actually, by comparing the number of unknowns and the number of equations of the class of models thus defined, one recognizes that the number of scalar unknowns exceeds the number of equations by a quantity of six. Therefore, the previously formulated problem is not well-posed. This evidence has an obvious physical motivation: the definition of a material model for the composite needs the introduction of additional equations that specificate somehow the interaction between component phases.

This additional set of equations will be referred to as *closure equations* and can be expressed in the most general form as follows:

$$f_i({}_f\bar{\boldsymbol{\varepsilon}},\ {}_m\bar{\boldsymbol{\varepsilon}},\ {}_f\boldsymbol{\beta},\ {}_m\boldsymbol{\beta}) = 0\ , \quad i = 1, ..., 6. \tag{3.23}$$

Even if not strictly necessary, it is useful to incorporate in the general expression of the constraint (3.23) also the average stresses:

$$f_i({}_f\bar{\boldsymbol{\varepsilon}},\ {}_m\bar{\boldsymbol{\varepsilon}},\ {}_f\boldsymbol{\beta},\ {}_m\boldsymbol{\beta},\ {}_f\bar{\boldsymbol{\sigma}},\ {}_m\bar{\boldsymbol{\sigma}}) = 0\ , \quad i = 1, ..., 6. \tag{3.24}$$

Of course the resulting material model will crucially depend on the specific closure equation selected since it characterizes completely the mechanical problem at the microscale. We will refer to the above defined family of models as the *composition* of the component constitutive models.

This approach converts the problem at the microscale essentially in an algebraic problem.

Even if this approach, to the best of the author's knowledge, is original, at least two composite material models reported in the literature belong to this class of constitutive models. The *Mixing Theory*, proposed by Car and Oller [20], adopts as closure equations the hypothesis, traditionally known as *Rule Of Mixtures*, of identical strain state in the two component materials: ${}_f\boldsymbol{\varepsilon} = {}_m\boldsymbol{\varepsilon}$. This closure equation corresponds to Voigt's assumption for the determination of an upper bound for stiffness (as well as, the closure equation ${}_f\boldsymbol{\sigma} = {}_m\boldsymbol{\sigma}$ originates a model which exhibits a stiffness coincident with the lower bound determined by Reuss [99]).

An additional model belonging to this class in the one proposed by Dvorak et al. [32] for the definition of an isotropic plasticity model of fibrous composites (summarized in chapter two). This model results from the composition of an elastoplastic law for the matrix and an elastic one for the fiber, in conjunction with a set of closure equations specifically devised for materials with a cylindrical RVE that exhibits a transversely isotropic behavior.

3.4 Closure equations for Long Fiber Composites (LFCs)

In this section we will analyze the application of some closure equations to be adopted in conjuction with the *composition of constitutive models* defined above and specifically devised for the simulation of the behaviour of biphasic long fiber composites.

The distinctive feature of long fiber composites is the cylindrical symmetry possessed by the RVE. This characteristic leads to the well known strongly anisotropic mechanical properties of this type of material. An appropriate closure equation devised for this specific problem should possess the following properties:

1) it should retain the essential axial constraint of the phases and recover transverse isotropy in the direction of cylindrical symmetry whenever component materials exhibit this property;

2) it should allow to recover at least a correct initial stiffness when no inelastic phenomena have occurred;

3) last but not least, it should retain a character of simplicity since the convenience of an approximate model, like the proposed one, stands in the possibility of avoiding the complex calculations required by a complete double-scale analysis [22], [129] especially in view of the final goal of the present work which is a reliable finite element analysis of real composite structures.

Besides, with the aim of defining a constitutive model that is independent from the specific models of component phases we will assume that the closure equation (3.24) does not depend on the internal variables ${}_f\boldsymbol{\beta}$ and ${}_m\boldsymbol{\beta}$. This requisite implies that the closure equation has to account only for the morphological properties of the unit cell and will have the form:

$$f_i({}_f\bar{\boldsymbol{\varepsilon}}, {}_m\bar{\boldsymbol{\varepsilon}}, {}_f\bar{\boldsymbol{\sigma}}, {}_m\bar{\boldsymbol{\sigma}}) = 0 \ , \quad i = 1, ..., 6. \tag{3.25}$$

A convenient approach which allows one to condense the fundamental morphological features of the unit cell in a simple set of algebraic equations could be the algebrization method adopted by Aboudi in the Method Of Cells (MOC) [2], [77], [5]. This method relies on two effective approximations: the original geometry of the unit cell is fitted with a regular arrangement of $N_\alpha \times N_\beta \times N_\gamma$ hexahedral subregions (square if the problem is in 2D); each of these subcells is considered to be filled by one single material and for each one a linear expansion of the displacement field is assumed. For a unit cell in which each side is divided into an equal number of N_c segments this approximation implies that the kinematics of the whole RVE is determined by $9 \times N_c^3$ unknown components of the

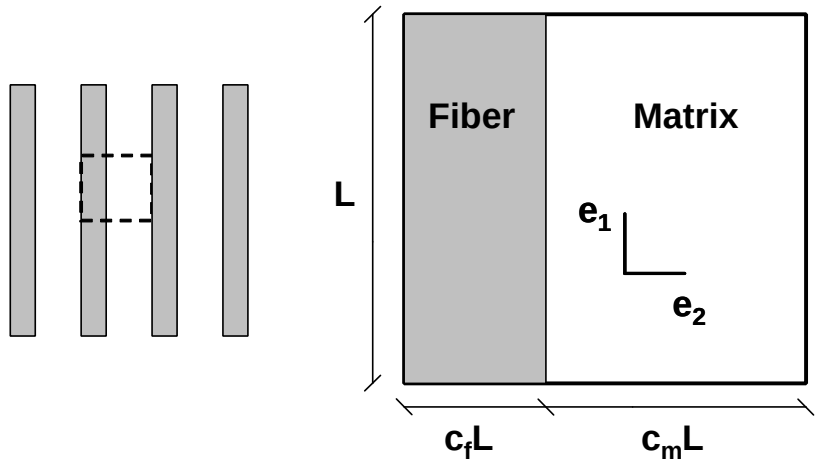

Figure 3.3: Unit cell for a biphasic bidimensional unidirectional array of stripes.

subcells deformation gradients plus $3 \times N_c^3$ displacements of the center of mass of each subcell . These unknowns are balanced by $3 \times 3 \times N_c^2(N_c - 1)$ displacement continuity conditions imposed in an average sense at the interfaces of the subcells, by $3 \times 3 \times N_c^2$ equations that originate from the kinematic conditions of indistiguishibility of the unit cell from its neighbours and by $3 \times N_c^3$ independent conditions of equilibrium for the subcells.

The original form of the method of Aboudi reduces the microstructural problem to an analytical problem where the unknowns are the components of stress and strains of four hexahedral subcells (one for the fiber and three for the matrix). This approach appears to be a reasonable compromise between simplicity of the approximation and accuracy of the modelization of the LFC unit cell. Unfortunately, these equations are still too complex to be used as closure equations in a constitutive model. Furthermore, since the unit cell is divided by Aboudi into four regions, a model based on this approach should possess a set of four groups of state variable in order to fully exploit this solution. This is not the case since, as stated above, we are looking for a closure equation suitable for a *binary composition* model which possesses one group of state variables for the fiber and one for the matrix.

With a view to achieve this result, let us first consider the two-dimensional biphasic cell shown in figure 3.3. Specializing the MOC to this 2D case, we only

have to subdivide the unit cell into $N_\alpha \times N_\beta$ subcells. Choosing $N_\alpha = 2$ and $N_\beta = 1$, we obtain only two 'stripes', one for the fiber and one for the matrix. Hence, the closure equations are easily obtained as:

$$\begin{cases} {}_m\varepsilon_1 = {}_f\varepsilon_1 \\ {}_m\sigma_2 = {}_f\sigma_2 \\ {}_m\tau_{12} = {}_f\tau_{12} \end{cases} . \tag{3.26}$$

These equations have an immediate interpretation: as physically reasonable the composite material shows a different behavior along the fibers and in the transverse direction. In analogy with simple spring models one would say that the model exhibits for matrix and fiber a 'parallel behavior' in the direction of the stripes and a 'serial behavior' in the transverse direction, as shown in figure 3.4. We will refer to (3.26) as the *2D Serial-Parallel* closure equation.

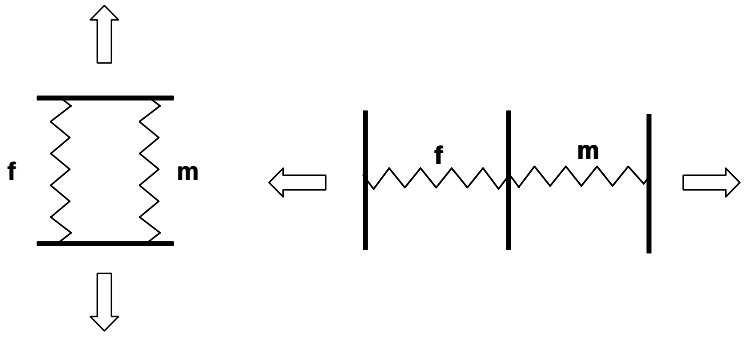

Figure 3.4: Scheme of the behaviour expressed by the 2D Serial-Parallel closure equation.

3.4.1 BSP closure equations

An extension of the *2D Serial-Parallel* closure equations (3.26) to the three-dimensional case can be formulated by assuming an isostrain hypothesis between fiber and matrix in the direction parallel to the fiber and an isostress hypothesis for the remaining components of stress:

$${}_m\bar{\boldsymbol{\varepsilon}}_P = {}_f\bar{\boldsymbol{\varepsilon}}_P, \tag{3.27}$$

$${}_m\bar{\boldsymbol{\sigma}}_S = {}_f\bar{\boldsymbol{\sigma}}_S. \tag{3.28}$$

These equations have been exploited by Dvorak et al. [32] to define an anisotropic plasticity model and by Rastellini and Oller [92],[93] to formulate a model denominated advanced serial-parallel mixing theory. Component materials have the same axial strain in the direction of the fiber while all components of stress that differ from the normal stress along the fiber are equal.

Relations (3.27) and (3.28) will be referred to henceforth as *Basic Serial Parallel (BSP)* closure equations. In this case the system of differential equations that govern the model is:

$$\begin{cases} \dot{{}_m\bar{\boldsymbol{\sigma}}} = {}_m\boldsymbol{g}\left({}_m\bar{\boldsymbol{\varepsilon}},\ {}_m\boldsymbol{\beta},\ \dot{{}_m\bar{\boldsymbol{\varepsilon}}} \right) \\ \dot{{}_m\boldsymbol{\beta}} = {}_m\boldsymbol{h}\left({}_m\bar{\boldsymbol{\varepsilon}},\ {}_m\boldsymbol{\beta},\ \dot{{}_m\bar{\boldsymbol{\varepsilon}}} \right) \\ \dot{{}_f\bar{\boldsymbol{\sigma}}} = {}_f\boldsymbol{g}\left({}_f\bar{\boldsymbol{\varepsilon}},\ {}_f\boldsymbol{\beta},\ \dot{{}_f\bar{\boldsymbol{\varepsilon}}} \right) \\ \dot{{}_f\boldsymbol{\beta}} = {}_f\boldsymbol{h}\left({}_f\bar{\boldsymbol{\varepsilon}},\ {}_f\boldsymbol{\beta},\ \dot{{}_f\bar{\boldsymbol{\varepsilon}}} \right) \\ \bar{\boldsymbol{\varepsilon}} = {}_fc\,{}_f\bar{\boldsymbol{\varepsilon}} + {}_mc\,{}_m\bar{\boldsymbol{\varepsilon}} \\ {}_m\bar{\boldsymbol{\varepsilon}}_P = {}_f\bar{\boldsymbol{\varepsilon}}_P \\ {}_m\bar{\boldsymbol{\sigma}}_S = {}_f\bar{\boldsymbol{\sigma}}_S \end{cases} . \tag{3.29}$$

It is well known that equation (3.28) determines a poor estimation of the transversal behaviour typically expressed by the inverse ROM [32]. The isostress assumption provides transversal tangential stiffness estimates below the lower bound determined by Hill for cylindrical RVE [50] and are not suitable for the definition of a realistic model of LFC.

3.5 Closure equations of the Enhanced Serial Parallel (ESP) model

3.5.1 One-dimensional case

The main reason for the unsatisfactory results obtained with the BSP closure equations is due to the fact that they do not take into account the lack of uniformity (non-uniformity) of stresses and strains in the plane orthogonal to the fibers; in other words what we have called the serial components of the stress and strain tensors are far from being uniformly distributed as implied by the BSP closure equations. For this reason we propose a novel constitutive model, denominated Enhanced Serial Parallel (ESP) model, which partly overcomes these drawbacks by addressing in an average sense this issue.

The rationale of our approach is based upon the use of the elastic energy of the composite. To fix the ideas and initially avoid unnecessary formal complications we make reference to a one dimensional linear elastic spring. The average elastic energy per unit length is then given by:

$$U = \frac{1}{2L}\int_0^L \sigma\,\varepsilon\,dx = \frac{1}{2L}\int_0^L E\varepsilon^2\,dx = \frac{1}{2}E\left(\sqrt{\frac{\int_0^L \varepsilon^2\,dx}{L}}\right)^2 = \frac{1}{2}E\hat{\varepsilon}^2, \qquad (3.30)$$

where:

$$\hat{\varepsilon} = (\operatorname{sgn}\bar{\varepsilon})\sqrt{\frac{\int_0^L \varepsilon^2\,dx}{L}},$$

is the one-dimensional counterpart of the analogous quantity defined by (3.2). If the strain is not uniform then the quadratic average strain $\hat{\varepsilon}$ will not coincide, in general, with the average strain $\bar{\varepsilon}$ defined by:

$$\bar{\varepsilon} = \frac{\int_0^L \varepsilon\,dx}{L}.$$

Therefore it is convenient to introduce the ratio:

$$\alpha = \frac{\hat{\varepsilon}}{\bar{\varepsilon}} = \frac{(\operatorname{sgn}\bar{\varepsilon})\sqrt{\int_0^L \varepsilon^2\,dx}}{\int_0^L \varepsilon\,dx};\;\; \hat{\varepsilon} = \alpha\bar{\varepsilon},$$

which represents a measure, when $\alpha \neq 1$, of the lack of uniformity of the strain field in the spring. Denoting with $\hat{\sigma}$ the quadratic average stress, $\hat{\sigma} = E\hat{\varepsilon}$, the energy can also be expressed in terms of quadratic average quantities as follows:

$$U = \frac{1}{2}E\hat{\varepsilon}^2 = \frac{1}{2}\hat{\sigma}\hat{\varepsilon}. \qquad (3.31)$$

Let us now consider a one-dimensional rod consisting of two elements, indicated with the symbols f and m, connected in a serial way and having lengths L_f and L_m, respectively. The average strain for this element is given by:

$$\bar{\varepsilon} = {}_fc\;\overline{{}_f\varepsilon} + {}_mc\;\overline{{}_m\varepsilon},$$

where ${}_fc = \dfrac{L_f}{L_f + L_m}$ and ${}_mc = \dfrac{L_m}{L_f + L_m}$.

We introduce now the hypothesis that the uniaxial strain state is not uniform along the rod; this hypothesis stems out from the necessity to consider an additional interaction due the other rod element, different from the serial connection.

Having supposed that the stress is not uniform in the elements f and m, the energy per unit length is given by:

$$U = {}_fc\ {}_fU + {}_mc\ {}_mU = \frac{1}{2}\,{}_fc\,{}_f\hat{\sigma}\ {}_f\hat{\varepsilon} + \frac{1}{2}\,{}_mc\,{}_m\hat{\sigma}\ {}_m\hat{\varepsilon}. \tag{3.32}$$

Since:

$${}_f\hat{\varepsilon} = {}_f\alpha\,\overline{{}_f\varepsilon}\ \ ,\ {}_m\hat{\varepsilon} = {}_m\alpha\,\overline{{}_m\varepsilon}, \tag{3.33}$$

we can re-write equation (3.32) in the equivalent form:

$$U = \frac{1}{2}\,{}_fc\ {}_f\alpha\,{}_f\hat{\sigma}\,\overline{{}_f\varepsilon} + \frac{1}{2}\,{}_mc\ {}_m\alpha\,{}_m\hat{\sigma}\,\overline{{}_m\varepsilon}. \tag{3.34}$$

Let us now express the elastic energy as function of stress and average strain pertaining to the whole composite:

$$U = \frac{1}{2}\sigma\bar{\varepsilon} = \frac{1}{2}\,{}_fc\,\sigma\,\overline{{}_f\varepsilon} + \frac{1}{2}\,{}_mc\,\sigma\,\overline{{}_m\varepsilon}. \tag{3.35}$$

Equating the amount of elastic energy separately stored in the matrix and in the fiber we thus infer:

$$\begin{aligned} {}_fc\ {}_f\alpha\,{}_f\hat{\sigma}\,\overline{{}_f\varepsilon} &= {}_fc\,\sigma\ \overline{{}_f\varepsilon}, \\ {}_mc\ {}_m\alpha\,{}_m\hat{\sigma}\,\overline{{}_m\varepsilon} &= {}_mc\,\sigma\ \overline{{}_m\varepsilon}, \end{aligned} \tag{3.36}$$

from which the following equalities can be deduced:

$$\sigma = {}_f\alpha\,{}_f\hat{\sigma} \qquad\qquad \sigma = {}_m\alpha\,{}_m\hat{\sigma}. \tag{3.37}$$

The previous equations motivate the part "*Enhanced Serial*" chosen for the denomination of the proposed model since when uniformity of the fields in the matrix and the fiber is re-introduced, that is ${}_f\alpha = {}_m\alpha = 1$, one recovers the well-known property of equal stress for elements, matrix and fiber connected in series:

$$\sigma = {}_f\hat{\sigma} = {}_m\hat{\sigma} = {}_f\bar{\sigma} = {}_m\bar{\sigma}.$$

Clearly, the further property of equal values within each phase between average and quadratic average stress is consequence of the uniformity assumption.

3.5.2 Extension to three dimensions

The model examined in the previous section has been intended to motivate in the simpler one-dimensional case the governing ESP closure equation that we are going to detail in the more general three-dimensional setting. The ideas which have led to equations (3.33) and (3.37) will be used in this section to modify the serial part of the BSP closure equations. This enhancement is carried out in order to avoid the previously mentioned drawbacks resulting from the non-uniformity of the serial part of the stress tensor along a plane transversal to the axis of simmetry.

In particular, taking into account the cylindrical symmetry of the RVE, the proposed model is based on the following assumptions:

- *The parallel part of stress and strain tensors is assumed to remain uniform within each one of the subdomains* ${}_m\Omega$ *and* ${}_f\Omega$:

$$\begin{aligned} \widehat{{}_f\boldsymbol{\varepsilon}}_P &= \overline{{}_f\boldsymbol{\varepsilon}}_P \quad \widehat{{}_m\boldsymbol{\varepsilon}}_P = \overline{{}_m\boldsymbol{\varepsilon}}_P, \\ \widehat{{}_f\boldsymbol{\sigma}}_P &= \overline{{}_f\boldsymbol{\sigma}}_P \quad \widehat{{}_m\boldsymbol{\sigma}}_P = \overline{{}_m\boldsymbol{\sigma}}_P. \end{aligned} \tag{3.38}$$

- *The equality condition of parallel strains remains unchanged with respect to the BSP model:*

$$\overline{{}_m\boldsymbol{\varepsilon}}_P = \overline{{}_f\boldsymbol{\varepsilon}}_P. \tag{3.39}$$

- *Within each one of the subdomains* ${}_m\Omega$ *and* ${}_f\Omega$*, the ratio between the homologous components of the quadratic and the linear average strain is assumed to be constant:*

$$\frac{\widehat{{}_f\boldsymbol{\varepsilon}}_{ij}}{\overline{{}_f\boldsymbol{\varepsilon}}_{ij}} = {}_f\alpha_{ij} \qquad \frac{\widehat{{}_m\boldsymbol{\varepsilon}}_{ij}}{\overline{{}_m\boldsymbol{\varepsilon}}_{ij}} = {}_m\alpha_{ij} \ . \tag{3.40}$$

Let us now comment in detail some consequences of the previous assumptions.

On account of equation (3.5) the hypothesis (3.39) implies that the parallel strain of the components will coincide with the parallel strain of the whole composite:

$$\overline{{}_m\boldsymbol{\varepsilon}}_P = \overline{{}_f\boldsymbol{\varepsilon}}_P = \bar{\boldsymbol{\varepsilon}}_P.$$

The previous relation, combined with (3.38) can also be reformulated in terms of quadratic average strain components along the fiber:

$$\widehat{{}_m\boldsymbol{\varepsilon}}_P = \widehat{{}_f\boldsymbol{\varepsilon}}_P. \tag{3.41}$$

Finally, we observe that expressing (3.38) in indicial notation:

$$\begin{aligned} \widehat{{}_f\boldsymbol{\varepsilon}}_{11} &= \overline{{}_f\boldsymbol{\varepsilon}}_{11} \quad \widehat{{}_m\boldsymbol{\varepsilon}}_{11} = \overline{{}_m\boldsymbol{\varepsilon}}_{11}, \\ \widehat{{}_f\boldsymbol{\sigma}}_{11} &= \overline{{}_f\boldsymbol{\sigma}}_{11} \quad \widehat{{}_m\boldsymbol{\sigma}}_{11} = \overline{{}_m\boldsymbol{\sigma}}_{11}, \end{aligned}$$

it turns out to be:

$${}_f\alpha_{11} = {}_m\alpha_{11} = 1.$$

We are now ready to derive closure equations which enhance the serial behaviour of the composite predicted by the BSP closure equations.

Following an argument similar to the one detailed in the previous section for the one dimensional rod, we decompose the elastic energy in two contributions related to the serial and to the parallel components of the stress:

$$U = U_P + U_S.$$

Actually, our aim is to enhance the predictive capabilities of the BSP model in the plane transverse to the fiber, that is what we have called the serial part of the model. For this reason we shall concentrate on the *serial* part of the elastic energy by writing it in the form:

$$U_S = \frac{1}{2}\,{}_f c\,\widehat{{}_f\boldsymbol{\sigma}}_S \cdot \widehat{{}_f\boldsymbol{\varepsilon}}_S + \frac{1}{2}\,{}_m c\,\widehat{{}_m\boldsymbol{\sigma}}_S \cdot \widehat{{}_m\boldsymbol{\varepsilon}}_S,$$

so as to make explicit the separate contribution of the fiber and of the matrix.

For the subsequent developments it is convenient to express the relation (3.40) between the averages and the quadratic averages of the strain tensor in the more compact form:

$$\widehat{{}_f\boldsymbol{\varepsilon}} = {}_f\mathbb{L}\,\overline{{}_f\boldsymbol{\varepsilon}} \qquad \widehat{{}_m\boldsymbol{\varepsilon}} = {}_m\mathbb{L}\,\overline{{}_m\boldsymbol{\varepsilon}}\ , \tag{3.42}$$

where ${}_f\mathbb{L}$ and ${}_m\mathbb{L}$ are positive-definite rank-four tensors which, in Voigt's notation, are represented by the diagonal matrices:

$$\begin{aligned} {}_f\mathbb{L} &= \text{diag}\,({}_f\alpha_{11},\, {}_f\alpha_{22},\, {}_f\alpha_{33},\, {}_f\alpha_{23},\, {}_f\alpha_{13},\, {}_f\alpha_{12})\,, \\ {}_m\mathbb{L} &= \text{diag}\,({}_m\alpha_{11},\, {}_f\alpha_{22},\, {}_m\alpha_{33},\, {}_m\alpha_{23},\, {}_m\alpha_{13},\, {}_m\alpha_{12})\,. \end{aligned}$$

Hence, the serial part of the elastic energy assumes the form:

$$U_S = \frac{1}{2}\,{}_f c\,\widehat{{}_f\boldsymbol{\sigma}}_S \cdot {}_f\mathbb{L}\,\overline{{}_f\boldsymbol{\varepsilon}}_S + \frac{1}{2}\,{}_m c\,\widehat{{}_m\boldsymbol{\sigma}}_S \cdot {}_m\mathbb{L}\,\overline{{}_m\boldsymbol{\varepsilon}}_S. \tag{3.43}$$

Writing the serial part of the elastic energy of the composite as:

$$U_S = \frac{1}{2}\boldsymbol{\sigma}_S \cdot \bar{\boldsymbol{\varepsilon}}_S = \frac{1}{2}\,{}_f c\,\boldsymbol{\sigma}_S \cdot \overline{{}_f\boldsymbol{\varepsilon}}_S + \frac{1}{2}\,{}_m c\,\boldsymbol{\sigma}_S \cdot \overline{{}_m\boldsymbol{\varepsilon}}_S, \tag{3.44}$$

and comparing the terms pertaining to the fiber and to the matrix with the analogous terms in (3.43) one infers the following identities:

$$\boldsymbol{\sigma}_S = {}_f\mathbb{L}\,\widehat{{}_f\boldsymbol{\sigma}}_S \qquad \boldsymbol{\sigma}_S = {}_m\mathbb{L}\,\widehat{{}_m\boldsymbol{\sigma}}_S, \tag{3.45}$$

which represent the closure equations of the proposed enhanced Serial-Parallel model. They generalize to the three-dimensional case relations (3.37) obtained in the one-dimensional case. Actually, assuming uniformity of the stress and strain state ${}_f\mathbb{K} = {}_m\mathbb{K} = \mathbb{I}$, the closure equations (3.28) of the BSP model are recovered.

For completeness we also report the expression of the *parallel* part of the elastic energy:

$$U_P = {}_f c\,{}_f U_P + {}_m c\,{}_m U_P = \frac{1}{2}\,{}_f c\,\widehat{{}_f\boldsymbol{\sigma}}_P \cdot \widehat{{}_f\boldsymbol{\varepsilon}}_P + \frac{1}{2}\,{}_m c\,\widehat{{}_m\boldsymbol{\sigma}}_P \cdot \widehat{{}_m\boldsymbol{\varepsilon}}.$$

Invoking (3.38) and (3.41) it turns out to be:

$$U_P = \frac{1}{2}\,{}_f c\,\overline{{}_f\boldsymbol{\sigma}}_P \cdot \bar{\boldsymbol{\varepsilon}}_P + \frac{1}{2}\,{}_m c\,\overline{{}_m\boldsymbol{\sigma}}_P \cdot \bar{\boldsymbol{\varepsilon}}_P = \frac{1}{2}\,\boldsymbol{\sigma}_P \cdot \bar{\boldsymbol{\varepsilon}}_P,$$

where $\boldsymbol{\sigma}_P = {}_f c\,\overline{{}_f\boldsymbol{\sigma}}_P + {}_m c\,\overline{{}_m\boldsymbol{\sigma}}_P$.

Summarizing, the ESP model proposed is governed by the following system of equations:

$$\begin{cases} \dot{\widehat{{}_m\boldsymbol{\sigma}}} = {}_m g\left(\widehat{{}_m\boldsymbol{\varepsilon}},\ {}_m\boldsymbol{\beta},\ \dot{\widehat{{}_m\boldsymbol{\varepsilon}}}\right) \\ \dot{{}_m\boldsymbol{\beta}} = {}_m h\left(\widehat{{}_m\boldsymbol{\varepsilon}},\ {}_m\boldsymbol{\beta},\ \dot{\widehat{{}_m\boldsymbol{\varepsilon}}}\right) \\ \dot{\widehat{{}_f\boldsymbol{\sigma}}} = {}_f g\left(\widehat{{}_f\boldsymbol{\varepsilon}},\ {}_f\boldsymbol{\beta},\ \dot{\widehat{{}_f\boldsymbol{\varepsilon}}}\right) \\ \dot{{}_f\boldsymbol{\beta}} = {}_f h\left(\widehat{{}_f\boldsymbol{\varepsilon}},\ {}_f\boldsymbol{\beta},\ \dot{\widehat{{}_f\boldsymbol{\varepsilon}}}\right) \\ {}_f\mathbb{L}\,\widehat{{}_f\boldsymbol{\sigma}}_S = {}_m\mathbb{L}\,\widehat{{}_m\boldsymbol{\sigma}}_S \\ \\ \widehat{{}_m\boldsymbol{\varepsilon}}_P = \widehat{{}_f\boldsymbol{\varepsilon}}_P \\ \bar{\boldsymbol{\varepsilon}} = {}_f c\,\overline{{}_f\boldsymbol{\varepsilon}} + {}_m c\,\overline{{}_m\boldsymbol{\varepsilon}}. \\ \widehat{{}_m\boldsymbol{\varepsilon}}_P = \widehat{{}_f\boldsymbol{\varepsilon}}_P = \bar{\boldsymbol{\varepsilon}}_P \\ \widehat{{}_f\boldsymbol{\varepsilon}} = {}_f\mathbb{L}\,\overline{{}_f\boldsymbol{\varepsilon}} \qquad \widehat{{}_m\boldsymbol{\varepsilon}} = {}_m\mathbb{L}\,\overline{{}_m\boldsymbol{\varepsilon}}. \end{cases} \tag{3.46}$$

If we perform the following change of variables:

$$ {}_f\boldsymbol{\varepsilon}^* = {}_f\mathbb{K}^{-1}\,\widehat{{}_f\boldsymbol{\varepsilon}} \qquad {}_m\boldsymbol{\varepsilon}^* = {}_m\mathbb{K}^{-1}\,\widehat{{}_m\boldsymbol{\varepsilon}}, \tag{3.47} $$

$$ {}_f\boldsymbol{\sigma}^* = {}_f\mathbb{K}\,\widehat{{}_f\boldsymbol{\sigma}} \qquad {}_m\boldsymbol{\sigma}^* = {}_m\mathbb{K}\,\widehat{{}_m\boldsymbol{\sigma}}, \tag{3.48} $$

the system (3.46) can be re-arranged in a form analogous to the system of equations that governs the BSP model:

$$ \begin{cases} \dot{\widehat{{}_m\boldsymbol{\sigma}}} = {}_mg\left(\widehat{{}_m\boldsymbol{\varepsilon}},\ {}_m\boldsymbol{\beta},\ \dot{\widehat{{}_m\boldsymbol{\varepsilon}}}\right) \\ {}_m\dot{\boldsymbol{\beta}} = {}_mh\left(\widehat{{}_m\boldsymbol{\varepsilon}},\ {}_m\boldsymbol{\beta},\ \dot{\widehat{{}_m\boldsymbol{\varepsilon}}}\right) \\ \\ \dot{\widehat{{}_f\boldsymbol{\sigma}}} = {}_fg\left(\widehat{{}_f\boldsymbol{\varepsilon}},\ {}_f\boldsymbol{\beta},\ \dot{\widehat{{}_f\boldsymbol{\varepsilon}}}\right) \\ {}_f\dot{\boldsymbol{\beta}} = {}_fh\left(\widehat{{}_f\boldsymbol{\varepsilon}},\ {}_f\boldsymbol{\beta},\ \dot{\widehat{{}_f\boldsymbol{\varepsilon}}}\right) \\ \\ \boldsymbol{\varepsilon}^* = {}_fc\,{}_f\boldsymbol{\varepsilon}^* + {}_mc\,{}_m\boldsymbol{\varepsilon}^* \\ {}_f\boldsymbol{\sigma}_S^* = {}_m\boldsymbol{\sigma}_S^* \\ {}_f\boldsymbol{\varepsilon}_P^* = {}_m\boldsymbol{\varepsilon}_P^*. \end{cases} . \tag{3.49} $$

In conclusion we remark that, conforming to the closure equation (3.45) which is expressed in terms of quadratic averages, the ESP is formulated in terms of quadratic averages of strain and stress fields.

3.6 Calculation of the coefficients ${}_f\alpha$ and ${}_m\alpha$

To determine proper values for the coefficients ${}_f\alpha_{ij}$ e ${}_m\alpha_{ij}$ which appear in the matrixes ${}_f\mathbb{K}$ and ${}_m\mathbb{K}$, approximated models to calculate the ratios of formulas (3.40) are employed. The parallel isostrain hypothesis implies: ${}_f\alpha_{11} = {}_m\alpha_{11} = 1$; therefore only the remaining coefficients have to be estimated. In this section we describe a simplified model used for evaluating the coefficients ${}_f\alpha_{22}$, ${}_f\alpha_{33}$, ${}_m\alpha_{22}$ and ${}_m\alpha_{33}$.

For the evalution of coefficients regarding transverse normal stresses the scheme described at continuation can be followed. Since for all normal stresses the deformed configuration preserves the cylindrical symmetry, the resulting

stress and strain state are independent from the particular transverse section of the RVE considered and the problem may be analyzed as a 2D problem in a generic transverse section. In figure 3.5 the transverse section is assimilated to the union of three rectangular regions. One region is occupied by the fiber (f) and the other two regions are occupied by the matrix. This square section of the RVE, when subjected to an horizontal stress, is assumed to behave similarly to the three springs shown in figure 3.6. The region of matrix, labeled (mp), behaves 'in parallel' with the fiber region and, therefore shares the same horizontal strain of the fiber, while the remaining region of matrix, labeled (ms), behaves as a serially connected spring. This simplification is also reminiscent of the initially impredictable placement of the unit cell with respect to fiber and matrix and of the fact that the actual relative position between the components in the composite is absolutely random. The volumes of the three regions are accordingly indicated with the symbols V_f, V_{mp} e V_{ms}.

The volumetric fractions of the matrix subregions are denoted by:

$$_{mp}c = \frac{V_{mp}}{V},$$

$$_{ms}c = \frac{V_{ms}}{V}.$$

while η indicates the ratio that measures the amount of matrix behaving in parallel:

$$\eta = \frac{V_{mp}}{V_m}. \tag{3.50}$$

Evidently:

$$_{mp}c + \ _{ms}c = \ _{m}c.$$

The estimation of $_{f}\alpha$ and $_{m}\alpha$ is performed in the elastic range. Denoting by E_f and E_m the elastic moduli of the fiber and of the matrix, respectively, we indicate by R the ratio:

$$R = \frac{E_f}{E_m}.$$

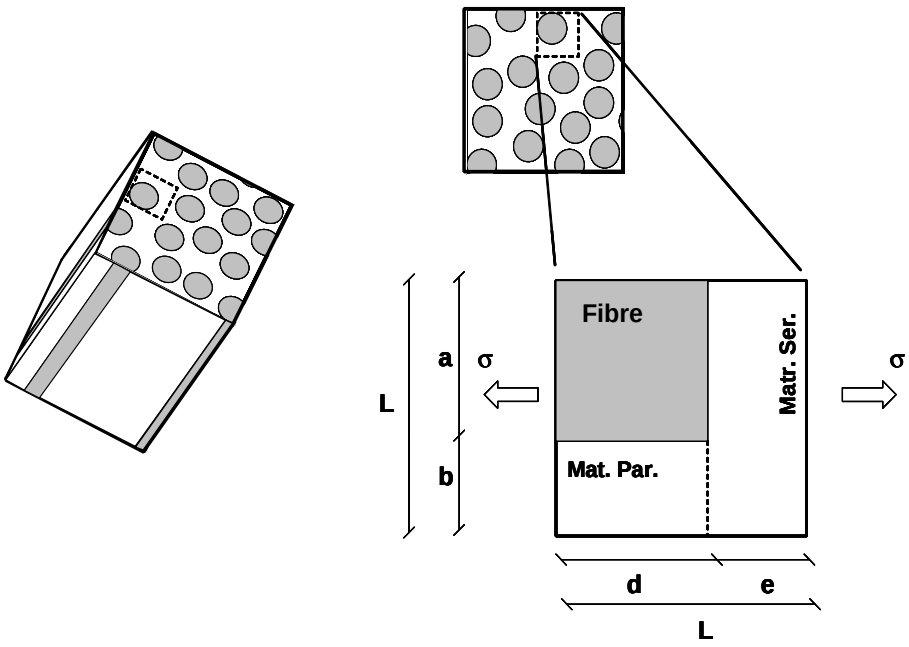

Figure 3.5: Schematic representation of the transversal section of the cylindrical cell.

Since L is the length of the side of the RVE square section, the significat dimensions can be expressed as:

$$\begin{aligned} a &= \frac{V_f}{V_f + V_{mp}} L = \frac{V_f}{V} \frac{V}{V_f + V_{mp}} L = \frac{{}_f c}{{}_f c + \eta\, {}_m c} L \\ b &= \frac{V_{mp}}{V_f + V_{mp}} L = \frac{V_{mp}}{V} \frac{V}{V_f + V_{mp}} L = \frac{\eta\, {}_m c}{{}_f c + \eta\, {}_m c} L. \end{aligned} \tag{3.51}$$

Therefore, omitting the unit thickness of the transverse section in the calculations, the stiffness of the springs are:

$$\begin{aligned} K_f &= R E_m \frac{a}{d} \\ K_{mp} &= E_m \frac{b}{d} \\ K_{ms} &= E_m \frac{L}{e} \end{aligned}$$

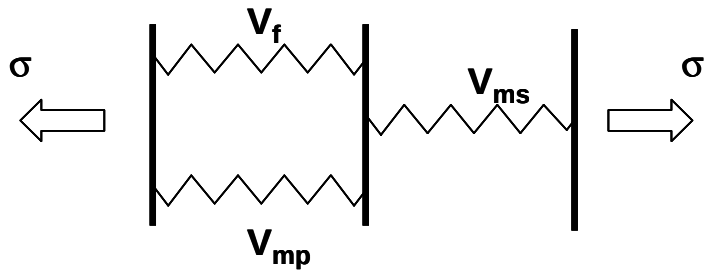

Figure 3.6: Spring system model adopted to schematize the transversal normal behaviour.

The stiffness of the set constituted by the two springs connected in parallel is given by the sum of component spring's stiffnesses:

$$K_p = K_f + K_{mp} = \left(R\frac{a}{d} + \frac{b}{d} \right) E_m$$

The condition of equilibrium for the springs that are serially connected is instead:

$$K_p \varepsilon_p d = K_{ms} \varepsilon_{ms} e,$$

so that:

$$(Ra + b)\, \varepsilon_p = L \varepsilon_{ms}.$$

By virtue of (3.51) one has:

$$\frac{R\, {}_f c + \eta\, {}_m c}{{}_f c + \eta\, {}_m c} \varepsilon_p = \varepsilon_{ms};$$

it is interesting to remark that ε_p and ε_{ms} coincide whenever $R = 1$, that is when fiber and matrix have the same elastic modulus.

The average strain is given by:

$$\overline{\varepsilon_m} = \frac{\varepsilon_{mp} V_{mp} + \varepsilon_{ms} V_{ms}}{V_m} = \left(\eta + \frac{R\, {}_f c + \eta\, {}_m c}{{}_f c + \eta\, {}_m c} (1 - \eta) \right) \varepsilon_p,$$

while the square average is, instead, given by :

$$\widehat{\varepsilon_m} = \sqrt{\frac{\varepsilon_{mp}^2 V_{mp} + \varepsilon_{ms}^2 V_{ms}}{V_m}} = \left(\sqrt{\eta + \left(\frac{R\, {}_f c + \eta\, {}_m c}{{}_f c + \eta\, {}_m c} \right)^2 (1 - \eta)} \right) \varepsilon_p$$

In conclusion, the definition (3.40) supplies:

$$ {}_m\alpha_{22} = \frac{\widehat{\varepsilon_m}}{\overline{\varepsilon_m}} = \frac{\left(\sqrt{\eta + \left(\frac{R\,{}_f c + \eta\,{}_m c}{{}_f c + \eta\,{}_m c} \right)^2 (1-\eta)} \right)}{\left(\eta + \frac{R\,{}_f c + \eta\,{}_m c}{{}_f c + \eta\,{}_m c} (1-\eta) \right)}. \tag{3.52} $$

Of course, ${}_f\alpha = 1$ since the stress remains uniform in the fiber.

It remains only to relate η to the fiber volume fraction c_f. The geometrical condition that the fiber region is square implies:

$$ a = d = \sqrt{V_f}, $$

while the squareness of the transversal section of the unit cell provides:

$$ L = \sqrt{V}. $$

Hence, for (3.50), the ratio η results:

$$ \begin{aligned} \eta &= \frac{bd}{V_m} = \frac{\sqrt{V_f}\left(\sqrt{V} - \sqrt{V_f}\right)}{V - V_f} = \frac{\sqrt{\frac{V_f}{V}} - \frac{V_f}{V}}{1 - \frac{V_f}{V}} = \\ &= \frac{\sqrt{c_f} - c_f}{1 - c_f} = \frac{\sqrt{c_f}\left(1 - \sqrt{c_f}\right)}{\left(1 + \sqrt{c_f}\right)\left(1 - \sqrt{c_f}\right)} = \frac{\sqrt{c_f}}{1 + c_f}. \end{aligned} \tag{3.53} $$

Such a value has to be substituted in (3.52) to provide the required value of ${}_m\alpha_{22}$. Notice that, owing to the transverse isotropy of the model, it tuns out to be:

$$ \begin{aligned} {}_m\alpha_{22} &= {}_m\alpha_{33}, \\ {}_f\alpha_{22} &= {}_f\alpha_{33}. \end{aligned} $$

For what concerns the longitudinal shear coefficients, a similar rationale, based on assimilating the longitudinal shear response (figure 3.6) to a system of

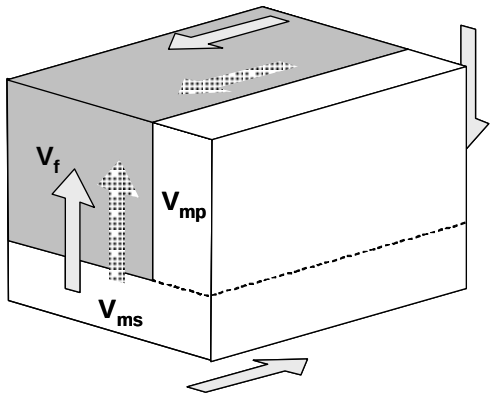

springs analogous to the one of figure 3.6, leads to the following expression:

$$ {}_m\alpha_{12} = {}_m\alpha_{13} = \frac{\left(\sqrt{\frac{\sqrt{c_f}}{1+c_f} + \left(\frac{S\,{}_fc + \frac{\sqrt{c_f}}{1+c_f}\,{}_mc}{{}_fc + \frac{\sqrt{c_f}}{1+c_f}\,{}_mc} \right)^2 \left(\frac{1+c_f-\sqrt{c_f}}{1+c_f} \right)} \right)}{\left(\frac{\sqrt{c_f}}{1+c_f} + \frac{S\,{}_fc + \frac{\sqrt{c_f}}{1+c_f}\,{}_mc}{{}_fc + \frac{\sqrt{c_f}}{1+c_f}\,{}_mc} \left(\frac{1+c_f-\sqrt{c_f}}{1+c_f} \right) \right)} \tag{3.54} $$

$$ {}_f\alpha_{12} = {}_f\alpha_{13} = 1, $$

where S is now the ratio between the longitudinal shear moduli of fiber and matrix:

$$ R = \frac{G_f}{G_m}. $$

For the coefficients related to the transversal shear behaviour it is assumed:

$$ {}_m\alpha_{23} = {}_f\alpha_{23} = 1; \tag{3.55} $$

these values determine for this component of strain a perfect serial behaviour, as well as in the BSP model.

3.7 Algorithm for the solution of BSP model

In order to carry out a direct comparison between the results provided by the BSP and the ESP model we first illustrate the algorithmic details concerning the numerical implementation of the BSP model. Incidentally, we remark that the structure of the two algorithms is quite similar.

The BSP model is summarized as follows. The state variables that define the problem are the average strains in the component phases ${}_f\bar{\boldsymbol{\varepsilon}}, {}_m\bar{\boldsymbol{\varepsilon}} \in \mathrm{Sym}$, ${}_f\boldsymbol{\beta} \in {}_fI$, ${}_m\boldsymbol{\beta} \in {}_mI$ plus the composite average strain $\bar{\boldsymbol{\varepsilon}}$. The equations governing the problem are

- 1) the constitutive laws of both materials:

$$\begin{aligned} {}_m\dot{\boldsymbol{\sigma}} &= {}_m\boldsymbol{g}\left({}_m\bar{\boldsymbol{\varepsilon}},\ {}_m\boldsymbol{\beta},\ {}_m\dot{\bar{\boldsymbol{\varepsilon}}}\right) \\ {}_m\dot{\boldsymbol{\beta}} &= {}_m\boldsymbol{h}\left({}_m\bar{\boldsymbol{\varepsilon}},\ {}_m\boldsymbol{\beta},\ {}_m\dot{\bar{\boldsymbol{\varepsilon}}}\right) \end{aligned} \quad . \tag{3.56}$$

$$\begin{aligned} {}_f\dot{\boldsymbol{\sigma}} &= {}_f\boldsymbol{g}\left({}_f\bar{\boldsymbol{\varepsilon}},\ {}_f\boldsymbol{\beta},\ {}_f\dot{\bar{\boldsymbol{\varepsilon}}}\right) \\ {}_f\dot{\boldsymbol{\beta}} &= {}_f\boldsymbol{h}\left({}_f\bar{\boldsymbol{\varepsilon}},\ {}_f\boldsymbol{\beta},\ {}_f\dot{\bar{\boldsymbol{\varepsilon}}}\right) \end{aligned} \tag{3.57}$$

- 2) the equation relating the average strains:

$$\bar{\boldsymbol{\varepsilon}} = {}_fc\ {}_f\bar{\boldsymbol{\varepsilon}} + {}_mc\ {}_m\bar{\boldsymbol{\varepsilon}}, \tag{3.58}$$

- 3) the BSP closure equations:

$$ {}_m\bar{\boldsymbol{\varepsilon}}_P = {}_f\bar{\boldsymbol{\varepsilon}}_P, \tag{3.59a}$$

$$ {}_m\bar{\boldsymbol{\sigma}}_S = {}_f\bar{\boldsymbol{\sigma}}_S. \tag{3.59b}$$

The algorithmic problem, regarded as a strain driven problem, can be schematized in the following way: given the state variables at time t:

$$ {}^t\left[{}_f\bar{\boldsymbol{\varepsilon}}\right], {}^t\left[{}_m\bar{\boldsymbol{\varepsilon}}\right], {}^t\left[{}_f\boldsymbol{\beta}\right], {}^t\left[{}_m\boldsymbol{\beta}\right], {}^t\left[\bar{\boldsymbol{\varepsilon}}\right], $$

and the composite strain at time $t + \Delta t$: ${}^{t+\Delta t}\left[\boldsymbol{\varepsilon}\right]$, find the updated state of the composite at time $t + \Delta t$, defined by the set of variables:

$$ {}^{t+\Delta t}\left[{}_f\bar{\boldsymbol{\varepsilon}}\right], {}^{t+\Delta t}\left[{}_m\bar{\boldsymbol{\varepsilon}}\right], {}^{t+\Delta t}\left[{}_f\boldsymbol{\beta}\right], {}^{t+\Delta t}\left[{}_m\boldsymbol{\beta}\right], {}^{t+\Delta t}\left[\bar{\boldsymbol{\varepsilon}}\right], $$

satisfying equations (3.56), (3.57), (3.58), (3.59a) and (3.59b).

In the following it will be shown that the system of non-linear equations defining the problem can be solved via a specifically devised Newton-Raphson iterative strategy.

The proposed algorithm relies upon the assumption that two independent solution algorithms for the constitutive problem of each single component material are provided. Thus we assume that at each Gauss point of a given element mesh we dispose of a constitutive algorithm for the local integration of the evolution equations according to the schemes sinthetically reported below:

$$\underbrace{\left\{ {}^{t}\left[{}_{f}\bar{\boldsymbol{\varepsilon}}\right], {}^{t}\left[{}_{f}\boldsymbol{\beta}\right]\right\} \; ; \; {}^{t+\Delta t}\left[{}_{f}\bar{\boldsymbol{\varepsilon}}\right]}_{\Downarrow}$$
$$\boxed{\begin{array}{c}\text{Constituve}\\ \text{Algorithm}\\ \text{of the Fiber}\end{array}}$$
$$\underbrace{{}^{t+\Delta t}\left[{}_{f}\boldsymbol{\beta}\right] \; ; \; {}^{t+\Delta t}\left[{}_{f}\bar{\boldsymbol{\sigma}}\right]}$$

$$\underbrace{\left\{ {}^{t}\left[{}_{m}\bar{\boldsymbol{\varepsilon}}\right], {}^{t}\left[{}_{m}\boldsymbol{\beta}\right]\right\} \; ; \; {}^{t+\Delta t}\left[{}_{m}\bar{\boldsymbol{\varepsilon}}\right]}_{\Downarrow}$$
$$\boxed{\begin{array}{c}\text{Constituve}\\ \text{Algorithm}\\ \text{of the Matrix}\end{array}}$$
$$\underbrace{{}^{t+\Delta t}\left[{}_{m}\boldsymbol{\beta}\right] \; ; \; {}^{t+\Delta t}\left[{}_{m}\bar{\boldsymbol{\sigma}}\right]}$$

. (3.60)

The constitutive algorithms for each component material have been denoted by *fiber/matrix constitutive algorithms* as opposite to the solution algorithm pertaining to the whole BSP model denoted by *composite algorithm*. Furthermore, we will refer to the linearization at a generic time τ of the function ${}^{\tau+\Delta\tau}\left[{}_{f}\bar{\boldsymbol{\varepsilon}}\right] \longrightarrow {}^{\tau+\Delta\tau}\left[{}_{f}\bar{\boldsymbol{\sigma}}\right]$, implicitly defined by the constitutive algorithm of the fiber sketched in (3.60), as the *fiber algorithmic tangent operator* ${}^{\tau}\left[{}_{f}\mathbb{C}\right] = \left.\dfrac{\partial^{\tau+\Delta\tau}\left[{}_{f}\bar{\boldsymbol{\sigma}}\right]}{\partial^{\tau+\Delta\tau}\left[{}_{f}\bar{\boldsymbol{\varepsilon}}\right]}\right|_{\Delta\tau=0}$. This definition is trivially extended to the matrix material.

The composite algorithm will make crucial use of the following decomposition of tangent operators induced by the previously detailed serial-parallel decomposition:

$${}_{c}\mathbb{C} = \begin{bmatrix} \dfrac{\partial_{c}\bar{\boldsymbol{\sigma}}_{P}}{\partial_{c}\bar{\boldsymbol{\varepsilon}}_{P}} & \dfrac{\partial_{c}\bar{\boldsymbol{\sigma}}_{P}}{\partial_{c}\bar{\boldsymbol{\varepsilon}}_{S}} \\ \\ \dfrac{\partial_{c}\bar{\boldsymbol{\sigma}}_{S}}{\partial_{c}\bar{\boldsymbol{\varepsilon}}_{P}} & \dfrac{\partial_{c}\bar{\boldsymbol{\sigma}}_{S}}{\partial_{c}\bar{\boldsymbol{\varepsilon}}_{S}} \end{bmatrix} = \begin{bmatrix} {}_{c}\mathbb{C}_{PP} & {}_{c}\mathbb{C}_{PS} \\ {}_{c}\mathbb{C}_{SP} & {}_{c}\mathbb{C}_{SS} \end{bmatrix}, \tag{3.61}$$

where:

$$\begin{cases} {}_c\mathbb{C}_{PP} = \mathbb{P}_P : {}_c\mathbb{C} : \mathbb{P}_P \\ {}_c\mathbb{C}_{PS} = \mathbb{P}_P : {}_c\mathbb{C} : \mathbb{P}_S \\ {}_c\mathbb{C}_{SP} = \mathbb{P}_S : {}_c\mathbb{C} : \mathbb{P}_P \\ {}_c\mathbb{C}_{SS} = \mathbb{P}_S : {}_c\mathbb{C} : \mathbb{P}_S \end{cases} \qquad \text{with:} \quad c = m,\ f.$$

The serial part of the matrix strain ${}_m\bar{\boldsymbol{\varepsilon}}_S$ is selected as the independent variable of the Newton-Raphson scheme to be adopted for the composite algorithm. Such a choice is completely arbitrary since the algorithm could be equivalently formulated in terms of the serial part of the fiber strain. The lack of balance in the serial stresses $\Delta\bar{\boldsymbol{\sigma}}_S$ is adopted as the residual, in the sense that at the end of the algorithm it has to be set equal to zero the difference:

$$\Delta\bar{\boldsymbol{\sigma}}_S \ = \ {}_m\bar{\boldsymbol{\sigma}}_S \ - \ {}_f\bar{\boldsymbol{\sigma}}_S. \tag{3.62}$$

The generic iteration of the Newton Raphson method will be denoted with the index k. In order to avoid a too complex notation, when no ambiguity can arise, we will refer with $[\bullet]_k$ to the trial quantities ${}^{t+\Delta t}[\bullet]_k$. Thus the iterative scheme to exploit is given by:

$$[\Delta\bar{\boldsymbol{\sigma}}_S]_k + [\mathbb{J}]_k \left([\,{}_m\bar{\boldsymbol{\varepsilon}}_S]_{k+1} - [\,{}_m\bar{\boldsymbol{\varepsilon}}_S]_k \right) = \mathbf{0}, \tag{3.63}$$

where the Jacobian $[\mathbb{J}]_k$ is:

$$[\mathbb{J}]_k = \left. \frac{\partial\,[\Delta\bar{\boldsymbol{\sigma}}_S]}{\partial\,{}_m\bar{\boldsymbol{\varepsilon}}_S} \right|_{{}_m\bar{\boldsymbol{\varepsilon}}_S = [\,{}_m\bar{\boldsymbol{\varepsilon}}_S]_k}.$$

Its explicit expression is obtained by differentiating the residual function with respect to the unknown ${}_m\boldsymbol{\varepsilon}_S$:

$$\mathbb{J} = \frac{\partial\Delta\bar{\boldsymbol{\sigma}}_S}{\partial_m\bar{\boldsymbol{\varepsilon}}_S} = \frac{\partial\,({}_m\bar{\boldsymbol{\sigma}}_S - \ {}_f\bar{\boldsymbol{\sigma}}_S)}{\partial_m\bar{\boldsymbol{\varepsilon}}_S} = \ \frac{\partial_m\bar{\boldsymbol{\sigma}}_S}{\partial_m\bar{\boldsymbol{\varepsilon}}_S} - \ \frac{\partial_f\bar{\boldsymbol{\sigma}}_S}{\partial_f\bar{\boldsymbol{\varepsilon}}_S}\ \frac{\partial_f\bar{\boldsymbol{\varepsilon}}_S}{\partial_m\bar{\boldsymbol{\varepsilon}}_S}.$$

In particular, invoking the relation between the fiber and the matrix serial strain provided by (3.58):

$${}_f\bar{\boldsymbol{\varepsilon}}_S = \frac{1}{{}_fc}\ \bar{\boldsymbol{\varepsilon}}_S - \frac{{}_mc}{{}_fc}\ {}_m\bar{\boldsymbol{\varepsilon}}_S, \tag{3.64}$$

and, denoting by $\mathbb{I}$, the identity matrix in the 5x5 subspace of the serial components of Sym, it turns out to be:

$$\frac{\partial_f\bar{\boldsymbol{\varepsilon}}_S}{\partial_m\bar{\boldsymbol{\varepsilon}}_S} = -\frac{{}_mc}{{}_fc}\mathbb{I},$$

since the serial part $\boldsymbol{\varepsilon}_S$ of the composite strain $\boldsymbol{\varepsilon}$ is a given fixed quantity at time $t + \Delta t$. Thus the Jacobian may be written as:

$$\mathbb{J} = {}_m\mathbb{C}_{SS} - {}_f\mathbb{C}_{SS}\left(-\frac{{}^m c}{{}^f c}\mathbb{I}\right) = {}_m\mathbb{C}_{SS} + \frac{{}^m c}{{}^f c}\,{}_f\mathbb{C}_{SS},$$

and turns out to be a positive-definite tensor as linear combination of the positive-definite tensors ${}_m\mathbb{C}_{SS}$ and ${}_f\mathbb{C}_{SS}$ with positive coefficients. Accordingly, the solution of (3.63) provides an updated $(k+1)-th$ value for the unknown serial part of matrix strain as:

$$\left[{}_m\bar{\boldsymbol{\varepsilon}}_S\right]_{k+1} = \left[{}_m\bar{\boldsymbol{\varepsilon}}_S\right]_k - \left[\mathbb{J}\right]_k^{-1}\left[\Delta\bar{\boldsymbol{\sigma}}_S\right]_k .$$

In the following part of the section we describe in detail the tasks required in the implementation of the proposed algorithm.

3.7.1 Initial approximation

The composite algorithm requires the definition of an initial trial value for the independent variables i.e. for the matrix serial strain $\left[{}_m\bar{\boldsymbol{\varepsilon}}_S\right]_{k=0}$. The accuracy of this initial approximation is important since it strongly influences the number of iterations needed for the algorithm to converge. A natural way to perform this preliminary evaluation is to consider for each material a linear behaviour whose tangent matrix coincides with the tangent of the last converged load step. This approximation presents also the advantage of retrieving the exact solution when both materials remain elastic. In formulas this assumption reads:

$$\begin{aligned}
{}^{t+\Delta t}\left[{}_m\bar{\boldsymbol{\sigma}}\right] &= {}^{t}\left[{}_m\bar{\boldsymbol{\sigma}}\right] + {}^{t}\left[{}_m\mathbb{C}\right]\left({}^{t+\Delta t}\left[{}_m\bar{\boldsymbol{\varepsilon}}\right]_0 - {}^{t}\left[{}_m\bar{\boldsymbol{\varepsilon}}\right]\right) && \text{(3.65a)}\\
{}^{t+\Delta t}\left[{}_f\bar{\boldsymbol{\sigma}}\right] &= {}^{t}\left[{}_f\bar{\boldsymbol{\sigma}}\right] + {}^{t}\left[{}_f\mathbb{C}\right]\left({}^{t+\Delta t}\left[{}_f\bar{\boldsymbol{\varepsilon}}\right]_0 - {}^{t}\left[{}_f\bar{\boldsymbol{\varepsilon}}\right]\right). && \text{(3.65b)}
\end{aligned}$$

Subtracting (3.65b) from (3.65a) and taking the serial part of the resulting equation we obtain:

$$\begin{aligned}
{}^{t+\Delta t}\left[\Delta\bar{\boldsymbol{\sigma}}_S\right] &= {}^{t}\left[\Delta\bar{\boldsymbol{\sigma}}_S\right] + {}^{t}\left[{}_m\mathbb{C}_{SS}\right]\left(\left[{}_m\bar{\boldsymbol{\varepsilon}}_S\right]_0 - {}^{t}\left[{}_m\bar{\boldsymbol{\varepsilon}}_S\right]\right) + && \text{(3.66)}\\
&\quad + {}^{t}\left[{}_m\mathbb{C}_{SP}\right]\left({}^{t+\Delta t}\left[{}_m\bar{\boldsymbol{\varepsilon}}_P\right] - {}^{t}\left[{}_m\bar{\boldsymbol{\varepsilon}}_P\right]\right) - && \text{(3.67)}\\
&\quad - {}^{t}\left[{}_f\mathbb{C}_{SS}\right]\left({}^{t+\Delta t}\left[{}_f\bar{\boldsymbol{\varepsilon}}_S\right]_0 - {}^{t}\left[{}_f\bar{\boldsymbol{\varepsilon}}_S\right]\right) - {}^{t}\left[{}_f\mathbb{C}_{SP}\right]\left({}^{t+\Delta t}\left[{}_f\bar{\boldsymbol{\varepsilon}}_P\right] - {}^{t}\left[{}_f\bar{\boldsymbol{\varepsilon}}_P\right]\right). && \text{(3.68)}
\end{aligned}$$

Considering that (3.59a) and (3.59b) are satisfied both at time t and $t+\Delta t$, we have:

$$\begin{aligned} {}^{t}[\Delta\bar{\boldsymbol{\sigma}}_S] &= {}^{t+\Delta t}[\Delta\bar{\boldsymbol{\sigma}}_S] = 0, \\ {}^{t}[{}_m\bar{\boldsymbol{\varepsilon}}_P] &= {}^{t}[{}_f\bar{\boldsymbol{\varepsilon}}_P] = {}^{t}[\bar{\boldsymbol{\varepsilon}}_P] \\ {}^{t+\Delta t}[{}_m\bar{\boldsymbol{\varepsilon}}_P] &= {}^{t+\Delta t}[{}_f\bar{\boldsymbol{\varepsilon}}_P] = {}^{t+\Delta t}[\bar{\boldsymbol{\varepsilon}}_P] \end{aligned}$$

Furthermore, by use of (3.64) we can make appear in (3.66), as the only unknown, the initial increment of matrix serial strain $\left([{}_m\bar{\boldsymbol{\varepsilon}}_S]_0 - {}^{t}[{}_m\bar{\boldsymbol{\varepsilon}}_S]\right)$:

$$\left({}^{t}[{}_m\mathbb{C}_{SS}] + \frac{{}_mc}{{}_fc}\,{}^{t}[{}_f\mathbb{C}_{SS}]\right)\left([{}_m\bar{\boldsymbol{\varepsilon}}_S]_0 - {}^{t}[{}_m\bar{\boldsymbol{\varepsilon}}_S]\right) =$$
$$= \frac{1}{{}_fc}\,{}^{t}[{}_f\mathbb{C}_{SS}]\left({}^{t+\Delta t}[\bar{\boldsymbol{\varepsilon}}_S] - {}^{t}[\bar{\boldsymbol{\varepsilon}}_S]\right) + \left({}^{t}[{}_f\mathbb{C}_{SP}] - {}^{t}[{}_m\mathbb{C}_{SP}]\right)\left({}^{t+\Delta t}[\bar{\boldsymbol{\varepsilon}}_P] - {}^{t}[\bar{\boldsymbol{\varepsilon}}_P]\right).$$

Solving the previous equation we obtain the expression of the initial increment. Setting:

$$\mathbb{A} = \left({}_fc\,{}^{t}[{}_m\mathbb{C}_{SS}] + {}_mc\,{}^{t}[{}_f\mathbb{C}_{SS}]\right)^{-1},$$

we have:

$$[{}_m\bar{\boldsymbol{\varepsilon}}_S]_0 = {}^{t}[{}_m\bar{\boldsymbol{\varepsilon}}_S] + \mathbb{A}\left\{\begin{array}{c} {}^{t}[{}_f\mathbb{C}_{SS}]\left({}^{t+\Delta t}[\bar{\boldsymbol{\varepsilon}}_S] - {}^{t}[\bar{\boldsymbol{\varepsilon}}_S]\right) + \\ + {}_fc\left({}^{t}[{}_f\mathbb{C}_{SP}] - {}^{t}[{}_m\mathbb{C}_{SP}]\right)\left({}^{t+\Delta t}[\bar{\boldsymbol{\varepsilon}}_P] - {}^{t}[\bar{\boldsymbol{\varepsilon}}_P]\right) \end{array}\right\}. \tag{3.69}$$

A second option for the definition of a initial trial value for matrix serial strain, specific for the case of plasticity, may be that of considering for each material a linear elastic behaviour with 'frozen' plastic variables. The calculation leads to a formula analogous to (3.69) in which the corresponding elastic Serial-Parallel partitioned submatrixes ${}_f\mathbb{C}^{trial}_{SS}$, ${}_m\mathbb{C}^{trial}_{SS}$, ${}_f\mathbb{C}^{trial}_{SP}$, ${}_m\mathbb{C}^{trial}_{SP}$ appear. This initial approximation would perform better for plastic component materials in case of a cyclic load history.

3.7.2 Evaluation of the residual

The evaluation of the residual consists in associating, at each iteration k, the corresponding residual $[\Delta\bar{\boldsymbol{\sigma}}_S]_k$ with the last approximated value of the independent

variables $[{}_m\bar{\boldsymbol{\varepsilon}}_S]_k$. In our case this operation requires the execution of the algorithms devised to solve the components' constitutive models and thus is a task more complex than usual. The knowledge of $[{}_m\bar{\boldsymbol{\varepsilon}}_S]_k$ allows one to reconstruct the distribution of strain between the two materials:

$$\begin{aligned} [{}_m\bar{\boldsymbol{\varepsilon}}]_k &= [{}_m\bar{\boldsymbol{\varepsilon}}_S]_k + [\bar{\boldsymbol{\varepsilon}}_P]_k \\ [{}_f\bar{\boldsymbol{\varepsilon}}]_k &= \frac{1}{{}_fc}\,{}^{t+\Delta t}[\bar{\boldsymbol{\varepsilon}}_S] - \frac{{}_mc}{{}_fc}\,[{}_m\bar{\boldsymbol{\varepsilon}}_S]_k + [\bar{\boldsymbol{\varepsilon}}_P]_k\,. \end{aligned}$$

The constitutive algorithms of each component material provide the trial stresses $[{}_m\bar{\boldsymbol{\sigma}}]_k$, $[{}_f\bar{\boldsymbol{\sigma}}]_k$:

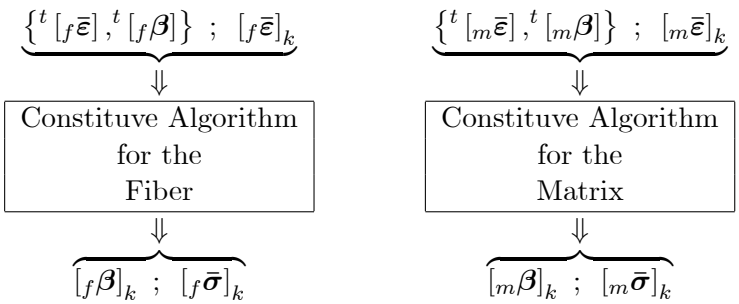

and, consequently, the residual: $[\Delta\bar{\boldsymbol{\sigma}}_S]_k = [\,{}_m\bar{\boldsymbol{\sigma}}_S]_k - [\,{}_f\bar{\boldsymbol{\sigma}}_S]_k$.

We remind that, provided the relevant solution algorithms are defined, any constitutive model can be adopted for component materials, e.g. elasticity, plasticity, continuum damage, and so on, since the described solution strategy is irrespective of the specific component constitutive models selected for fiber and matrix.

3.7.3 Convergence check

The convergence check requires the definition of a reference value which the residual norm is compared with. In the present case such a reference value has been proportioned to the order of magnitude of the serial stresses norm; clearly, according to the mechanical properties of fiber and matrix, it may differ from the order of magnitude of the parallel stresses norm. Thus, it has been chosen:

$$\begin{aligned} \mathrm{REFER} &= \min\{\mathrm{REFE1}, \mathrm{REFE2}\}\,, \\ \mathrm{REFE1} &= \min\left\{\left\|\,{}^t[\,{}_m\bar{\boldsymbol{\sigma}}_S]\right\|, \left\|\,{}^t[\,{}_f\bar{\boldsymbol{\sigma}}_S]\right\|\right\} \\ \mathrm{REFE2} &= \min\left\{\left\|\,{}^t[{}_m\mathbb{C}_{SS}] : [\bar{\boldsymbol{\varepsilon}}_S]\;\right\|, \left\|\,{}^t[{}_f\mathbb{C}_{SS}] : [\bar{\boldsymbol{\varepsilon}}_S]\;\right\|\right\}, \end{aligned}$$

provided that REFER is different from zero. The assumed tolerance is provided by:

$$\text{TOLER} = h \cdot \text{REFER},$$

where for the implementation in COMET it was set $h = 10^{-4}$. In conclusion when

$$\|[\Delta\bar{\boldsymbol{\sigma}}_S]_k\| \leq \text{TOLER},$$

the iterations are stopped.

3.8 Tangent operator of the BSP model

The solution of the structural problem requires, in addition to the resolution of the algorithm for the integration of the constitutive laws of the composite model, the calculation of the constitutive tangent operator. Actually, assuming that the structural problem is solved via the Finite Element Method, this operation is required to evaluate the stiffness matrix of the structural model. The composite constitutive algorithm may be schematized as follows:

$$\underbrace{\left\{{}^{t}\left[{}_{f}\bar{\boldsymbol{\varepsilon}}\right], {}^{t}\left[{}_{m}\bar{\boldsymbol{\varepsilon}}\right], {}^{t}\left[{}_{f}\boldsymbol{\beta}\right], {}^{t}\left[{}_{m}\boldsymbol{\beta}\right]\right\} \;;\; {}^{t+\Delta t}\left[\bar{\boldsymbol{\varepsilon}}\right]}$$

$$\Downarrow$$

$$\boxed{\begin{array}{c}\text{Constitutive}\\ \text{Algorithm}\\ \text{of the}\\ \text{BSP Model}\end{array}}$$

$$\Downarrow$$

$$\overbrace{\left\{{}^{t+\Delta t}\left[{}_{f}\bar{\boldsymbol{\varepsilon}}\right], {}^{t+\Delta t}\left[{}_{m}\bar{\boldsymbol{\varepsilon}}\right], {}^{t+\Delta t}\left[{}_{f}\boldsymbol{\beta}\right], {}^{t+\Delta t}\left[{}_{m}\boldsymbol{\beta}\right]\right\} \;;\; {}^{t+\Delta t}\left[\bar{\boldsymbol{\sigma}}\right]}$$

.

The *algorithmic tangent operator of the composite* at a generic time τ is the linearization of the function implicitly defined by the composite constitutive algorithm ${}^{\tau+\Delta\tau}\left[\boldsymbol{\varepsilon}\right] \longrightarrow {}^{\tau+\Delta\tau}\left[\boldsymbol{\sigma}\right]$:

$${}^{\tau}\left[\mathbb{C}\right] = \left.\frac{\partial^{\tau+\Delta\tau}\left[\bar{\boldsymbol{\sigma}}\right]}{\partial^{\tau+\Delta\tau}\left[\bar{\boldsymbol{\varepsilon}}\right]}\right|_{\Delta\tau=0}.$$

The derivation of the tangent matrix of the composite is performed by linearizing the system constituted by equations (3.56)-(3.59b), that governs the

BSP model, and by equation (3.6), that relates average stresses. Denoting the infinitesimal increments with a d prefix, the linearized system of equations reads:

$$\begin{cases} d_f\,\bar{\boldsymbol{\sigma}} = \dfrac{\partial_f \bar{\boldsymbol{\sigma}}}{\partial_f \bar{\boldsymbol{\varepsilon}}}\, d_f\,\bar{\boldsymbol{\varepsilon}} = {}_f\mathbb{C}\, d_f \bar{\boldsymbol{\varepsilon}} \\ d_m\,\bar{\boldsymbol{\sigma}} = \dfrac{\partial_m \bar{\boldsymbol{\sigma}}}{\partial_m \bar{\boldsymbol{\varepsilon}}}\, d_m\,\bar{\boldsymbol{\varepsilon}} = {}_f\mathbb{C}\, d_m \bar{\boldsymbol{\varepsilon}} \\ d\bar{\boldsymbol{\varepsilon}} = {}_f c\; d_f\bar{\boldsymbol{\varepsilon}} + {}_m c\; d_m\bar{\boldsymbol{\varepsilon}} \\ d_m\bar{\boldsymbol{\varepsilon}}_P = d_f\bar{\boldsymbol{\varepsilon}}_P. \\ d_m\bar{\boldsymbol{\sigma}}_S = d_f\bar{\boldsymbol{\sigma}}_S \\ d\bar{\boldsymbol{\sigma}} = {}_f c\, d_f\bar{\boldsymbol{\sigma}} + {}_m c\, d_m\bar{\boldsymbol{\sigma}}. \end{cases} \tag{3.70}$$

The set of equations (3.70) constitutes a linear system of 30 equations in the $6 \times 5 = 30$ unknowns represented by: $d_f\bar{\boldsymbol{\varepsilon}}$, $d_m\bar{\boldsymbol{\varepsilon}}$, $d_f\bar{\boldsymbol{\sigma}}$, $d_m\bar{\boldsymbol{\sigma}}$, $d\bar{\boldsymbol{\sigma}}$, and can be conveniently rearranged using decomposition (**??**):

$$d_f\bar{\boldsymbol{\sigma}}_P = {}_f\mathbb{C}_{PP}\; d_f\bar{\boldsymbol{\varepsilon}}_P + {}_f\mathbb{C}_{PS}\; d_f\bar{\boldsymbol{\varepsilon}}_S \tag{3.71a}$$
$$d_f\bar{\boldsymbol{\sigma}}_S = {}_f\mathbb{C}_{SP}\; d_f\bar{\boldsymbol{\varepsilon}}_P + {}_f\mathbb{C}_{SS}\; d_f\bar{\boldsymbol{\varepsilon}}_S \tag{3.71b}$$
$$d_m\bar{\boldsymbol{\sigma}}_P = {}_m\mathbb{C}_{PP}\; d_m\bar{\boldsymbol{\varepsilon}}_P + {}_m\mathbb{C}_{PS}\; d_m\bar{\boldsymbol{\varepsilon}}_S \tag{3.71c}$$
$$d_m\bar{\boldsymbol{\sigma}}_S = {}_m\mathbb{C}_{SP}\; d_m\bar{\boldsymbol{\varepsilon}}_P + {}_m\mathbb{C}_{SS}\; d_m\bar{\boldsymbol{\varepsilon}}_S \tag{3.71d}$$
$$d\bar{\boldsymbol{\varepsilon}}_P = {}_f c\, d_f\bar{\boldsymbol{\varepsilon}}_P + {}_m c\, d_m\bar{\boldsymbol{\varepsilon}}_P \tag{3.71e}$$
$$d\bar{\boldsymbol{\varepsilon}}_S = {}_f c\, d_f\bar{\boldsymbol{\varepsilon}}_S + {}_m c\, d_m\bar{\boldsymbol{\varepsilon}}_S \tag{3.71f}$$
$$d\bar{\boldsymbol{\sigma}}_P = {}_f c\, d_f\bar{\boldsymbol{\sigma}}_P + {}_m c\, d_m\bar{\boldsymbol{\sigma}}_P \tag{3.71g}$$
$$d\bar{\boldsymbol{\sigma}}_S = {}_f c\, d_f\bar{\boldsymbol{\sigma}}_S + {}_m c\, d_m\bar{\boldsymbol{\sigma}}_S \tag{3.71h}$$
$$d_m\bar{\boldsymbol{\varepsilon}}_P = d_f\bar{\boldsymbol{\varepsilon}}_P \tag{3.71i}$$
$$d_m\bar{\boldsymbol{\sigma}}_S = d_f\bar{\boldsymbol{\sigma}}_S. \tag{3.71j}$$

The solution of the previous system is straightforwardly obtained once $d_f\bar{\boldsymbol{\varepsilon}}_S$ and $d_m\bar{\boldsymbol{\varepsilon}}_S$ are separated from the remaining variables. From (3.71i) and (3.71e) we obtain:

$$d_m\bar{\boldsymbol{\varepsilon}}_P = d_f\bar{\boldsymbol{\varepsilon}}_P = d\bar{\boldsymbol{\varepsilon}}_P. \tag{3.72}$$

On account of the previous relation and of (3.71j) relations (3.71b) and (3.71d) supply:

$$ {}_f\mathbb{C}_{SS}\; d_f\bar{\boldsymbol{\varepsilon}}_S = \; {}_m\mathbb{C}_{SS}\; d_m\bar{\boldsymbol{\varepsilon}}_S - ({}_f\mathbb{C}_{SP} - \; {}_m\mathbb{C}_{SP})\; d\bar{\boldsymbol{\varepsilon}}_P. \tag{3.73} $$

Premultiplying (3.71f) by ${}_f\mathbb{C}_{SS}$ and substituting it in the expression for ${}_f\mathbb{C}_{SS}\; d_f\boldsymbol{\varepsilon}_S$ provided by (3.73) we obtain:

$$ {}_f\mathbb{C}_{SS}\; d\bar{\boldsymbol{\varepsilon}}_S = \; {}_fc\,[{}_m\mathbb{C}_{SS}\; d_m\bar{\boldsymbol{\varepsilon}}_S - ({}_f\mathbb{C}_{SP} - \; {}_m\mathbb{C}_{SP})\; d\bar{\boldsymbol{\varepsilon}}_P] \; + \; {}_mc\,{}_f\mathbb{C}_{SS}\; d_m\bar{\boldsymbol{\varepsilon}}_S. $$

Upon rearranging:

$$ ({}_fc\,{}_m\mathbb{C}_{SS} + {}_m\,c\,{}_f\mathbb{C}_{SS})\, d_m\bar{\boldsymbol{\varepsilon}}_S = \; {}_f\mathbb{C}_{SS}\, d\bar{\boldsymbol{\varepsilon}}_S + \; {}_fc\; ({}_f\mathbb{C}_{SP} - \; {}_m\mathbb{C}_{SP})\; d\bar{\boldsymbol{\varepsilon}}_P, $$

one finally obtains:

$$ d_m\bar{\boldsymbol{\varepsilon}}_S = \mathbb{A}\,[{}_f\mathbb{C}_{SS}\, d\bar{\boldsymbol{\varepsilon}}_S + \; {}_fc\; ({}_f\mathbb{C}_{SP} - \; {}_m\mathbb{C}_{SP})\; d\bar{\boldsymbol{\varepsilon}}_P]\,, \tag{3.74} $$

where:

$$ \mathbb{A} = ({}_fc\,{}_m\mathbb{C}_{SS} + {}_m\,c\,{}_f\mathbb{C}_{SS})^{-1}\,. \tag{3.75} $$

Commuting indices f and m in equation (3.74) the solution for $d_f\boldsymbol{\varepsilon}_S$ is obtained:

$$ d_f\bar{\boldsymbol{\varepsilon}}_S = \mathbb{A}\,[{}_m\mathbb{C}_{SS}\, d\bar{\boldsymbol{\varepsilon}}_S + \; {}_mc\; ({}_m\mathbb{C}_{SP} - \; {}_f\mathbb{C}_{SP})\; d\bar{\boldsymbol{\varepsilon}}_P]\,. \tag{3.76} $$

The knowledge of $d_m\boldsymbol{\varepsilon}_S$ and $d_f\boldsymbol{\varepsilon}_S$ allows us to obtain the composite stiffness by direct substitution. In particular, substituting (3.71a), (3.71c) and (3.72) in (3.71g) yields the parallel part of composite tangent operator:

$$ d\bar{\boldsymbol{\sigma}}_P = \; {}_fc\;(\; {}_f\mathbb{C}_{PP}\; d\bar{\boldsymbol{\varepsilon}}_P + \; {}_f\mathbb{C}_{PS}\; d_f\bar{\boldsymbol{\varepsilon}}_S) \; + \; {}_mc\,(\; {}_m\mathbb{C}_{PP}\; d\bar{\boldsymbol{\varepsilon}}_P + \; {}_m\mathbb{C}_{PS}\; d_m\bar{\boldsymbol{\varepsilon}}_S)\,, $$

which, upon substituting (3.74) and (3.76), provides finally:

$$ \begin{aligned} d\bar{\boldsymbol{\sigma}}_P = \quad & {}_fc\,\{{}_f\mathbb{C}_{PP}\; d\bar{\boldsymbol{\varepsilon}}_P + \; {}_f\mathbb{C}_{PS}\; \mathbb{A}\,[{}_m\mathbb{C}_{SS}\, d\bar{\boldsymbol{\varepsilon}}_S + \; {}_mc\; ({}_m\mathbb{C}_{SP} - \; {}_f\mathbb{C}_{SP})\; d\bar{\boldsymbol{\varepsilon}}_P]\} + \\ & + {}_mc\{\; {}_m\mathbb{C}_{PP}\; d\bar{\boldsymbol{\varepsilon}}_P + \; {}_m\mathbb{C}_{PS}\; \mathbb{A}\,[{}_f\mathbb{C}_{SS}\, d\bar{\boldsymbol{\varepsilon}}_S + \; {}_fc\; ({}_f\mathbb{C}_{SP} - \; {}_m\mathbb{C}_{SP})\; d\bar{\boldsymbol{\varepsilon}}_P]\}\,. \end{aligned} $$

Expanding the previous expression and rearranging the terms one obtains:

$$ \begin{aligned} d\bar{\boldsymbol{\sigma}}_P = \quad & [(\; {}_fc\,{}_f\mathbb{C}_{PP} + \; {}_mc\; {}_m\mathbb{C}_{PP}) + \; {}_mc\,{}_fc\; ({}_f\mathbb{C}_{PS} - \; {}_m\mathbb{C}_{PS})\; \mathbb{A}\,({}_m\mathbb{C}_{SP} - \; {}_f\mathbb{C}_{SP})]\, d\bar{\boldsymbol{\varepsilon}}_P + \\ & + ({}_fc\; {}_f\mathbb{C}_{PS}\; \mathbb{A}\; {}_m\mathbb{C}_{SS} + \; {}_mc\; {}_m\mathbb{C}_{PS}\; \mathbb{A}\; {}_f\mathbb{C}_{SS})\; d\bar{\boldsymbol{\varepsilon}}_S. \end{aligned} \tag{3.77} $$

For what concerns the serial part of composite tangent matrix, (3.71h) and (3.71j) yield:

$$d\bar{\boldsymbol{\sigma}}_S = d_f\bar{\boldsymbol{\sigma}}_S \tag{3.78}$$

$$d\bar{\boldsymbol{\sigma}}_S = d_m\bar{\boldsymbol{\sigma}}_S. \tag{3.79}$$

Equation (3.78) combined with (3.71b), (3.72) and (3.76) provides:

$$\begin{aligned} d\bar{\boldsymbol{\sigma}}_S &= {}_f\mathbb{C}_{SP}\, d\boldsymbol{\varepsilon}_P + {}_f\mathbb{C}_{SS}\,\mathbb{A}\,[{}_m\mathbb{C}_{SS}\, d\bar{\boldsymbol{\varepsilon}}_S + {}_mc\,({}_m\mathbb{C}_{SP} - {}_f\mathbb{C}_{SP})\, d\bar{\boldsymbol{\varepsilon}}_P] \\ &= ({}_f\mathbb{C}_{SS}\,\mathbb{A}\,{}_m\mathbb{C}_{SS})\, d\bar{\boldsymbol{\varepsilon}}_S + [\,{}_f\mathbb{C}_{SP} + {}_mc\,{}_f\mathbb{C}_{SS}\,\mathbb{A}\,({}_m\mathbb{C}_{SP} - {}_f\mathbb{C}_{SP})]\, d\bar{\boldsymbol{\varepsilon}}_P. \end{aligned} \tag{3.80}$$

On the other hand equation (3.79) combined with (3.71d), (3.72) and (3.74) supplies:

$$\begin{aligned} d\bar{\boldsymbol{\sigma}}_S &= {}_m\mathbb{C}_{SP}\, d\bar{\boldsymbol{\varepsilon}}_P + {}_m\mathbb{C}_{SS}\,\mathbb{A}\,[{}_f\mathbb{C}_{SS}\, d\bar{\boldsymbol{\varepsilon}}_S + {}_fc\,({}_f\mathbb{C}_{SP} - {}_m\mathbb{C}_{SP})\, d\bar{\boldsymbol{\varepsilon}}_P] \\ &= ({}_m\mathbb{C}_{SS}\,\mathbb{A}\,{}_f\mathbb{C}_{SS})\, d\bar{\boldsymbol{\varepsilon}}_S + [\,{}_m\mathbb{C}_{SP} + {}_fc\,{}_m\mathbb{C}_{SS}\,\mathbb{A}\,({}_f\mathbb{C}_{SP} - {}_m\mathbb{C}_{SP})]\, d\bar{\boldsymbol{\varepsilon}}_P. \end{aligned} \tag{3.81}$$

that is an expression completely similar to (3.80) provided that indices m and f are commuted. The addition of (3.80) and (3.81) yields:

$$\begin{aligned} d\bar{\boldsymbol{\sigma}}_S = {} & \tfrac{1}{2}\,[\,{}_m\mathbb{C}_{SS}\,\mathbb{A}\,{}_f\mathbb{C}_{SS} + {}_f\mathbb{C}_{SS}\,\mathbb{A}\,{}_m\mathbb{C}_{SS}\,]\, d\bar{\boldsymbol{\varepsilon}}_S + \\ & + \tfrac{1}{2}\,({}_m\mathbb{C}_{SP} + {}_f\mathbb{C}_{SP})\, d\bar{\boldsymbol{\varepsilon}}_P + \\ & + \tfrac{1}{2}\,[\,{}_mc\,{}_f\mathbb{C}_{SS}\,\mathbb{A}\,({}_m\mathbb{C}_{SP} - {}_f\mathbb{C}_{SP}) + {}_fc\,{}_m\mathbb{C}_{SS}\,\mathbb{A}\,({}_f\mathbb{C}_{SP} - {}_m\mathbb{C}_{SP})]\, d\bar{\boldsymbol{\varepsilon}}_P. \end{aligned} \tag{3.82}$$

Taking into account (3.75) and the following identity:

$$\begin{aligned} \frac{1}{2}\,({}_m\mathbb{C}_{SP} + {}_f\mathbb{C}_{SP}) &= \frac{1}{2}\mathbb{A}^{-1}\mathbb{A}\,({}_m\mathbb{C}_{SP} + {}_f\mathbb{C}_{SP}) = \\ &= \frac{1}{2}\,({}_fc\,{}_m\mathbb{C}_{SS} + {}_mc\,{}_f\mathbb{C}_{SS})\,\mathbb{A}\,({}_m\mathbb{C}_{SP} + {}_f\mathbb{C}_{SP}) = \\ &= \frac{1}{2}\,{}_fc\,{}_m\mathbb{C}_{SS}\mathbb{A}\,{}_m\mathbb{C}_{SP} + \frac{1}{2}\,{}_fc\,{}_m\mathbb{C}_{SS}\mathbb{A}\,{}_f\mathbb{C}_{SP} + \\ &\quad + \frac{1}{2}\,{}_mc\,{}_f\mathbb{C}_{SS}\mathbb{A}\,{}_m\mathbb{C}_{SP} + \frac{1}{2}\,{}_mc\,{}_f\mathbb{C}_{SS}\mathbb{A}\,{}_f\mathbb{C}_{SP}, \end{aligned}$$

(3.80) gets the final expression:

$$\begin{aligned} d\bar{\boldsymbol{\sigma}}_S = {} & \frac{1}{2}\,[\,{}_m\mathbb{C}_{SS}\,\mathbb{A}\,{}_f\mathbb{C}_{SS} + {}_f\mathbb{C}_{SS}\,\mathbb{A}\,{}_m\mathbb{C}_{SS}\,]\, d\bar{\boldsymbol{\varepsilon}}_S + \\ & + ({}_mc\,{}_f\mathbb{C}_{SS}\,\mathbb{A}\,{}_m\mathbb{C}_{SP} + {}_fc\,{}_m\mathbb{C}_{SS}\,\mathbb{A}\,{}_f\mathbb{C}_{SP})\, d\bar{\boldsymbol{\varepsilon}}_P. \end{aligned} \tag{3.83}$$

In conclusion, adopting the decomposition (**??**), the tangent operator of the BSP model becomes:

$$\mathbb{C} = \begin{bmatrix} \dfrac{\partial \boldsymbol{\sigma}_P}{\partial \boldsymbol{\varepsilon}_P} & \dfrac{\partial \boldsymbol{\sigma}_P}{\partial \boldsymbol{\varepsilon}_S} \\ \dfrac{\partial \boldsymbol{\sigma}_S}{\partial \boldsymbol{\varepsilon}_P} & \dfrac{\partial \boldsymbol{\sigma}_S}{\partial \boldsymbol{\varepsilon}_S} \end{bmatrix} = \begin{bmatrix} \mathbb{C}_{PP} & \mathbb{C}_{PS} \\ \mathbb{C}_{SP} & \mathbb{C}_{SS} \end{bmatrix},$$

where:

$$\mathbb{C}_{PP} = \begin{bmatrix} ({}_f c\, {}_f\mathbb{C}_{PP} + {}_m c\, {}_m\mathbb{C}_{PP}) + \\ + {}_m c\, {}_f c\ ({}_f\mathbb{C}_{PS} - {}_m\mathbb{C}_{PS})\ \mathbb{A}\, ({}_m\mathbb{C}_{SP} - {}_f\mathbb{C}_{SP}) \end{bmatrix} \tag{3.84a}$$

$$\mathbb{C}_{PS} = ({}_f c\ {}_f\mathbb{C}_{PS}\ \mathbb{A}\ {}_m\mathbb{C}_{SS} + {}_m c\ {}_m\mathbb{C}_{PS}\ \mathbb{A}\ {}_f\mathbb{C}_{SS}) \tag{3.84b}$$

$$\mathbb{C}_{SP} = ({}_m c\, {}_f\mathbb{C}_{SS}\, \mathbb{A}\, {}_m\mathbb{C}_{SP} + {}_f c\, {}_m\mathbb{C}_{SS}\, \mathbb{A}\, {}_f\mathbb{C}_{SP}) \tag{3.84c}$$

$$\mathbb{C}_{SS} = \frac{1}{2}\left[({}_m\mathbb{C}_{SS}\, \mathbb{A}\, {}_f\mathbb{C}_{SS}) + ({}_f\mathbb{C}_{SS}\, \mathbb{A}\, {}_m\mathbb{C}_{SS})\right]. \tag{3.84d}$$

Provided that the tangent operators of the component materials are symmetric:

$${}_c\mathbb{C}_{SS} = {}_c\mathbb{C}_{SS}^T, \quad {}_c\mathbb{C}_{SP} = {}_c\mathbb{C}_{PS}^T, \quad \text{with } \ c = m,\, f,$$

it is immediate to verify that:

$$\mathbb{C}_{SS} = \mathbb{C}_{SS}^T, \quad \mathbb{C}_{SP} = \mathbb{C}_{PS}^T,$$

so that the composite tangent operator is symmetric as well.

In the particular case of both linear isotropic component materials, indicating with ${}_f E$ and ${}_m E$ the Young moduli of fiber and matrix, and with ${}_f\nu$ and ${}_m\nu$ the respective Poisson ratios, formulas (3.84a-3.84d) provide the following compliance matrix $\mathbb{D} = \mathbb{C}^{-1}$:

$$\mathbb{D} = \begin{bmatrix} D_{11} & D_{12} & D_{13} & 0 & 0 & 0 \\ D_{12} & D_{22} & D_{23} & 0 & 0 & 0 \\ D_{13} & D_{23} & D_{33} & 0 & 0 & 0 \\ 0 & 0 & 0 & D_{44} & 0 & 0 \\ 0 & 0 & 0 & 0 & D_{55} & 0 \\ 0 & 0 & 0 & 0 & 0 & D_{66} \end{bmatrix},$$

with:

$$
\begin{aligned}
D_{11} &= \frac{1}{E_P}, \\
D_{12} &= D_{13} = -\frac{{}_f\nu\,{}_fE + {}_m\nu\,{}_mE}{E_P}, \\
D_{22} &= D_{33} = \frac{E'_S E_P - {}_fc\,{}_mc\,{}_f\nu^2\,{}_m\nu^2\left(\frac{{}_mE}{{}_mc} - \frac{{}_fE}{{}_fc}\right)^2}{({}_mE\,{}_fE)\,E_P} = \\
&= \frac{E'_S}{({}_mE\,{}_fE)}\left(1 - \frac{{}_fc\,{}_mc\,{}_f\nu^2\,{}_m\nu^2\left(\frac{{}_mE}{{}_mc} - \frac{{}_fE}{{}_fc}\right)^2}{E'_S E_P}\right), \\
D_{23} &= D_{22} - \frac{{}_f\nu\,{}_mE\,(1 + {}_f\nu) + {}_m\nu\,{}_fE\,(1 + {}_m\nu)}{{}_mE\,{}_fE}, \\
D_{44} &= D_{55} = D_{66} = \frac{1}{G_S},
\end{aligned}
\tag{3.85}
$$

where:

$$
\begin{aligned}
E_P &= {}_fc\,{}_fE + {}_mc\,{}_mE, \\
E'_S &= {}_mc\,{}_fE + {}_fc\,{}_mE, \\
\frac{1}{G_S} &= \left({}_fc\frac{2\,(1 + {}_f\nu)}{{}_fE} + {}_mc\frac{2\,(1 + {}_m\nu)}{{}_mE}\right).
\end{aligned}
$$

It is clear that in this case the tangent operator $\mathbb{C}$ possesses the symmetry property of transverse isotropy. The transverse Young modulus of the composite

$E_2 = E_3 = \dfrac{1}{D_{22}}$ can be written in an expressive form as follows:

$$\begin{aligned} E_2 &= \frac{1}{\left(\dfrac{{}_mc}{{}_mE} + \dfrac{{}_fc}{{}_fE}\right)} \left(\frac{1}{1-\rho_\nu}\right), \\ \rho_\nu &= \frac{{}_fc\,{}_mc\,{}_f\nu^2\,{}_m\nu^2 \left(\dfrac{{}_mE}{{}_mc} - \dfrac{{}_fE}{{}_fc}\right)^2}{E'_S E_P}, \end{aligned}$$

where ρ_ν can be interpreted as a factor accounting for the stiffening effect due to coupling between serial and parallel behaviours by means of the Poisson transverse contraction. This factor vanishes whenever either ${}_f\nu = 0$, ${}_m\nu = 0$ or $\dfrac{{}_mE}{{}_mc} = \dfrac{{}_fE}{{}_fc}$.

3.9 Algorithm for the solution of the ESP model

The set of equations that governs the ESP model does not significantly differ from the one that governs the BSP model. Accordingly, the solution can be achieved by following a strategy very similar to the Newton-Raphson scheme detailed in the previous section. The solution scheme thus will be described in a shorter form, remarking the main differences with the previous one.

The ESP model can be summarized as follows. The state variables that define the problem are the state variables of component materials in the point of square averages: $\widehat{{}_f\boldsymbol{\varepsilon}}, \widehat{{}_m\boldsymbol{\varepsilon}} \in \mathrm{Sym}$, ${}_f\boldsymbol{\xi} \in {}_fI$, ${}_m\boldsymbol{\xi} \in {}_mI$, plus the composite average strain $\boldsymbol{\varepsilon}^*$. The equations governing the problem are 1) the constitutive laws of both materials:

$$\begin{aligned} \dot{\widehat{{}_m\boldsymbol{\sigma}}} &= {}_m\boldsymbol{g}\left(\widehat{{}_m\boldsymbol{\varepsilon}},\ {}_m\boldsymbol{\beta},\ \dot{\widehat{{}_m\boldsymbol{\varepsilon}}}\right) \\ \dot{{}_m\boldsymbol{\xi}} &= {}_m\boldsymbol{h}\left(\widehat{{}_m\boldsymbol{\varepsilon}},\ {}_m\boldsymbol{\beta},\ \dot{\widehat{{}_m\boldsymbol{\varepsilon}}}\right) \end{aligned} . \tag{3.86}$$

$$\begin{aligned} \dot{\widehat{{}_f\boldsymbol{\sigma}}} &= {}_f\boldsymbol{g}\left(\widehat{{}_f\boldsymbol{\varepsilon}},\ {}_f\boldsymbol{\beta},\ \dot{\widehat{{}_f\boldsymbol{\varepsilon}}}\right) \\ \dot{{}_f\boldsymbol{\xi}} &= {}_f\boldsymbol{h}\left(\widehat{{}_f\boldsymbol{\varepsilon}},\ {}_f\boldsymbol{\beta},\ \dot{\widehat{{}_f\boldsymbol{\varepsilon}}}\right) \end{aligned} . \tag{3.87}$$

2) The equations relating square averages to linear averages:

$${}_f\boldsymbol{\varepsilon}^* = {}_f\mathbb{L}^{-1}\,\widehat{{}_f\boldsymbol{\varepsilon}} \qquad {}_m\boldsymbol{\varepsilon}^* = {}_m\mathbb{L}^{-1}\,\widehat{{}_m\boldsymbol{\varepsilon}} \tag{3.88}$$

$$ {}_f\boldsymbol{\sigma}^* = {}_f\mathbb{L}\,\widehat{{}_f\boldsymbol{\sigma}} \qquad {}_m\boldsymbol{\sigma}^* = {}_m\mathbb{L}\,\widehat{{}_m\boldsymbol{\sigma}} \tag{3.89} $$

2) the equation relating average strains:

$$ \boldsymbol{\varepsilon}^* = {}_fc\,{}_f\boldsymbol{\varepsilon}^* + {}_mc\,{}_m\boldsymbol{\varepsilon}^*, \tag{3.90} $$

3) the SE-SP closure equations expressed through the change of variables:

$$ {}_f\boldsymbol{\varepsilon}^*_P = {}_m\boldsymbol{\varepsilon}^*_P, \tag{3.91a} $$

$$ {}_f\boldsymbol{\sigma}^*_S = {}_m\boldsymbol{\sigma}^*_S \tag{3.91b} $$

The algorithmic problem can be stated in a form analogous to BSP: given the state variables of the whole composite at time t:

$$ {}^t\left[\widehat{{}_f\boldsymbol{\varepsilon}}\right], {}^t\left[\widehat{{}_m\boldsymbol{\varepsilon}}\right], {}^t\left[{}_f\boldsymbol{\beta}\right], {}^t\left[{}_m\boldsymbol{\beta}\right], {}^t\left[\boldsymbol{\varepsilon}^*\right], $$

and the composite strain at time $t+\Delta t$: ${}^{t+\Delta t}\left[\boldsymbol{\varepsilon}^*\right]$, find the updated state of the composite at time $t+\Delta t$, defined by the set of variables:

$$ {}^{t+\Delta t}\left[\widehat{{}_f\boldsymbol{\varepsilon}}\right], {}^{t+\Delta t}\left[\widehat{{}_m\boldsymbol{\varepsilon}}\right], {}^{t+\Delta t}\left[{}_f\boldsymbol{\beta}\right], {}^{t+\Delta t}\left[{}_m\boldsymbol{\beta}\right], {}^{t+\Delta t}\left[\boldsymbol{\varepsilon}^*\right], $$

satisfying equations (3.56), (3.57), (3.90) and (3.91a)-(3.91b) in the interval $[t, t+\Delta t]$.

This system of non-linear equations defining the problem is again solved using a Newton-Raphson strategy that assumes the existence of the algorithms for the integration of the constitutive problems of each single component:

$$ \underbrace{\left\{{}^t\left[\widehat{{}_f\boldsymbol{\varepsilon}}\right], {}^t\left[{}_f\boldsymbol{\beta}\right]\right\} \;;\; {}^{t+\Delta t}\left[\widehat{{}_f\boldsymbol{\varepsilon}}\right]}_{\Downarrow} \qquad \underbrace{\left\{{}^t\left[\widehat{{}_m\boldsymbol{\varepsilon}}\right], {}^t\left[{}_m\boldsymbol{\beta}\right]\right\} \;;\; {}^{t+\Delta t}\left[\widehat{{}_m\boldsymbol{\varepsilon}}\right]}_{\Downarrow} $$

$$ \boxed{\begin{array}{c}\text{Algorithm}\\ \text{solving the}\\ \text{Constituve Model of}\\ \text{Fiber}\end{array}} \qquad \boxed{\begin{array}{c}\text{Algorithm}\\ \text{solving the}\\ \text{Constituve Model of}\\ \text{Matrix}\end{array}} $$

$$ \overbrace{{}^{t+\Delta t}\left[{}_f\boldsymbol{\beta}\right] \;;\; {}^{t+\Delta t}\left[\widehat{{}_f\boldsymbol{\sigma}}\right]}^{\Downarrow} \qquad \overbrace{{}^{t+\Delta t}\left[{}_m\boldsymbol{\beta}\right] \;;\; {}^{t+\Delta t}\left[\widehat{{}_m\boldsymbol{\sigma}}\right]}^{\Downarrow} $$

The tangent operators of components integration algorithms are denoted with:

$$ {}^t\left[{}_f\mathbb{C}\right] = \left.\frac{\partial^{t+\Delta t}\left[\widehat{{}_f\boldsymbol{\sigma}}\right]}{\partial^{t+\Delta t}\left[\widehat{{}_f\boldsymbol{\varepsilon}}\right]}\right|_{\Delta t=0} $$

$$ {}^t\left[{}_m\mathbb{C}\right] = \left.\frac{\partial^{t+\Delta t}\left[\widehat{{}_m\boldsymbol{\sigma}}\right]}{\partial^{t+\Delta t}\left[\widehat{{}_m\boldsymbol{\varepsilon}}\right]}\right|_{\Delta t=0} $$

The serial-parallel decomposition for tangent operators is performed as usual:

$$
{}_c\mathbb{C} \;=\; \left[\begin{array}{cc} \dfrac{\partial_c \boldsymbol{\sigma}_P}{\partial_c \boldsymbol{\varepsilon}_P} & \dfrac{\partial_c \boldsymbol{\sigma}_P}{\partial_c \boldsymbol{\varepsilon}_S} \\ \dfrac{\partial_c \boldsymbol{\sigma}_S}{\partial_c \boldsymbol{\varepsilon}_P} & \dfrac{\partial_c \boldsymbol{\sigma}_S}{\partial_c \boldsymbol{\varepsilon}_S} \end{array}\right] = \left[\begin{array}{cc} {}_c\mathbb{C}_{PP} & {}_c\mathbb{C}_{PS} \\ {}_c\mathbb{C}_{SP} & {}_c\mathbb{C}_{SS} \end{array}\right], \tag{3.92}
$$

$$
\text{where} \quad : \quad \left\{\begin{array}{ll} {}_c\mathbb{C}_{PP} = \mathbb{P}_P : {}_c\mathbb{C} : \mathbb{P}_P & \\ {}_c\mathbb{C}_{PS} = \mathbb{P}_P : {}_c\mathbb{C} : \mathbb{P}_S & \\ {}_c\mathbb{C}_{SP} = \mathbb{P}_S : {}_c\mathbb{C} : \mathbb{P}_P & \\ {}_c\mathbb{C}_{SS} = \mathbb{P}_S : {}_c\mathbb{C} : \mathbb{P}_S & \end{array}\right. \qquad \text{with:} \quad c = m,\, f.
$$

The solution strategy is based, also in this case, on a Newton-Raphson scheme. This time, the serial part of matrix average strain ${}_m\boldsymbol{\varepsilon}^*_S$ is adopted as independent variable and the lack of balance in serial average stresses $\Delta\boldsymbol{\sigma}^*_S$:

$$
\Delta\boldsymbol{\sigma}^*_S \;=\; {}_m\boldsymbol{\sigma}^*_S \;-\; {}_f\boldsymbol{\sigma}^*_S. \tag{3.93}
$$

is adopted as target variable whose value has to be set to zero. The residual at each iteration k is:

$$
[\Delta\boldsymbol{\sigma}^*_S]_k = [\,{}_m\boldsymbol{\sigma}^*_S]_k - [\,{}_f\boldsymbol{\sigma}^*_S]_k\,.
$$

The Jacobian $[\mathbb{J}]_k$ is given by:

$$
[\mathbb{J}]_k = \left.\frac{\partial\,[\Delta\boldsymbol{\sigma}^*_S]}{\partial\,{}_m\boldsymbol{\varepsilon}^*_S}\right|_{{}_m\boldsymbol{\varepsilon}^*_S = [\,{}_m\boldsymbol{\varepsilon}^*_S]_k}.
$$

The fiber serial strain is related to matrix serial strain by (3.58):

$$
{}_f\boldsymbol{\varepsilon}^*_S = \frac{1}{{}_f c}\;\boldsymbol{\varepsilon}^*_S - \frac{{}_m c}{{}_f c}\;{}_m\boldsymbol{\varepsilon}^*_S. \tag{3.94}
$$

The Jacobian is given by:

$$
\begin{aligned}
\mathbb{J} \;&=\; \frac{\partial\Delta\boldsymbol{\sigma}^*_S}{\partial_m\boldsymbol{\varepsilon}^*_S} = \frac{\partial\,({}_m\boldsymbol{\sigma}^*_S - {}_f\,\boldsymbol{\sigma}^*_S)}{\partial_m\boldsymbol{\varepsilon}^*_S} = \frac{\partial_m\boldsymbol{\sigma}^*_S}{\partial_m\boldsymbol{\varepsilon}^*_S} - \frac{\partial_f\boldsymbol{\sigma}^*_S}{\partial_f\boldsymbol{\varepsilon}^*_S} \;:\; \frac{\partial_f\boldsymbol{\varepsilon}^*_S}{\partial_m\boldsymbol{\varepsilon}^*_S} = \\
&=\; \frac{\partial_m\boldsymbol{\sigma}^*_S}{\partial\widehat{{}_m\boldsymbol{\sigma}}_S}\frac{\partial\widehat{{}_m\boldsymbol{\sigma}}_S}{\partial\widehat{{}_m\boldsymbol{\varepsilon}}_S}.\frac{\partial\widehat{{}_m\boldsymbol{\varepsilon}}_S}{\partial_m\boldsymbol{\varepsilon}^*_S} - \frac{\partial_f\boldsymbol{\sigma}^*_S}{\partial\widehat{{}_f\boldsymbol{\sigma}}_S}\frac{\partial\widehat{{}_f\boldsymbol{\sigma}}_S}{\partial\widehat{{}_f\boldsymbol{\varepsilon}}_S}.\frac{\partial\widehat{{}_f\boldsymbol{\varepsilon}}_S}{\partial_f\boldsymbol{\varepsilon}^*_S} \;:\; \frac{\partial_f\boldsymbol{\varepsilon}^*_S}{\partial_m\boldsymbol{\varepsilon}^*_S}.
\end{aligned}
$$

From (3.88) and (3.89) we have:

$$\begin{aligned} \frac{\partial \widehat{{}_m\boldsymbol{\varepsilon}_S}}{\partial {}_m\boldsymbol{\varepsilon}^*_S} &= {}_m\mathbb{L}_{SS}, \qquad \frac{\partial \widehat{{}_f\boldsymbol{\varepsilon}_S}}{\partial {}_f\boldsymbol{\varepsilon}^*_S} = {}_f\mathbb{L}_{SS} \\ \frac{\partial {}_m\boldsymbol{\sigma}^*_S}{\partial \widehat{{}_m\boldsymbol{\sigma}_S}} &= {}_m\mathbb{L}_{SS}, \qquad \frac{\partial {}_f\boldsymbol{\sigma}^*_S}{\partial \widehat{{}_f\boldsymbol{\sigma}_S}} = {}_f\mathbb{L}_{SS}. \end{aligned}$$

(3.94) provides:

$$\frac{\partial {}_f\boldsymbol{\varepsilon}_S}{\partial {}_m\boldsymbol{\varepsilon}_S} = -\frac{{}_mc}{{}_fc}\mathbb{I},$$

being $\mathbb{I}$, in this case, the identity in the serial 5x5 subspace. Using (3.92) the Jacobian is:

$$\mathbb{J} = {}_m\mathbb{L}_{SS}\,{}_m\mathbb{C}_{SS}\,{}_m\mathbb{L}_{SS} + \frac{{}_mc}{{}_fc}\,{}_f\mathbb{L}_{SS}\,{}_f\mathbb{C}_{SS}\,{}_f\mathbb{L}_{SS}.$$

Defining:

$${}_m\mathbb{C}^*_{SS} = {}_m\mathbb{L}_{SS}\,{}_m\mathbb{C}_{SS}\,{}_m\mathbb{L}_{SS}, \qquad {}_f\mathbb{C}^*_{SS} = {}_f\mathbb{L}_{SS}\,{}_f\mathbb{C}_{SS}\,{}_f\mathbb{L}_{SS}, \tag{3.95}$$

the Jacobian may also be written:

$$\mathbb{J} = {}_m\mathbb{C}^*_{SS} + \frac{{}_mc}{{}_fc}\,{}_f\mathbb{C}^*_{SS}.$$

With position (3.95) the initial approximation and the tangent operator of the ESP model also obtain a form similar to the corresponding formulas seen for the BSP model. An initial approximation of the unknown that retrieves the exact solution when both fiber and matrix remain elastic is:

$$\mathbb{A}^* = \left({}_fc\,{}^t\left[{}_m\mathbb{C}^*_{SS}\right] + {}_mc\,{}^t\left[{}_f\mathbb{C}^*_{SS}\right]\right)^{-1},$$

we have:

$$\left[{}_m\boldsymbol{\varepsilon}^*_S\right]_0 = {}^t\left[{}_m\boldsymbol{\varepsilon}^*_S\right] + \mathbb{A}^* \left\{ \begin{array}{c} {}^t\left[{}_f\mathbb{C}^*_{SS}\right]\left({}^{t+\Delta t}\left[\boldsymbol{\varepsilon}^*_S\right] - {}^t\left[\boldsymbol{\varepsilon}^*_S\right]\right) + \\ + {}_fc\left({}^t\left[{}_f\mathbb{C}^*_{SP}\right] - {}^t\left[{}_m\mathbb{C}^*_{SP}\right]\right)\left({}^{t+\Delta t}\left[\boldsymbol{\varepsilon}^*_P\right] - {}^t\left[\boldsymbol{\varepsilon}^*_P\right]\right) \end{array} \right\}. \tag{3.96}$$

The evaluation of the residual checks if the actual value of the unknown $\left[{}_m\boldsymbol{\varepsilon}^*_S\right]_k$ satisfies the SE-SP problem. It is performed with the following steps: 1) reconstruction of average strains:

$$\begin{aligned} \left[{}_m\boldsymbol{\varepsilon}^*\right]_k &= \left[{}_m\boldsymbol{\varepsilon}^*_S\right]_k + \left[\boldsymbol{\varepsilon}^*_P\right]_k \\ \left[{}_f\boldsymbol{\varepsilon}\right]_k &= \frac{1}{{}_fc}\,{}^{t+\Delta t}\left[\boldsymbol{\varepsilon}^*_S\right] - \frac{{}_mc}{{}_fc}\,\left[{}_m\boldsymbol{\varepsilon}^*_S\right]_k + \left[\boldsymbol{\varepsilon}^*_P\right]_k; \end{aligned}$$

2) trasformation of average strain in the corresponding square average values:

$$[\widehat{m\boldsymbol{\varepsilon}}]_k \;=\; {}_m\mathbb{L}\,[{}_m\boldsymbol{\varepsilon}^*]_k$$

$$[\widehat{f\boldsymbol{\varepsilon}}]_k \;=\; {}_f\mathbb{L}\,[{}_f\boldsymbol{\varepsilon}^*]_k\,;$$

3) execution of the return mapping algorithms of component materials:

$$\underbrace{\left\{{}^t[\widehat{f\boldsymbol{\varepsilon}}]\,,{}^t[{}_f\boldsymbol{\beta}]\right\}\;;\;[\widehat{f\boldsymbol{\varepsilon}}]_k}_{\Downarrow}\qquad \underbrace{\left\{{}^t[\widehat{m\boldsymbol{\varepsilon}}]\,,{}^t[{}_m\boldsymbol{\beta}]\right\}\;;\;[\widehat{m\boldsymbol{\varepsilon}}]_k}_{\Downarrow}$$

$$\boxed{\begin{array}{c}\text{Algorithm}\\ \text{solving the}\\ \text{Constituve Model of}\\ \text{Fiber}\end{array}}\qquad \boxed{\begin{array}{c}\text{Algorithm}\\ \text{solving the}\\ \text{Constituve Model of}\\ \text{Matrix}\end{array}}$$

$$\Downarrow\qquad\qquad \Downarrow$$

$$\overbrace{[{}_f\boldsymbol{\beta}]_k\;;\;[\widehat{f\boldsymbol{\sigma}}]_k}\qquad \overbrace{[{}_m\boldsymbol{\beta}]_k\;;\;[\widehat{m\boldsymbol{\sigma}}]_k}$$

4) trasformation of square average strain in the corresponding average value:

$$[{}_f\boldsymbol{\sigma}^*]_k = {}_f\mathbb{L}\,[\widehat{f\boldsymbol{\sigma}}]_k \qquad [{}_m\boldsymbol{\sigma}^*]_k = {}_m\mathbb{L}\,[\widehat{m\boldsymbol{\sigma}}]_k\;; \tag{3.97}$$

5) calculation of the residual: $[\Delta\boldsymbol{\sigma}^*_S]_k = [\,{}_m\boldsymbol{\sigma}^*_S]_k - [\,{}_f\boldsymbol{\sigma}^*_S]_k$.

3.10 Tangent operator of the ESP model

The analogy between the governing equations of the BSP model, (3.29), and those governing the ESP model, (3.49), can be fully exploited also in the derivation of the tangent operator of the latter model. The calculation of the tangent operator requires the linearization of the ESP algorithm described in the previous section:

$$\underbrace{\left\{{}^t[\widehat{f\boldsymbol{\varepsilon}}]\,,{}^t[\widehat{m\boldsymbol{\varepsilon}}]\,,{}^t[{}_f\boldsymbol{\beta}]\,,{}^t[{}_m\boldsymbol{\beta}]\right\}\;;\;{}^{t+\Delta t}[\bar{\boldsymbol{\varepsilon}}]}_{\Downarrow}$$

$$\boxed{\begin{array}{c}\text{Algorithm}\\ \text{solving the}\\ \text{ESP Constituve Model}\end{array}}$$

$$\Downarrow$$

$$\overbrace{\left\{{}^{t+\Delta t}[\widehat{f\boldsymbol{\varepsilon}}]\,,{}^{t+\Delta t}[\widehat{m\boldsymbol{\varepsilon}}]\,,{}^{t+\Delta t}[{}_f\boldsymbol{\beta}]\,,{}^{t+\Delta t}[{}_m\boldsymbol{\beta}]\right\}\;;\;{}^{t+\Delta t}[\boldsymbol{\sigma}]}$$

.

The system of linearized ESP equations is:

$$\begin{cases} d_f\widehat{\boldsymbol{\sigma}} = \dfrac{\partial \widehat{f\boldsymbol{\sigma}}}{\partial \widehat{f\boldsymbol{\varepsilon}}}\, d_f\widehat{\boldsymbol{\varepsilon}} = {}_f\mathbb{C}\, d_f\widehat{\boldsymbol{\varepsilon}} \\ d_m\widehat{\boldsymbol{\sigma}} = \dfrac{\partial \widehat{m\boldsymbol{\sigma}}}{\partial \widehat{m\boldsymbol{\varepsilon}}}\, d_m\widehat{\boldsymbol{\varepsilon}} = {}_m\mathbb{C}\, d_m\widehat{\boldsymbol{\varepsilon}} \\ d\boldsymbol{\varepsilon}^* = {}_f c\, d_f\boldsymbol{\varepsilon}^* + {}_m c\, d_m\boldsymbol{\varepsilon}^* \\ d_f\boldsymbol{\sigma}^*_S = d_m\boldsymbol{\sigma}^*_S \\ d_f\boldsymbol{\varepsilon}^*_P = d_m\boldsymbol{\varepsilon}^*_P. \end{cases} . \tag{3.98}$$

Use of the chain rule and of eqt. (3.88) and (3.89) provides:

$$d_m\boldsymbol{\sigma}^* = \frac{\partial_m\boldsymbol{\sigma}^*}{\partial_m\boldsymbol{\varepsilon}^*} d_m\boldsymbol{\varepsilon}^* = d_m\boldsymbol{\sigma}^* \frac{\partial_m\boldsymbol{\sigma}^*}{\partial \widehat{m\boldsymbol{\sigma}}} \frac{\partial \widehat{m\boldsymbol{\sigma}}}{\partial \widehat{m\boldsymbol{\varepsilon}}} . \frac{\partial \widehat{m\boldsymbol{\varepsilon}}}{\partial_m\boldsymbol{\varepsilon}^*} d_m\boldsymbol{\varepsilon}^* = d_m\boldsymbol{\sigma}^*\, {}_m\mathbb{L}\, {}_m\mathbb{C}\, {}_m\mathbb{L}\, d_m\boldsymbol{\varepsilon}^*,$$

$$d_f\boldsymbol{\sigma}^* = \frac{\partial_f\boldsymbol{\sigma}^*}{\partial_f\boldsymbol{\varepsilon}^*} d_m\boldsymbol{\varepsilon}^* = d_m\boldsymbol{\sigma}^* \frac{\partial_f\boldsymbol{\sigma}^*}{\partial \widehat{f\boldsymbol{\sigma}}} \frac{\partial \widehat{f\boldsymbol{\sigma}}}{\partial \widehat{f\boldsymbol{\varepsilon}}} . \frac{\partial \widehat{f\boldsymbol{\varepsilon}}}{\partial_f\boldsymbol{\varepsilon}^*} d_m\boldsymbol{\varepsilon}^* = d_m\boldsymbol{\sigma}^*\, {}_f\mathbb{L}\, {}_f\mathbb{C}\, {}_f\mathbb{L}\, d_m\boldsymbol{\varepsilon}^*.$$

Defining:

$${}_m\mathbb{C}^* = {}_m\mathbb{L}\, {}_m\mathbb{C}\, {}_m\mathbb{L},$$

$${}_f\mathbb{C}^* = {}_f\mathbb{L}\, {}_f\mathbb{C}\, {}_f\mathbb{L},$$

system (3.98) acquires a form analogous to system (3.70):

$$\begin{cases} d_f\boldsymbol{\sigma}^* = {}_f\mathbb{C}^* d_f\boldsymbol{\varepsilon}^* \\ d_m\boldsymbol{\sigma}^* = {}_m\mathbb{C}^* d_m\boldsymbol{\varepsilon}^* \\ d\boldsymbol{\varepsilon}^* = {}_f c\, d_f\boldsymbol{\varepsilon}^* + {}_m c\, d_m\boldsymbol{\varepsilon}^* \\ d_f\boldsymbol{\sigma}^*_S = d_m\boldsymbol{\sigma}^*_S \\ d_f\boldsymbol{\varepsilon}^*_P = d_m\boldsymbol{\varepsilon}^*_P. \end{cases} . \tag{3.99}$$

The resolution of the previous system can accordingly be done following thoroughly the passages used for the derivation of the BSP tangent operator and employing decomposition (**??**):

$$\begin{aligned}
d_f\boldsymbol{\sigma}^*_P &= {}_f\mathbb{C}^*_{PP}\, d_f\boldsymbol{\varepsilon}^*_P + {}_f\mathbb{C}^*_{PS}\, d_f\boldsymbol{\varepsilon}^*_S \\
d_f\boldsymbol{\sigma}^*_S &= {}_f\mathbb{C}^*_{SP}\, d_f\boldsymbol{\varepsilon}_P + {}_f\mathbb{C}^*_{SS}\, d_f\boldsymbol{\varepsilon}^*_S \\
d_m\boldsymbol{\sigma}^*_P &= {}_m\mathbb{C}^*_{PP}\, d_m\boldsymbol{\varepsilon}^*_P + {}_m\mathbb{C}^*_{PS}\, d_m\boldsymbol{\varepsilon}^*_S \\
d_m\boldsymbol{\sigma}^*_S &= {}_m\mathbb{C}^*_{SP}\, d_m\boldsymbol{\varepsilon}^*_P + {}_m\mathbb{C}^*_{SS}\, d_m\boldsymbol{\varepsilon}^*_S \\
d\boldsymbol{\varepsilon}^*_P &= {}_fc\, d_f\boldsymbol{\varepsilon}^*_P + {}_mc\, d_m\boldsymbol{\varepsilon}^*_P \\
d\boldsymbol{\varepsilon}^*_S &= {}_fc\, d_f\boldsymbol{\varepsilon}^*_S + {}_mc\, d_m\boldsymbol{\varepsilon}^*_S \\
d\boldsymbol{\sigma}^*_P &= {}_fc\, d_f\boldsymbol{\sigma}^*_P + {}_mc\, d_m\boldsymbol{\sigma}^*_P \\
d\boldsymbol{\sigma}^*_S &= {}_fc\, d_f\boldsymbol{\sigma}^*_S + {}_mc\, d_m\boldsymbol{\sigma}^*_S \\
d_m\boldsymbol{\varepsilon}^*_P &= d_f\boldsymbol{\varepsilon}^*_P \\
d_m\boldsymbol{\sigma}^*_S &= d_f\boldsymbol{\sigma}^*_S.
\end{aligned}$$

The resulting tangent operator of the composite, adopting decomposition (**??**), results:

$$\mathbb{C}^* = \begin{bmatrix} \dfrac{\partial\boldsymbol{\sigma}^*_P}{\partial\boldsymbol{\varepsilon}^*_P} & \dfrac{\partial\boldsymbol{\sigma}^*_P}{\partial\boldsymbol{\varepsilon}^*_S} \\ \dfrac{\partial\boldsymbol{\sigma}^*_S}{\partial\boldsymbol{\varepsilon}^*_P} & \dfrac{\partial\boldsymbol{\sigma}^*_S}{\partial\boldsymbol{\varepsilon}^*_S} \end{bmatrix} = \begin{bmatrix} \mathbb{C}^*_{PP} & \mathbb{C}^*_{PS} \\ \mathbb{C}^*_{SP} & \mathbb{C}^*_{SS} \end{bmatrix},$$

where:

$$\mathbb{C}^*_{PP} = \begin{bmatrix} ({}_fc\,{}_f\mathbb{C}^*_{PP} + {}_mc\,{}_m\mathbb{C}^*_{PP}) + \\ + {}_mc\,{}_fc\,\left({}_f\mathbb{C}^*_{PS} - {}_m\mathbb{C}^*_{PS}\right)\,\mathbb{A}^*\,({}_m\mathbb{C}^*_{SP} - {}_f\mathbb{C}^*_{SP}) \end{bmatrix} \tag{3.100a}$$

$$\mathbb{C}^*_{PS} = ({}_fc\,{}_f\mathbb{C}^*_{PS}\,\mathbb{A}^*\,{}_m\mathbb{C}^*_{SS} + {}_mc\,{}_m\mathbb{C}^*_{PS}\,\mathbb{A}^*\,{}_f\mathbb{C}^*_{SS}) \tag{3.100b}$$

$$\mathbb{C}^*_{SP} = ({}_mc\,{}_f\mathbb{C}^*_{SS}\,\mathbb{A}^*\,{}_m\mathbb{C}^*_{SP} + {}_fc\,{}_m\mathbb{C}^*_{SS}\,\mathbb{A}^*\,{}_f\mathbb{C}^*_{SP}) \tag{3.100c}$$

$$\mathbb{C}^*_{SS} = \frac{1}{2}\left[({}_m\mathbb{C}^*_{SS}\,\mathbb{A}^*\,{}_f\mathbb{C}^*_{SS}) + ({}_f\mathbb{C}^*_{SS}\,\mathbb{A}^*\,{}_m\mathbb{C}^*_{SS})\right]. \tag{3.100d}$$

The tensor $\mathbb{A}^*$ has an expression analogous to (3.75):

$$\mathbb{A}^* = ({}_fc\,{}_m\mathbb{C}^*_{SS} + {}_m\,c\,{}_f\mathbb{C}^*_{SS})^{-1}.$$

It is again immediately recognized that the composite tangent operator results symmetric when the same property is possessed by the tangent operators of component materials since this last hypothesis implies:

$$ {}_c\mathbb{C}^*_{SS} = {}_c\mathbb{C}^{*T}_{SS}, \quad {}_c\mathbb{C}^*_{SP} = {}_c\mathbb{C}^{*T}_{PS}. $$

Chapter 4

Numerical validations

The purpose of this section is to show and discuss the results of several numerical analysis devised to test the response of BSP and ESP models from both the point of view of the reliability of the predicted constitutive response and the computational one. The proposed models depend crucially from the selected constitutive laws of component materials, then it is compulsory to precise the specific constitutive laws adopted for component phases in each test case considered. When the general response of the model is investigated, simple hardening and softening J2 plasticity laws are used to model component phases. (In this case, as it will be shown, ESP and BSP models inherit the quadratic convergence of component models). On the other hand when the objective is that of reproducing as accurately as possible the mechanical response of real composite materials, a not-iso-resistent damage constitutive law is selected for both fiber and matrix and a calibration procedure, detailed in the following, is employed. Accordingly the tests reported can be divided in two groups: group a) tests for general validation of the model performed on the unidirectional lamina and group b) tests to assess the predictive capability against experimental data. Among the validations of the first group there are numerical simulations devised to investigate the fulfilment of the closure equation, the general behaviour of the model, the response given for stiffness and for strength and the computational performance. The data for the validations of the latter group are instead taken from the Worlwide Failure Exercise [109], [108] which is considered to be a reliable and complete set of benchmark test cases.

Since the response is verified 'locally' the validations are performed on an isoparametric hexahedral element with, whenever required, a laminated struc-

ture. On each ply of the laminate BSP or ESP constitutive laws are adopted according to the model examinated.

4.1 Group a - General validations on the unidirectional lamina

The validations presented in this subsection have the purpose of drawing an overview on the general response determined by the BSP and the ESP models in the linear and non-linear ranges. For this reason, in this preliminary validations the constitutive laws of component materials are selected with no aim of performing a proper modelization of a real composite lamina of any material, but with the purpose of checking the fulfilment of the closure equation in the elastic and in the non-linear range. Since the sections present mixed validations performed over the BSP and the ESP models, it is important to state precisely in advance that, whenever for sake of simplicity the results presented are illustrated only for the BSP model, an analogous result is obtained also with the ESP model.

4.1.1 Preliminary validations

Superimposed strain in parallel direction with J2 perfect plasticity for both matrix and fiber.

In order to test the behavior in parallel direction of the proposed BSP model, a load-unload controlled longitudinal deformation in fibers direction is superimposed to an hexahedral element with such constitutive law. Simple J2 perfect plasticity [104] is assigned to both component materials. This analysis is instructive because provides a survey on the general behaviour of the BSP model in parallel direction and the simplicity of perfect plasticity makes easier the understanding of the main characteristics exhibited by the BSP model.

The constraints are devised in order to allow free transverse contraction. The values selected for the parameters that define the analysis are reported in table 4.1.

The diagram of fig.4.1shows the response obtained for parallel strain ε_P vs. parallel stress σ_P. From the simulation emerges that the closure equation is correctly fulfilled and parallel strain are equal in both fiber and matrix as well as in

	Material 'M'	Material 'F'
Constitutive law	J2 perfect plasticity	J2 perfect plasticity
Young modulus [MPa]	40000	80000
Elastic limit [MPa]	1000	3480
Poisson ratio	0.0	0.0
Volume fraction	0.58	0.42

Table 4.1: Mechanical properties of constituents selected to test BSP model under controlled parallel deformation.

the whole composite, at each load step. Four ranges can be immediately located. These ranges are delimited by the discontinuity points due to the attainment of the elastic-plastic thresholds in matrix and in fiber and by the load to unload limit. In the first elastic branch from the analysis emerges that perfect R.O.M. stiffness is recovered for the composite i.e.:

$$E = E_f + E_m.$$

The second interval is characterized by the yielding of matrix, while the fiber remains in the elastic range. The third interval, instead, is characterized by both component material being in the plastic range. At complete unload plasticity induces a residual stress state which is auto-equilibrated since the resultant stress in the composite is zero, as fig.4.1shows.

As it will be detailed in a following section, with the selected constitutive laws, quadratic convergence is achieved throughout the whole load-unload process.

Superimposed strain in transverse direction with d^+/d^- damage for matrix and J2 hardening plasticity for fiber.

In order to examine the response of the BSP model in the serial direction, an hexahedral isoparametric element is subjected to controlled transversal deformation. The test is performed by applying a load-unload transversal controlled deformation up to 5% strain. The constitutive law selected for the material 'M' is an isotropic damage model with two different damage variables for tension and

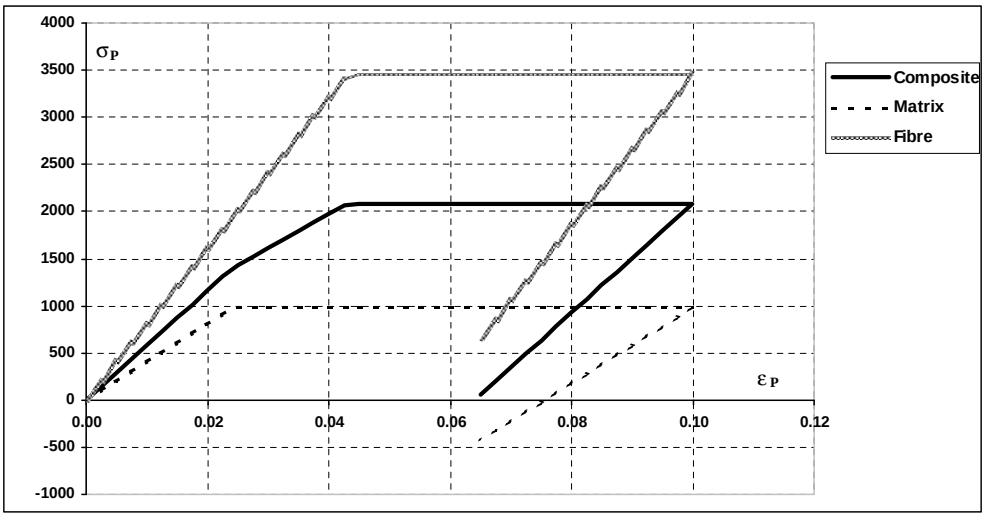

Figure 4.1: Parallel strain ε_P vs. parallel stress σ_P for strain controlled deformation in parallel direction.

compression [24], while for the material 'F', a J2 plasticity model with exponential hardening is chosen. Material 'F' volumetric fraction is 50%. The mechanical properties of these materials are resumed in table 4.2.

Material 'F' is selected as to possess a stiffness and an elastic limit lower than the corresponding values for material 'M'. Note that Poisson ratios at this stage of the validation process have been set equal to zero on purpose, only for a reason of clarity, in order to avoid "coupling" with longitudinal behaviour. In any case the model performs well with any value of the Poisson's ratios, as it will be showed afterwards.

In Figure 4.2, the transversal normal stresses σ_S observed in all materials during the validation process are plotted against their respective transversal strains ε_S. The simulation shows that at each step of the analysis the closure equation is exactly fulfilled throughout the whole load history; this is denoted by the fact that at each step the serial stresses are identical for all materials in all load steps.

In the first elastic branch (O-A), the emerging composite transversal stiffness,

	Material 'M'	Material 'F'
Constitutive law	D+/D- damage with softening	J2 hardening plasticity
Young modulus [MPa]	3000	2000
Elastic limit [MPa]	60	40
Poisson ratio	0.0	0.0
Volume fraction	0.5	0.5

Table 4.2: Mechanical properties of constituents selected to test BSP model under serial controlled deformation.

given by the BSP model, is in accordance with the inverse R.O.M.:

$$\frac{1}{E} = \frac{1}{E_f} + \frac{1}{E_m}$$

When material 'F' reaches the yielding threshold –point (A) in the composite– , this material experiments plastic deformations but keeps on incrementing its stress, due to its hardening law. This fact also determines a reduction in the composite stiffness along the branch (A-B), while material 'M' remains elastic up to point (B) when its damage begins.

Along branch (B-C), material 'M' experiments damage and determines a decreasing shape in the stress-strain curve of all materials; in material 'F' an elastic unload is produced.

From point (C) on, the sign of the applied deformation is reversed (unloading), consequently all materials undergo elastic unload. Note that the material 'M' unloads with a reduced stiffness, due to internal damage. Note also that the material 'F' unloads with the virgin elastic stiffness and at complete unload retains plastic residual strains.

4.1.2 Stiffness validations

Off-axis stiffness

In this validation an hexahedral finite element composed, through the BSP model, of two isotropic elastic materials is subjected to uniaxial stress applied in several directions, rotated by an angle θ with respect to fiber direction.

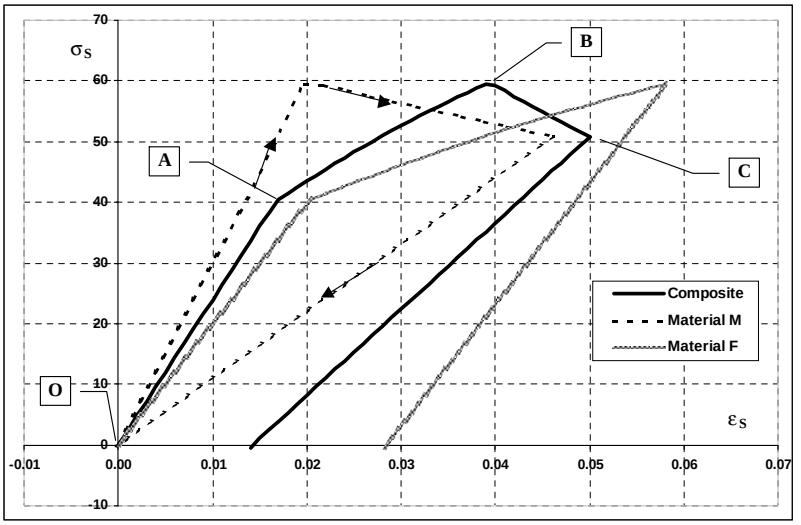

Figure 4.2: Serial strain ε_S vs. serial stress σ_S for strain controlled deformation in serial direction.

The mechanical properties of these materials are shown in table 4.3.

As shown in figure 4.3, the curve obtained by plotting the resulting stiffness vs. the angle θ trivially coincides with the curve given by coordinate transformation of material compliance coefficients formulas [97]:

$$\begin{aligned}\frac{1}{E_\theta} &= D_{11}\cos^4\theta - 2D_{16}\cos^3\theta\sin\theta + (2D_{12}+D_{66})\cos^2\theta\sin^2\theta \\ &\quad -2D_{16}\cos\theta\sin^3\theta + D_{22}\sin^4\theta,\end{aligned}$$

	fiber	**Matrix**
Material	glass	epoxy
Young modulus [MPa]	105950	5000
Poisson ratio	0.22	0.38
Volume fraction	0.6	0.4

Table 4.3: Mechanical properties of constituents adopted to validate off-axis stiffness.

where D_{ij} indicates the coefficients of the compliance matrix.

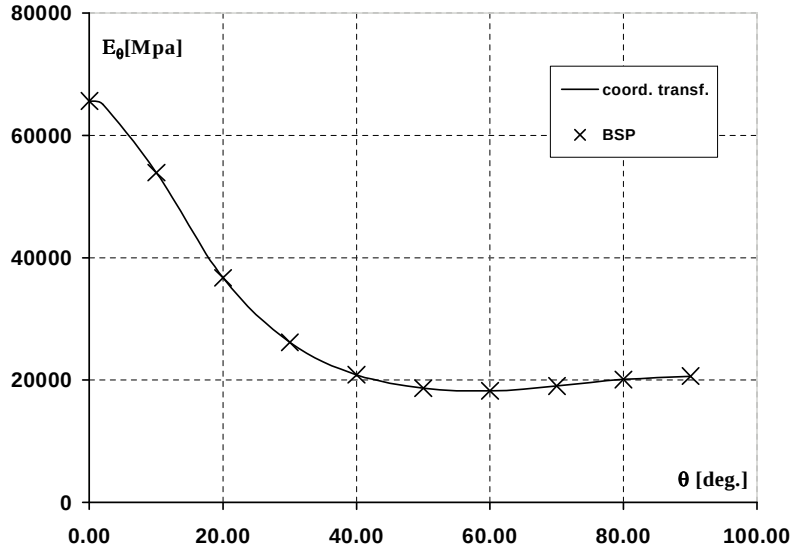

Figure 4.3: Off-axis stiffness diagram resulting from the formulas of coordinate transformation of compliance coefficients and from the BSP model.

Longitudinal stiffness vs. fiber volume fraction

Materials with the same elastic properties used in the previous validation (see tab.4.3) are now employed to study the influence of fiber volume fraction to the longitudinal stiffness as predicted by BSP model.

In Figure 4.4, the longitudinal stiffness E_1, obtained with the BSP model, is plotted against fiber volume fraction V_f. As expected, the model reproduces exactly a ROM prediction in parallel direction, which implies a linear variation between 5000 and 105950 MPa i.e.matrix and fiber Young modulus, respectively.

Transversal stiffness vs. fiber volume fraction

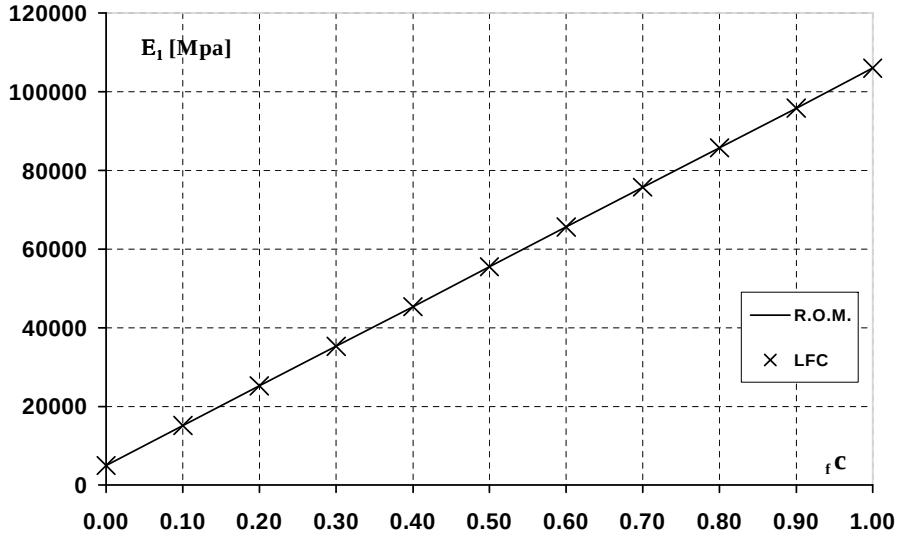

Figure 4.4: Longitudinal stiffness E_1 [MPa] vs. fibre volume fraction V_f. Comparison between ROM formula and the result given by the proposed BSP model.

In this validation the predictions of BSP and ESP models within the transversal stiffness of a glass-epoxy laminate with E_F/E_M=21.19, $\nu_F = 0.22$, $\nu_M = 0.38$ (same component materials specified in Table 4.3) are compared against experimental data and against the approximation given by broadly-used semi-empirical formulas. The validation consists in subjecting an hexahedral composite element to pure transversal loading, at different fiber volume fractions.

In Figure 4.5, the adimensional curves E_2/E_M vs. V_F resulting from the simulations with BSP and ESB are reported together with experimental values taken from Barbero [12]. In the same figure, for comparison the curves resulting from perfect inverse ROM and from Halpin-Tsai equation [44] are also reported:

$$\frac{E_2}{E_M} = \frac{1+\xi\eta V_F}{1-\eta V_F} \text{ with } \eta = \frac{\left(\frac{E_F}{E_M}\right)-1}{\left(\frac{E_F}{E_M}\right)+\xi} \tag{4.1}$$

In the use of formula (4.1) the coefficient ξ is set equal to 2, as usual for circular fibers in a square array, see Jones [59].

The following considerations are worth to be pointed out. The transversal

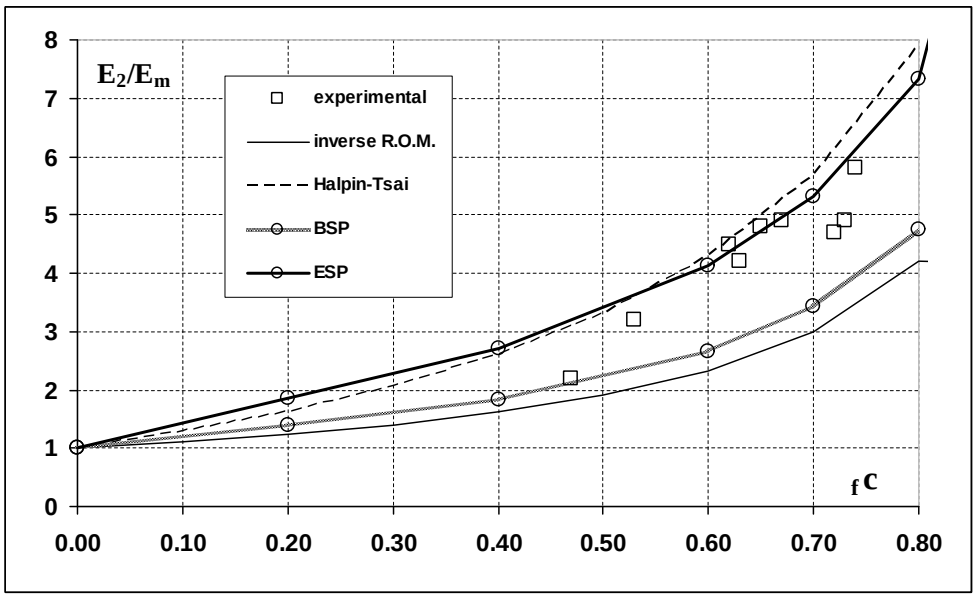

Figure 4.5: Relative transversal stiffness E_2/E_M versus fibre volume fraction V_f. Comparison between the result given by the proposed models, experimental data, inverse ROM and Halpin-Tsai equation.

stiffness obtained by simple BSP model results to be slightly greater than the one given by inverse ROM, due to the combination of the Poisson effects and the fiber longitudinal constraint. For isotropic elastic constituents, in fact, the transversal stiffness of the BSP model results to be provided by the following formulas, obtained in chapter 3, and hereafter recalled:

$$E_2 = \frac{1}{\left(\frac{{}_fc}{E_f} + \frac{{}_mc}{E_m}\right)} \left(\frac{1}{1-\rho_\nu}\right),$$

with:

$$\rho_\nu = \nu_m^2 \nu_f^2 \, {}_mc \, {}_fc \frac{\left(\frac{E_m}{\nu_m} - \frac{E_f}{\nu_f}\right)^2}{E'_S E_P},$$

where the simbology used is the following:

E_2	Composite transversal stiffness considering fiber longitudinal constrain
$E_f; E_m$	Fiber and Matrix Young modulus
$\nu_f; \nu_m$	Fiber and Matrix Poisson ratios
${}_fc;\ {}_mc$	Fiber and Matrix volume fractions
E'_S	Serial (transversal) stiffness considering inverse ROM
E_P	Parallel (longitudinal) stiffness considering ROM

As expected, when Poisson ratios are set equal to zero a perfect inverse ROM curve is recovered. The graph of figure 4.5shows that simple BSP model, as well as inverse ROM, appreciably underestimates the experimental values (for the latter this is an already well known evidence). On the other hand, the Enhanced Serial Parallel model, with the evaluation of coefficients ${}_f\alpha$ and ${}_m\alpha$ detailed in chapter 3, gives an approximation to experimental data as good as the one given by Halpin-Tsai equation, which is notoriously one of the most used formulas in presence of limited experimental information. It is important to remark that in ESP model no experimental coefficient was introduced to fit experimental data, since this model is only based on micro-mechanical considerations.

Only for scarcely used fiber volume fractions lower than 40% the stiffness is slightly overestimated by ESP model. This can be attributed to the fact that for low fiber volume fractions, the.parallel contribution of matrix with fiber in transverse direction is far less significant than what assumed by the simplified model of chapter 3 used to evaluate the coefficients for the enhanced model.

In-plane shear stiffness vs. fiber volume fraction

In this validation the predictions of BSP and ESP models for in-plane shear stiffness of a glass-epoxy laminate with $G_F/G_M = 20.0$ are compared against experimental data and against the approximation given by Halpin-Tsai equation.

Table 4.4specifies the mechanical properties adopted for component materials:

The validation consists in subjecting an hexahedral composite element to in-plane shear loading, at different fiber volume fractions.

In Figure 4.6, the adimensional curves G_{12}/G_M versus fiber volume fraction V_f resulting from BSP and ESP simulations are reported together with

	Fiber	Matrix
Material	E-glass	epoxy
Young modulus [MPa]	72300	4000
Poisson ratio	0.22	0.35
Shear modulus [MPa]	29631	1481

Table 4.4: Mechanical properties of constituents adopted to validate in-plane shear stiffness.

experimental values taken from [12]. In the same figure are also reported the curves resulting from perfect inverse ROM and the one obtained from Halpin-Tsai equation. In this case the value adopted for coefficient ξ is 1, as suggeted by Halpin-Tsai [44] and Adams and Doner [6].

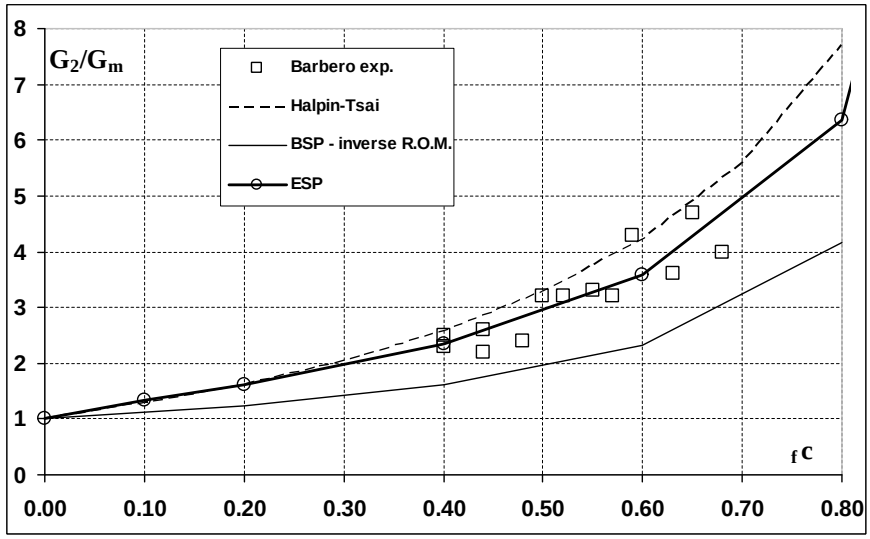

Figure 4.6: Relative shear stiffness G_{12}/G_M versus fibre volume fraction V_f. Comparison between experimental data, inverse ROM, Halpin-Tsai equation and results given by BSP and ESP models.

Since within infinitesimal kinematics for shear there is no coupling with other solicitations (i.e. fiber longitudinal constraint does not affect shearing), the

transversal stiffness exhibited by the BSP model results to be coincident with the one given by inverse ROM. The graph shows that, in any case, this is a simple but not accurate prediction of the in-plane shear modulus.

The ESP model offers instead a better approximation to experimental data, which turns out to be as good as the one given by Halpin-Tsai equation.

The values adopted for the parameter ${}_f\alpha$ and ${}_m\alpha$ for the enhancement of shear behaviour are obtained with formulas 3.52-,3.55 of chapter 3.

4.1.3 Strength validations against theoretical formulas

This set of validation is devised in order to determine the general trend of the strength predictions provided by the BSP and ESP models as a function of the volumetric fraction of fiber. Components material properties are taken from literature. Matrix and fibers are both modelled with a J2 plasticity model, with hardening for the matrix and softening for the fiber. Such a rough calibration of component materials is performed because the objective of this subsection is only to get the general sensibility of the model to volume fraction and to test the performance in the non-linear range. We redirect the reader to the more extended validations made in the following part of this document for an effective calibration with experimental data.

Longitudinal tensile strength vs. fiber volume fraction

This validation analyses the longitudinal tensile strength resulting from the enriched serial-parallel (ESP) model as a function of volume fraction.

Both cases of glass-epoxy (GFRP) and carbon-epoxy (CFRP) composites are examined since, in the case of GFRP, epoxy matrix has usually a failure limit lower than glass fibers while, conversely, in CFRP laminates matrix has a failure limit strain higher than fiber. These two cases should then cover a wide range of cases.

The parameters adopted for the laminates are reported in tables 4.5 and 4.6.

		E_1 [MPa]	ν	G[MPa]	X_T [MPa]	ε_{1T}
Fiber	E-Glass	72345.0	0.220	29650.6	3450.0	0.048
Matrix	Epoxy 9310/9360@23	3120.0	0.380	1130.4	75.80	0.024

Table 4.5: Mechanical properties of GFRP constituents.

		E_1 [MPa]	ν	G[MPa]	X_T [MPa]	ε_{1
Fiber	Carbon Fiber CBX 400	250000.0	0.200	104166.7	3950.0	0.0
Matrix	Epoxy Vantico (ItalDesign)	3200.0	0.350	1185.2	77.0	0.0

Table 4.6: Mechanical properties of CFRP constituents.

Parallel loading is applied up to failure to both carbon and glass unidirectional laminas for variable fiber volume fractions.

The resulting ultimate strength in function of fiber volume fraction is reported in figure 4.7for GRP laminas, and in figure 4.8for CFRP laminas.

As the graphs of figures 4.7 and 4.8 show, in both cases the function obtained results to be very close to a linear combination between fiber and matrix ultimate strengths; for a theoretical comparison see [12] (pages 86, 17 and 23). As one may expect, within the mechanical parameters adopted, even at very low volume fractions the effect of redistribution is negligible.

Transverse strength vs. fiber volume fraction

This validation analyses the transversal tensile strength emerging from ESP model as a function of volume fraction. Matrix and fiber materials adopted for this test have the same mechanical properties used for the carbon-epoxy laminas of the previous validation (see table 4.6), i.e. J2 hardening for the matrix, J2 softening for the fiber.

The composite is subjected to a transversal deformation superior to the elastic strain limit of the matrix so that yielding occurs.

The behaviour of the composite model under transversal loading is similar to that of a series of springs (perfect serial behaviour) but simultaneously constrained in longitudinal (parallel to fibers) direction. This internal constraint makes the transverse response stiffer than perfect serial behaviour.

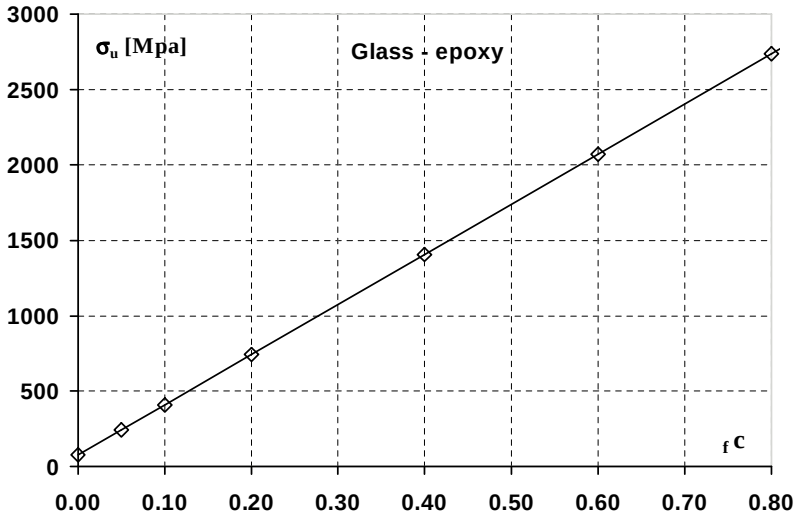

Figure 4.7: Ultimate stress [MPa] as a function of fibre volume fraction for a glass-epoxy unidirectional lamina subjected to parallel loading.

Since fibers are far stiffer than matrix, the fibers experiment a very small strain and remain in the elastic range, while the majority of the applied strain is borne by the matrix (softer material).

When matrix yields internal and global convergences are quadratic. This confirms the quality of the proposed model to retain quadratic convergence when this quality is also possessed by its component constitutive models. A detailed study of the convergence of ESP model is studied in a following section.

In figure 4.9 the diagram of ultimate transversal strength of the composite vs. the volume fraction $_fc$ is reported. Since the J2 plasticity model is iso-resistant, the absolute values obtained for tensile and compressive strength are identical.

The curve takes the value of tensile matrix strength of 77 MPa at 0% fiber volume fraction, as expected, then quickly moves to the value of 88.9 MPa and remains constant up to 99% fiber volume fraction. This variation in the strength may be attributed to the longitudinal constraining effect carried out by fibers that affects matrix J2 yielding flux and therefore induces an increased value in the ultimate strength.

This effect is emphasized in Fig. 4.10where transversal matrix stress vs.

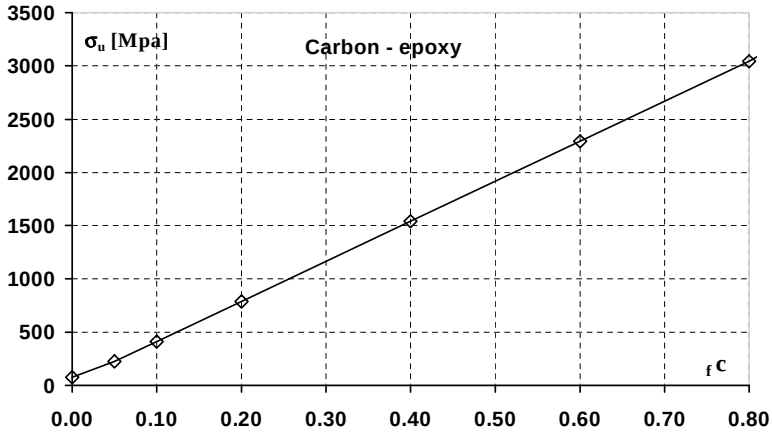

Figure 4.8: Ultimate stress [MPa] as a function of fibre volume fraction for a carbon-epoxy unidirectional lamina subjected to parallel loading.

transversal matrix strain is reported. The curve presents a maximum before tending toward the asymptotic value corresponding to the yielding stress of pure matrix.

Shear strength vs. fiber volume fraction

This validation analyses the shear strength emerging from the ESP model as a function of volume fraction. Also in this case, matrix and fiber materials adopted for this test have the same mechanical properties used for the carbon-epoxy laminate of table 4.6, i.e. J2 plasticity with hardening for the matrix, and J2 plasticity with softening for the fiber.

The composite is subjected to an in-plane shear deformation superior to the elastic shear strain limit allowed for matrix so that yielding occurs. Since the composite behaviour may be considered perfectly serial for shear loading, and fibers are far stiffer than matrix, the fibers experiment a very small shear strain and remain in the elastic range while the majority of the applied shear strain is borne by the matrix.

Also in this case, internal and global convergence is quadratic.

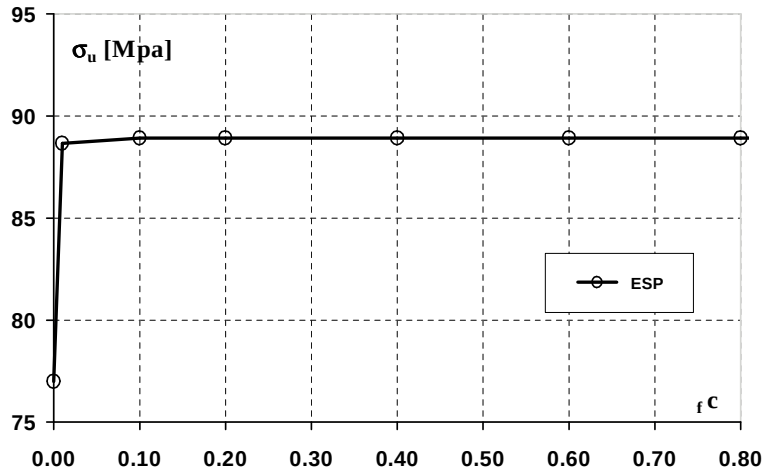

Figure 4.9: Ultimate transversal strength of the composite in function of fibre volume fraction for a carbon-epoxy unidirectional lamina subjected to transversal loading.

The composite ultimate shear strength results to be independent of fiber volume fraction, and equal to $\frac{\sigma_{mu}}{\sqrt{3}}$ due to the J2 model adopted.

Contrarily to the previous validation, no increment for the value of ultimate shear strength is detected because there is no constraining effect. The peak effect in matrix shear stress-strain diagram reported in the previous validation for transversal strength is accordingly not detected in this case.

Off-axis strength

In this validation an hexahedral composite element, composed of the same materials used in previous strength validations for carbon-epoxy laminates and with ${}_fc = 0.60$, is subjected to uniaxial stress (in a force-controlled loading) applied in a direction rotated by an angle θ with respect to fiber direction. In figure 4.11 the ultimate strength provided by the proposed model as a function of the angle θ is reported.

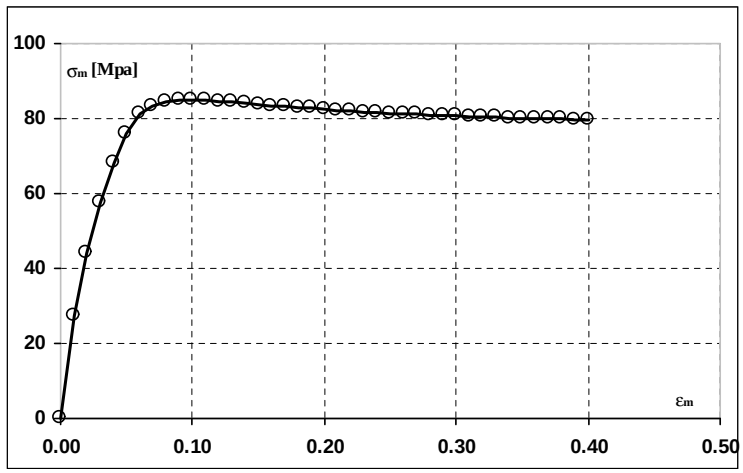

Figure 4.10: Transversal matrix stress [MPa] vs. transversal matrix strain for a carbon-epoxy unidirectional lamina subjected to transversal loading.

The curve obtained by the ESP model matches almost exactly the one corresponding to Tsai-Hill criterion, given by:

$$X_{\theta TH} = \frac{1}{\sqrt{\frac{\cos^4\theta}{X_1^2} + \frac{\sin^4\theta}{X_2^2} - \frac{\sin^2\theta\cos^2\theta}{X_1^2} + \frac{\sin^2\theta\cos^2\theta}{X_{12}^2}}}$$

Only for very small angles, as shown in figure 4.12, the curve presents a non-smooth shape which makes it more similar to the maximum stress criterion. This is due to the fact that ESP model distinguishes between fiber failure and matrix failure automatically.

4.1.4 Local and global convergence

The algorithm detailed in chapter 3 achieves the 'serial' stress equilibrium of components by an iterative process based on a Newton-Raphson method. In this section, the convergence rate is tested for both local and global settings.

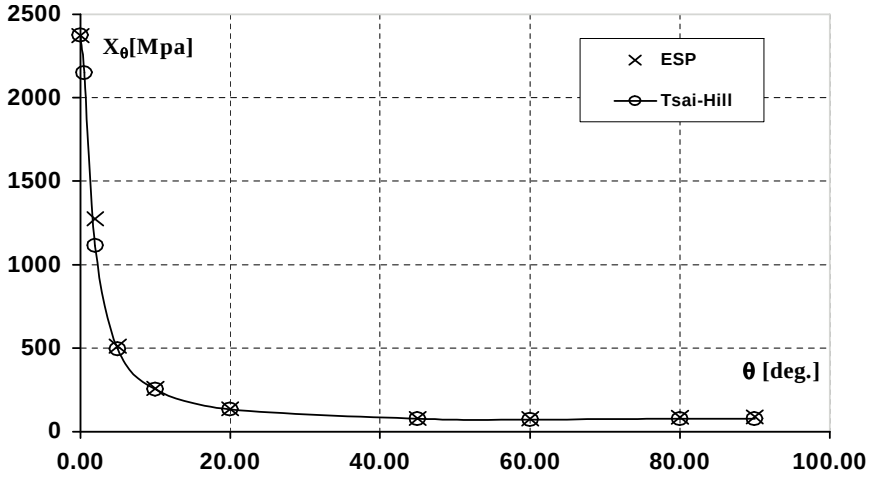

Figure 4.11: Off-axis strength [MPa] curve for a carbon-epoxy unidirectional lamina subjected to force-controlled loading applied at different angles.

The composite material is subjected to a transversal load-unload process. The numerical simulation employs large load steps in order to stress the convergence rate of the proposed model.

For both component materials elasto-plastic constitutive laws are selected. For material 'M' J2 softening is adopted while for material 'F' J2 hardening.

Table 4.7 reports the properties of the selected constitutive models.

Figure 4.13 shows serial stress-strain plots for the composite and component materials during the transversal load-unload process.

The plot reported results to be similar to the one showed in fig.4.2discussed in the preliminary validations of group a, where transversal loading was applied to a composite whose material 'M' was simulated with a damage model. In the present case, material 'M' is elasto-plastic, and Poisson ratios are different from zero.

Due to the non-zero values adopted for the Poisson ratios of component materials, the loading process also produces stresses and strains in parallel direction that are shown in Figure 4.14. Note that composite parallel stress is zero, components parallel stresses are opposite because of the equal volume fractions, and

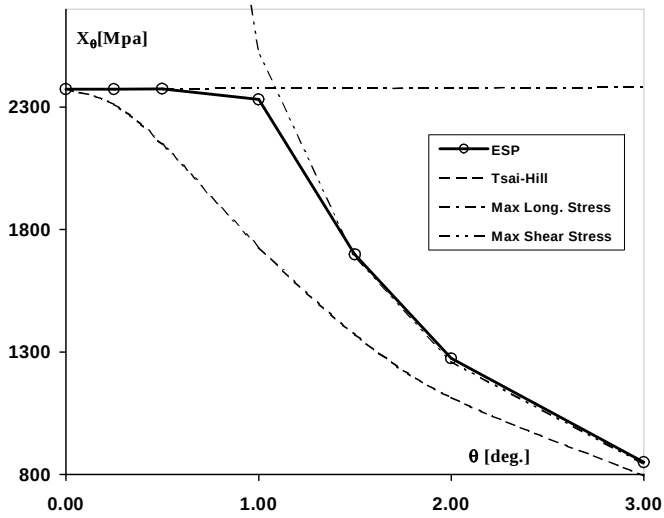

Figure 4.12: Detail of the ultimate composite strength [MPa] curve at very low off-axis angles for a carbon-epoxy unidirectional lamina. Comparison with broadly-used failure formulas.

that parallel strains are the same for all materials throughout the whole process, as expected, because of the parallel compatibility equation.

In the initial elastic region parallel stresses in component materials are originated, by the different Poisson ratios. The residual parallel stresses at complete unload are due to yielding.

The table of figure 4.15 reports the relative residual error and the required iterations for both local and global problems and for each step of the load-unload process.

Figure 4.16shows the global convergence diagram for load steps B, C, D and E of the load-unload process.

Local convergence is illustrated in Figure 4.17 for iteration 1 of step B ($\varepsilon_P = 0.0235$) and for iterations 1, 2 and 3 of step D ($\varepsilon_P = 0.036$).

It has to be remarked that, despite the interaction between component materials during this load process is quite complex, quadratic convergence is achieved

	Material 'M'	**Material 'F'**
Constitutive law	J2 hardening plasticity	J2 softening plasticity
Volume fraction	50 %	50 %
Young modulus [MPa]	3000	2000
Poisson ratio	0.35	0.2
Initial Yielding stress [MPa]	60	40
Final Yielding stress [MPa]	30	70
Exponential Hardening	30	30

Table 4.7: Materials properties adopted to analyse ESP model convergence.

for both local and global problems. Both local and global convergence rates depend on whether the constitutive models of component materials supply their algorithmic tangent tensors or not.

4.2 Group b - Validation of strength predictive capability against experimental data

The validation of the results provided by the ESP model against experimental data has a major importance in the assessment of the proposed model as a valid tool for FEM analysis of LFC structures. The test cases selected have been accurately searched in the related literature and finally the choice has gone to the benchmark tests proposed in [52], [108]. In particular the validation concerns the strength predictions for the E-glass/epoxy LY556 unidirectional laminae and for the E-glass/epoxy LY556 laminates among the set of 14 test cases presented in [109].

4.2.1 Calibration procedure of the constitutive parameters for the component materials

Preliminary considerations

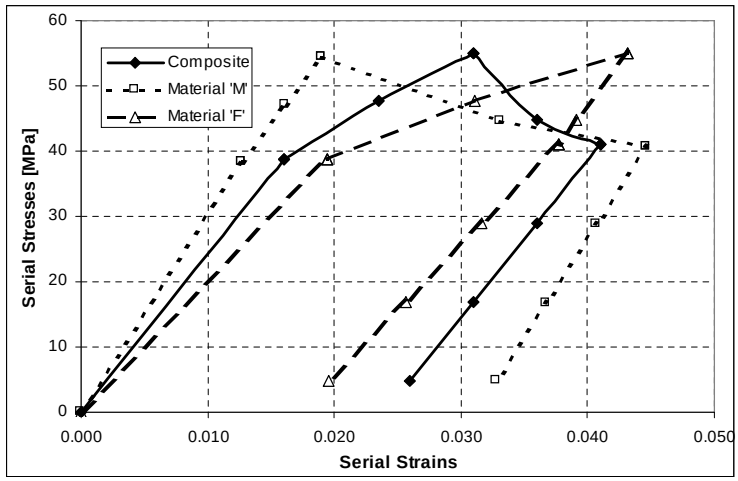

Figure 4.13: Serial stress-strain plots for the composite and component materials under transversal load-unload testing.

Before proceeding to the calibration of component materials properties against experimental data, some preliminary considerations are worth to be pointed out.

Not all of the mechanical properties of the lamina can be predicted by merely using the properties of the isolated component materials. This evidence is indeed remarked also by other authors such as Puck [84] and Aboudi [3].

Actually, a calibration procedure is required, which also depends on the constitutive models selected for component materials. The presence of an epoxy or metal matrix, for example, requires different constitutive laws and, consequently, different calibration procedures.

For the particular case of a fiber reinforced plastics, an important characteristic that the component models have to possess is not to be iso-resistant. For the epoxy matrix this is well known evidence due to its brittle nature. In the case of the fibers instead, the need for different tensile and compressive strength thresholds is to account for the phenomenon of micro-buckling, in lack of a more appropriate model.

In this perspective, for the present calibration procedure, the constitutive model adopted to simulate the behavior of the component materials is the isotropic damage model with two different damage variables for tension and compression d+/d- detailed in [24].

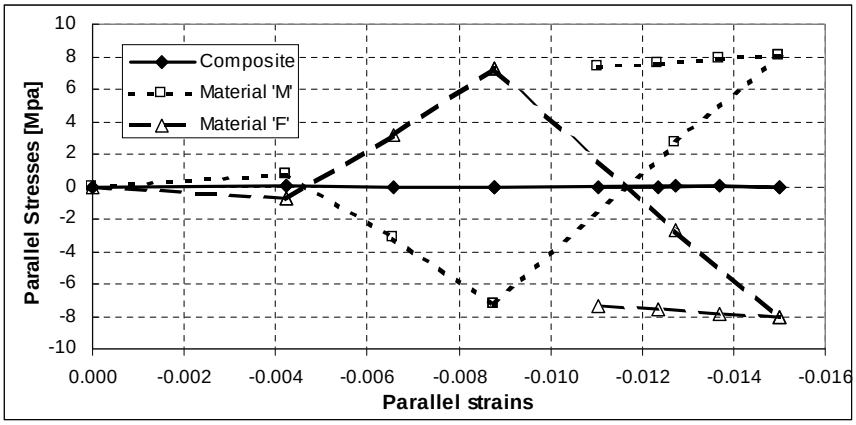

Figure 4.14: Parallel stress-strain plots for the composite and components under transversal load-unload testing.

Stiffness Properties	Matrix	Fiber
Young modulus [MPa]	3350	80000
Poisson ratio	0.35	0.20

Table 4.8: Stiffness parameters adopted for component materials of LY556 glass-epoxy laminae.

Stiffness parameters

The stiffness parameters for matrix and fiber are set equal to the values provided for isolated materials. The values selected are reported in table 4.8:

Strength parameters

Matrix compressive and tensile strengths are set equal to the corresponding transverse strengths exhibited by the unidirectional lamina(see table 4.9). The values adopted are given by Hütter et al. [58].

The initial elastic domain determined by the d^+/d^- and the parameters of table 4.9 is reported in figure 4.18.

Matrix strength properties	
Tensile strength X_{mT}[MPa]	40
Compressive strength X_{mC}[MPa]	135

Table 4.9: Strength properties for matrix of LY556 glass-epoxy laminae.

To calibrate tensile and compressive strength of fibers, it is not convenient to take the properties possessed by the components isolated, we account for their effective performance inside the lamina. Accordingly the quota of lamina strength attributed to fibers is:

$$X_{fT} = \frac{X_T - \sigma_{mT} V_m}{{}_f c},$$

$$X_{fC} = \frac{X_C - \sigma_{mC} V_m}{{}_f c},$$

where σ_{mT} and σ_{mC} are, respectively, the transverse stress in the matrix in correspondence with lamina ultimate longitudinal tensile and compressive strength.

The values σ_{mT} and σ_{mC} are deduced by the following considerations. Since in a GFRP the ultimate longitudinal tensile strain of fiber is greater than the one of matrix, it is assumed that in correspondence to fiber ultimate tensile strength, matrix has already failed and thus σ_{mT} at lamina failure is neglected. This assumption leads to:

$$X_{fT} = \frac{X_T}{{}_f c} = \frac{1140}{0.62} = 1839\, MPa. \tag{4.2}$$

For compressive strength, instead, in lack of a more appropriate model accounting for microbuckling, the simplifying assumptions that matrix is still in the elastic rangel when lamina fails is made, so that we can infer:

$$\sigma_{mC} = \frac{E_m}{E_f} X_{fC}. \tag{4.3}$$

Accordingly, substituting (4.3) in (4.2) the following value for X_{fC} is deduced:

$$X_{fC} = \frac{X_C}{{}_f c + {}_m c \dfrac{E_m}{E_f}} = \frac{570}{0.62 + 0.38 \dfrac{3.35}{80}} = 896\, MPa.$$

Fiber strength properties	
Tensile strength X_{fT}[MPa]	1839
Compressive strength X_{fC}[MPa]	896

Table 4.10: Strength properties for fibre of LY556 glass-epoxy laminas.

Mechanical Properties	**Fiber**	**Matrix**
Material	E-glass	epoxy
Constitutive law	Damage d+/d-	Damage d+/d-
Young modulus [MPa]	80000	3350
Poisson ratio	0.20	0.35
Tensile strength [MPa]	1839	40
Compressive strength [MPa]	896	135
Volume fraction	0.62	0.38

Table 4.11: Calibrated properties for component materials of LY556 glass-epoxy laminas.

With this process, the effect of fiber local buckling is taken into account by simply reducing the fiber compressive strength at compression, and not by real modelling fiber local instability. Therefore, this approach does not account for interaction between shear strain and compressive strength in the lamina.In table (4.10) are reported the strength parameters adopted for fibers.

The complete set of material properties adopted for LY556 unidirectional lamina is summarised in table 4.11:

Calibration of fracture energy by fitting the shear stress-strain curve

The last parameters left for the complete calibration of the constitutive models adopted for component materials are the fracture energies of the d^+/d^- [24] continuum damage models adopted for fiber and matrix. For the fiber low fracture energies are selected in orden to simulate a very brittle failure mode.The shear stress-strain curve, which was among the input data provided to the participants, is used instead to calibrate the fracture energy of matrix. The initial

shear modulus and the elastic threshold limit strength are in good agreement with experimental data and obviously do not depend from the fracture energies. The calibration is performed by adjusting the tensile and compressive fracture energies in order to fit the post-critical part of the experimental shear stress-strain curve with the numerical one. The result of this calibration is reported in fig. 4.19.

In point of fact, due to the elastic domain associated with the damage model adopted for the matrix, shown in figure 4.18, the elastic shear limit is equal to the tensile strength which is of 40 MPa. The additional amount of strength was obtained by setting the tensile fracture energy to a high value. This allows a 33% increase in shear strength in the non-linear range but gives to the matrix a ductility which in reality it does not possess. Even with high fracture energies the simulated post damage shear behaviour presents notable difference being 30% below the experimental value.(Fig. 4.19). This occurrence, in the opinion of the author, is ascribable, rather than to a not effective selection of the employed damage model, to an intrinsic limit of the small strain kinematics. The phenomenon, detectable only in a finite deformation setting, which is not properly reproduced by the present model, is the extensional excursion of the fiber in correspondence of in-plane shear deformation.

Resulting longitudinal tensile and compressive behaviour of the unidirectional lamina

When longitudinal tensile or compressive strain is applied on the composite, all materials present in the direction parallel to fibers the same strain but different stress, as shown in figure 4.20 for tensile loading and figure 4.21 for compressive loading.

In both cases, the ultimate strength for the composite occurrs when fiber reaches its ultimate value.

The post failure slope is determined by the tensile and compressive fracture energies selected.

Resulting transversal tensile behaviour of the unidirectional lamina

Figure 4.22 illustrates the plot of tensile serial stresses of composite and its component materials versus the composite serial strain. Note that the stress plotted for component materials are the quadratic average ones; consequently, at failure, the curve for matrix attains the value $\frac{X_{mT}}{{}_m\alpha}$.

The rather unrealistic postcritical horizontal branch is due to the high fracture energy employed to increase the shear ultimate strength (see subsection concerning the shear stress-strain curve calibration).

Lamina failure envelope for combined longitudinal and shear loading

Figure 4.24shows the biaxial failure envelope obtained with the ESP model, under combined longitudinal and shear loading (σ_x vs. τ_{xy}) for the E-glass/epoxy LY556 unidirectional lamina. The domain is obtained by subjecting an hexahedral element, with the proposed constitutive law, to an increasing stress applied at different fixed ratios $\sigma_x : \tau_{xy}$ up to failure.

Lamina failure envelope for combined transverse and shear loading

In Figure 4.23 is illustrated the biaxial failure envelope under combined transverse and shear loading (σ_y vs. τ_{xy}) for the LY556 unidirectional lamina, as predicted by the ESP model together with the experimental failure data provided in [108]. For comparison the domain given by Puck & Schürmann [84] is also reported.

Failure envelope for $[90°/\pm 30°/90°]$ GFRP laminate

The failure envelopes for a $[90°/\pm 30°/90°]$ laminate made of E-glass/epoxy LY556 are considered. The lay-up configuration is shown in figure 4.25.

In figure 4.26, the experimental data points for failure under combined longitudinal and shear loading (σ_x vs. τ_{xy}) are reported together with the failure envelope supplied the prediction of the ESP model.

It is worth to be remarked that in the zones where our model slightly overestimates the strength (i.e. for pure compressive σ_x and in the central zone of maximum τ_{xy}) the collapse is due to delamination and local buckling in the fibers. This phenomenon seems to be also governed by the interaction in the lamina between shear stress and compressive strength. In the current version of the model we do not account for this phenomenon.

In Figure 4.27, the experimental data points for failure under combined direct stresses (σ_x vs. σ_y) are reported together with the failure envelope obtained with the ESP model. The failure envelope predicted in [84] is also reported for comparison.

The few test results carried out under external pressure and axial compression were reported to be governed by global buckling in the tubular specimens, thus, in the quadrant $\sigma_x < 0$, $\sigma_y < 0$, the experimental data cannot be directly compared with the theoretical predictions which do not consider global buckling.

		GLOBAL CONVERGENCE		LOCAL CONVERGENCE	
STEP	STRAIN	IITER	**Relative Global Residue** RATIO/TOLER	KITER	**Relative Local Residue** EUNOR/TOLRES
A	0.016	1	0	1	0
B	0.0235	1	1.091E+05	1	2.495E+03
				2	2.980E+01
				3	4.148E-03
		2	3.970E+02	1	2.120E+02
				2	1.820E-01
		3	3.580E+00	1	2.320E+02
				2	2.250E-01
		4	1.335E-02	1	2.320E+02
				2	2.250E-01
C	0.031	1	1.567E+04	1	1.820E+02
				2	1.680E-01
		2	5.250E+01	1	8.420E+01
				2	3.339E-02
		3	2.870E-01	1	8.760E+01
				2	3.638E-02
D	0.036	1	2.284E+05	1	9.970E+02
				2	2.219E+03
				3	6.540E+01
				4	2.853E-02
		2	7.721E+03	1	6.080E+02
				2	9.050E+00
				3	5.849E-05
		3	7.180E+00	1	8.060E+02
				2	1.490E+01
				3	1.058E-04
		4	1.414E-04	1	8.010E+02
				2	1.407E+02
				3	1.043E-04
E	0.041	1	6.483E+04	1	4.630E+02
				2	5.753E-02
		2	9.830E+02	1	3.570E+02
				2	1.730E+00
				3	4.148E-06
		3	1.920E-01	1	3.610E+02
				2	1.750E+00
				3	4.133E-06
F	0.046	1	4.260E+05	1	8.011E+03
				2	5.199E-12
		2	5.997E-04	1	4.525E-06
G	0.051	1	0.000E+00	1	6.416E-06
H	0.056	1	0.000E+00	1	1.103E-05

Figure 4.15: Table reporting the relative residual error and the required iterations for both local and global problems.

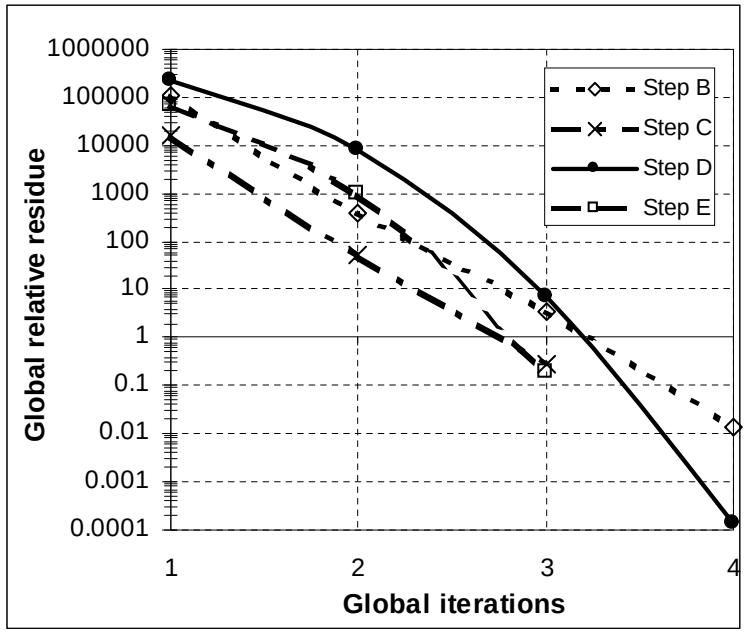

Figure 4.16: Global convergence at different steps of the load-unload process.

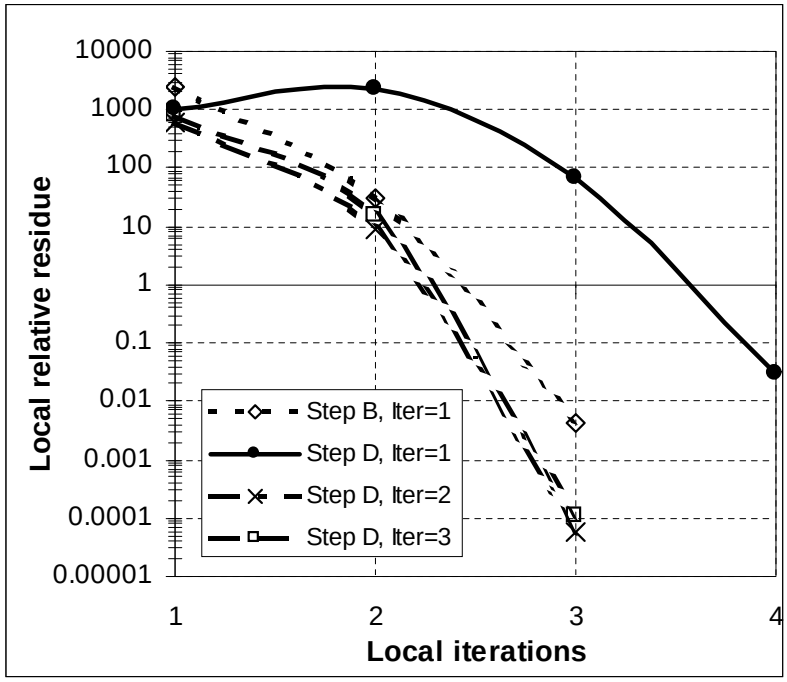

Figure 4.17: Local convergence at different steps of the load-unload process.

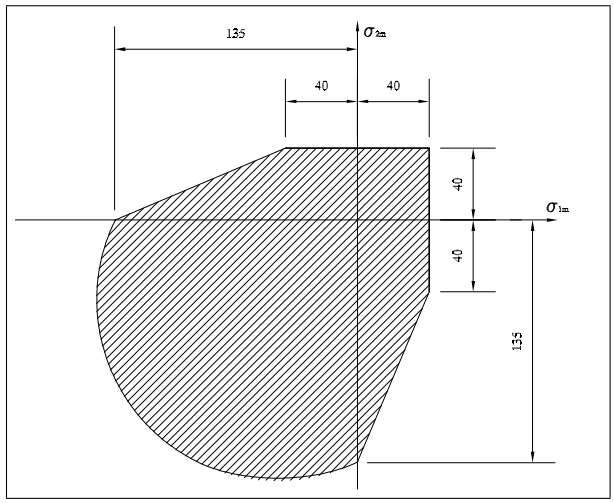

Figure 4.18: Initial elastic domain of the d^+/d^- model adopted for modeling matrix.

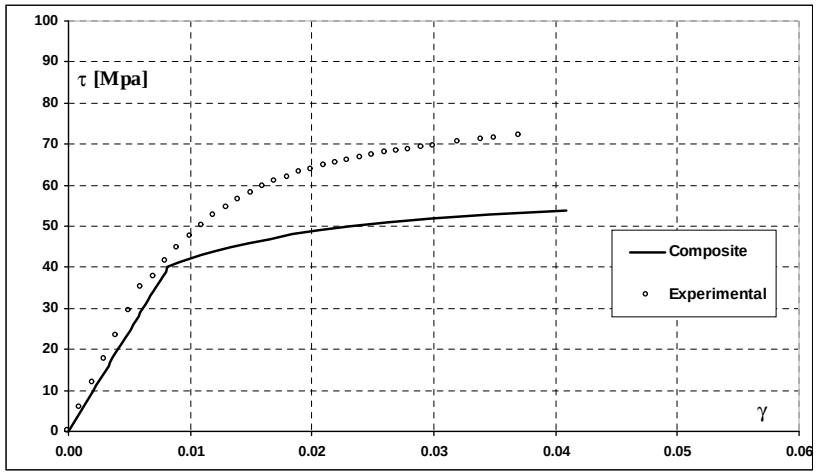

Figure 4.19: Numerical and experimental shear stress-strain responses of the unidirectional LY-556 lamina.

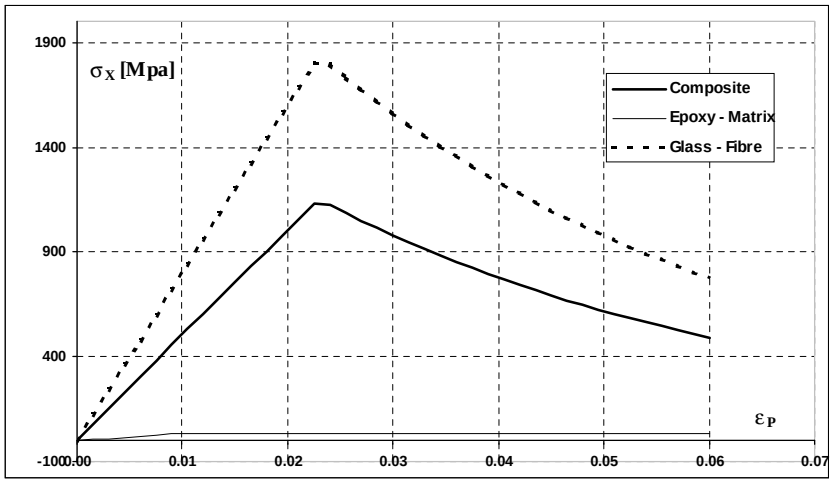

Figure 4.20: Longitudinal tensile behaviour of composite and components using the ESP model.

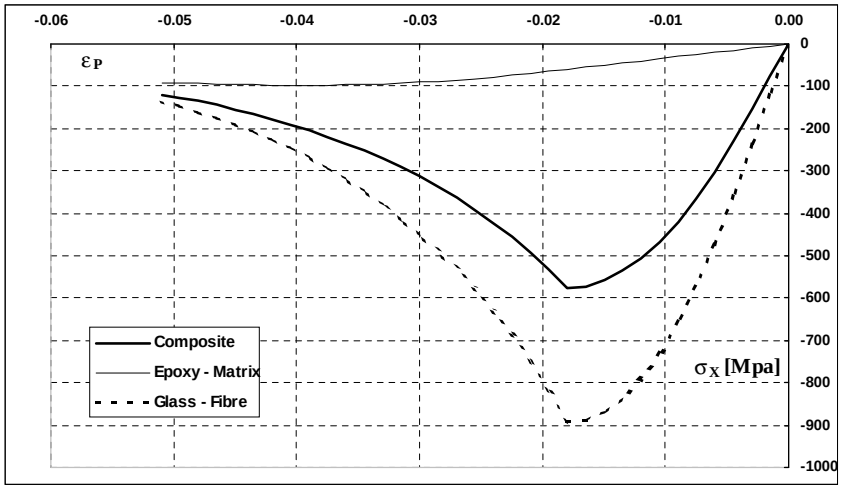

Figure 4.21: Longitudinal compressive behaviour of composite and components using the ESP model.

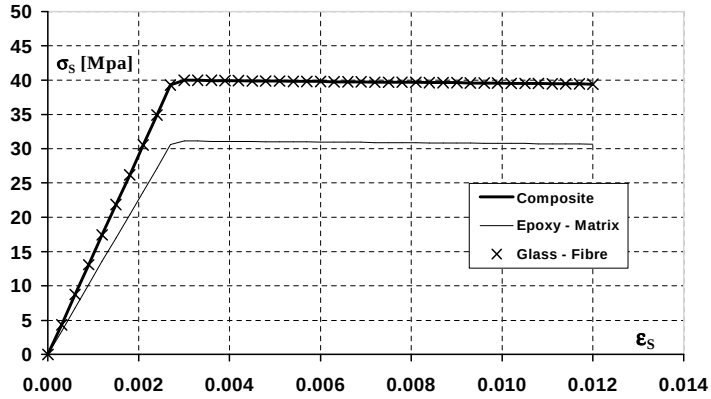

Figure 4.22: Transversal tensile stresses for composite and components versus composite transversal strain provided by the ESP model.

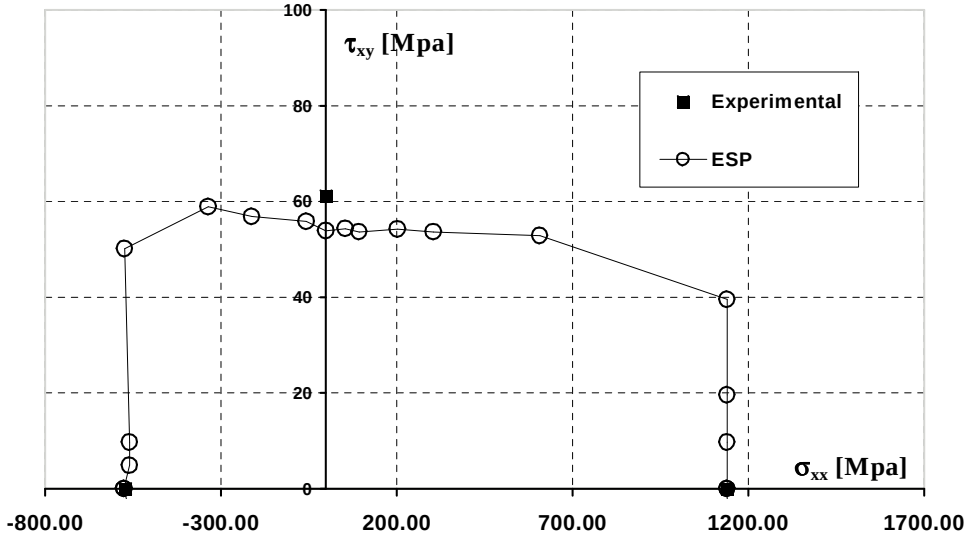

Figure 4.23: Biaxial failure envelope for glass-epoxy LY556 unidirectional lamina under combined longitudinal and shear loading.

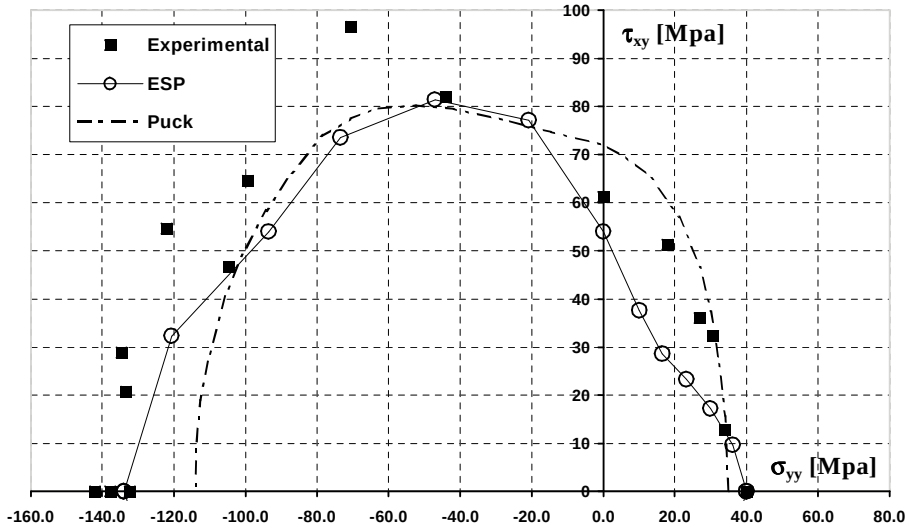

Figure 4.24: Biaxial failure envelope for glass-epoxy LY556 unidirectional lamina under combined transversal and shear loading. Comparison with experimental data and Puck's estimation.

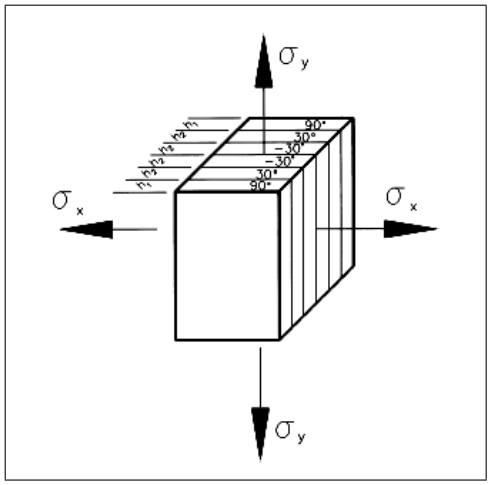

Figure 4.25: Lay-up scheme for $[90°/\pm 30°/90°]$ glass-epoxy LY556 laminate.

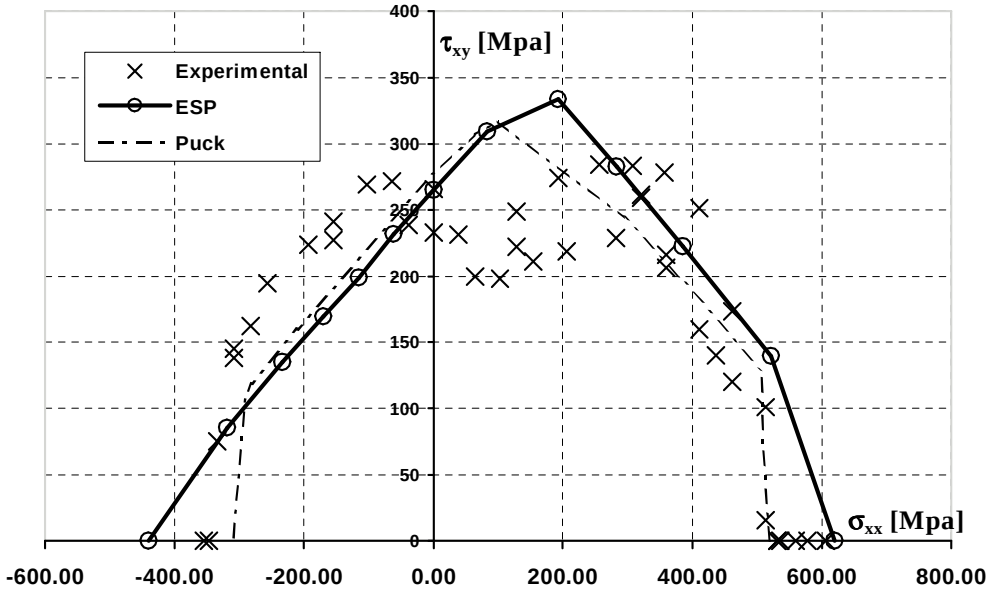

Figure 4.26: Biaxial failure envelope for glass-epoxy LY556 [90°/ ± 30°/90°] laminate under combined longitudinal and shear loading. Comparison with experimental data and Puck's estimation.

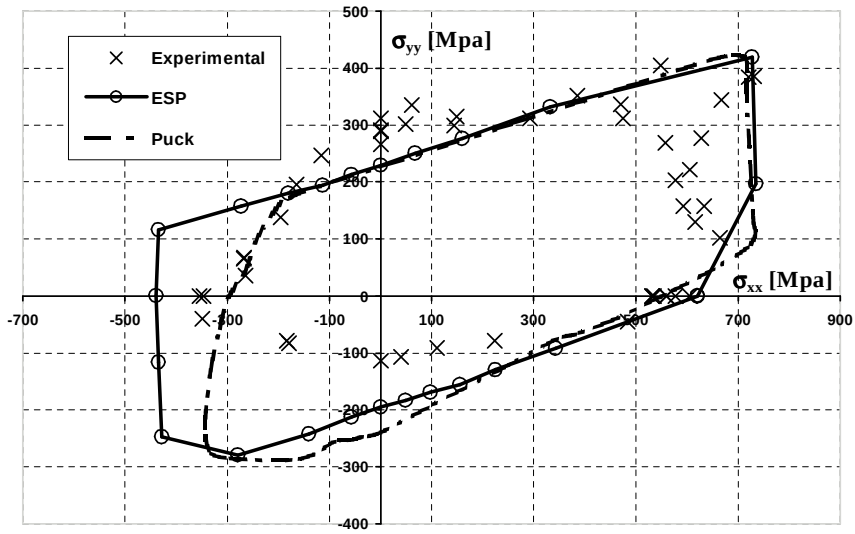

Figure 4.27: Biaxial failure envelope for glass-epoxy LY556 [90°/ ± 30°/90°] laminate under combined longitudinal and transverse loading. Comparison with experimental data and Puck's estimation.

Chapter 5

Shell finite elements for large scale structural simulations

5.1 Introduction

The assessment of BSP and ESP constitutive models performed in the previous chapter ensures the good correspondence between numerical and experimental results in case of uniform strain states. The positive response of such validations allows the extension of the numerical simulations to industrial structural elements of greater complexity and dimension. This chapter is devoted to the theoretical and computational issues concerning an effective analysis of laminated composite large scale structures via the finite element method employing the constitutive model discussed in chapters 3 and 4 combined with isoparametric 3D elements and laminated shell elements. The reason for the use of the latter type of elements is motivated and discussed together with the problematics connected with the reliability of equivalent single layer theories in the analysis of composite laminated structures.

The theoretical formulation and the operations required for the implementation of a new constitutive model in 3D isoparametric elements are rather standard and, consequently, are not examined. Conversely, for what concerns the analysis with shell elements, the theoretical issues of the structural theory employed and the FEM formulation and implementation are thoroughly detailed. A subsection is devoted to the assessment with benchmark tests of the correct implementation of the proposed laminated shell element in COMET's elements library.

5.2 Analysis of large scale laminated shell structures

5.2.1 Preliminary considerations

The laminated structural elements employed in the automotive and aeronatical industries typically exhibit complex lay-up configurations with stacking layers of different LFC materials and fiber orientation and usually possess planar dimensions one or two orders of magnitude larger than their thickness dimension.

In a computer aided calculation, the discretization of this laminated structure can be performed in full detail by using 3D meshes of elements whose constitutive law accounts for the different fiber orientation throughout the thickness. This approach allows a complete reproduction of the kinematics of the laminate throughout the thickness but, at the same time, when modeling large scale structural elements, leads to meshes with a very large number of elements, since the characteristic dimension of the elements to be employed needs to be adjusted to the thickness of the single laminas. This occurrence increases the computational cost of the analysis. Besides, the resulting large number of degrees of freedom is even more computationally expensive in a non-linear analysis with complex constitutive laws. Consequently, the employment of 2D shell elements with a laminated structure appears to be a very useful instrument in the analysis since it allows a strong reduction of the degrees of freedom required in the analysis.

An approach extensively applied in the structural analysis of shell laminated structures consists in the employment Equivalent Single Layer theories. These theories are based on the same kinematic assumptions used in membrane and plate theories for homogeneous structures. Analogous hypotheses on the kinematics of deformation through the thickness of the laminate are enforced, allowing to simplify the kinematic from a formulation based on 3D fields to a 2D based one. These laminated shell theories turn out to be very useful since they allow a great reduction in the number of degrees of freedom and consequently, a great simplification of the problem, and a minor computational cost of the related numerical methods.

The discriminant on a proper employment of ESL theories in the analysis LFC laminated structures regards the reliability of the founding kinematic hypotheses in presence of a laminated stacked structure. The analysis of fiber-reinforced, laminated composite structures, in fact, presents many difficulties. Unlike their homogeneous isotropic counterparts, the heterogeneous anisotropic constitution of LFC structures often results in the appearance of many unique phenomena that can occur on vastly different geometric scales, i.e. at the global or lami-

nate level, the ply level, or the microscopic fiber/matrix level. At the ply level, laminated composites often exhibit transverse stress concentrations near material and geometric discontinuities (the so-called free edge effect) that can lead to damage in the form of delamination, matrix cracking and adhesive joint separation. Once significant damage occurs at the ply level, the kinematic and material description of the problem must be changed before further analysis can proceed. When the main emphasis of the analysis is to determine the global response of the laminated component (for example, gross deflections, critical buckling loads, fundamental vibration sequences, and associated mode shapes), the simplified ESL theories can be used to accurately determine such global behaviour and, especially for very thin laminates, the problem is then strongly simplified.

A more accurate analysis which includes the assessment of localized regions of potential damage initiation requires the determination of the complete three-dimensional state of stress and strain at the ply level. The simple ESL laminate theories are most often incapable of accurately determining the 3D stress field at the ply level since the simplification of the kinematics through the thickness implies a discontinuity of the stress field which can violate the equilibrium in this direction at the ply interfaces. For thin laminates the error introduced due to discontinuous interlaminar stresses can be negligible; however for thick laminates, the ESL theories can give erroneous results for all stresses, requiring the employment of theories with a richer kinematic like complete 3D analysis ([87], [88], [89], [110], [111], [68], [69], [102], [125], [98]) or layerwise theories ([127], [117], [103], [25], [96], [11], [75], [76]).

In this chapter a laminated shell element which is formulated on the basis of a ESL theory is presented. The specific ESL theory selected is the Classical Laminated Plate (CLP) theory which is an extension of Kirchhoff's plate theory to laminated composite plates. This choice is motivated from the consideration that the laminated structures that we intend to analyze numerically possess a thickness dimension very small, compared to the planar dimensions. The choice of CLP theory determines that both transverse shear and transverse normal effects are neglected and, consequently, the deformation is assumed to be entirely due to bending resulting in an in-plane stress state in each one of the consituent laminas.

On account of all the previous considerations, a reasonable approach in the structural analysis of thin laminated FRP structures can be followed via the Finite Element Method with the following strategy: 1) employing exahedral isoparametric elements for thicker primary structural elements or whenever it

is important the achievement of an accurate determination of the 3D stresses and strains in each lamina (e.g. when assessing the localized region of potential damage initiation); 2) performing a FEM analysis with thin laminated shell elements formulated with the CLP - ESL theory for thinner structural elements.

5.3 Elements for the structural analysis of homogeneous thin shell structures

The FEM analysis of thin shell structures using a bi-dimensional formulation is strongly characterized by the way the coupling between bending and membrane behaviours is considered. A first class of shell elements is obtained by using and discretizing a particular shell theory in which the coupling is already built-in the variational formulation [41], [40]. A second approach for the definition of a shell bi-dimensional element is to define separately a membrane and a plate bending elements and subsequently superimpose and assemble the element stiffnesses in a global coordinate system.

The latter approach, with the use of triangular flat elements having displacements and rotations at the corner nodes as degrees of freedom is convenient for many practical reasons. The flexibility of the triangular shape allows the modelling of arbitrary shell geometries while the presence of the rotational degrees of freedom allows to include the modelling of beam stiffeners. Standard 3-noded shell elements have a total of 18 degrees of freedom (3 translations and 3 rotations at each node) or 15 degrees of freedom (3 translations and 2 rotations) depending on whether the rotation about the normal to the shell is included as a degree of freedom [72], [54], [8]. We restrict the selection of the specific membrane and plate bending elements to low order elements that, though exhibit a slower convergence, are computationally economical (therefore more suitable in the non-linear analysis) and easy to implement. In this view, as membrane element it has been selected goes the Constant Stress Triangle (CST) [132].

The definition of a corresponding plate bending theory element, of first order, suitable for the aforementioned shell elements, has generated in the past a large discussion ([26], [7], [65], [14], [95], [30], [31], [38], [39], [37]). Our choice goes to the Discrete Kirchoff Theory (DKT) element. Batoz and Bathe [15], indeed, have identified in this element an optimum solution for the general linear analysis, giving specific attention to the numerical efficiency and reliability for structural analysis.

A source of difficulty which is encountered in the effective employment of this DKT-CST shell element in structures possessing a general curvature in space concerns the management of the rotational degree of freedom about the normal to the shell surface. The inclusion of these rotations can lead to singularities of the global stiffness when the discretized geometry presents elements co-planarity in the nodes, whereas the usual method of omitting these rotations [27], interferes with the rigid body motion [132], [29]. In the exposition of the shell element theory we consider preliminarily that the element has 18 degrees of freedom leaving to a following subsection the details on the solution to the problem of co-planarity.

5.4 The DKT-CST homogeneous shell element

We denote with $\boldsymbol{x}$ the position vector of the midplane points, with z the coordinate across the thickness, and with $\boldsymbol{e}_3'$ the normal to the shell element. The kinematics of the shell is described by the displacement vector field $\boldsymbol{u}(\boldsymbol{x})$ of the midplane surface and by the vector field of the rotations of shell's transversal sections $\boldsymbol{\vartheta}$. While $\boldsymbol{u}$ belongs to the whole 3-dimensional space, $\boldsymbol{\vartheta}(\boldsymbol{x})$ belongs, instead, to the 2-dimensional tangent space of the shell in the point $\boldsymbol{x}$. The fields $\boldsymbol{\vartheta}$ and $\boldsymbol{u}$ determine the whole displacements field as follows:

$$\boldsymbol{u}_G(\boldsymbol{x}, z) = \boldsymbol{u}(\boldsymbol{x}) + \boldsymbol{\vartheta} \times z\boldsymbol{e}_3'. \tag{5.1}$$

As we have said above, the approach that we follow to account for the mechanical membrane-bending behaviour of te shell consists in defining separately a membrane and a plate bending elements and subsequently superimpose and assemble the element stiffnesses in a global coordinate system. In this approach, then, the enforcement of the governing equation is subordinate to the discretization of the geometry and the definition of the elemental parameters.

For a clear exposition of the formulation of the DKT-CST shell element it is convenient to introduce initially the degrees of freedom of the element in the global reference. The element is flat, triangular and has 18 DOF, consisting in a 3-dimensional vector of translational global displacements $\boldsymbol{u}^k$ and a 3-dimensional vector of rotational global displacements $\boldsymbol{\vartheta}^k$ for each node k. We consider a global orthogonal reference frame with unit vectors $\boldsymbol{e}_1$, $\boldsymbol{e}_2$, $\boldsymbol{e}_3$ and, associated with each node j, a reference frame for the description of the nodal rotational DOFs, namely $\boldsymbol{e}_1^{(\vartheta)j}$, $\boldsymbol{e}_2^{(\vartheta)j}$, $\boldsymbol{e}_3^{(\vartheta)j}$. Denoting with e non-bold the index

of the triangular element, with a the index of the nodes in the elemental numbering ($a = 1, ..., 3$), and with $k(e, a)$ the connection matrix that relates elemental to global nodal indexes, the vector of elemental DOF is:

$$\mathcal{G}^{(e)} = \left\{ \begin{array}{l} \left[\left(\begin{array}{c} u_1^{k(e,1)} \\ u_2^{k(e,1)} \\ u_3^{k(e,1)} \end{array} \right), \left(\begin{array}{c} \vartheta_1^{k(e,1)} \\ \vartheta_2^{k(e,1)} \\ \vartheta_3^{k(e,1)} \end{array} \right) \right], \\ \left[\left(\begin{array}{c} u_1^{k(e,2)} \\ u_2^{k(e,2)} \\ u_3^{k(e,2)} \end{array} \right), \left(\begin{array}{c} \vartheta_1^{k(e,2)} \\ \vartheta_2^{k(e,2)} \\ \vartheta_3^{k(e,2)} \end{array} \right) \right], \\ \left[\left(\begin{array}{c} u_1^{k(e,3)} \\ u_2^{k(e,3)} \\ u_3^{k(e,3)} \end{array} \right), \left(\begin{array}{c} \vartheta_1^{k(e,3)} \\ \vartheta_2^{k(e,3)} \\ \vartheta_3^{k(e,3)} \end{array} \right) \right] \end{array} \right\}, \tag{5.2}$$

where:

$$\begin{aligned} u_i^k &= \boldsymbol{u}^k \cdot \boldsymbol{e}_i, \\ \vartheta_i^k &= \boldsymbol{\vartheta}^k \cdot \boldsymbol{e}_i^{(\vartheta)k}, \end{aligned}$$

with no sum over the index k. Associated with each triangular element e we consider an orthogonal unit reference frame $\boldsymbol{e}_1'^{(e)}$, $\boldsymbol{e}_2'^{(e)}$, $\boldsymbol{e}_3'^{(e)}$ oriented so that the third vector $\boldsymbol{e}_3'^{(e)}$ is parallel to the outward normal to the plane of the element. Even if not compulsory, the first vector $\boldsymbol{e}_1'^{(e)}$ is considered to be oriented as the side $1-2$ of the triangle and $\boldsymbol{e}_2'^{(e)}$ normal to $\boldsymbol{e}_1'^{(e)}$ and $\boldsymbol{e}_3'^{(e)}$; it is also convenient to set the frame so that $\boldsymbol{e}_3'^{(e)} = \boldsymbol{e}_1'^{(e)} \times \boldsymbol{e}_2'^{(e)}$. Accordingly, the apex will denote henceforth all the quantities related to the element and expressed in the elemental frame. Analogously $x\prime$, $y\prime$ will denote the in-plane component of the position vector $\boldsymbol{x}$ in the generic element:

$$\begin{aligned} x\prime &= \boldsymbol{x} \cdot \boldsymbol{e}_1'^{(e)}, \\ y\prime &= \boldsymbol{x} \cdot \boldsymbol{e}_2'^{(e)}. \end{aligned}$$

The nodal positions vectors are accordingly indicated with $\boldsymbol{x}^j$, with $j = 1, 2, 3$.

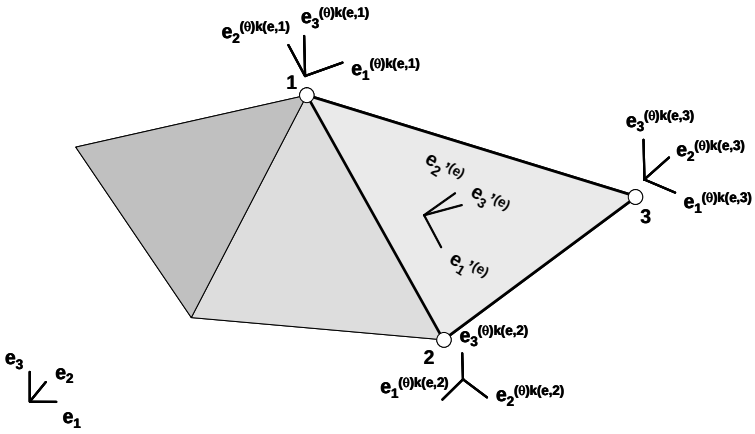

5.4.1 Geometry interpolation

Both the CST and the DKT formulation are based on a first order interpolation of the geometry, through use of the functions:

$$N_1 = 1 - \xi - \eta, \quad N_1 = \xi, \quad N_1 = \eta, \tag{5.3}$$

where ξ and η are the coordinates that map the points of the unit triangle in the natural space. The geometry is interpolated then with the invertible vectorial function:

$$\boldsymbol{x}(\xi,\eta) = \sum_{i=1}^{3} \boldsymbol{x}^i N_i = \boldsymbol{x}^1 + (\boldsymbol{x}^2 - \boldsymbol{x}^1)\xi + (\boldsymbol{x}^3 - \boldsymbol{x}^1)\eta,$$

whose image is the triangle in the Cartesian space.

5.4.2 Constant Stress Triangle (CST) membrane element

The membrane behaviour is ruled by the plane-stress linear elastic theory [120]. The fields that define the relevant kinematics are the two in-plane components of displacement $u_{x'}$ and $u_{y'}$ defined over the triangular surface of the element:

$$\begin{aligned} u_{x'}(x',y') &= \boldsymbol{u}(x',y') \cdot \boldsymbol{e}_1'^{(e)}, \\ u_{y'}(x',y') &= \boldsymbol{u}(x',y') \cdot \boldsymbol{e}_2'^{(e)}. \end{aligned}$$

The nodal values are:

$$\begin{aligned} u_{x'}^{(k)} &= \boldsymbol{u}^k \cdot \boldsymbol{e}_1'^{(e)} = \sum_{i=1}^{3} u_i^k \boldsymbol{e}_i \cdot \boldsymbol{e}_1'^{(e)} \\ u_{y'}^{(k)} &= \boldsymbol{u}^k \cdot \boldsymbol{e}_2'^{(e)} = \sum_{i=1}^{3} u_i^k \boldsymbol{e}_i \cdot \boldsymbol{e}_2'^{(e)} \end{aligned} \tag{5.4}$$

Denoting with $\boldsymbol{\varepsilon}_m'$ the membrane strains vector and with $\varepsilon_{x'}$, $\varepsilon_{y'}$ and $\gamma_{x'y'}$ its components , these quantities are related to the kinematic fields as follows:

$$\boldsymbol{\varepsilon}_m' = \left\{ \begin{array}{c} \varepsilon_{x'} \\ \varepsilon_{y'} \\ \gamma_{x'y'} \end{array} \right\} = \left[\begin{array}{cc} \frac{\partial}{\partial x'} & 0 \\ 0 & \frac{\partial}{\partial y'} \\ \frac{\partial}{\partial y'} & \frac{\partial}{\partial x'} \end{array} \right] \left\{ \begin{array}{c} u_{x'} \\ u_{y'} \end{array} \right\}. \tag{5.5}$$

Denoting with A and h the element area and thickness, the bilinear form that characterizes the membrane stiffness of the element reads:

$$U_m = \int_A \left\{ \begin{array}{c} \varepsilon_{x'} \\ \varepsilon_{y'} \\ \gamma_{x'y'} \end{array} \right\}^T \hat{\boldsymbol{D}}_m \left\{ \begin{array}{c} \varepsilon_{x'} \\ \varepsilon_{y'} \\ \gamma_{x'y'} \end{array} \right\} dA,$$

where $\hat{\boldsymbol{D}}_m = h\boldsymbol{D}_m$.and $\boldsymbol{D}_m$ is the linear elastic plane stress stiffness matrix, that for an isotropic material is:

$$\boldsymbol{D}_m = \frac{E}{1-\nu^2} \left[\begin{array}{ccc} 1 & \nu & 0 \\ \nu & 1 & 0 \\ 0 & 0 & \frac{1-\nu}{2} \end{array} \right]. \tag{5.6}$$

In the CST element both the geometry and the displacement fields are interpolated through the functions N_k in (5.3); accordingly the displacements are interpolated as:

$$\left\{ \begin{array}{c} u_{x'} \\ u_{y'} \end{array} \right\} = \sum_{k=1}^{3} \left[\begin{array}{cc} N_k & 0 \\ 0 & N_k \end{array} \right] \left\{ \begin{array}{c} u_{x'}^{(k)} \\ u_{y'}^{(k)} \end{array} \right\}. \tag{5.7}$$

The whole couple of natural coordinates (ξ, η) will be indicated with $\boldsymbol{\xi}$. From

(5.7), (5.5) and (5.4) we have:

$$\left\{ \begin{array}{c} \varepsilon_{x'} \\ \varepsilon_{y'} \\ \gamma_{x'y'} \end{array} \right\} = \left[\begin{array}{cc} \frac{\partial}{\partial x'} & 0 \\ 0 & \frac{\partial}{\partial y'} \\ \frac{\partial}{\partial y'} & \frac{\partial}{\partial x'} \end{array} \right] \sum_{k=1}^{3} \left[\begin{array}{cc} N_k & 0 \\ 0 & N_k \end{array} \right] \left\{ \begin{array}{c} \sum\limits_{i=1}^{3} \left(\boldsymbol{e}_i \cdot \boldsymbol{e}_1^{\prime(e)} \right) u_i^k \\ \sum\limits_{i=1}^{3} \left(\boldsymbol{e}_i \cdot \boldsymbol{e}_2^{\prime(e)} \right) u_i^k \end{array} \right\} = \tag{5.8}$$

$$= \sum_{k=1}^{3} \left\{ \begin{array}{c} \sum\limits_{i=1}^{3} \left[\frac{\partial N_k}{\partial x'} \left(\boldsymbol{e}_i \cdot \boldsymbol{e}_1^{\prime(e)} \right) \right] u_i^k \\ \sum\limits_{i=1}^{3} \left[\frac{\partial N_k}{\partial y'} \left(\boldsymbol{e}_i \cdot \boldsymbol{e}_2^{\prime(e)} \right) \right] u_i^k \\ \sum\limits_{i=1}^{3} \left[\frac{\partial N_k}{\partial y'} \left(\boldsymbol{e}_i \cdot \boldsymbol{e}_1^{\prime(e)} \right) + \frac{\partial N_k}{\partial x'} \left(\boldsymbol{e}_i \cdot \boldsymbol{e}_2^{\prime(e)} \right) \right] u_i^k \end{array} \right\}.$$

The last formula can be used to compute the 3×18 matrix $\boldsymbol{B}_m^{(e)}$ that relates membrane strains to the global degrees of freedom of the element $\mathcal{G}^{(e)}$:

$$\boldsymbol{\varepsilon}'_m = \left\{ \begin{array}{c} \varepsilon_{x'} \\ \varepsilon_{y'} \\ \gamma_{x'y'} \end{array} \right\} = \boldsymbol{B}_m^{(e)} \left\{ \mathcal{G}^{(e)} \right\}. \tag{5.9}$$

The 18×18 membrane stiffness matrix is then:

$$\boldsymbol{K}_m^{(e)} = \int_A \left(\boldsymbol{B}_m^{(e)} \right)^T \hat{\boldsymbol{D}}_m \boldsymbol{B}_m^{(e)} \, dA,$$

while the elemental nodal forces vector is given by:

$$\boldsymbol{F}_m^{(e)} = h \int_A \left(\boldsymbol{B}_m^{(e)} \right)^T \left\{ \begin{array}{c} \sigma_{x'} \\ \sigma_{y'} \\ \tau_{x'y'} \end{array} \right\} dA.$$

Since the integrals are calculated via a numerical quadrature, then the formulas to be implemented are:

$$\boldsymbol{K}_m^{(e)} = \sum_{g=1}^{n_g} \left[\left(\boldsymbol{B}_m^{(e)} \left(\boldsymbol{\xi}_g \right) \right)^T \hat{\boldsymbol{D}}_m \boldsymbol{B}_m^{(e)} \left(\boldsymbol{\xi}_g \right) \right] W_g,$$

$$\boldsymbol{F}_m^{(e)} = h \sum_{g=1}^{n_g} \left(\boldsymbol{B}_m^{(e)} \left(\boldsymbol{\xi}_g \right) \right)^T \left\{ \begin{array}{c} \sigma_{x'} \\ \sigma_{y'} \\ \tau_{x'y'} \end{array} \right\} W_g,$$

where n_g is the number of Gauss points and W_g is the weight associated with the Gauss point of index g.

5.4.3 Discrete Kirchhoff Triangle (DKT) plate bending element

The formulation of the 9 dof DKT element is based on the discrete Kirchhoff theory for bending of thin plates. This theory is obtained by first considering a theory of plates including transverse shear deformations (the plate theory of Reissner-Mindlin [128]). In this theory the independent kinematic fields are the deflection $w\prime$ and the rotations $\vartheta_{x'}$ and $\vartheta_{y'}$ and only C^0 continuity continuity requirements need to be satisfied. The transverse shear energy is neglected altogether and the Kirchhoff hypothesis is introduced in a discrete form along the edges to relate the rotations to the transverse displacements. It has been proved in [61], through the derivation of error estimates associated with the DKT model, that the displacements and the free vibration eigenvalues converge quadratically to the C^1 Kirchhoff solution of thin plates. This theoretical result is in agreement with the results obtained in [39], [37], [38]. The generally good behaviour of this element has also been proved in [15].

We resume briefly the theory of plates with transverse shear deformation included. The scalar fields $w\prime$, $\vartheta_{x'}$ and $\vartheta_{y'}$ are the projection of the global kinematic fields in the element reference system:

$$w\prime = \boldsymbol{u} \cdot \boldsymbol{e}_3^{\prime(e)}, \tag{5.10}$$

$$\vartheta_{x'} = \boldsymbol{\vartheta} \cdot \boldsymbol{e}_1^{\prime(e)},$$

$$\vartheta_{y'} = \boldsymbol{\vartheta} \cdot \boldsymbol{e}_2^{\prime(e)}.$$

The part of the displacement field represented in (5.1) that is involved in the small displacement theory of plates with transverse shear included is:

$$\boldsymbol{u}_B(x', y') = w\prime \boldsymbol{e}_3^{\prime(e)} + \boldsymbol{\vartheta} \times z\boldsymbol{e}_3'. \tag{5.11}$$

Introducing the vector:

$$\boldsymbol{\beta}' = -\boldsymbol{e}_3' \times \boldsymbol{\vartheta}, \tag{5.12}$$

with components $\beta_{x'} = \boldsymbol{\beta} \cdot \boldsymbol{e}_1'^{(e)}$, $\beta_{y'} = \boldsymbol{\beta} \cdot \boldsymbol{e}_2'^{(e)}$, the in plane components of displacement are expressed as:

$$u' = \boldsymbol{u}_B \cdot \boldsymbol{e}_1'^{(e)} = \boldsymbol{\vartheta} \times z\boldsymbol{e}_3' \cdot \boldsymbol{e}_1'^{(e)} = z\boldsymbol{\beta} \cdot \boldsymbol{e}_1'^{(e)} = z\beta_{x'},$$

$$v' = \boldsymbol{u}_B \cdot \boldsymbol{e}_2'^{(e)} = \boldsymbol{\vartheta} \times z\boldsymbol{e}_3' \cdot \boldsymbol{e}_2'^{(e)} = z\boldsymbol{\beta} \cdot \boldsymbol{e}_1'^{(e)} = z\beta_{y'}.$$

Recapitulating, the displacements expressed in scalar form are:

$$u' = z\beta_{x'}(x', y'), \quad v' = z\beta_{y'}(x', y'), \quad w\prime = w\prime(x', y').$$

The bending strains are:

$$\begin{aligned} \boldsymbol{\varepsilon}_b' &= \left\{ \begin{array}{c} \varepsilon_{x'} \\ \varepsilon_{y'} \\ \gamma_{x'y'} \end{array} \right\} = \left[\begin{array}{cc} \frac{\partial}{\partial x'} & 0 \\ 0 & \frac{\partial}{\partial y'} \\ \frac{\partial}{\partial y'} & \frac{\partial}{\partial x'} \end{array} \right] \left\{ \begin{array}{c} z\beta_{x'} \\ z\beta_{y'} \end{array} \right\} = \\ &= \left\{ \begin{array}{c} z\beta_{x',x'} \\ z\beta_{y',y'} \\ z\beta_{x',y'} + z\beta_{y',x'} \end{array} \right\} = z\hat{\boldsymbol{\varepsilon}}_b', \end{aligned} \tag{5.13}$$

where $\hat{\boldsymbol{\varepsilon}}_b'$ are the generalized bending strains. The transverse shear strains are:

$$\boldsymbol{\varepsilon}_s' = \left\{ \begin{array}{c} w\prime_{,x'} + \beta_{x'} \\ w\prime_{,y'} + \beta_{y'} \end{array} \right\} = \operatorname{grad} w\prime + \boldsymbol{\beta}'$$

In the isotropic linear elastic theory the in-plane stress-strain relations are:

$$\boldsymbol{\sigma}_b' = \left\{ \begin{array}{c} \sigma_{x'} \\ \sigma_{y'} \\ \tau_{x'y'} \end{array} \right\} = \boldsymbol{D}_m \boldsymbol{\varepsilon}_b',$$

while, setting $G = \dfrac{E}{2(1+\nu)}$, the stress-strain relations for shear result:

$$\boldsymbol{\sigma}_s' = \left\{ \begin{array}{c} \tau_{x'z'} \\ \tau_{y'z'} \end{array} \right\} = G\boldsymbol{\varepsilon}_s'.$$

The elastic bending energy is written:

$$\begin{aligned} U_b &= \frac{1}{2} \int_A \left[\int_{-\frac{h}{2}}^{\frac{h}{2}} z^2 \left[\left(\hat{\boldsymbol{\varepsilon}}_b' \right)^T \boldsymbol{D}_m \hat{\boldsymbol{\varepsilon}}_b' \right] dz \right] dA = \\ &= \frac{1}{2} \frac{h^3}{12} \int_A \left[\left(\hat{\boldsymbol{\varepsilon}}_b' \right)^T \boldsymbol{D}_m \hat{\boldsymbol{\varepsilon}}_b' \right] dA = \frac{1}{2} \int_A \left[\left(\hat{\boldsymbol{\varepsilon}}_b' \right)^T \hat{\boldsymbol{D}}_b \hat{\boldsymbol{\varepsilon}}_b' \right] dA, \end{aligned} \tag{5.14}$$

where $\hat{\boldsymbol{D}}_b = \frac{h^3}{12}\boldsymbol{D}_m$. The shear energy is:

$$\begin{aligned} U_s &= \frac{1}{2}k\int_A \left[\int_{-\frac{h}{2}}^{\frac{h}{2}} G\left[\left(\boldsymbol{\varepsilon}'_s\right)^T \boldsymbol{\varepsilon}'_s\right] dz\right] dA = \\ &= \frac{1}{2}k\int_A hG\left[\left(\boldsymbol{\varepsilon}'_s\right)^T \boldsymbol{\varepsilon}'_s\right] dA, \end{aligned}$$

where k is the shear correcton factor usually taken eaqual to 5/6.

The formulation of the DKT element is based on the following considerations:

- The transverse shear energy U_s is omitted since for thin plates it is negligible compared to the bending energy; consequently the only kinematic field to be interpolated is $\boldsymbol{\beta}'$.
- In order to grant a thin plate behaviour, the Kirchoff hypothesis $\boldsymbol{\varepsilon}'_s = 0$ is imposed in a discrete form over the family of interpolating functions.
- The triangular element has 9 dof; that is the deflection $w\prime$ and the 2 components of its gradient grad $w\prime$ at the three corner nodes. Consequently the space of functions interpolating $\boldsymbol{\beta}'$ must have the same dimension.
- Conformity of $\boldsymbol{\beta}'$ must be must be granted at the sides of the triangle.

For the interpolation of functions $\beta_{x'}$ and $\beta_{y'}$ a set $\mathcal{B}$ of 9 parameters is adopted:

$$\mathcal{B} = \left\{\beta_{x'}^{\prime(1)}, \beta_{y'}^{\prime(1)}, \beta_{x'}^{\prime(2)}, \beta_{y'}^{\prime(2)}, \beta_{x'}^{\prime(3)}, \beta_{y'}^{\prime(3)}, \beta^{\prime(23)}, \beta^{\prime(13)}, \beta^{\prime(12)}\right\}.$$

In order to assure conformity for $\boldsymbol{\beta}'$ across the sides shared by two adjacent elements the following 9-parameters interpolation is adopted:

$$\begin{aligned} \boldsymbol{\beta}' &= N_1\boldsymbol{\beta}^{\prime(1)} + N_2\boldsymbol{\beta}^{\prime(2)} + N_3\boldsymbol{\beta}^{\prime(3)} + \\ &\quad + N_4\boldsymbol{e}'_{23}\beta^{\prime(23)} + N_5\boldsymbol{e}'_{13}\beta^{\prime(13)} + N_6\boldsymbol{e}'_{12}\beta^{\prime(12)}, \end{aligned} \tag{5.15}$$

where N_1, N_2, N_3 are defined in (5.3), $\boldsymbol{e}'_{ij}$ is the unit vector parallel to side $i-j$:

$$\boldsymbol{e}'_{ij} = \frac{\boldsymbol{x}_j - \boldsymbol{x}_i}{\|\boldsymbol{x}_j - \boldsymbol{x}_i\|},$$

and N_4, N_5, N_6 are the natural functions defined as follows:

$$N_4 = 4\xi\eta, \quad N_5 = 4\eta(1-\xi-\eta), \quad N_6 = 4\xi(1-\xi-\eta).$$

The conformity is achieved since the value of $\boldsymbol{\beta}'$ on a given side $i-j$ depends only on the terms of the interpolation relative to the same side in which the indexes i and j appear. In more explicit form interpolation (5.15) is written:

$$\left\{ \begin{array}{c} \beta_{x'} \\ \beta_{y'} \end{array} \right\} = \sum_{k=1}^{3} \left[\begin{array}{cc} N_k & 0 \\ 0 & N_k \end{array} \right] \left\{ \begin{array}{c} \beta'^{(k)}_{x'} \\ \beta'^{(k)}_{y'} \end{array} \right\} + \sum_{k=4}^{6} \left[\begin{array}{c} N_k(\boldsymbol{e}'_{ij(k)} \cdot \boldsymbol{e}'_1) \\ N_k(\boldsymbol{e}'_{ij(k)} \cdot \boldsymbol{e}'_2) \end{array} \right] \beta'^{(ij(k))}, \quad (5.16)$$

with $ij(4) = 12$, $ij(5) = 13$, $ij(6) = 12$.

Generalized bending strain for (5.13) adquires the interpolated expression:

$$\begin{aligned} \hat{\boldsymbol{\varepsilon}}'_b \;=\; & \sum_{k=1}^{3} \left[\begin{array}{cc} \frac{\partial N_k}{\partial x'} & 0 \\ 0 & \frac{\partial N_k}{\partial y'} \\ \frac{\partial N_k}{\partial y'} & \frac{\partial N_k}{\partial x'} \end{array} \right] \left\{ \begin{array}{c} \beta'^{(k)}_{x'} \\ \beta'^{(k)}_{y'} \end{array} \right\} + \\ & + \sum_{k=4}^{6} \left[\begin{array}{c} \frac{\partial N_k}{\partial x'}(\boldsymbol{e}'_{ij(k)} \cdot \boldsymbol{e}'_1) \\ \frac{\partial N_k}{\partial y'}(\boldsymbol{e}'_{ij(k)} \cdot \boldsymbol{e}'_2) \\ \frac{\partial N_k}{\partial y'}(\boldsymbol{e}'_{ij(k)} \cdot \boldsymbol{e}'_1) + \frac{\partial N_k}{\partial x'}(\boldsymbol{e}'_{ij(k)} \cdot \boldsymbol{e}'_2) \end{array} \right] \beta'^{(ij(k))}. \end{aligned} \quad (5.17)$$

The local dofs of the DKT are the value of the deflection and its derivatives at the corner nodes. The set $\mathcal{F}$ of this 9 nodal parameters is:

$$\mathcal{F} = \left\{ w\prime^{(1)}, w\prime^{(1)}_{,x'}, w\prime^{(1)}_{,y'}, w\prime^{(2)}, w\prime^{(2)}_{,x'}, w\prime^{(2)}_{,y'}, w\prime^{(3)}, w\prime^{(3)}_{,x'}, w\prime^{(3)}_{,y'} \right\}.$$

The parameters of set $\mathcal{B}$ are appropriately expressed as a linear combination of those of $\mathcal{F}$ through the enforcement of Kirchoff's hypothesis $\boldsymbol{\varepsilon}'_s = 0$.

This condition is enforced:

- at each corner node k:

$$\operatorname{grad} w\prime^{(k)} + \boldsymbol{\beta}'^{(k)} = 0 \quad (5.18)$$

- along each side $i-j$ of the triangle in the direction of the side. Indicating with s the curvilinear coordinate of the side:

$$\operatorname{grad} w\prime(s) \cdot \boldsymbol{e}'_{ij} + \boldsymbol{\beta}'(s) \cdot \boldsymbol{e}'_{ij} = 0. \quad (5.19)$$

Condition (5.19) is imposed by assuming that the deflection is cubic along each side. In this hypothesis $\dfrac{\partial w'}{\partial s} = \operatorname{grad} w\prime(s) \cdot \boldsymbol{e}'_{ij}$ is quadratic; it is sufficient then the imposition of (5.19) in 3 points for each side to grant its fulfillment along the whole length. In a natural form the points selected are the two extremal points and the midpoint:

$$\left\{ \begin{array}{r} \left.\begin{array}{rl} \boldsymbol{\beta}'^{(i)} \cdot \boldsymbol{e}'_{ij} = -\operatorname{grad} w\prime^{(i)} \cdot \boldsymbol{e}'_{ij} & \text{Node } i \\ \boldsymbol{\beta}'^{(j)} \cdot \boldsymbol{e}'_{ij} = -\operatorname{grad} w\prime^{(j)} \cdot \boldsymbol{e}'_{ij} & \text{Node } j \end{array}\right\} i,j = 1,2,3 \\ \boldsymbol{\beta}'(\boldsymbol{x}^m_{ij}) \cdot \boldsymbol{e}'_{ij} = -\operatorname{grad} w\prime(\boldsymbol{x}^m_{ij}) \cdot \boldsymbol{e}'_{ij}, \quad \text{Mid point } \; i-j, \quad ij = 12,23,13 \end{array} \right. , \tag{5.20}$$

where $\boldsymbol{x}^m_{ij}$ denotes the position vector of the mid point of side $i-j$.

Employing interpolation (5.15), the last equation in system (5.20) is rewritten as a function of the parameters of set $\mathcal{B}$:

$$\frac{1}{2}\boldsymbol{\beta}'^{(i)} \cdot \boldsymbol{e}'_{ij} + \frac{1}{2}\boldsymbol{\beta}'^{(j)} \cdot \boldsymbol{e}'_{ij} + \beta'^{(ij)} = -\operatorname{grad} w\prime(\boldsymbol{x}^m_{ij}) \cdot \boldsymbol{e}'_{ij}, \tag{5.21}$$

which provides:

$$\beta'^{(ij)} = -\operatorname{grad} w\prime(\boldsymbol{x}^m_{ij}) \cdot \boldsymbol{e}'_{ij} - \frac{1}{2}\boldsymbol{\beta}'^{(i)} \cdot \boldsymbol{e}'_{ij} - \frac{1}{2}\boldsymbol{\beta}'^{(j)} \cdot \boldsymbol{e}'_{ij}. \tag{5.22}$$

The term $\operatorname{grad} w\prime(\boldsymbol{x}^m_{ij}) \cdot \boldsymbol{e}'_{ij}$ is the value in the midpoint of the function $\dfrac{\partial w'}{\partial s}$. Since $w\prime$ is assumed to be a third-grade polynomial function of the curvilinear coordinate s, the value of $\dfrac{\partial w'}{\partial s}$ at the midpoint can be expressed as a function the nodal values:

$$\begin{array}{rcl} w\prime(s_i) & = & w\prime(\boldsymbol{x}_i), \quad w\prime(s_j) = w\prime(\boldsymbol{x}_j), \\ \dfrac{\partial w'}{\partial s}(s_i) & = & \operatorname{grad} w\prime(\boldsymbol{x}_i) \cdot \boldsymbol{e}'_{ij}, \quad \dfrac{\partial w'}{\partial s}(s_j) = \operatorname{grad} w\prime(\boldsymbol{x}_j) \cdot \boldsymbol{e}'_{ij}. \end{array} \tag{5.23}$$

This relation is easily obtained expressing the polynomial as:

$$w\prime(s) = a + bs + cs^2 + ds^3.$$

Associating the value $s = 0$ to node i and $s = l_{ij}$ to node j, the coefficient a, b,

c, d are obtained solving the following system:

$$\begin{bmatrix} 1 & 0 & 0 & 0 \\ 1 & l_{ij} & l_{ij}^2 & l_{ij}^3 \\ 0 & 1 & 0 & 0 \\ 0 & 1 & 2l_{ij} & 3l_{ij}^2 \end{bmatrix} \begin{Bmatrix} a \\ b \\ c \\ d \end{Bmatrix} = \begin{Bmatrix} w\prime(s_i) \\ w\prime(s_j) \\ \dfrac{\partial w'}{\partial s}(s_i) \\ \dfrac{\partial w'}{\partial s}(s_j) \end{Bmatrix} = \begin{Bmatrix} w\prime(\boldsymbol{x}_i) \\ w\prime(\boldsymbol{x}_j) \\ \operatorname{grad} w\prime(\boldsymbol{x}_i)\cdot \boldsymbol{e}'_{ij} \\ \operatorname{grad} w\prime(\boldsymbol{x}_j)\cdot \boldsymbol{e}'_{ij} \end{Bmatrix}. \tag{5.24}$$

The derivate at the midpoint is:

$$\operatorname{grad} w\prime(\boldsymbol{x}_{ij}^m)\cdot \boldsymbol{e}'_{ij} = w\prime(\frac{l_{ij}}{2}) = b + cl_{ij} + \frac{3}{4}dl_{ij}^2. \tag{5.25}$$

Substituting the solution of system (5.24) in (5.25) and taking into account (5.23) the term $\operatorname{grad} w\prime(\boldsymbol{x}_{ij}^m)\cdot \boldsymbol{e}'_{ij}$ gets the following expression:

$$\operatorname{grad} w\prime(\boldsymbol{x}_{ij}^m)\cdot \boldsymbol{e}'_{ij} = \frac{3}{2l_{ij}}w\prime(\boldsymbol{x}_i) - \frac{3}{2l_{ij}}w\prime(\boldsymbol{x}_j) + \frac{1}{4}\operatorname{grad} w\prime(\boldsymbol{x}_i)\cdot \boldsymbol{e}'_{ij} + \frac{1}{4}\operatorname{grad} w\prime(\boldsymbol{x}_j)\cdot \boldsymbol{e}'_{ij}. \tag{5.26}$$

Substituting (5.26) in (5.22) one gets the expression that relates $\beta'^{(ij)}$ to the parameters of the set $\mathcal{F}$:

$$\beta'^{(ij)} = \frac{3}{2l_{ij}}w\prime(\boldsymbol{x}_i) - \frac{3}{2l_{ij}}w\prime(\boldsymbol{x}_j) + \frac{3}{4}\operatorname{grad} w\prime(\boldsymbol{x}_i)\cdot \boldsymbol{e}'_{ij} + \frac{3}{4}\operatorname{grad} w\prime(\boldsymbol{x}_j)\cdot \boldsymbol{e}'_{ij}. \tag{5.27}$$

The system of (5.18) and (5.27) provides the required explicit linear relation between the parameters of sets $\mathcal{B}$ and $\mathcal{F}$. Substituting this relation in (5.17) we can write:

$$\begin{aligned} \hat{\boldsymbol{\varepsilon}}'_b \;=\; & \sum_{k=1}^{3} \begin{bmatrix} \frac{\partial N_k}{\partial x'} & 0 \\ 0 & \frac{\partial N_k}{\partial y'} \\ \frac{\partial N_k}{\partial y'} & \frac{\partial N_k}{\partial x'} \end{bmatrix} \begin{Bmatrix} w\prime^{(k)} \\ w\prime^{(k)}_{,x'} \\ w\prime^{(k)}_{,y'} \end{Bmatrix} + \\ & + \sum_{k=4}^{6} \begin{bmatrix} \frac{\partial N_k}{\partial x'}(\boldsymbol{e}'_{ij(k)}\cdot \boldsymbol{e}'_1) \\ \frac{\partial N_k}{\partial y'}(\boldsymbol{e}'_{ij(k)}\cdot \boldsymbol{e}'_2) \\ \frac{\partial N_k}{\partial y'}(\boldsymbol{e}'_{ij(k)}\cdot \boldsymbol{e}'_1) + \frac{\partial N_k}{\partial x'}(\boldsymbol{e}'_{ij(k)}\cdot \boldsymbol{e}'_2) \end{bmatrix} \begin{pmatrix} \frac{3}{2l_{ij}}w\prime^{(i)} \\ -\frac{3}{2l_{ij}}w\prime^{(j)} \\ +\frac{3}{4}\operatorname{grad} w\prime(\boldsymbol{x}_i)\cdot \boldsymbol{e}'_{ij} \\ +\frac{3}{4}\operatorname{grad} w\prime(\boldsymbol{x}_j)\cdot \boldsymbol{e}'_{ij} \end{pmatrix}. \end{aligned} \tag{5.28}$$

Interpolation (5.17) allows to formulate the element in the local system. The formulation of the DKT for the shell element requires correlation of the parameters in $\mathcal{F}$ to the global array of 18 dof $\mathcal{G}^{(e)}$in (5.2). The relation sought is given

by (5.10) and (5.12):

$$\begin{aligned} w\prime^{(k)} &= \boldsymbol{u}^k \cdot \boldsymbol{e}_3^{\prime(e)} \\ \operatorname{grad} w\prime(\boldsymbol{x}_i) &= -\boldsymbol{\beta}^{\prime(k)} = \boldsymbol{e}'_3 \times \boldsymbol{\vartheta}^{(k)}; \end{aligned}$$

componentwise the previous relations read:

$$w\prime^{(k)} = \sum_{i=1}^{3} \left(\boldsymbol{e}_i \cdot \boldsymbol{e}'_3\right) u_i^k \tag{5.29}$$

$$\left\{ \begin{array}{c} w\prime^{(k)}_{,x'} \\ w\prime^{(k)}_{,y'} \end{array} \right\} = \left\{ \begin{array}{c} -\sum\limits_{j=1}^{3} \left(\boldsymbol{e}_j^{(\vartheta)p(e,k)} \cdot \boldsymbol{e}'_2\right) \vartheta_j^{p(e,k)} \\ \sum\limits_{j=1}^{3} \left(\boldsymbol{e}_j^{(\vartheta)p(e,k)} \cdot \boldsymbol{e}'_1\right) \vartheta_j^{p(e,k)} \end{array} \right\}.$$

Substitution of (5.29) in (5.28) provides the final expression of interpolation in function of the global set of dof $\mathcal{G}^{(e)}$. Since:

$$\operatorname{grad} w\prime(\boldsymbol{x}_i) = \left[-\sum_{r=1}^{3} \left(\boldsymbol{e}_r^{(\vartheta)p(e,k)} \cdot \boldsymbol{e}'_2\right) \vartheta_r^{p(e,k)} \boldsymbol{e}'_1 + \sum_{r=1}^{3} \left(\boldsymbol{e}_r^{(\vartheta)p(e,k)} \cdot \boldsymbol{e}'_1\right) \vartheta_r^{p(e,k)} \boldsymbol{e}'_2 \right]$$

$$\begin{aligned} \hat{\boldsymbol{\varepsilon}}'_b = & \sum_{k=1}^{3} \left[\begin{array}{cc} \frac{\partial N_k}{\partial x'} & 0 \\ 0 & \frac{\partial N_k}{\partial y'} \\ \frac{\partial N_k}{\partial y'} & \frac{\partial N_k}{\partial x'} \end{array} \right] \left\{ \begin{array}{c} -\sum\limits_{r=1}^{3} \left(\boldsymbol{e}_r^{(\vartheta)p(e,k)} \cdot \boldsymbol{e}'_2\right) \vartheta_r^{p(e,k)} \\ \sum\limits_{r=1}^{3} \left(\boldsymbol{e}_r^{(\vartheta)p(e,k)} \cdot \boldsymbol{e}'_1\right) \vartheta_r^{p(e,k)} \end{array} \right\} + \\ & + \sum_{k=4}^{6} \left[\begin{array}{c} \frac{\partial N_k}{\partial x'} (\boldsymbol{e}'_{ij} \cdot \boldsymbol{e}'_1) \\ \frac{\partial N_k}{\partial y'} (\boldsymbol{e}'_{ij} \cdot \boldsymbol{e}'_2) \\ \frac{\partial N_k}{\partial y'} (\boldsymbol{e}'_{ij} \cdot \boldsymbol{e}'_1) + \frac{\partial N_k}{\partial x'} (\boldsymbol{e}'_{ij} \cdot \boldsymbol{e}'_2) \end{array} \right] A_k, \end{aligned} \tag{5.30}$$

where:

$$A_k = \left(\begin{array}{c} \frac{3}{2l_{ij}} \sum\limits_{r=1}^{3} \left(\boldsymbol{e}_r \cdot \boldsymbol{e}'_3\right) u_r^i \\ -\frac{3}{2l_{ij}} \sum\limits_{r=1}^{3} \left(\boldsymbol{e}_r \cdot \boldsymbol{e}'_3\right) u_r^j \\ +\frac{3}{4} \left[-\sum\limits_{r=1}^{3} \left(\boldsymbol{e}_r^{(\vartheta)p(e,i)} \cdot \boldsymbol{e}'_2\right) \vartheta_r^{p(e,i)} \left(\boldsymbol{e}'_{ij} \cdot \boldsymbol{e}'_1\right) + \sum\limits_{r=1}^{3} \left(\boldsymbol{e}_r^{(\vartheta)p(e,i)} \cdot \boldsymbol{e}'_1\right) \vartheta_r^{p(e,i)} \left(\boldsymbol{e}'_{ij} \cdot \boldsymbol{e}'_2\right) \right] \\ +\frac{3}{4} \left[-\sum\limits_{r=1}^{3} \left(\boldsymbol{e}_r^{(\vartheta)p(e,j)} \cdot \boldsymbol{e}'_2\right) \vartheta_r^{p(e,j)} \left(\boldsymbol{e}'_{ij} \cdot \boldsymbol{e}'_1\right) + \sum\limits_{r=1}^{3} \left(\boldsymbol{e}_r^{(\vartheta)p(e,j)} \cdot \boldsymbol{e}'_1\right) \vartheta_r^{p(e,j)} \left(\boldsymbol{e}'_{ij} \cdot \boldsymbol{e}'_2\right) \right] \end{array} \right),$$

and $ij(k=4)=23$, $ij(k=5)=13$, $ij(k=6)=12$. Expression (5.30) is used to compute operationally the 3×18 matrix $\boldsymbol{B}_b^{(e)}$ that relates plate bending generalized strains to the global degrees of freedom of the element $\mathcal{G}^{(e)}$:

$$\hat{\boldsymbol{\varepsilon}}_b' = \boldsymbol{B}_b^{(e)} \left\{ \mathcal{G}^{(e)} \right\}. \tag{5.31}$$

The 18×18 matrix that represents the plate bending contribution to the stiffness of the DKT-CST shell element is then:

$$\boldsymbol{K}_b^{(e)} = \int_A \left(\boldsymbol{B}_b^{(e)} \right)^T \hat{\boldsymbol{D}}_b \boldsymbol{B}_b^{(e)} \, dA,$$

while the elemental nodal forces vector is given by:

$$\boldsymbol{F}_b^{(e)} = \int_A \left(\boldsymbol{B}_b^{(e)} \right)^T \left(\int_{-\frac{h}{2}}^{\frac{h}{2}} z \left\{ \begin{array}{c} \sigma_{x'} \\ \sigma_{y'} \\ \tau_{x'y'} \end{array} \right\} dz \right) dA.$$

Since the integrals are calculated via a numerical quadrature, then the formulas to be implemented are:

$$\begin{aligned} \boldsymbol{K}_b^{(e)} &= \sum_{g=1}^{n_g} \left[\left(\boldsymbol{B}_b^{(e)} \left(\boldsymbol{\xi}_g \right) \right)^T \hat{\boldsymbol{D}}_b \boldsymbol{B}_b^{(e)} \left(\boldsymbol{\xi}_g \right) \right] W_g, \\ \boldsymbol{F}_b^{(e)} &= \sum_{g=1}^{n_g} \left(\boldsymbol{B}_b^{(e)} \left(\boldsymbol{\xi}_g \right) \right)^T \sum_{l=1}^{n_l} z_l \left\{ \begin{array}{c} \sigma_{x'} \left(z_l \right) \\ \sigma_{y'} \left(z_l \right) \\ \tau_{x'y'} \left(z_l \right) \end{array} \right\} H_l W_g. \end{aligned}$$

5.4.4 Coplanarity management

When dealing with flat shell elements with rotational degrees of freedom included at the corner nodes, special attention is needed for the management of coplanarity. Normally with each node three translations and three rotations are associated. In the most general case of a node which is connected to elements possessing mid-planes with different orientations in space, no special treatment is needed. Conversely, if the elements connected to a node are all coplanar or quasi-coplanar, then no stiffness or no appreciable stiffness is associated with the rotational degree of freedom around an axis normal to the coplanarity plane. This occurrence can lead to singularities of the global stiffness matrix. Such

problem has been circumvented in the past by omitting the rotational degree of freedom in the direction normal to the shell surface at each node. Even if this solution has been widely used [27], [112], [29], and for many commonly employed shell test problems the numerical performance is unaffected by this modification, Carpenter et al [23] have discovered serious difficulties with certain shell problems presenting nodes with quasi-complanarity as a result of omitting these rotations. Actually, in a finite element formulation simply omitting a degree of freedom is equivalent to constraining that degree of freedom; in some cases this constraint does not preserve stress-free rigid body motions as it is shown hereafter.

Let us suppose that the node 1 of a triangular element presents quasi-coplanarity and that the rotational reference frame in node 1 is defined so that its third vector $\boldsymbol{e}_3^{(\vartheta)1}$ coincides with the normal to the shell in node 1. If the degree of freedom ϑ_3^1, associated with such rotation about the normal to the shell $\boldsymbol{e}_3^{(\vartheta)1}$, is constrained then, as we are going to show, there is no global vector of degrees of freedom able to represent an infinitesimal rigid body rotation about an axis contained in the plane of the triangular element.

Let indeed $\boldsymbol{\vartheta}$ be the axial vector of such rotation with $\boldsymbol{\vartheta} = \vartheta_{x'}\,\boldsymbol{e}_1^{\prime(e)} + \vartheta_{y'}\,\boldsymbol{e}_2^{\prime(e)}$ and let node 1 be fixed. The vector $\boldsymbol{u}^{\vartheta 1}$ of local displacements of the element associated with such kinematics is:

$$\boldsymbol{u}^{\vartheta 1} = \left\{ \begin{array}{c} (0,0,0)\,,\left(\vartheta_{x'},\vartheta_{y'},0\right) \\ \left(0,0,A_1^{12}\vartheta_{x'} + A_2^{12}\vartheta_{y'}\right),\left(\vartheta_{x'},\vartheta_{y'},0\right) \\ \left(0,0,A_1^{13}\vartheta_{x'} + A_2^{13}\vartheta_{y'}\right),\left(\vartheta_{x'},\vartheta_{y'},0\right) \end{array} \right\},$$

with:

$$\mathbf{A}^1 = \left[\begin{array}{cc} A_1^{12} & A_2^{12} \\ A_1^{13} & A_2^{13} \end{array} \right] = \left[\begin{array}{cc} \boldsymbol{e}_1' \times \left(\boldsymbol{x}^2 - \boldsymbol{x}^1\right) \cdot \boldsymbol{e}_3' & \boldsymbol{e}_2' \times \left(\boldsymbol{x}^2 - \boldsymbol{x}^1\right) \cdot \boldsymbol{e}_3' \\ \boldsymbol{e}_1' \times \left(\boldsymbol{x}^3 - \boldsymbol{x}^1\right) \cdot \boldsymbol{e}_3' & \boldsymbol{e}_2' \times \left(\boldsymbol{x}^3 - \boldsymbol{x}^1\right) \cdot \boldsymbol{e}_3' \end{array} \right].$$

Hence:

$$\left[\begin{array}{c} w\prime^{(2)} \\ w\prime^{(3)} \end{array} \right] = \mathbf{A}^1 \left[\begin{array}{c} \vartheta_{x'} \\ \vartheta_{y'} \end{array} \right]. \tag{5.32}$$

The 18×18 matrix transforming the 18 local degrees of freedom of the DKT

element into the corresponding 18 global degrees of freedom is:

$$\mathbb{P} = \begin{bmatrix} \mathbb{R}_1 & \mathbf{0}_{6\times6} & \mathbf{0}_{6\times6} \\ \mathbf{0}_{6\times6} & \mathbb{R}_2 & \mathbf{0}_{6\times6} \\ \mathbf{0}_{6\times6} & \mathbf{0}_{6\times6} & \mathbb{R}_3 \end{bmatrix},$$

where $\mathbf{0}_{l\times m}$ is a $l \times m$ zero matrix and:

$$\mathbb{R}_k = \begin{bmatrix} \begin{bmatrix} \boldsymbol{e}_1\cdot\boldsymbol{e}'_1 & \boldsymbol{e}_1\cdot\boldsymbol{e}'_2 & \boldsymbol{e}_1\cdot\boldsymbol{e}'_3 \\ \boldsymbol{e}_2\cdot\boldsymbol{e}'_1 & \boldsymbol{e}_2\cdot\boldsymbol{e}'_2 & \boldsymbol{e}_2\cdot\boldsymbol{e}'_3 \\ \boldsymbol{e}_3\cdot\boldsymbol{e}'_1 & \boldsymbol{e}_3\cdot\boldsymbol{e}'_2 & \boldsymbol{e}_3\cdot\boldsymbol{e}'_3 \end{bmatrix} & \mathbf{0}_{3\times3} \\ \mathbf{0}_{3\times3} & \begin{bmatrix} \boldsymbol{e}_1^{(\vartheta)k}\cdot\boldsymbol{e}'_1 & \boldsymbol{e}_1^{(\vartheta)k}\cdot\boldsymbol{e}'_2 & \boldsymbol{e}_1^{(\vartheta)k}\cdot\boldsymbol{e}'_3 \\ \boldsymbol{e}_2^{(\vartheta)k}\cdot\boldsymbol{e}'_1 & \boldsymbol{e}_2^{(\vartheta)k}\cdot\boldsymbol{e}'_2 & \boldsymbol{e}_2^{(\vartheta)k}\cdot\boldsymbol{e}'_3 \\ \boldsymbol{e}_3^{(\vartheta)k}\cdot\boldsymbol{e}'_1 & \boldsymbol{e}_3^{(\vartheta)k}\cdot\boldsymbol{e}'_2 & \boldsymbol{e}_3^{(\vartheta)k}\cdot\boldsymbol{e}'_3 \end{bmatrix} \end{bmatrix}.$$

Therefore, the vector $\boldsymbol{u}^{\vartheta 1}$ in global coordinates is represented by the vector $\boldsymbol{u}^{\vartheta 1G}$:

$$\boldsymbol{u}^{\vartheta 1G} = \mathbb{P}\boldsymbol{u}^{\vartheta_{x'}},$$

which explicitly andcomponentwise is written:

$$\boldsymbol{u}^{\vartheta 1G} = \left\{ \begin{array}{l} \left[\begin{pmatrix} 0 \\ 0 \\ 0 \end{pmatrix}, \begin{pmatrix} \vartheta_{x'}\left(\boldsymbol{e}_1^{(\vartheta)1}\cdot\boldsymbol{e}'_1\right)+\vartheta_{y'}\left(\boldsymbol{e}_1^{(\vartheta)1}\cdot\boldsymbol{e}'_2\right) \\ \vartheta_{x'}\left(\boldsymbol{e}_2^{(\vartheta)1}\cdot\boldsymbol{e}'_1\right)+\vartheta_{y'}\left(\boldsymbol{e}_2^{(\vartheta)1}\cdot\boldsymbol{e}'_2\right) \\ \vartheta_{x'}\left(\boldsymbol{e}_3^{(\vartheta)1}\cdot\boldsymbol{e}'_1\right)+\vartheta_{y'}\left(\boldsymbol{e}_3^{(\vartheta)1}\cdot\boldsymbol{e}'_2\right) \end{pmatrix} \right] \\ \left[\begin{pmatrix} \left(A_1^{12}\vartheta_{x'}+A_2^{12}\vartheta_{y'}\right)\left(\boldsymbol{e}_1\cdot\boldsymbol{e}'_3\right) \\ \left(A_1^{12}\vartheta_{x'}+A_2^{12}\vartheta_{y'}\right)\left(\boldsymbol{e}_2\cdot\boldsymbol{e}'_3\right) \\ \left(A_1^{12}\vartheta_{x'}+A_2^{12}\vartheta_{y'}\right)\left(\boldsymbol{e}_3\cdot\boldsymbol{e}'_3\right) \end{pmatrix}, \begin{pmatrix} \vartheta_{x'}\left(\boldsymbol{e}_1^{(\vartheta)2}\cdot\boldsymbol{e}'_1\right)+\vartheta_{y'}\left(\boldsymbol{e}_1^{(\vartheta)2}\cdot\boldsymbol{e}'_2\right) \\ \vartheta_{x'}\left(\boldsymbol{e}_2^{(\vartheta)2}\cdot\boldsymbol{e}'_1\right)+\vartheta_{y'}\left(\boldsymbol{e}_2^{(\vartheta)2}\cdot\boldsymbol{e}'_2\right) \\ \vartheta_{x'}\left(\boldsymbol{e}_3^{(\vartheta)2}\cdot\boldsymbol{e}'_1\right)+\vartheta_{y'}\left(\boldsymbol{e}_3^{(\vartheta)2}\cdot\boldsymbol{e}'_2\right) \end{pmatrix} \right] \\ \left[\begin{pmatrix} \left(A_1^{13}\vartheta_{x'}+A_2^{13}\vartheta_{y'}\right)\left(\boldsymbol{e}_1\cdot\boldsymbol{e}'_3\right) \\ \left(A_1^{13}\vartheta_{x'}+A_2^{13}\vartheta_{y'}\right)\left(\boldsymbol{e}_2\cdot\boldsymbol{e}'_3\right) \\ \left(A_1^{13}\vartheta_{x'}+A_2^{13}\vartheta_{y'}\right)\left(\boldsymbol{e}_3\cdot\boldsymbol{e}'_3\right) \end{pmatrix}, \begin{pmatrix} \vartheta_{x'}\left(\boldsymbol{e}_1^{(\vartheta)3}\cdot\boldsymbol{e}'_1\right)+\vartheta_{y'}\left(\boldsymbol{e}_1^{(\vartheta)3}\cdot\boldsymbol{e}'_2\right) \\ \vartheta_{x'}\left(\boldsymbol{e}_2^{(\vartheta)3}\cdot\boldsymbol{e}'_1\right)+\vartheta_{y'}\left(\boldsymbol{e}_2^{(\vartheta)3}\cdot\boldsymbol{e}'_2\right) \\ \vartheta_{x'}\left(\boldsymbol{e}_3^{(\vartheta)3}\cdot\boldsymbol{e}'_1\right)+\vartheta_{y'}\left(\boldsymbol{e}_3^{(\vartheta)3}\cdot\boldsymbol{e}'_2\right) \end{pmatrix} \right] \end{array} \right. \tag{5.33}$$

Constraining the rotation about the normal to the shell $\boldsymbol{e}_3^{(\vartheta)1}$ corresponds to setting the sixth term in vector (5.33) to zero:

$$\vartheta_3^{1G} = \vartheta_{x'}\left(\boldsymbol{e}_3^{(\vartheta)1}\cdot\boldsymbol{e}_1'\right) + \vartheta_{y'}\left(\boldsymbol{e}_3^{(\vartheta)1}\cdot\boldsymbol{e}_2'\right) := 0. \tag{5.34}$$

This operation impedes the representation of the aforementioned rigid body rotations. Carpenter et al. [23] suggest a modified relation $\mathbb{P}^*$ between local and global coordinates to avoid this problem, which preserves the possibility of representing of this class of rotations. The relation between the gradient of the deflection, expressed in local coordinates, in the first corner node given by (5.29) is modified in order to include the contribute due to ϑ_1^{3G}:

$$\left\{\begin{array}{c} w\prime_{,x'}^{(1)} \\ w\prime_{,y'}^{(1)} \end{array}\right\} = \left\{\begin{array}{c} -\sum\limits_{j=1}^{2}\left(\boldsymbol{e}_j^{(\vartheta)1}\cdot\boldsymbol{e}_2'\right)\vartheta_j^1 - \left(\boldsymbol{e}_3^{(\vartheta)1}\cdot\boldsymbol{e}_2'\right)\vartheta_3^{1G} \\ \sum\limits_{j=1}^{2}\left(\boldsymbol{e}_j^{(\vartheta)1}\cdot\boldsymbol{e}_1'\right)\vartheta_j^1 + \left(\boldsymbol{e}_3^{(\vartheta)1}\cdot\boldsymbol{e}_1'\right)\vartheta_3^{1G} \end{array}\right\}, \tag{5.35}$$

where ϑ_3^{1G} has to be associated to the rigid rotation corresponding to the global translational displacements of the element nodes. From (5.34) and (5.32) one obtains:

$$\vartheta_3^{1G} = \left[\begin{array}{cc} \left(\boldsymbol{e}_3^{(\vartheta)1}\cdot\boldsymbol{e}_1'\right) & \left(\boldsymbol{e}_3^{(\vartheta)1}\cdot\boldsymbol{e}_2'\right) \end{array}\right]\left(\mathbf{A}^1\right)^{-1}\left[\begin{array}{c} w\prime^{(2)} \\ w\prime^{(3)} \end{array}\right]. \tag{5.36}$$

$w\prime^{(2)}$ and $w\prime^{(3)}$ are also related to the global displacements:

$$\left[\begin{array}{c} w\prime^{(2)} \\ w\prime^{(3)} \end{array}\right] = \left[\begin{array}{c} \sum\limits_{i=1}^{3}\left(\boldsymbol{e}_i^2\cdot\boldsymbol{e}_3'\right)u_i^{(2)} \\ \sum\limits_{i=1}^{3}\left(\boldsymbol{e}_i^3\cdot\boldsymbol{e}_3'\right)u_i^{(3)} \end{array}\right]. \tag{5.37}$$

The combined use of (5.35), (5.36) and (5.37) provides the relation:

$$\begin{aligned} w\prime_{,x'}^{(1)} \;=\; & -\sum_{j=1}^{2}\left(\boldsymbol{e}_j^{(\vartheta)1}\cdot\boldsymbol{e}_2'\right)\vartheta_j^1 \\ & -\left(\boldsymbol{e}_3^{(\vartheta)1}\cdot\boldsymbol{e}_2'\right)\left[\sum_{l=1}^{2}\sum_{k=2,3}\left(\boldsymbol{e}_3^{(\vartheta)1}\cdot\boldsymbol{e}_l'\right)\left[\left(\mathbf{A}^1\right)^{-1}\right]_{lk}\sum_{i=1}^{3}\left(\boldsymbol{e}_i^k\cdot\boldsymbol{e}_3'\right)u_i^{(2)}\right]. \end{aligned} \tag{5.38}$$

$$w\prime^{(1)}_{,y'} = \sum_{j=1}^{2} \left(\boldsymbol{e}_j^{(\vartheta)1} \cdot \boldsymbol{e}'_1 \right) \vartheta_j^1 + \left(\boldsymbol{e}_3^{(\vartheta)1} \cdot \boldsymbol{e}'_1 \right) \left[\sum_{l=1}^{2} \sum_{k=2,3} \left(\boldsymbol{e}_3^{(\vartheta)1} \cdot \boldsymbol{e}'_l \right) \left[\left(\mathbf{A}^1 \right)^{-1} \right]_{lk} \sum_{i=1}^{3} \left(\boldsymbol{e}_i^k \cdot \boldsymbol{e}'_3 \right) u_i^{(3)} \right]. \tag{5.39}$$

Relation (5.38) and (5.39) are trivially extended to the remaining nodes with indexes 2 and 3 by cyclic permutation of the nodal indexes.

5.4.5 Numerical validations of the DKT-CST element

In view of the following applications, the DKT-CST shell element with the formulation detailed in the previous sections has been added in the element library of COMET FEM code [28] and thoroughly validated against the related benchmark tests present in literature in order to assess its correct implementation. A preliminary set of benchmark tests has been selected in order to validate membrane and bending behaviors separately; subsequently, test cases in which both behaviors are coupled have been considered.

The tests considered are:

- 1) Validations for the assessment of membrane behavior in plane geometry:
  - a) Plane cantilever subjected to a parabolic load
    - i) 1x4 cross mesh
    - ii) 2x8 cross mesh
    - iii) 4x16 cross mesh
- 2) Validations for the assessment of plate bending behavior in plane geometry
  - a) Patch tests
    - i) Translation orthogonal to the element plane
    - ii) Rotation about the fist side of the element
  - b) Cantilever beam subjected to a concentrated load oriented in the thickness direction at the free end

        * i) 1x4 cross mesh
        * ii) 2x8 cross mesh
        * iii) 4x16 cross mesh
        * iv) 8x32 cross mesh
        * v) 16x64 cross mesh
    - c) Uniformly loaded simply-supported square plate
        * i) 200 elements mesh
        * ii) 800 elements mesh
    - d) Simply supported square plate subjected to a central concentrated load
        * i) 800 elements mesh
        * ii) 1600 elements mesh
        * iii) 6400 elements mesh

- 3) Validation of the bending behavior in non-planar geometry
    - a) Slit cylinder bending
        * i) 16 elements mesh
        * ii) 32 elements mesh
        * iii) 48 elements mesh

- 4) Validations of the coupled membrane-bending behavior
    - a) Pinched cylinder
        * i) 64 elements mesh
        * ii) 1024 elements mesh
        * iii) 6400 elements mesh
        * iv) 4608 cross elements mesh
    - b) Scordelis-Lo roof
        * i) 8 elements mesh
        * ii) 32 elements mesh
        * iii) 800 elements mesh

5.4.6 Validations for the assessment of membrane behavior in plane geometry

Plane cantilever subjected to a parabolic load

Geometry and mechanical data:

This test consists in a cantilever beam subjected to a parabolic load at the free end, as shown in figure 5.1. The cantilever experiments a plane stress state and only the membrane stiffness is activated in the shell elements. The objective of the test is the validation of the correct membrane behaviour of the shell element.

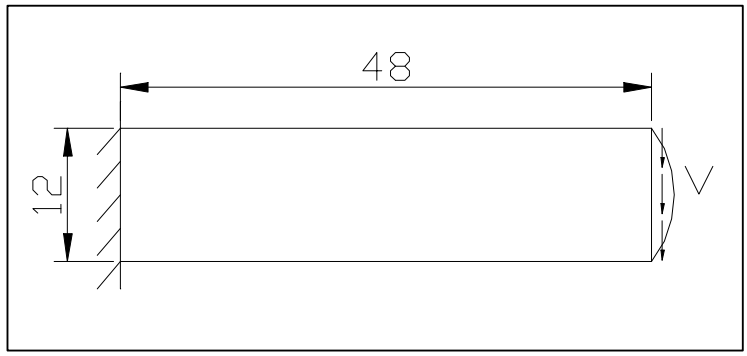

Figure 5.1: Plane stress cantilever subjected to a parabolic load at the free end - geometry and boundary conditions. Further data: Young modulus $E = 30000$, thickness $h = 0.01$, Poisson ratio $\nu = 0.25$, load $V = 40$.

Mesh details:

Structured meshes of $1 \times 4 \times 4$, $2 \times 8 \times 4$ and $4 \times 16 \times 4$ elements have been employed, with a total number of elements respectively of respectively 16, 64 and 256 elements. In figure 5.2 a frontal view of the $4 \times 16 \times 4$ mesh is reported.

Comparison of numerical results with known analytical solutions:

The maximum deflection calculated as the sum of the bending displacement (provided by the unidimensional Euler-Bernoully scheme of beam clamped at one end) and of the shear displacement is 0.3573. Carpenter [23] provides the value 0.3558. This is a more precise analytical solution which accounts also for the parabolic shape of the load at the free end. The relative error vs. the number of elements is plotted in figure 5.3 with the numerical values also reported in table 5.1.

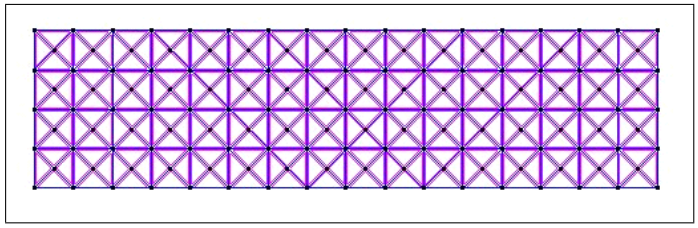

Figure 5.2: Frontal view of the $4 \times 16 \times 4$ mesh employed for the plane-stress cantilever beam.

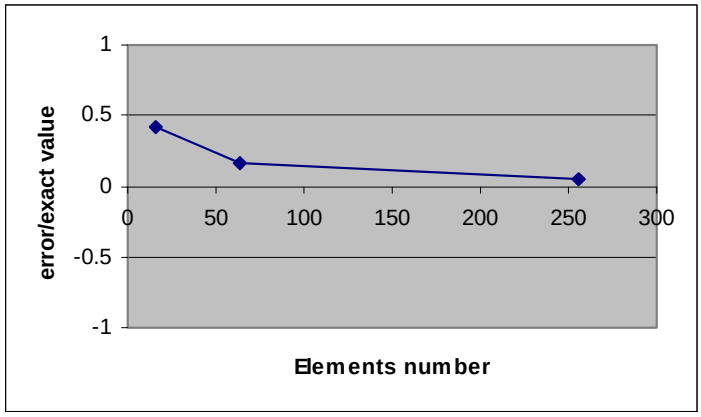

Figure 5.3: - Relative error vs. number of elements curve for the plane-stress cantilever beam -

5.4.7 Validations for the assessment of plate-bending behavior in plane geometry

Patch tests

Two patch tests were performed to assess the correct response of the shell element in presence of rigid displacements. In both tests all the dofs of the element

Mesh	$1 \times 4 \times 4$	$2 \times 8 \times 4$	$4 \times 16 \times 4$
Relative error	0.419	0.1613	0.0464

Table 5.1: Number of elements and corresponding relative error in the analysis of a plane cantilever subjected to a parabolic load.

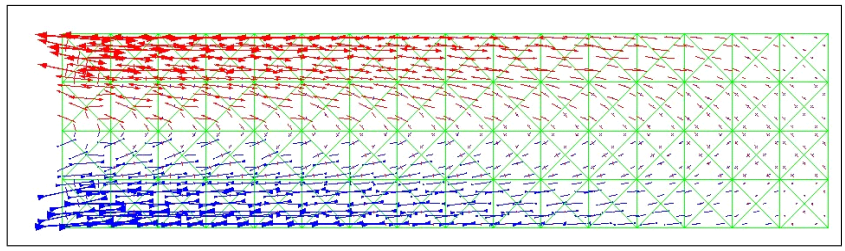

Figure 5.4: Principal membrane stresses in the plane stress cantilever.

are constrained. The first patch test consists in the enforcement of unit displacements in the transverse direction at the three nodes (see figure 5.5). In the second test rotations and displacements corresponding to a rigid rotation about an edge of the element are enforced, as shown in figure 5.6. From both tests no nodal force emerges, as expected.

Cantilever subjected to a concentrated load oriented in thickness direction

Geometry and mechanical data:

In this analysis bending behavior is tested by subjecting a cantilever beam to a concentrated load at the free end, as shown in figure 5.7. The maximum deflection is compared with the value calculated with the Euler-Bernoulli beam model. The cantilever experiments a plane stress.

Mesh details:

Structured meshes of $1 \times 4 \times 4$, $2 \times 8 \times 4$, $4 \times 16 \times 4$, $8 \times 32 \times 4$ and $16 \times 64 \times 4$ elements have been employed, with a total number of elements respectively of

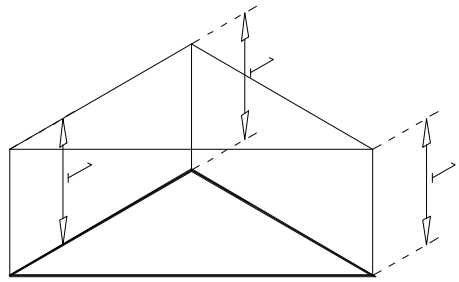

Figure 5.5: Nodal displacements enforced in the rigid translation patch test.

16, 64, 256, 1024 and 4096 elements. In figure 5.2 a view of the $4 \times 16 \times 4$ mesh is reported.

Comparison of numerical results with known analytical solutions:

The maximum deflection at the free end provided by the unidimensional beam model is:

$$w = \frac{Fl^3}{3EI} = \frac{40 \cdot 48^3 \cdot 12}{3 \cdot 30000 \cdot 1^3} = 49.152.$$

The contribution due to shear deformation is neglected since the thickness of the beam is very small. In figure 5.9 the error vs. number of elements curve is reported. Refining the mesh the maximum displacement converges towards the smaller value of 48.32. This is due to the fact that the FEM analysis with the DKT element is capable of catching in proximity of the fully displacement constrained zone a non-planar stress state. This effect is due to the horizontal constraint that impedes the contraction required by Poisson effect and determines a stiffer behaviour of the beam. When the Poisson ratio was set equal to zero the exact value provided by the bending beam theory was recovered.

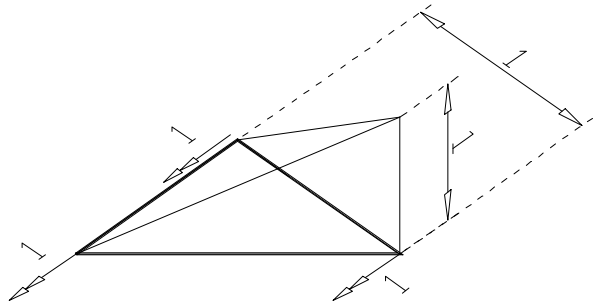

Figure 5.6: Nodal displacements enforced at the nodes in the rigid rotation patch test.

Uniformly loaded simply supported square plate

Geometry and mechanical data:

In this test the maximum central deflection of the simply supported square plate subject to uniform transversal load showed in fig.5.11 is compared with the value provided by Timoshenko.

Mesh details:

Two regular meshes of 200 ($10 \times 10 \times 2$) and 800 ($20 \times 20 \times 2$) elements were employed for one quarter of the plate. In fig.5.12 a view of the second mesh is shown.

Comparison of numerical results with known analytical solutions:

The maximum deflection obtained in the centre is given by [121]:

$$w = 0.00406\frac{qa^4}{D} = 0.00406\frac{120^4}{2666.66} = 0.2436.$$

The DKT analysis is in good agreement with such value. The values obtained are 0.2435 for the coarser mesh and 0.2437 with the 800 elements mesh.

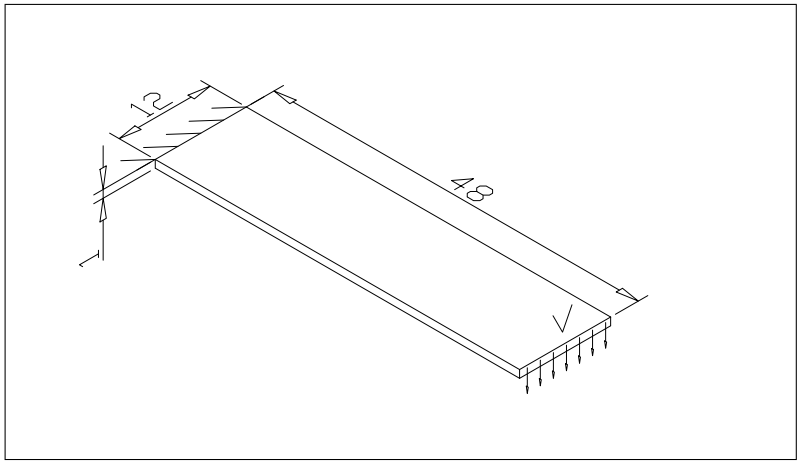

Figure 5.7: Cantilever subjected to a concentrated load at the free end in thickness direction - geometry and boundary conditions. Further data: Young modulus $E = 30000$, thickness $h = 0.01$, Poisson ratio $\nu = 0.25$, load $V = 40$.

Simply supported square plate subject to a central concentrated load

Geometry and mechanical data:

In this test the maximum central deflection of the simply supported square plate subject to a central concentrated load showed in fig.5.14 is compared with the value provided in [121].

Mesh details:

Three regular meshes of 800 ($20 \times 20 \times 2$), 1600 ($20 \times 20 \times 4$) and 6400 ($40 \times 40 \times 4$) elements were employed to model one quarter of the plate.

Comparison of numerical results with known analytical solutions:

The maximum deflection provided by [121] is given by:

$$w = 0.001160\frac{Pa^2}{D} = 0.001160\frac{1000 \cdot 20^2}{2666.66} = 1.74004.$$

The DKT analysis with 1600 elements provides 1.7403, in perfect agreement with the previous value.

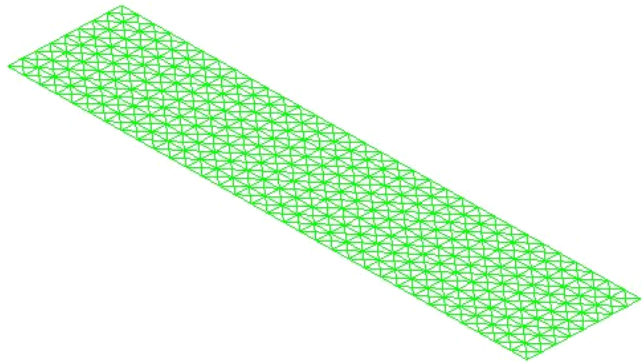

Figure 5.8: View of the $8 \times 32 \times 4$ mesh employed for the cantilever beam loaded in the thickness direction.

5.4.8 Validations for the assessment of bending behavior in non-planar geometry

Slit cylinder bending

Geometry and mechanical data:

This test is specifically devised to validate the behaviour of the shell element in presence of a non-planar geometry of the shell. The test consists in applying to the open ring of fig.5.16 a torsion moment in the free side of the horizontal cut. In the other side full constraints are enforced.The circular edges of the cylinder are constrained such as to grant plane strain.

Mesh details:

Three cross-hatch regular meshes of 16, 32 (see fig.5.17) and 48 elements were employed.

Comparison of numerical results with known analytical solutions:

The analytical values of the maximum tangential displacement and the rotation are given by:

$$V = 2\pi R^2 \frac{M}{D}, \qquad \theta = 2\pi R \frac{M}{D}.$$

The ratio between the displacement obtained with the 16 elements mesh and the analytical value is 0.974, while the same ratio for the 32 elements mesh is 0.994.

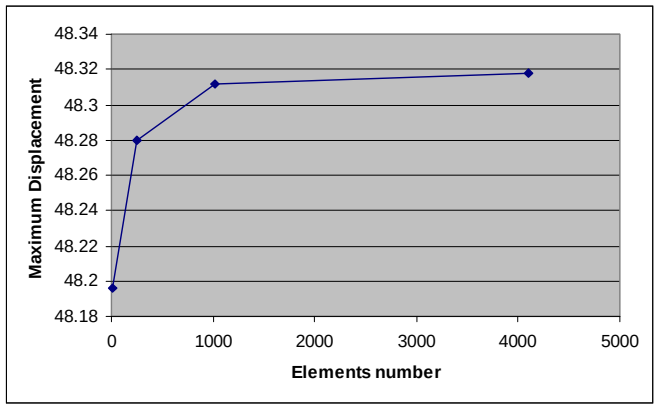

Figure 5.9: Relative error vs. number of elements curve for the plate-bending cantilever beam.

5.4.9 Coupled membrane-bending validations in non-planar geometry

Pinched cylinder

Geometry and mechanical data:

A cylinder is subject to two equilibrated radial forces applied in opposite point of the central diameter. Along the two circular edges a rigid diaphragm constraint is applied that prevents displacements normal to the cylinder axis. This test is specifically devised to validate the behaviour of the shell element in presence of a non-plane geometry of the shell.

Mesh details:

Three regular meshes of 64, 1024 and 6400 cross hatch elements and one mesh of 4608 cross diagonal elements were employed.

Comparison of numerical results with known analytical solutions:

The exact value of radial relative displacement along load direction is 1.8248×10^{-5} [34]. In the following table the numerical results obtained with the DKT element are resumed:

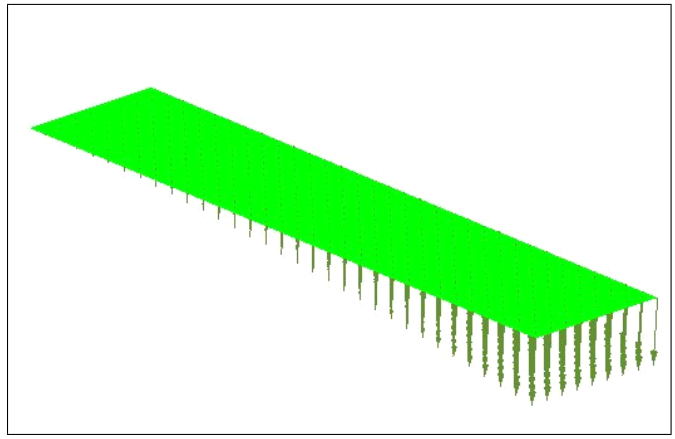

Figure 5.10: Displacement field of the plate bending cantilever beam, reported as vectors applied at the nodal points.

N° of elements	Displacement	Relative error
64	$1.052 \cdot 10^{-6}$	0.943
1024	$1.566 \cdot 10^{-5}$	0.14
4608 (cross diagonal)	$1.6058 \cdot 10^{-5}$	0.12
6400	$1.812 \cdot 10^{-5}$	0.01

Scordelis-Lo roof

Geometry and mechanical data:

This cylindrical shell, shown in fig.5.21, is subject to self dead weight and at the two curve edges only displacement parallel to the axis are allowed.

Mesh details:

Regular cross diagonal meshes of 8, 32 and 800 elements have been employed

Comparison of numerical results with known analytical solutions:

The deflection of the midpoint of the free border is considered to compare the solutions. The deflection provided by [64] is equal to 0.3024. In the following table the numerical results obtained with the DKT element are resumed:

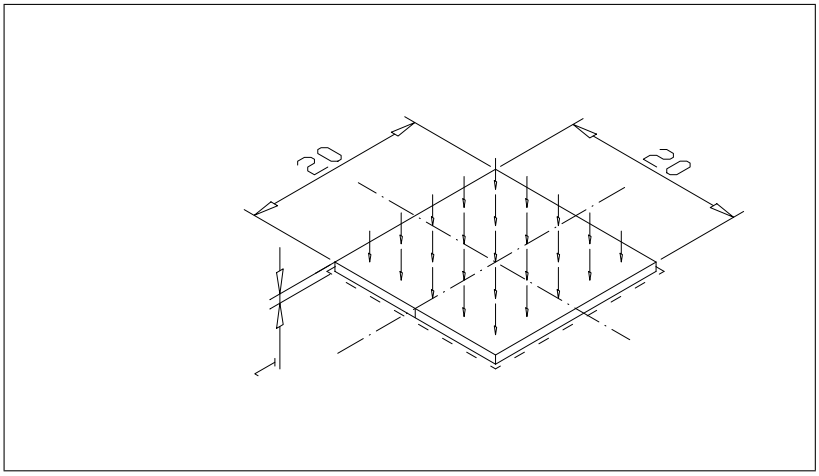

Figure 5.11: Uniformly loaded simply supported square plate - geometry and boundary conditions. Further data: Young modulus $E = 30000$, thickness $h = 1.0$, Poisson ratio $\nu = 0.25$, span load $q = 1$.

elements N°	Displacement	Relative error
8	0.2580	0.853
32	0.2119	0.700
800	0.2929	0.968

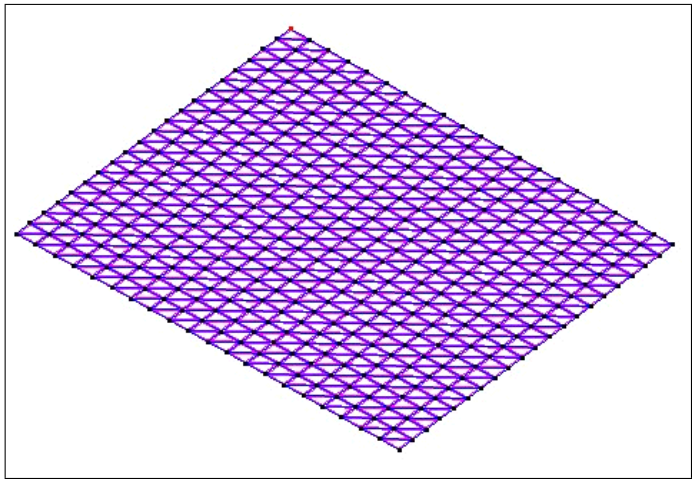

Figure 5.12: - View of the $20 \times 20 \times 2$ mesh employed for the uniformly loaded simply supported square plate -

5.5 The laminated DKT-CST element

In the equivalent single layer laminated shell theories the 3D continuum problem is reduced to a 2D problem by treating the eterogeneous laminated plate as a statically equivalent single shell having a complex constitutive behaviour. Irrespective of the homogeneity or heterogeneity of the shell, in these theories the displacement field $\boldsymbol{u}$ is characterized by the following representation:

$$\boldsymbol{u}(\xi,\eta,\zeta) = \sum_{j=1}^{N} \phi_j(\zeta)\boldsymbol{\varphi}_j(\xi,\eta), \tag{5.40}$$

where ξ and η are the coordinates of the parametric representation of the mid surface, ζ is the thickness coordinate and the vectorial functions $\boldsymbol{\varphi}_j(\xi,\eta)$ have to be regarded as the independent fields while the through-thickness scalar functions $\phi_j(\zeta)$ depend on the specific ESL shell theory selected. Representation (5.40) produces a great simplification when calculating the terms of the variational formulation that governs the mechanics since the functions $H(\zeta,\xi,\eta)$ that have to be integrated admit the following decomposition:

$$H(\xi,\eta,\zeta) = F(\zeta)G(\xi,\eta).$$

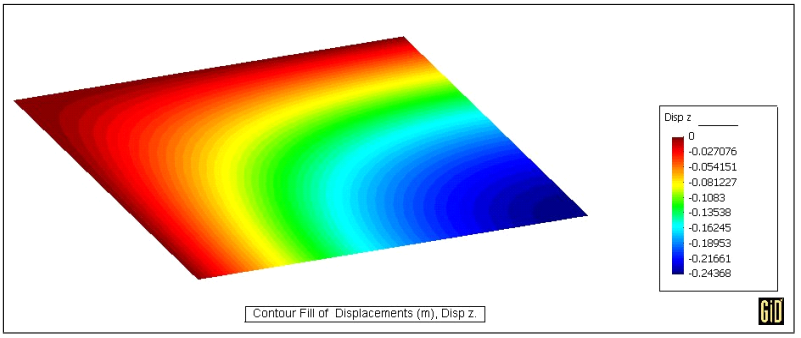

Figure 5.13: - Displacement contour fill diagram for one quarter of the uniformly loaded simply supported square plate -

Accordingly the integrals appearing in the variational formulation can be written in the form:

$$\int_V F(\zeta)G(\xi,\eta)\,dV = \int_{-\frac{h}{2}}^{\frac{h}{2}} F(\zeta)\left[\int_A G(\xi,\eta)\,dA\right]\,d\zeta. \tag{5.41}$$

For homogeneous shells and linear constitutive laws the simplification is even stronger since the integration through the thickness of the term $\int_{-\frac{h}{2}}^{\frac{h}{2}} F(\zeta)\,dz$ can be performed analitically. In case of a laminated shell this simplification is no longer admitted and the integration through the thickness has to account for the presence of the stack sequence of lamination and the integration has to be performed layerwise.

On account of the previous considerations, the simple ESL extension of the homogeneous DKT-CST element detailed in the previous sections to laminated structures requires only the redefinition of the step represented by (5.41). As a consequence, a first important difference with the homogeneous theory is that coupling between membrane and bending behaviours, even in presence of a flat shape, can not be excluded a priori. Therefore, in the expression of elastic energy membrane and bending strains have to be considered at the same time.

Overall in-plane strains $\boldsymbol{\varepsilon}'$ are related to generalized membrane and plate

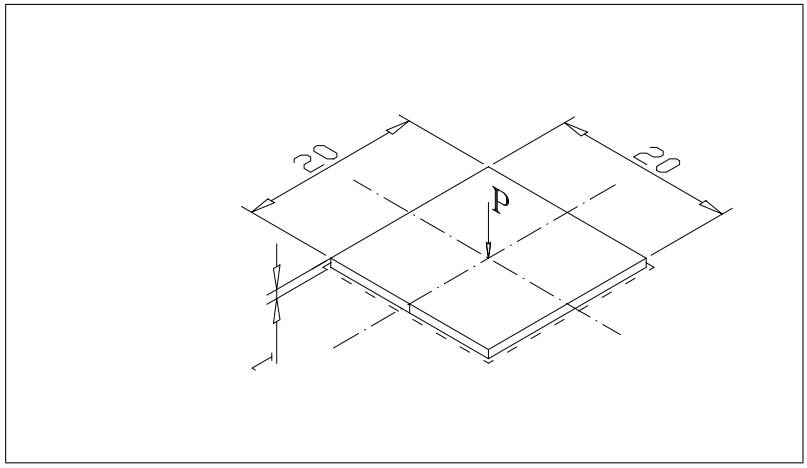

Figure 5.14: Simply supported square plate subject to a central concentrated load - geometry and boundary conditions. Further data: Young modulus $E = 30000$, thickness $h = 1.0$, Poisson ratio $\nu = 0.25$, point load $P = 1000$.

bending strain vectors by:

$$\boldsymbol{\varepsilon}'(z) = \boldsymbol{\varepsilon}'_m + z\hat{\boldsymbol{\varepsilon}}'_b.$$

The stacked structure, composed of N_L layer, is accounted by an array of contiguous intervals $]z_l, z_{l+1}[$, with $z_1 = -\frac{h}{2}$ and $z_{N_L} = \frac{h}{2}$. For each layer the associated constitutive law that depends on the specific fibers orientation angle θ_l and on the material has to be considered.

The satisfaction of the plane-stress hypothesis for the laminate in the linear elastic case can be achieved by using a reduced plane-stress elastic tensor obtained by condensation from the 3D elastic operator, analogously to what is done in the isotropic case to obtain the stiffness operator of equation (5.6). In a non-linear case an accurate step-size-independent satisfaction of the plane-stress assumption requires the development of a specific plane-stress reduced form of the BSP and ESP models proposed in chapter 3. This is not a simple task and is left outside the scope of this thesis. Instead, a condensation of the 3D tangent operator, based on the plane-stress assumption in rate form (i.e. $(\dot{\sigma}_{z'})_l = 0$), is used here. By making also use of the Kirchhoff hypothesis $(\gamma_{x'z'})_l = \left(\gamma_{y'z'}\right)_l = 0$ this condensation procedure leads the following reduced expression for the material

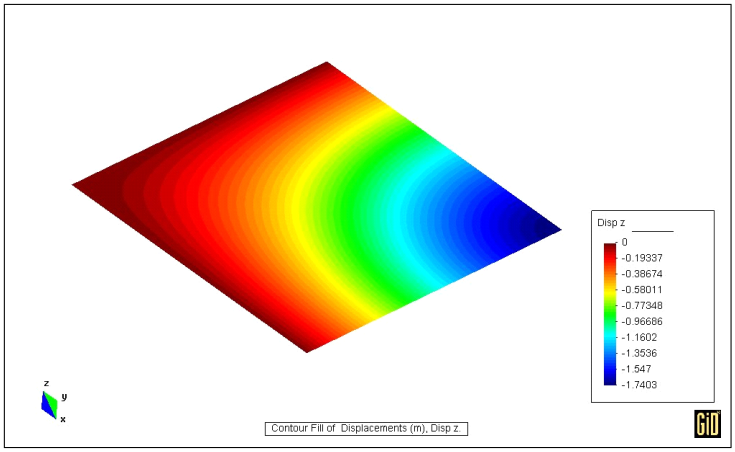

Figure 5.15: Displacement contour fill diagram for one quarter of the simply supported square plate subject to a central concentrated load.

tangent operator in the layer l:

$$\boldsymbol{D}_l = \begin{bmatrix} C_{11} & C_{12} & C_{13} \\ C_{21} & C_{22} & C_{23} \\ C_{31} & C_{32} & C_{33} \end{bmatrix} - \frac{1}{C_{44}} \begin{bmatrix} C_{14}C_{41} & C_{14}C_{42} & C_{14}C_{43} \\ C_{24}C_{41} & C_{24}C_{42} & C_{24}C_{43} \\ C_{34}C_{41} & C_{34}C_{42} & C_{34}C_{43} \end{bmatrix}.$$

This procedure has proved to give accurate results by simply avoiding the use of exceedingly large step sizes. Accordingly, the quadratic form of energy based on the above mentioned expression of the material tangent operator is:

$$\begin{aligned} U_t &= \frac{1}{2}\int_A \sum_{l=1}^{N_L} \left[\int_{z_l}^{z_{l+1}} \left(\boldsymbol{\varepsilon}'_m + z\hat{\boldsymbol{\varepsilon}}'_b\right)^T \boldsymbol{D}_l \left(\boldsymbol{\varepsilon}'_m + z\hat{\boldsymbol{\varepsilon}}'_b\right) dz \right] dA = \qquad (5.42) \\ &= \frac{1}{2}\int_A \sum_{l=1}^{N_L} \left[\int_{z_l}^{z_{l+1}} \left(\boldsymbol{\varepsilon}'_m\right)^T \boldsymbol{D}_l \boldsymbol{\varepsilon}'_m \, dz \right] dA + \frac{1}{2}\int_A \sum_{l=1}^{N_L} \left[\int_{z_l}^{z_{l+1}} z \left(\hat{\boldsymbol{\varepsilon}}'_b\right)^T \boldsymbol{D}_l \boldsymbol{\varepsilon}'_m \, dz \right] dA + \\ &\quad + \frac{1}{2}\int_A \sum_{l=1}^{N_L} \left[\int_{z_l}^{z_{l+1}} z \left(\boldsymbol{\varepsilon}'_m\right)^T \boldsymbol{D}_l \hat{\boldsymbol{\varepsilon}}'_b \, dz \right] dA + \frac{1}{2}\int_A \sum_{l=1}^{N_L} \left[\int_{z_l}^{z_{l+1}} z^2 \left(\hat{\boldsymbol{\varepsilon}}'_b\right)^T \boldsymbol{D}_l \hat{\boldsymbol{\varepsilon}}'_b \, dz \right] dA. \end{aligned}$$

Performing the integrals through the thickness via a numerical quadrature with

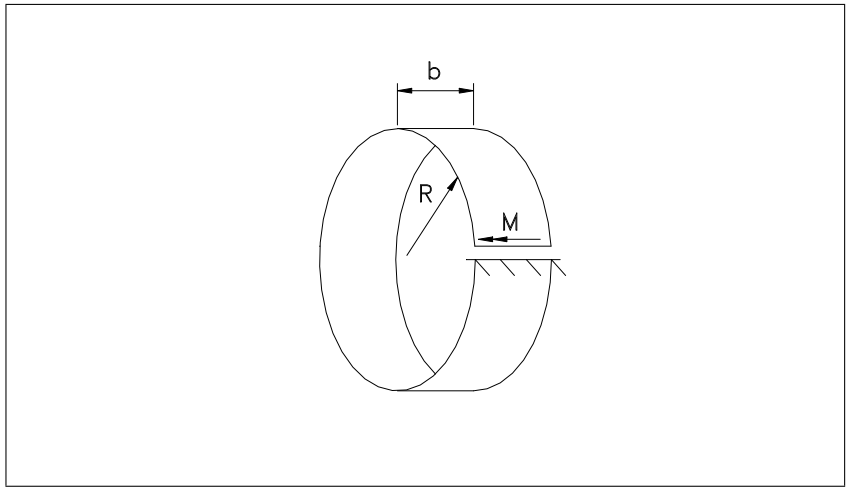

Figure 5.16: Slit cylinder bending - geometry and boundary conditions. Further data: Young modulus $E = 30000$, width $b = 2\pi R/N$, Poisson ratio $\nu = 0.30$, moment $M = 1.00$, thickness $h = 0.01$, radius $R = 100$.

one gauss point for layer one obtains:

$$\begin{aligned} U_t &= \frac{1}{2}\int_A \left[\sum_{l=1}^{N_L} h_l \left(\boldsymbol{\varepsilon}'_m\right)^T \boldsymbol{D}_l \boldsymbol{\varepsilon}'_m\right] dA + \frac{1}{2}\int_A \left[\sum_{l=1}^{N_L} h_l z_l^* \left(\hat{\boldsymbol{\varepsilon}}'_b\right)^T \boldsymbol{D}_l \boldsymbol{\varepsilon}'_m\right] dA \\ &+ \frac{1}{2}\int_A \left[\sum_{l=1}^{N_L} h_l z_l^* \left(\boldsymbol{\varepsilon}'_m\right)^T \boldsymbol{D}_l \hat{\boldsymbol{\varepsilon}}'_b\right] dA + \frac{1}{2}\int_A \left[\sum_{l=1}^{N_L} h_l z_l^{*2} \left(\hat{\boldsymbol{\varepsilon}}'_b\right)^T \boldsymbol{D}_l \hat{\boldsymbol{\varepsilon}}'_b\right] dA, \end{aligned} \tag{5.43}$$

where $h_l = \dfrac{z_{l+1} - z_l}{2}$ and $z_l^* = \dfrac{z_{l+1} + z_l}{2}$ is the midpoint of layer l. Notice that if the stacking sequence is symmetric with respect to the midplane, the second and third term appearing in (5.43) vanish and membrane and bending behaviour result again uncoupled.

The operative formulas for the implementation of the elemental stiffness matrix of the ESL extension of the homogeneous DKT-CST element above formulated are obtained from (5.43) by relating the generalized strains to the parameters of the triangular shell element through the 3×18 matrixes of (5.9) and (5.31) and invoking the quadrature formula for the area integral. The final result

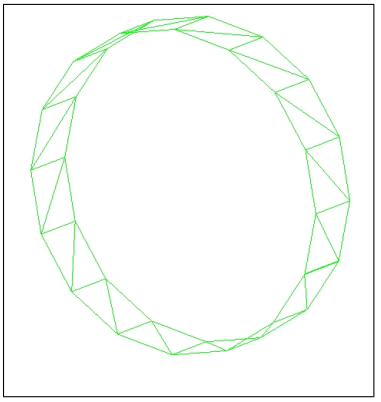

Figure 5.17: View of the 32 elements mesh employed for the slit cylinder bending.

is:

$$\boldsymbol{K}_{LAM}^{(e)} = \sum_{g=1}^{n_g} \sum_{l=1}^{N_L} \begin{bmatrix} h_l \left(\boldsymbol{B}_m^{(e)} \left(\boldsymbol{\xi}_g \right) \right)^T \boldsymbol{D}_l \left(\boldsymbol{\xi}_g \right) \boldsymbol{B}_m^{(e)} \left(\boldsymbol{\xi}_g \right) \\ +h_l z_l^* \left(\boldsymbol{B}_b^{(e)} \left(\boldsymbol{\xi}_g \right) \right)^T \boldsymbol{D}_l \left(\boldsymbol{\xi}_g \right) \boldsymbol{B}_m^{(e)} \left(\boldsymbol{\xi}_g \right) \\ +h_l z_l^* \left(\boldsymbol{B}_m^{(e)} \left(\boldsymbol{\xi}_g \right) \right)^T \boldsymbol{D}_l \left(\boldsymbol{\xi}_g \right) \boldsymbol{B}_b^{(e)} \left(\boldsymbol{\xi}_g \right) \\ +h_l z_l^{*2} \left(\boldsymbol{B}_b^{(e)} \left(\boldsymbol{\xi}_g \right) \right)^T \boldsymbol{D}_l \left(\boldsymbol{\xi}_g \right) \boldsymbol{B}_b^{(e)} \left(\boldsymbol{\xi}_g \right) \end{bmatrix} W_g.$$

Analogous considerations lead to the operative formula for the computation of the nodal forces vector:

$$\boldsymbol{F}_{LAM}^{(e)} = \sum_{g=1}^{n_g} \sum_{l=1}^{N_L} \left[h_l \left(\boldsymbol{B}_m^{(e)} \left(\boldsymbol{\xi}_g \right) \right)^T + h_l z_l^* \left(\boldsymbol{B}_b^{(e)} \left(\boldsymbol{\xi}_g \right) \right)^T \right] \left\{ \begin{array}{c} \sigma_{x'} \left(\boldsymbol{\xi}_g, z_l^* \right) \\ \sigma_{y'} \left(\boldsymbol{\xi}_g, z_l^* \right) \\ \tau_{x'y'} \left(\boldsymbol{\xi}_g, z_l^* \right) \end{array} \right\} W_g.$$

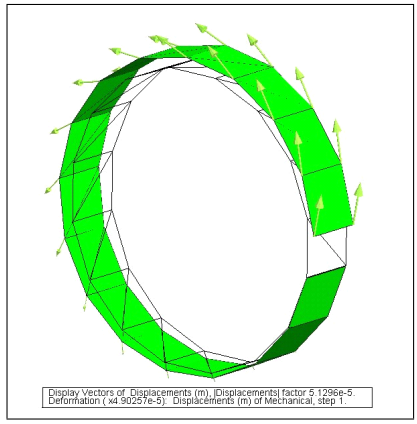

Figure 5.18: Displacement field of the slit cylinder, reported as vectors applied at the nodal points.

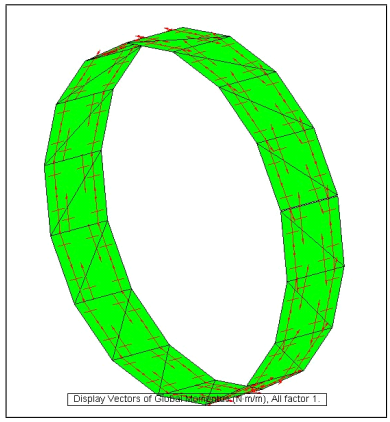

Figure 5.19: Principal bending moments of the slit cylinder at Gauss points.

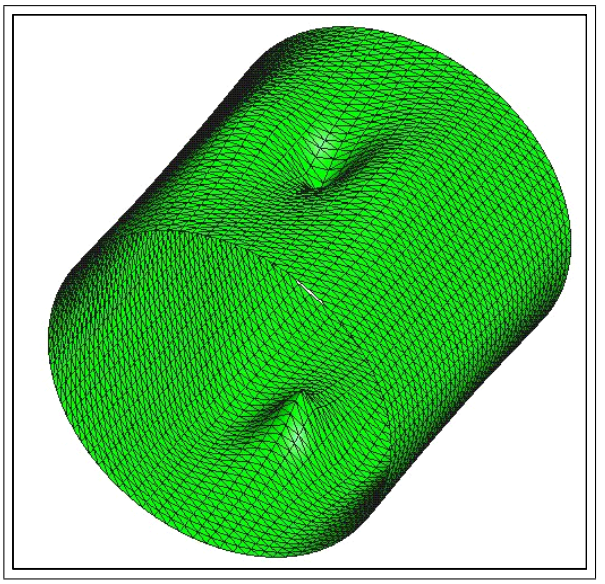

Figure 5.20: Pinched cylinder - deformed configuration. Further data: Young modulus $E = 3000000$, cylinder height $L = 600$, Poisson ratio $\nu = 0.30$, moment $M = 1.00$, thickness $h = 3.0$, radius $R = 300$.

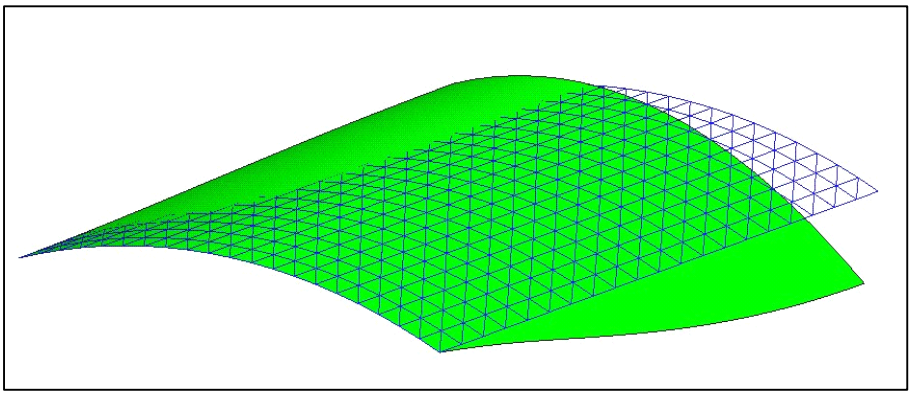

Figure 5.21: Scordelis-Lo roof - deformed configuration and undeformed mesh of 1/4 of structure. Further data: $E = 4.32 \times 10^8$, $L = 50$, $\nu = 0.0$, $F = 1.00$, $h = 0.25$, $R = 25$.

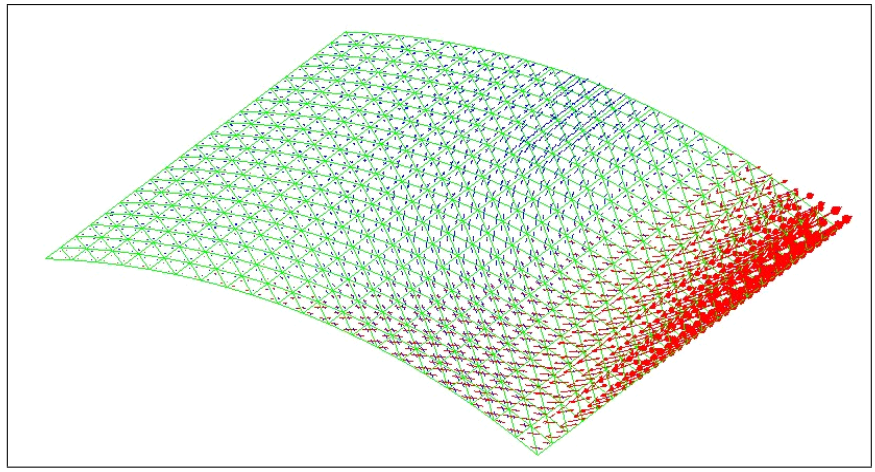

Figure 5.22: Scordelis-Lo roof - Principal membrane stresses obtained with the DKT-CST analysis.

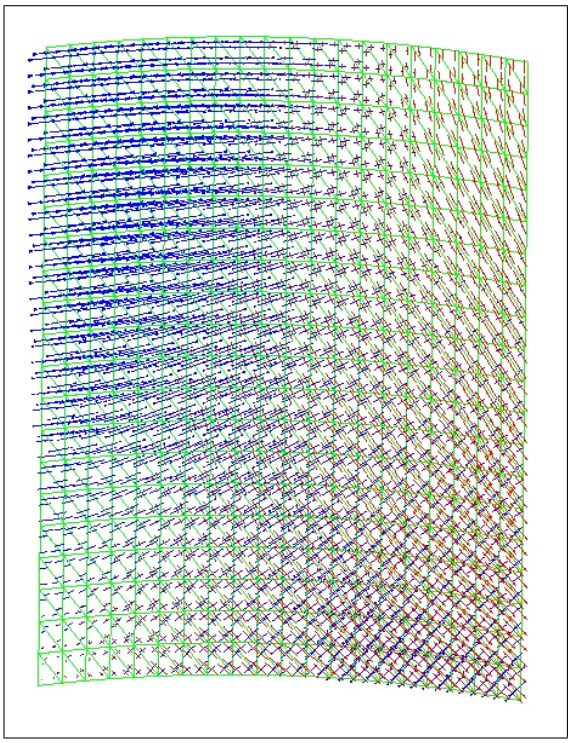

Figure 5.23: Scordelis-Lo roof - Principal bending moments obtained with the DKT-CST analysis.

Chapter 6

Numerical analysis of large scale structural elements

In the present chapter the results concerning the FEM analysis of structural elements made of glass-epoxy and carbon-epoxy LFC are presented. The analyses have been performed employing the ESP constitutive model, exahedral isoparametric first order elements and the ESL DKT-CST element detailed in chapter 5.

6.0.1 Traction tests

Two simple traction static tests up to rupture have been simulated numerically in order to reproduce analogous experimental laboratory tests. The traction tests were executed on two rectangular specimens respectively made up of the laminates carachterized by the ply sequence reported in the tables of figures 6.1(Cross-ply) and 6.2(Angle-ply). The calibrated mechanical properties adopted for component materials are reported in table 6.1.

The tested specimens have been simulated, for both ply sequences, discretizing the geometry with the mesh of triangular elements reported in figure 6.3 and employing DKT-CST laminated elements.

Material	V_f (%)	Angle	Thickness [m]
E-Glass Fiber EBX 400	36	90°	2.15E-04
E-Glass Fiber EBX 400	36	0°	2.15E-04
Carbon Fiber CBX 400	45	90°	5.00E-05
Carbon Fiber CBX 400	45	0°	5.00E-05
E-Glass Fiber EBX 400	36	90°	2.15E-04
E-Glass Fiber EBX 401	36	0°	2.15E-04
E-Glass Fiber EBX 402	36	90°	5.00E-05
E-Glass Fiber EBX 403	36	0°	5.00E-05
E-Glass Fiber EBX 404	36	90°	5.00E-05
E-Glass Fiber EBX 405	36	0°	5.00E-05
Carbon Fiber CBX 400	45	90°	5.00E-05
Carbon Fiber CBX 401	45	0°	5.00E-05
Carbon Fiber CBX 402	45	90°	2.25E-04
Carbon Fiber CBX 403	45	0°	2.25E-04

Figure 6.1: Details of one half of the ply sequence of the 0/90 (Cross-ply) laminate. The laminate is symmetric.

In figure 6.4 the unidirectional longitudinal stress-strain diagrams emerging from the experimental and the numerical tests carried out on the 0/90 laminate are compared. The two curves are in good agreement up to failure.

A photograph of the cross-ply fractured specimen after unloading is reported in figure 6.5.

	Young modulus E [MPa]	**Poisson ratio** ν
epoxy resin	3200	0.35
E-glass fiber	80000	0.22
Carbon fiber	250000	0.2
	Tens. strength Y_{xT} [MPa]	**Compr. strength** Y_{xC} [MPa]
epoxy resin	17	34
E-glass fiber	2650	1325
Carbon fiber	4410	2200

Table 6.1: Mechanical properties adopted for component materials in the traction tests

Material	V_f (%)	Angle	Thickness [m]
E-Glass Fiber EBX 400	36	+45°	2.15E-04
E-Glass Fiber EBX 400	36	-45°	2.15E-04
Carbon Fiber CBX 400	45	+45°	5.00E-05
Carbon Fiber CBX 400	45	-45°	5.00E-05
E-Glass Fiber EBX 400	36	+45°	2.15E-04
E-Glass Fiber EBX 401	36	-45°	2.15E-04
E-Glass Fiber EBX 402	36	+45°	5.00E-05
E-Glass Fiber EBX 403	36	-45°	5.00E-05
E-Glass Fiber EBX 404	36	+45°	5.00E-05
E-Glass Fiber EBX 405	36	-45°	5.00E-05
Carbon Fiber CBX 400	45	+45°	5.00E-05
Carbon Fiber CBX 401	45	-45°	5.00E-05
Carbon Fiber CBX 402	45	+45°	2.25E-04
Carbon Fiber CBX 403	45	-45°	2.25E-04

Figure 6.2: Details of one half of the ply sequence of the +45/-45 (Angle-ply) laminate. The laminate is symmetric.

In figure 6.6 the unidirectional longitudinal stress-strain diagrams emerging from the experimental and the numerical tests carried out on the +45/-45 laminate are compared. The two curves are in good agreement for small strains ($< 0.2\%$). In the range between 0.2% and 1% the numerical results overpredict the experimental results with a relative error around 18%. The ultimate strength emerging from the numerical model is in good agreement with a 13% error over the experimental ultimate strength. The opinion of the author is that the generally stiffer behaviour probably has to be addressed to the necessity of accounting for fiber rotations which are completely neglected by the small strain kinematics. In figure 6.7 a photograph of the angle-ply fractured specimen after unloading is reported.

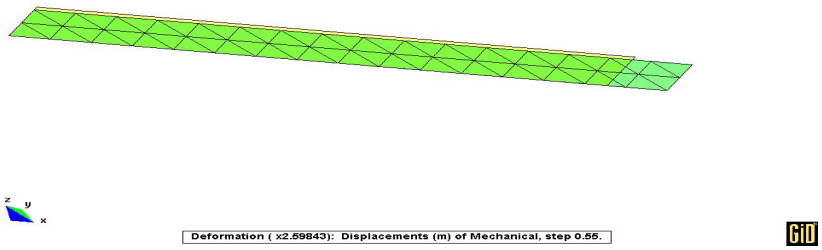

Figure 6.3: Deformed mesh and undeformed shape of the +45/-45 laminate.

6.0.2 Bending tests

Two numerical simulations with the DKT laminated elements and the ESP constitutive model laws are carried out in order to reproduce the experimental static plane-bending test upon two specimens constituted by the same materials and the cross-ply and angle-ply configurations of tables 6.1, 6.2 and 6.1. The geometry of the specimens is reported in figure 6.8.

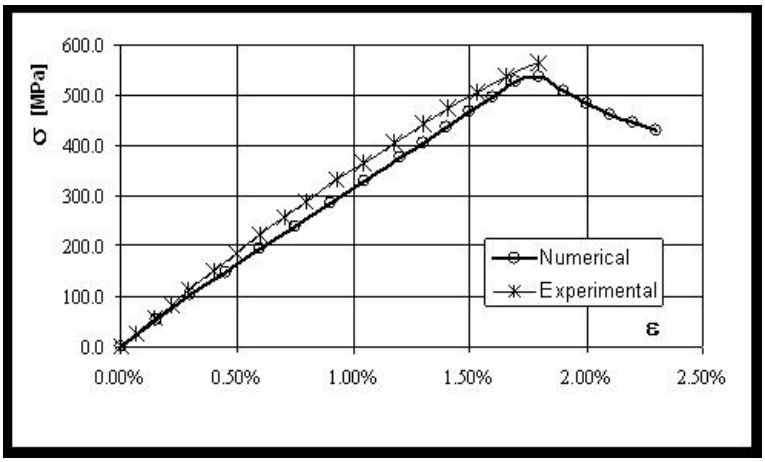

Figure 6.4: Longitudinal unidirectional stress-strain diagram for the 0/90 laminate. Experimental and numerical results.

One quarter of the central rectangular stripe of the cross-ply specimen has been modeled and the relative mesh adopted is reported (in the deformed configuration) in figure 6.10. The mesh reproduces one quarter of the actual geometry of the specimen relying on the double symmetry. In figure 6.9 a comparison of the resulting numerical and experimental deflection vs. load diagrams is reported. The incapability of the numerical model in detecting the lower ultimate strength is due to the structural formulation of the laminated element which neglects the shear deformation and thus is not able to predict the debonding fracture phenomena that occur at the meso-scale.

Figure 6.5: Photograph of the cross-ply specimen at the end of the tensile test.

The mesh reproducing one quarter of the geometry for the angle ply specimen is reported in figure 6.11. The comparison of the resulting numerical and experimental deflection vs. load diagrams shows a poor agreement between numerical and experimental results. The reason for such a lack of correspondence has to be addressed to the same arguments considered for the previous test cases.

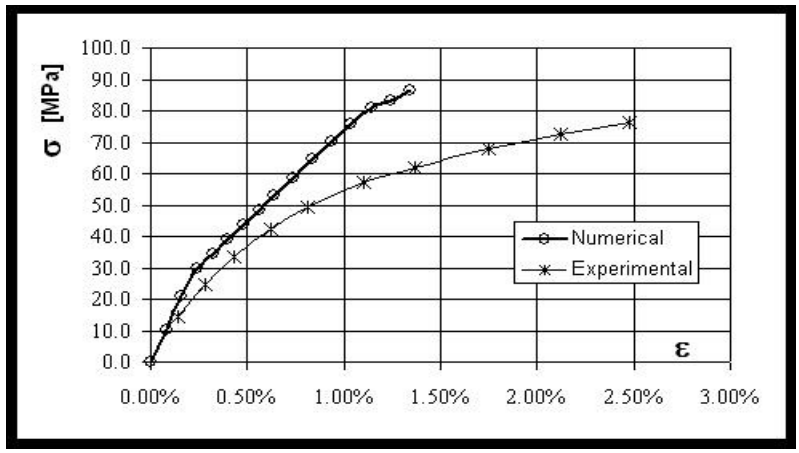

Figure 6.6: Longitudinal unidirectional stress-strain diagram for the +45/-45 laminate. Experimental and numerical results.

In figure 6.13 the principal bending moments drawn at the Gauss points in the deformed configuration of on one quarter of the specimen are reported.

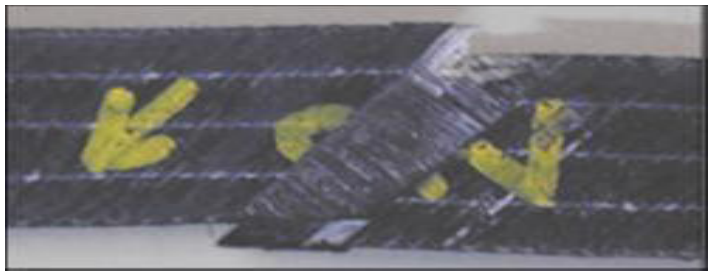

Figure 6.7: Photograph of the angle-ply specimen at the end of the tensile test.

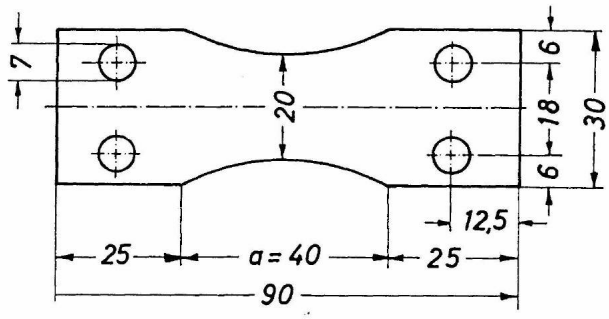

Figure 6.8: Geometry of the specimens subjected to bending tests.

Thin walled sandwich

A four point static bending test performed upon a CFRP thin-walled sandwiches with aluminium honeycomb core is simulated employng exahedral isoparametric elements. The sequence of materials through the thickness of the sandwich is CFRP skin / adhesive / core / adhesive / CFRPskin, as reported in figure 6.14.

The materials and the related properties adopted in the simulation are presented in table 6.2.

.

The CFRP laminate is built with a $(+60/0/-60)$ lamination scheme where each one of the three plies has a thickness of 0.07 mm and a fiber volume fraction

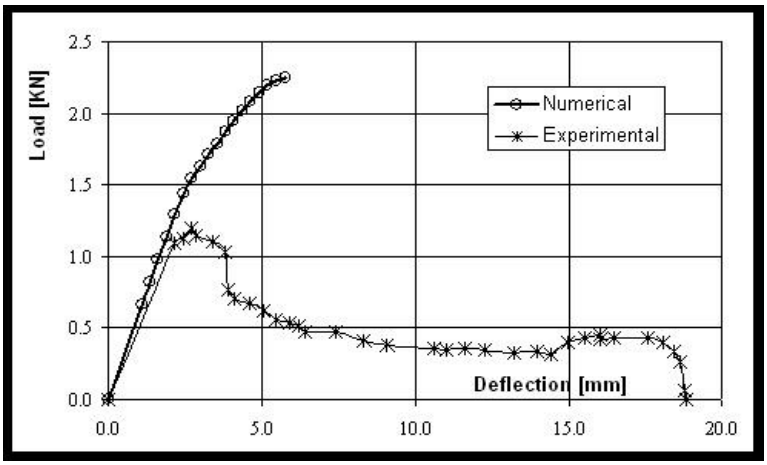

Figure 6.9: Esperimental and numerical load vs. deflection diagrams for the static plane-bending test of the cross-ply specimen.

	Young modulus E [MPa]	**Poiss. ratio** ν
Adhesive	4000	0.39
Aluminium honeycomb	200	0.32
	Tens. strength Y_{xT} [MPa]	**Compr. strength** Y_{xC}
Adhesive	17	17
Aluminium honeycomb	3.5	3.5

Table 6.2: Summary of the mechanical properties adopted in the numerical simulations for the thin walled sandwich.

$V_f = 0.58$. The material properties adopted for the constituent materials are reported in table 6.3.

On the right side of the specimen a region of 40 mm where the adhesive film is damaged is inserted, as reported in figure 6.15.

Figure 6.16 shows a view of the mesh adopted while figures 6.17 and 6.18 show the deformed configuration resulting from the FEM analysis.

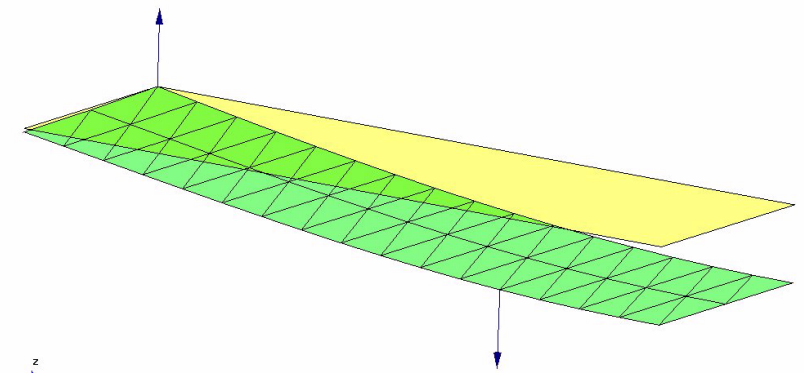

Figure 6.10: Example of the deformed mesh for the bending test on the cross-ply laminate.

	Young modulus E [MPa]	**Poisson ratio** ν
Matrix	4000	0.39
Carbon fiber	500000	0.23
	Tens.strength Y_{xT} [MPa]	**Compr.strength** Y_{xC} [MPa]
Matrix	17	17
Carbon fiber	3500	3500

Table 6.3: Summary of the material properties used for the calibration of the CFRP laminate.

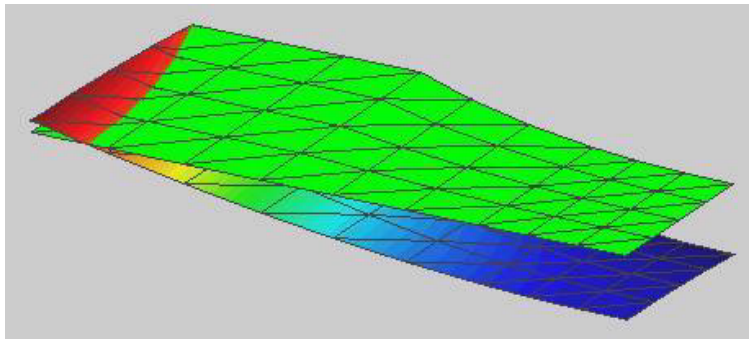

Figure 6.11: Mesh adopted for discretizing the geometry (one quarter) in the simulation of the static bending test on the angle-ply specimen. Undeformed configuration and contour fill of the displacements.

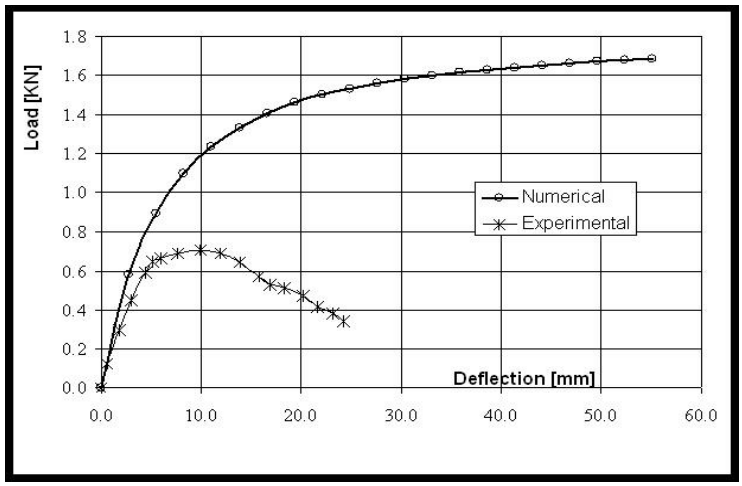

Figure 6.12: Esperimental and numerical load vs. deflection diagrams for the static plane-bending test of the angle-ply specimen.

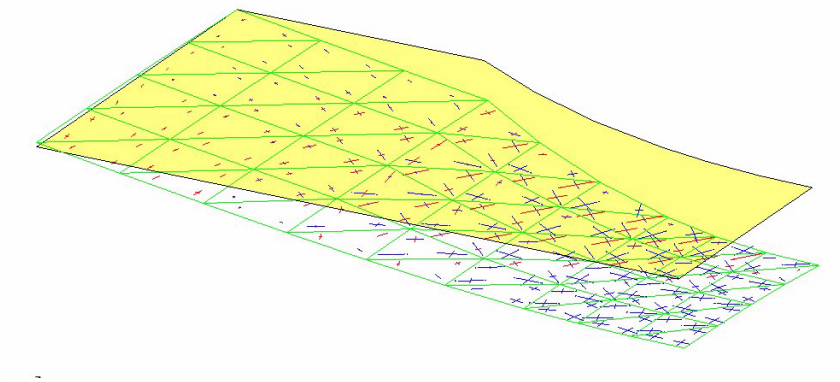

Figure 6.13: Angle-ply specimen subjected to plane-bending test. Mesh in the deformed configuration and representation of the principal moments.

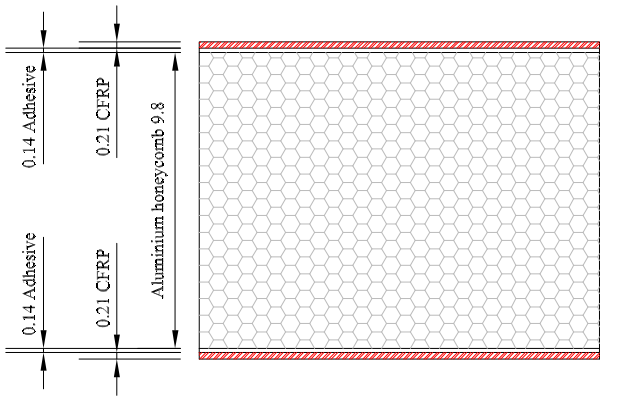

Figure 6.14: Stack sequence of the materials through the thickness of the sandwich.

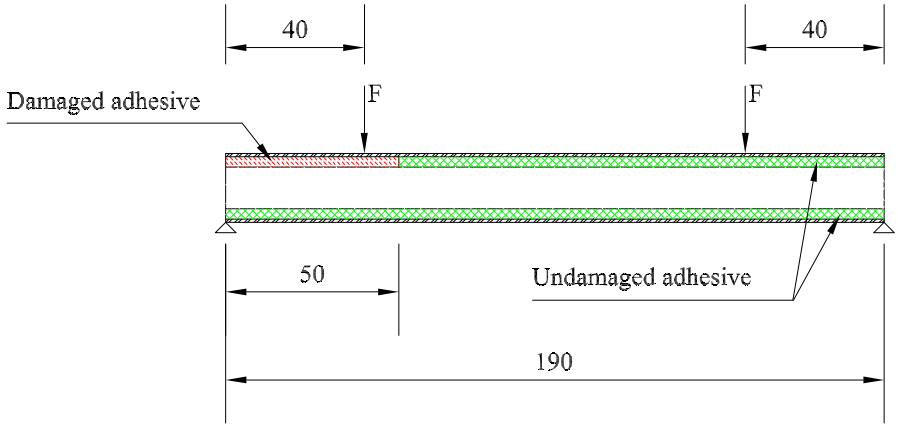

Figure 6.15: Longitudinal geometry of the sandwich (horizontal and vertical drawing scales do not coincide).

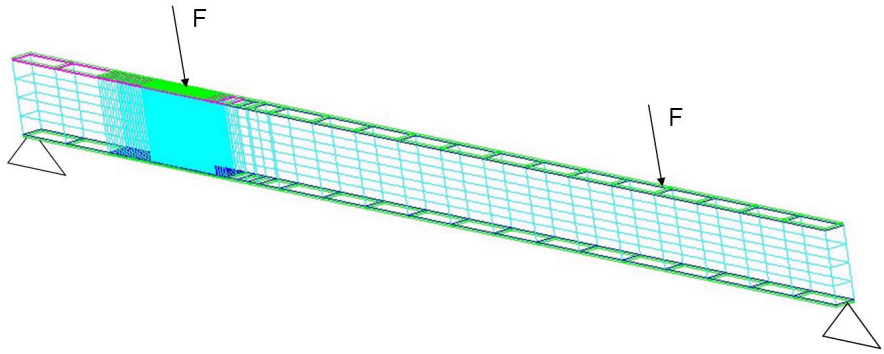

Figure 6.16: View of the 3D mesh of exahedral isoparametric elements; scheme of the constraints and of the loads applied.

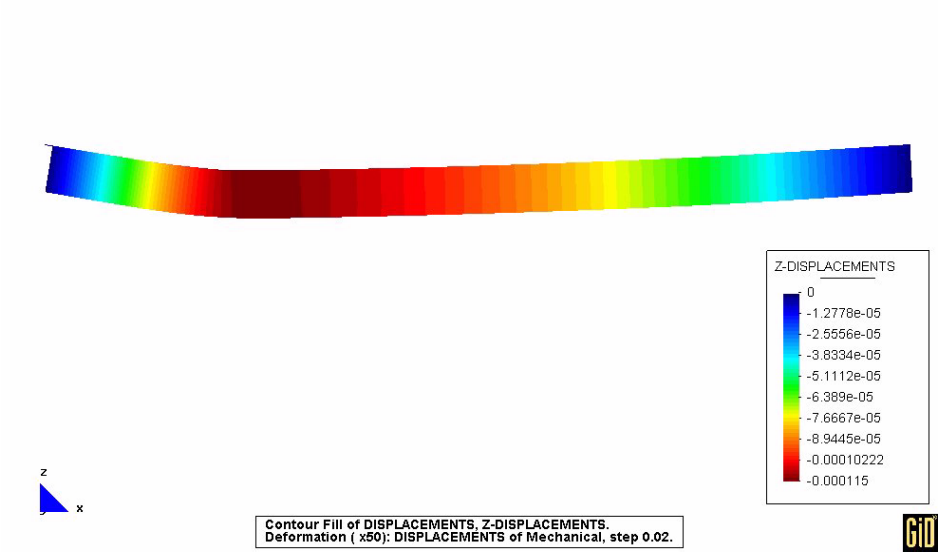

Figure 6.17: Deformed configuration and contour fill of the deflection. Displacements amplified $\times 50$ times.

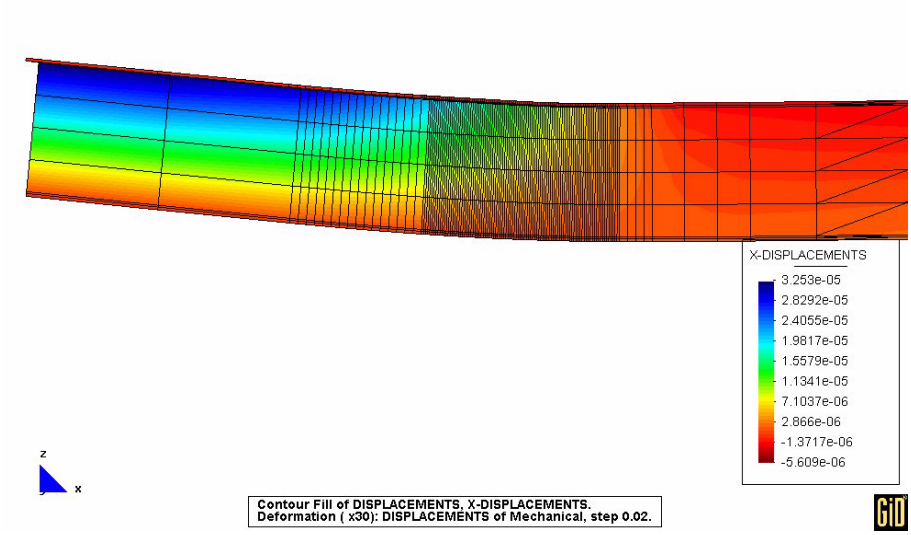

Figure 6.18: Detail of the deformed configuration in the damaged region. Displacements amplified $\times 30$ times.

Chapter 7

Conclusions

In the present thesis a novel constitutive model of composite material with unidirectional long fibers has been formulated with a specific view towards the nonlinear analysis of composite laminated structures by means of the finite element method. The model employs a characterization of the mechanics at the microscale by means of an analytical approach which is based on the combined use of arbitrary constitutive models of component materials, considered to behave as isolated continua, together with an additional *closure equation* that characterizes the micromechanics of the composite from a morphological point of view. Attention has been restricted to linearized kinematics and to a purely mechanical theory; in addition arbitrary constitutive models can be exploited for each phase.

The rationale of the proposed model is represented by a Serial-Parallel continuum approach which has been developed assuming that component materials, i.e. fiber and matrix, behave in parallel along the fibers alignment direction and in series along all directions orthogonal to the fibers. The basic version of the proposed model, denominated Basic Serial-Parallel (BSP), assumes equal component strains in the fiber direction and equal stresses in the transverse directions by means of a closure equation originally exploited by Dvorak et al. [32] and by Rastellini et al. [93].The enhanced version of the model, denominated Enhanced Serial-Parallel (ESP), encompasses generalized closure equations specifically devised to account for the non-uniformity of the transverse strain and stress fields and entails improved estimates of the transversal stiffness predicted by the BSP.

A computational methodology for the solution of the governing equations has been devised both for the BSP and the ESP models. Its implementation in a finite element code has been used to perform an extensive set of numerical simulations.

To this end both models, which refer to a single composite lamina, have been further combined with classical lamination theory to describe the behaviour of laminates consisting of unidirectional continuously reinforced layers.

The accuracy attained in the simulation of the non-linear response of FRP composite laminates has been ascertained by comparing the numerical results with analogous analytic formulations and experimental findings published in the literature. Specifically, the validation of the constitutive model by means of experimental results has been achieved by adopting the general protocol set forth in the blind prediction named *WorldWide Failure Exercise (WWFE)*, proposed in 1998 in a special edition of the journal *Composites Science and Technology.* To this end an isotropic damage model with two different damage variables for tension and compression has been selected from the literature as component constitutive law for both fiber and matrix and a calibration procedure to transform the input provided by the benchmark into the parameters of the component constitutive models has been defined.

The main outcome of this set of validations is a good overall performance of the ESP model which can be summarized as follows:

1. accurate estimates of the initial elastic stiffness, in good agreement with the values provided by Halpin-Tsai formulas;

2. accurate modelling of the nonlinear stress-strain curves of the composite;

3. estimates of the failure envelopes which are comparable with those obtained by Puck [84] and Tsai [63], i.e. the authors who ranked at the first places in the WWFE;

4. quadratic convergence of the nonlinear constitutive algorithm under the assumption that the constitutive algorithms employed for each component material do possess the same feature.

On the basis of the above mentioned validation tests, the ESP model can be considered as a reliable tool in the non-linear analysis of LFC proving to be, at the same time, competitive from the computational point of view when compared to multi-scale analysis techniques.

For small strains ($\varepsilon < 0.2\%$) the mechanical response of large scale structures predicted by isoparametric hexahedral finite elements endowed with the ESP constitutive law turned out to be in good agreement with experimental results

while, for larger strains, the numerical results overpredict the experimental ones due to the assumed kinematical setting.

Future lines of research will be directed towards a further enhancement of the micromechanical description aiming at improving the predictive capabilities of the proposed model for the determination of failure envelopes and, more generally, for the simulation of the mechanical behaviours of LFC in the non-linear range. The first line of research will concern the effect of local buckling and its coupling with the influence of shear stress states on the lamina longitudinal compressive strength. Furthermore the constitutive formulation presented in this thesis will be extended to a finite deformation setting and damage models specifically devised for polymer materials will be incorporated in the ESP model.

Bibliography

[1] Aboudi J. (1988). Micromechanical analysis of the strength of unidirectional fiber composites, *Composite Science and Technology*, **33**, 79-96.

[2] Aboudi J. (1989). Micromechanical analysis of composites by the method of cells, *Applied Mechanics Review*, **42**, 193-221.

[3] Aboudi J. (1991). *Mechanics of Composite Materials: a Unified Micromechanical Approach*, Elsevier, Amsterdam.

[4] Aboudi J. and Pindera M.J. (1992). Micromechanics of metal matrix composites using the Generalized Method of Cell model (GMC): user's guide, NASA CR 190756.

[5] Aboudi, J., (1996). Micromechanical analysis of composites by the method of cells-update. *Applied Mechanics Review*, **49**(10), S83-S91.

[6] Adams D.F. and Doner D.R. (1967). Longitudinal shear loading of a unidirectional composite, *Journal of Composite Materials*, January, 4-17.

[7] Allwood R.J. and Cornes G.M. (1969). A polygonal finite element for plate bending problems using the assumed stress approach, *International Journal for Numerical Methods in Engineering*, **1**, 135-149.

[8] Argirys J.H., Dunne P.C., Malejannakis G.A. and Shelkle E. (1977). A simple triangular facet shell element with applications to linear and nonlinear equilibrium and elastic stability problems, *Computer Methods Applied to Mechanical Engineering*, **10**, 371-403.

[9] Bahei-El-Din Y.A., and Dvorak G.J. (1979). Plastic yielding at a circular hole in a laminated FP-AL Plate, *Modern Developments in Composite Materials and Structures*, J. R. Vision, ed. ASME, 123-147.

[10] Bahei-El-Din Y.A., Dvorak G.J. and Utku S. (1980). Finite element analysis of elastic-plastic fibrous composite structures, *Computers and Sructures*, **13**, 321-330.

[11] Barbero E.J., Reddy J.N. and Teply J.L. (1990). General two-dimensional theory of laminated cylindrical shells, *A.I.A.A. Journal*, **28**(3), 544-553.

[12] Barbero E.J. (1998). *Introduction to composite materials design*, Taylor and Francis, London (UK).

[13] Barbero E.J. and De Vivo L. (2001). A constitutive model for elastic damage in fiber-reinforced PMC laminae, *Journal of Damage Mechanics*, **10**(1) 73-93.

[14] Bartholomew P. (1976). Comment on hybrid finite elements, *International Journal for Numerical Methods in Engineering*, **10**(4), 968-973.

[15] Batoz J.L., Bathe K.L., Ho L.W. (1980). A study of three node triangular plate-bending elements, *International Journal for Numerical Methods in Engineering*, **15**, 1771–1812.

[16] Batoz J.L. (1982). An Explicit Formulation for an Efficient Triangular Plate-Bending Element, *International Journal for Numerical Methods in Engineering*, **18**, 1077–1089.

[17] Betten J. (1981). Creep theory of anisotropic solids, *Journal of Rheology*, **25**, 565-581.

[18] Betten J. (1988). Application of tensor functions to the formulation of yield criteria for anisotropic materials, *International Journal of Plasticity*, **4,** 29-46.

[19] Böhm H.J. and Rammerstorfer F.G. (1995). Fiber arrangement effects on the microscale stresses of continuously reinforced MMCs, in *Microstructure-Property Interactions in Composite Materials*, (Ed. R. Pyrz),51-62, Kluwer Acad. Publ., Dordrecht, The Netherlands.

[20] Car E., Oller S., Oñate E. (2000). An anisotropic elastoplastic constitutive model for large strain analysis of fiber reinforced composite materials, *Computer Methods Applied to Mechanical Engineering*, **185** (2), 245–277.

[21] Car E., Oller S., Oñate, E. (2001). A large strain plasticity model for anisotropic materials-composite material application, *International Journal of Plasticity*, **17** (11), 1437–1562.

[22] Car E., Zalamea F., Oller S., Miquel J., Oñate E., (2002). Numerical simulation of fiber reinforced composite materials-two procedures, *International Journal for Solids and Structures*, **39** 1967–1986.

[23] Carpenter N., Stolarski H., Belytschko T. (1986). Improvements in 3-Node Triangular Shell Elements, *International Journal for Numerical Methods in Engineering*, **23**, 1643–1667.

[24] Cervera M. (2003). Viscoelasticity and rate dependent continuum damage models, *Informe Técnico CIMNE*, IT-M79.

[25] Chaudhuri R.A. and Seide P. (1987). Triangular finite element for analysis of thick laminated plates, *International Journal for Numerical Methods in Engineering*, **24**, 1203-1224.

[26] Clough R.W. and Tocher J.L. (1965). Finite element stiffness matrices for analysis of plate bending, *Proc. Conf. on Matrix Methods in Structural Mechanic, WPAFB*, Ohio, 515-545.

[27] Clough R.W. and Johnson C.P. (1968). A finite element approximation for the analysis of thin shells, *International Journal for Solids and Structures*, **4**, 43-60.

[28] Cervera M., Agelet C. and Chiumenti M. (2002). *COMET: "Coupled Mechanical and Thermal Analysis" Data input manual*, Technical Report CIMNE N^o IT-308. Barcelona.

[29] Cook R.D., Malkus D.S., Plesha M.E. (1989). *Concepts and Applications of Finite Element Analysis*, Third Edition, Wiley.

[30] Dhatt G. (1969). Numerical analysis of thin shells by curved triangular elements based on discrete Kirchhoff hypotesis, *Proc. ASCE symp. On application of FEM in Civil Engineering*, Vanderbilt Univ., Nashville, Tenn., 13-14.

[31] Dhatt G. (1970). An efficient triangular shell element, *A.I.A.A. Journal*, **8**, 2100-2102.

[32] Dvorak G.J. and Bahei-El-Din Y.A. (1982). Plasticity analysis of fibrous composites, *ASME Journal of Applied Mechanics*, **49**, 327-335.

[33] Dvorak G.J. and Johnson W.S. (1980). Fracture of metal matrix composites, *International Journal of Fracture*, **16**, 585-607.

[34] Dvorkin E.N., Bathe K.J. (1984). A continuum mechanics four-node shell element for general nonlinear analysis, *Engineering Computations*, **1**, 77–88.

[35] Edge E. C. (1994). Does transverse and shear loading affect thecompression strength of unidirectional CFC? A reply to Dr Hart-Smith, *Composites*, **25**, 159-164.

[36] Forster R, Knappe W. (1970). Kunststoffe, **60**(12), 1053.

[37] Fried I. (1973). Shear in C^0 and C^1 bending finite elements, *International Journal for Solids and Structures*, **9**(4), 449-460.

[38] Fried I. (1974). Residual energy balancing technique in the generation of plate bending finite elements, *Computers and Structures*, **4**(4), 771—778.

[39] Fried I. and Yang S.K. (1973). Triangular, nine-degrees of freedom, C^0 plate bending element of quadratic accuracy, *Quarterly of Applied Mathematics*, **31**(3), 303—312.

[40] Gallagher R.H. (1975). Shell elements, *Proc. World Congr. on F.E.M., in Structural Mechanics*, **1**, Bournemouth, England.

[41] Gallagher R.H. (1977). Geometrically nonlinear shell analysis, *Proc. Int. Conf. in Nonlinear Solid and Structural Mechanics*, Col-1/Col-26, Gelio, Norway.

[42] Green A. and Naghdi P. (1965). A dynamical theory of interacting continua, *Journal Engineering Science*, 3 3-231.

[43] Greenwood J. H. (1977). German work on GRP design. *Composites*, 175-184.

[44] Halpin J.C. and Tsai S.W. (1969). Effects of environmental factors on composite materials, Air Force Materials Lab-Technical report, Department of Defense, (USA), 67-423.

[45] Halpin J. C. and Kardos J. L. (1976). The Halpin-Tsai equations: A review, *Polymer Engineering and Science*, **52**, 344-352.

[46] Hart-Smith L. J. (1993). Fibrous composite failure criteria - Fact and fantasy. *7th Int. Conf. on Composite Structures*, Paisley, UK, McDonnell Douglas MDC 93 K0047.

[47] Hashin Z. and Rosen B.W. (1964).The elastic moduli of fibre-reinforced materials, *Journal of Applied Mechanics*, **31**, 223-232.

[48] Hashin Z. (1980). Failure criteria for unidirectional fiber composites, *Journal of Applied Mechanics*, 1980, **47**, 329-334.

[49] Hashin Z., (1983). Analysis of Composite materials, a survey, *Journal of Applied Mechanics*, **50**, 481-505.

[50] Hill R., (1964) Theory of mechanical properties of fibre strengthened materials: I - Elastic behavior, *Journal of the Mechanics and Physics of Solids*, **12**, 199-212.

[51] Hill R. A. (1965). Self-consistent mechanics of composite materials, *Journal of the Mechanics and Physics of Solids*, **13**, 213-225.

[52] Hinton M. J. and Soden P. D. (1998). Predicting failure in composite laminates: the background to the exercise, *Composites Science and Technology*, **58**(7), 1001-1010.

[53] Hinton M.J., Kaddour A.S., Soden P.D. (2002). Comparison of the predictive capabilities of current failure theories for composite laminates, judged against experimental evidence, *Composites Science and Technology*, **62**, 1725–1797.

[54] Horrigmoe G. (1977). Hybrid stress finite element model for nonlinear shell problems, *Proc. 6th Canadian Conf. on Applied Mech.*, U.B.C. Vancouver, Canada.

[55] Hoskin B.C. and Baker A.A. (1986). *Composite Materials for Aircraft Structures*, 1st edition, AIAA, New York.

[56] Hsu K.F.J. and Fahrenthold E.P. (1991). Evaluation of the Vanishing-Fiber Diameter Model for Composite Plasticity, *Journal of Engineering Materials and Technology*, **113**, 465-474.

[57] Hull D. (1987). An introduction to composite materials, Cambridge University Press.

[58] Hütter U., Schelling H., Krauss H. (1974). An experimental study to determine failure envelope of composite materials with tubular specimen under combined loads and comparison between several classical criteria, in: *Failure Modes Of Composite Materials With Organic Matrices And Other Consequences On Design, NATO, AGRAD*, Conf Proc No. 163, Munich, Germany, 13–19 October 1974.

[59] Jones R.M. (1975). *Mechanics of composite materials*, McGraw-Hill, New York (USA).

[60] Kaddour A. S., Hinton M. J. & Soden P. D. (2004). "A comparison of the predictive capabilities of current failure theories for composite laminates: additional contributions". *Composites Science and Technology*, Vol. 64, 449-476.

[61] Kikuchi F. (1975). On a finite element scheme based on the discrete Kirchhoff assumption, *Numerische Mathematik* , **24**, 211—231.

[62] Krauss H, Schelling H. (1969). Kunststoffe, **59**(12), 911–7.

[63] Liu K.S. and Tsai S.W. (1998). A progressive quadratic failure criterion for a laminate, *Composites Science and Technology*, **58**, 1023–1032.

[64] MacNeal R.H., Harder R.L. (1985). A proposed standard set of problems to test finite elements accuracy, *Finite Elements in Analysis and Design*, **1**, 3-20.

[65] Neale B.K., Henshell R.D. and Edwards G. (1972). Hybrid plate bending elements, *Journal of Sound Vibration*, **23**(1), 101-112.

[66] Neamtu L., Oller S. and Oñate E. (1997). A generalized mixing theory elasto-damage-plastic model for finite element analysis of composites, in D. Owen, E. Oñate and E. Hinton (Eds.), *Computational Plasticity*, CIMNE, 1214-1219.

[67] Noguchi M. (1993). Present and future of composite materials for automotive application in Japan, in A. Miravete (Ed.), *Proceedings of the Ninth International Conference on Composite Materials ICCM 9 Metal Matrix Composites*, Zaragoza, Spain, 97-110.

[68] Noor A.K. (1973). Mixed finite-difference scheme for analysis of simply supported thick plates, *Computers and Structures*, **3**, 967-982.

[69] Noor A.K. (1973). Free vibrations of multilayered composite plates, *A.I.A.A. Journal*, **11**, 1038-1039.

[70] Oller S., Oñate E., Miquel J., Botello S. (1996). A plastic damage constitutive model for composite materials, *International Journal for Solids and Structures*, **33**(17), 2501-2518.

[71] Oller S., Botello S., Miquel J.,Oñate E. (1995). An anisotropic elastoplastic model based on an isotropic formulation, *Engineering Computations*, **12**(3) 245-262.

[72] Olson M.D., Bearden T.W. (1979). A simple flat triangular shell element revisited, *International Journal for Numerical Methods in Engineering*, **14**, 51-68.

[73] Ortiz M., Popov E. (1982). Plain concrete as a composite material, *Mechanics of Materials,* **1** 139-150.

[74] Owen M. J. and Rice D. I. (1982). Biaxial strength behaviour of glass-reinforced polyester resins, *Composite materials: testing and design*, ASTM STP 787, ed. I.M. Daniel, 124-144.

[75] Owen D.R.J. and Li Z.H. (1987). A refined analysis of laminated plates by finite element displacement methods - I. Fundamentals and static analysis, *Computers and Structures*, **26**(6), 907-914.

[76] Owen D.R.J. and Li Z.H. (1987). A refined analysis of laminated plates by finite element displacement methods - II. Vibration and stability, *Computers and Structures*, **26**(6), 915-923.

[77] Paley M. and Aboudi J. (1992). Micromechanics analysis of composites by the generalized cell model, *Mechanics of Materials*, **14**, 127-139.

[78] Parry T. V. and Wronski A. S. (1982). Kinking and compressive failure in unaxially aligned carbon fibre tested under superimposed hydrostatic pressure, *Journal of Materials Science*, **17**, 893-900.

[79] Puck A. (1969). Calculating the strength of glass fibre/plastic laminates under combined load, *Kunststoffe-German Plastics*, **55**, 18-19.

[80] Puck A. and Schneider W. (1969). On failure mechanisms and failure criteria of filament-wound glass-fibre/resin composites, *Plastics and Polymers*, Feb., 33-43.

[81] Puck A. (1992). Fracture criteria for highly stressed fibre-plastic composites which meet requirements of design practice. *Kunststoffe-German Plastics*, **82**, 34-38 (German text 49-155).

[82] Puck A. (1992) Should fibre-plastics composites be designed with strain or stress criteria?, *Kunststoffe-German Plastics*, **82**, 34-36.

[83] Puck A. (1996). *Festigkeitsanalyse von Faser-Matrix-Laminaten, Modelle für die Praxis (Strength Analysis of Fibre-Matrix/Laminates, Models for Design Practice)*, Carl Hanser Verlag, Munich, Germany.

[84] Puck A., Schürmann H. (1998). Failure analysis of FRP laminates by means of physically based phenomenological models, *Composites Science and Technology.*, **58**, 1045–1057.

[85] Puck A., Kopp J. and Knops M. (2002). Guidelines for the determination of the parameters in Puck's action plane strength criterion, *Composites Science and Technology*, **62**, 371-378.

[86] Puck A., Schürmann H. (2002). Failure analysis of FRP laminates by means of physically based phenomenological models, *Composites Science and Technology*, **62**, 1633–1662.

[87] Pagano N.J. (1969). Exact solutions for composite laminates in cylindrical bending, *Journal of Composite Materials*, **3**, 398–411.

[88] Pagano N.J. (1970). Exact solutions for rectangular bidirectional composites and sandwich plates, *Journal of Composite Materials*, **4**, 20—34.

[89] Pagano N.J. and Hatfield S.J. (1972). Elastic behavior of multilayered bidirectional composites, *A.I.A.A. Journal*, **10**, 931-933.

[90] Ramberg W. and Osgood W. R. (1943). Description of stress-strain curves by three parameters. Tech. Note 902, National Advisory Committee for Aeronautics, Washington

[91] Rastellini F., Oller S., Salomón O., Oñate E. (2003). Teoría de mezclas serie-paralelo avanzada para el análisis de materiales compuestos. *Materiales Compuestos 2003 - AEMAC*, Zaragoza, 729-741.

[92] Rastellini F., Oller S., Salomón O., Oñate E., (2003). Advanced serial-parallel mixing theory for composite materials analysis. Continuum basis and finite element applications. *7th Int. Conf. on Computational Plasticity – Complas VII*. Ed. E. Oñate, D. R. Owen, Barcelona, CIMNE, on CD-ROM.

[93] Rastellini F., Oller S., (2004). Modelado numérico de no linealidad constitutiva en laminados compuestos - Teoría de mezclas, *Métodos Computacionais em Engenharia. Lisboa* (Portugal): APMTAC.

[94] Rastellini F., Serpieri R. (2004). Implementación del elemento lámina lineal y triangular tipo DKT-CST en el código FEM COMET, *Informe Técnico CIMNE IT-434*.

[95] Razzaque A. (1973). Program for triangular bending elements with derivative smoothing, *International Journal for Numerical Methods in Engineering*, **6**, 333-343.

[96] Reddy J.N. (1987). A generalization of two-dimensional theories of laminated composite plates, *Communications in Applied Numerical Methods*, **3**, 173-180.

[97] Reddy J.N. (2004). *Mechanics of laminated composite plates and shells - Theory and analysis*, 2nd edition. CRC Press, New York (USA).

[98] Ren J.G. (1987). Exact solutions for Laminated cylindrical shells in cylindrical bending, *Composite Science and Technology*, **29**, 169-187.

[99] Reuss A., (1929). Berechnung der fliebgrenze von mischkristallen auf grund der plastizitätsbedingungfür einkristalle, *Z.A.M.M.*, **9**, 49-58.

[100] Rosen B. (1965), *Fiber Composite Materials*, ASM Metals Park, Ohio, 37-45.

[101] Failure of polymeric composite structures: Mechanisms and Criteria for Prediction of Performance, *SERC/ I.Mech.E Annual Expert Meeting*, 23-25 September 1991, Sopwell House, St.Albans, UK (A report compiled by C.E. Neal-Sturgress).

[102] Savoia M. and Reddy J.N. (1992). A variational approach to three-dimensional elasticity solutions of laminated composite plates, *Journal of Applied Mechanics*, **59**, S166-S175.

[103] Seide P. (1980). An improved approximate theory for the bending of laminated plates, *Mechanics Today*, **5**, 451-466.

[104] Simo J.C. and Hughes T.J.R. (1998). *Computational inelasticity*, Springer Verlag, Berlin.

[105] Simo J.C. and Ju, J.W. (1987). Strain- and stress-based continuum damage models I. Formulation., *International Journal of Solids and Structures*, **23**, 821-840.

[106] Simo J.C. and Ju J.W. (1987). Strain- and stress-based continuum damage models II. Computational aspects., *International Journal of Solids and Structures*, **23**, 841-869.

[107] Soden P. D., Hinton M. J. and Kaddour A. S. (1998). A comparison of the predictive capabilities of current failure theories for composite laminates, *Composites Science and Technology*, **58**, 1225-1254.

[108] Soden P. D., Hinton M. J. and Kaddour A. S. (2002). Biaxial test results for strength and deformation of a range of E-glass and carbon fibre reinforced composite laminates: failure exercise benchmark data, *Composites Science and Technology*, **62**, 1489–1514.

[109] Soden P. D., Hinton M. J. and Kaddour A. S. (1998). Lamina properties, lay-up configurations and loading conditions for a range of fibre-reinforced composite laminates, *Composites Science and Technology*, **58**(7), 1011-1022.

[110] Srinivas S., Joga Rao C.V. and Rao A.K. (1970). An exact analysis for vibration of simply supported homogeneous and laminated thick rectangular plates, *Journal of Sound and Vibration*, **12**, 187-199.

[111] Srinivas S. and Rao A.K. (1970). Bending, vibration and buckling of simply supported thick orthotropic rectangular plates and laminates, *International Journal of Solids and Structures*, **6**, 1463-1481.

[112] Strickland G.E. and Loden W.A. (1968). A doubly curved triangular shell element, *Proc. II Conf. Matrix Methods in Structural Mechanics*, Wright-Patterson Air Force Base, Ohio.

[113] Stricklin J.A., Haisler W., Tisdale P., Gunderson R. (1969). A rapidly converging triangular plate element, *A.I.A.A. Journal*, **7**, 180-181.

[114] Sun C. and Chen J.L. (1989). A simple flow rule for characterizing the nonlinear behavior of fiber composites, *Journal of Composite Materials*, **23**, 1009-1020.

[115] Suquet P. (1987). *Homogeneization techniques for composite media - Elements of homogeneization for inelastic solid mechanics*, 193-279, Springer Verlag, Berlin.

[116] Swanson S. R. and Christoforou A. P. (1987). Progressive failure in carbon/epoxylaminates under biaxial stress. *J. Eng. Mat. Tech*, Trans. ASME, **109**, 12-16.

[117] Swift J.W. and Heller R.A. (1974). Layered beam analysis, *Journal of the Engineering Mechanics Division, ASCE*, **100**, 267-282.

[118] Tang P. (1988). A multiaxial failure criterion for composites, *Computational Probabilistic Methods*, AMD/ASME, V93, ASME, New York, USA, 1988, 87-96.

[119] Teply J.L. and Reddy J.N. (1990). Unified formulation of micromechanics models of fiber-reinforced composites, *Inelastic Deformation of Composite Materials*, Dvorak G.J., Springer-Verlag, New York, 341-370.

[120] Timoshenko S., Goodier J.N. (1968). *Teoría de la elasticidad*, Urmo, Bilbao.

[121] Timoshenko S., Woinowsky S. (1969). *Theory of plates and shells*, McGraw-Hill, New York.

[122] Trusdell C. and Toupin R. (1960). *The classical Field Theories. Handbuch der Physik III/I*, Springer Verlag, Berlin.

[123] Tsai S. W. and Wu E. M. (1971). A general theory of strength for anisotropic materials. *Journal of Composite Materials*, **5**, 58-80.

[124] Tsai S. W. (1992). *Theory of Composites Design*, Think Composites, Palo Alto.

[125] Varadan T.K. and Bhaskar K. (1991). Bending of laminated orthotropic cylindrical shells - an elasticity approach, *Composite Structures*, **17**, 141-156.

[126] Voyiadjis G.Z. and Thiagarajan G. (1995). An anisotropic yield surface model for directionally reinforced metal matrix composites, *International Journal of Plasticity*, **11**, 867-894.

[127] Whitney J.M. (1969). The effect of transverse shear deformation in the bending of laminated plates, *Journal of Composite Materials*, **3**, 534-547.

[128] Washizu K. (1975). *Variational Methods in Elasticity and Plasticity*, 2nd ed, Pergamon Press, Oxford.

[129] Zalamea F., (2001). *Tratamiento Numérico de Materiales Compuestos Mediante la teoria de Homogeneización*. Ph.D. Thesis, Universidad Polit ecnica de Cataluña.

[130] Car E., Zalamea F., Oller S., Miquel J. and Oñate E. (2002). Numerical simulation of fiber reinforced composite materials - two procedures, *International Journal of Solids and Structures,* **39**, 1967–1986.

[131] Ziegler H. (1959). A modification of Prager hardening rule, *Quarterly of Applied Mathematics*, **17**, 55-65.

[132] Zienkiewicz O.C. and Taylor R. (1994). *El Método de Elementos Finitos, Vol. I*, McGraw-Hill Cimne.